Itinerant Spin Dynamics in Iron-based Superconductors and Cerium-based Heavy-Fermion Antiferromagnets

Von der Fakultät Mathematik und Physik der Universität Stuttgart
zur Erlangung der Würde eines Doktors der Naturwissenschaften
(Dr. rer. nat.) genehmigte Abhandlung

vorgelegt von

Gerd Friemel
aus Meißen

Hauptberichter:	Prof. Dr. Bernhard Keimer
Mitberichter:	Prof. Dr. Martin Dressel
Tag der mündlichen Prüfung:	26. Mai 2014

Max Planck Institut für Festkörperforschung

Stuttgart 2014

Contents

Abbreviations vii

Zusammenfassung in deutscher Sprache ix

Abstract xiii

1 Introduction 1
1.1 Scope of the thesis . . . 3

2 The phase diagram of correlated electron systems 7
2.1 The family of iron arsenide superconductors . . . 7
2.1.1 Electronic structure and Fermi surface of FeSC . . . 10
2.1.2 Reciprocal-space structure of the spin fluctuations in FeSC . . . 12
2.1.3 Unconventional order parameter in the superconducting phase of FeSC . . . 13
2.2 The family of alkali-metal iron selenide superconductors . . . 15
2.2.1 Electronic structure of the superconducting phase . . . 16
2.2.2 $A_xFe_{2-y}Se_2$: Phase separation into insulating $A_2Fe_4Se_5$ and superconducting $A_xFe_2Se_2$ . . . 17
2.3 Unconventional superconductivity in heavy-fermion compounds . . . 20
2.4 The magnetic phase diagram of CeB_6 . . . 21
2.4.1 Crystal structure and ground state of CeB_6 . . . 21
2.4.2 Magnetic structure in the antiferromagnetic and antiferroquadrupolar phase of CeB_6 . . . 23
2.4.3 Mean-field description of the phase diagram . . . 26
2.4.4 Electronic properties of CeB_6 . . . 29
2.4.5 Alternative approach to phase II . . . 33
2.4.6 Appearance of phase IV in $Ce_{1-x}La_xB_6$ . . . 35
2.4.7 Non-Fermi-liquid regime of $Ce_{1-x}La_xB_6$ . . . 37
2.4.8 Status of the CeB_6 problem at the outset of the thesis . . . 38

3 Magnetism and spin dynamics in metals: theoretical considerations 41
3.1 The physics of heavy-fermion systems . . . 41
3.1.1 Kondo lattice systems . . . 43
3.1.2 Itinerant *vs.* localized behavior . . . 45

3.2 Itinerant ferro- and antiferromagnetism 47
3.2.1 Spin fluctuations in nearly ferro-and antiferromagnetic materials 50
3.2.2 Dynamical susceptibility in nearly antiferromagnetic heavy-fermion systems 52
3.2.3 Spin waves in itinerant ferromagnets 53
3.3 The magnetic resonant mode 54

4 Experimental Methods **57**
4.1 Preparation of $A_xFe_{2-y}Se_2$ (A = K, Rb) single crystals 57
4.2 Preparation of $Ce_{1-x}La_xB_6$ single crystals 60
4.3 The experimental technique of neutron scattering 62
4.3.1 Triple-axis neutron spectroscopy 63
4.3.2 Resolution and background of a triple-axis spectrometer 65
4.3.3 Time-of-flight spectroscopy 69
4.4 The theory of neutron scattering 70
4.4.1 Magnetic neutron scattering 71

5 Spin fluctuations in $A_xFe_{2-y}Se_2$ **79**
5.1 The resonant mode in $A_xFe_{2-y}Se_2$ 79
5.2 Spin excitations in $Rb_{0.8}Fe_{1.6}Se_2$ 80
5.3 Spin excitations in $K_xFe_{2-y}Se_2$ 85
5.4 The resonant-mode spectrum in $A_xFe_{2-y}Se_2$ 88

6 Neutron scattering studies on CeB_6 **93**
6.1 Temp. and field dependence of the AFM and AFQ OP's in $Ce_{1-x}La_xB_6$ 93
6.1.1 Observation of a zero-field SDW order parameter in $Ce_{1-x}La_xB_6$ 93
6.1.2 Field dependence of the SDW and AFQ Bragg peaks in CeB_6 . 96
6.1.3 The magnetic phase diagram of $Ce_{0.82}La_{0.18}B_6$ 97
6.1.4 The magnetic phase diagram of $Ce_{0.77}La_{0.23}B_6$ 99
6.1.5 The magnetic phase diagram of $Ce_{0.72}La_{0.28}B_6$ 100
6.1.6 Summary of the neutron diffraction studies of $Ce_{1-x}La_xB_6$ . . . 106
6.2 Spin dynamics in $Ce_{1-x}La_xB_6$ 107
6.2.1 The observation of a resonant spin exciton in the AFM phase of CeB_6 107
6.2.2 The observation of ferromagnetic correlations in the AFM phase of CeB_6 110
6.2.3 Spin waves in the AFM state 112
6.2.4 Observation of a charge gap in the AFM state 114
6.2.5 Itinerant description of the spin dynamics in CeB_6 116
6.2.6 Magnetic-field dependence of the spin exciton in CeB_6 119
6.2.7 Evolution of the spin exciton in $Ce_{1-x}La_xB_6$ 120

6.2.8 Magnetic-field dependence of the ferromagnetic mode 127
6.3 Summary 130

7 Summary and Discussion **133**
7.1 Indications of strongly correlated physics in FeSe122 133
7.2 The exciton in CeB_6 as a fingerprint for itinerant spin dynamics 136

Appendices **139**

Physical constants **143**

Bibliography **145**

Publication List **161**

Acknowledgements **163**

Abbreviations

AFM	... Antiferromagnetic
AFQ	... Antiferroquadrupolar
ARPES	... Angle-resolved photoemission spectroscopy
BCS	... Bardeen, Cooper and Schrieffer
BZ	... Brillouin zone
CEF	... Crystalline electric field
cnts, cts	... Counts
CW	... Curie-Weiss
dHvA	... de Haas-van Alphen
DOS	... Density of states
EDX	... Energy-dispersive X-ray spectroscopy
ESR	... Electron spin resonance
ENS	... Elastic neutron scattering
FeSC	... Iron-based superconductors
FeSe122	... Alkali-metal iron chalcogenides
FWHM	... Full-width-half-maximum
FL	... Fermi liquid
FM	... Ferromagnetic
FS	... Fermi surface
f.u.	... Formula unit
HWHM	... Half-width-half-maximum
HF	... Heavy fermion
INS	... Inelastic neutron scattering
KL	... Kondo lattice
LRO	... Long-range order
MFA	... Mean-field approximation
MPI-FKF	... Max Planck Institute for Solid State Research
ND	... Neutron diffraction
NFL	... Non-Fermi-liquid
NMR	... Nuclear magnetic resonance
OP	... Order parameter
QCP	... Quantum critical point
RKKY	... Rudermann-Kittel-Kasuya-Yosida
RPA	... Random-phase approximation
RXS	... Resonant X-ray scattering

r.l.u. ... Reciprocal lattice units
SC ... superconducting
SCR ... Self-consistent renormalization
SDW ... Spin-density wave
s.d. ... Standard deviation
SRO ... Short-range order
STM, STS ... Scanning tunneling microscopy/spectroscopy
TOF ... Time of flight
μSR ... Muon-spin relaxation

Zusammenfassung in deutscher Sprache

Itinerante Spinanregungen in Eisen-basierten Supraleitern und Cer-basierten schweren Fermionen

Im Rahmen dieser Dissertation wurden der Magnetismus und die Spindynamik von zwei unterschiedlichen metallischen Elektronensystemen mittels inelastischer Neutronenstreuung untersucht. Die Materialien umfassen die neue Familie der Alkali-Eisenselenide (FeSe122) $A_xFe_{2-y}Se_2$ (A=K, Rb) [1], welche strukturell den 2008 entdeckten unkonventionellen Eisen-basierten Hochtemperatursupraleitern, wie zum Beispiel LaOFeAs, ähneln [2] und eine beachtliche Sprungtemperatur von $T_c = 32\,\mathrm{K}$ aufweisen. Jedoch besitzen diese Verbindungen eine qualitativ einzigartige elektronische Struktur unter den Eisen-basierten Supraleitern. Es wurde vorhergesagt [3], dass Spinfluktuationen die Cooper-Paarung, analog zu den Eisenpniktiden, vermitteln. Der Beweis der Existenz und die Charakterisierung der Spinfluktuation konnten in der vorliegenden Arbeit erbracht werden. Des Weiteren wurden die Spinanregungen in dem Schwerfermion-Antiferromagneten CeB_6 gemessen. Dieses System ist vor allem durch die Realisierung einer antiferroorbitalen Quadrupolordnung (AFQ) der $4f$ Elektronen von Ce^{3+}, welche unterhalb von $T_Q = 3{,}2\,\mathrm{K}$ einsetzt, und einer antiferromagnetischen Ordnung unterhalb $T_N = 2{,}3\,\mathrm{K}$ vorausgeht, von Interesse.

Beide Systeme verbindet eine verblüffende Veränderung der Spindynamik unterhalb ihrer jeweiligen Übergangstemperatur. In den FeSe122 Supraleitern konzentrieren sich die Spinfluktuationen um den Wellenvektor $\boldsymbol{Q}_{sf} = (\frac{1}{2}\ \frac{1}{4})$. Während das Einteilchen-Spinanregungsspektrum $\chi''(\boldsymbol{Q}_{sf}, \omega)$, welches durch inelastische Neutronenstreuung direkt gemessen werden kann, im Normalzustand nahezu monoton und kontinuierlich ist, ändert sich es drastisch mit dem Öffnen der supraleitenden Energielücke 2Δ unterhalb von T_c.[1] Einteilchen-Anregungen unterhalb 2Δ sind normalerweise unterdrückt ($\chi_0''(\boldsymbol{Q}_{sf}, \omega) = 0$ für $\omega < 2\Delta$). Jedoch wurde eine starke und energetisch schmale Anregung bei $\hbar\omega_{res} = 14\,\mathrm{meV} < 2\Delta$ beobachtet, die parallel mit der Energielücke unterhalb von T_c erscheint. So eine Resonanzmode wurde schon in ähnlicher Form in den supraleitenden Kupraten und in den Eisenpniktiden beobachtet und gilt als Indikator für einen unkonventionellen Ordnungsparameter im supraleitenden Zustand. Das Wechselspiel zwischen Magnetismus und Supraleitung, welches die Beobachtung der Resonanzmode verkörpert, wird als Beweis der magnetisch vermittelten Supraleitung angeführt [5]. Die Ergebnisse dieser Dissertation unterstützen diese Hypothese und liefern weitere experimentelle Informationen, die das Verständnis des Mechanismus der

[1] Im Fall der $A_xFe_{2-y}Se_2$ Supraleiter beträgt die Energielücke $\Delta = 10{,}3\,\mathrm{meV}$ [4].

Hochtemperatursupraleitung verbessern könnten.

Im Gegensatz zu den Eisen-basierten Supraleitern wurde CeB_6 mit dem Kondo-Gitter-Modell beschrieben, wo lokalisierte f-Spins in einem Meer von Leitungselektronen eingebettet sind. Der Grundzustand wird durch das Γ_8 Multiplett gebildet, welches zwei orbitale und zwei Spinfreiheitsgrade einschließt. Die AFQ und die AFM Ordnung heben jeweils die Orbital-und die Spinentartung auf. Die Quadrupole und die Spins verschiedener Ce-Atome sind dabei über die Rudermann-Kittel-Kasuya-Yosida (RKKY) Wechselwirkung gekoppelt. Hierbei zeigt speziell die antiferromagnetische Phase nicht-kollineare Spinordnung mit multiplen Propagationsvektoren in einer $2\boldsymbol{q}-\boldsymbol{q}'$ Struktur, die mit $\boldsymbol{q}_1 = \Sigma(\frac{1}{4}\ \frac{1}{4}\ 0)$ und $\boldsymbol{q}_1' = S(\frac{1}{4}\ \frac{1}{4}\ \frac{1}{2})$ beschrieben wird. Jene sind verschieden vom Propagationsvektor $\boldsymbol{Q}_{\mathrm{AFQ}} = (\frac{1}{2}\ \frac{1}{2}\ \frac{1}{2})$ der AFQ Phase. In der Literatur konnte das magnetische Phasendiagramm mittels eines lokalisierten multipolaren Modells in *Mean-field* Näherung, unter Einbeziehung der Dipole, Quadrupole und Oktupole, reproduziert werden.

Dieses Modell, welches den Magnetismus der Leitungsbänder vernachlässigt, wird durch die Existenz von starken itineranten Spinanregungen, die in dieser Arbeit festgestellt wurden, erheblich in Frage gestellt. Analog zu einem Supraleiter induziert die AFM Ordnung eine Energielücke im Spektrum der Leitungselektronen.[2] Die Spinanregung im *Nullfeld*, welche oberhalb von T_{N} durch quasielastische Einteilchenanregungen charakterisiert werden, erfahren eine drastische Änderung mit Übergang in die antiferromagnetische Phase. Am Wellenvektor des AFQ Ordnungsparameters $\boldsymbol{Q}_{\mathrm{AFQ}}$ erscheint eine starke und scharf definierte Anregung bei $\hbar\omega = 0{,}5\,\mathrm{meV}$. Diese liegt, charakteristisch für ein Exziton, unterhalb des Einteilchenanregungskontinuums, welches bei höheren Energien $\hbar\omega_2 \approx 0,95\,\mathrm{meV}$ beginnt. Weiterhin bildet sich eine starke ferromagnetische Mode in der *antiferromagnetischen* Phase aus, deren Spinlücke $\hbar\omega_\Gamma = 0.25\,\mathrm{meV}$ beträgt. Diese Anregungen sind ausgedehnt im reziproken Raum und intensiver als die konventionellen Spinwellen, die von den magnetischen Bragg Positionen bei $\boldsymbol{q}_1$ und $\boldsymbol{q}_1'$ ausgehen. Erstere müssen daher von den itineranten Quasiteilchen stammen. Sie gehen so ein interessantes Wechselspiel mit den lokalisierten f-Elektronen ein, welche die antiferromagnetische Ordnung erzeugen.

Beide Moden, die Resonanzmode in $A_xFe_{2-y}Se_2$ und das Exziton in CeB_6, ähneln sich qualitativ sehr stark. Ihre Diskussion und theoretische Beschreibung sind folgerichtig analog vorgenommen worden. Beide lassen sich in der *Random-Phase-Approximation* (RPA) als kollektive Mode beschreiben. Durch das Öffnen der Energielücke wird die Lindhardfunktion $\chi_0(\boldsymbol{q},\omega)$, die bei $\boldsymbol{Q}_{\mathrm{sf}}$ (oder $\boldsymbol{Q}_{\mathrm{AFQ}}$) maximal in der Brillouin Zone ist, zusätzlich bei kleinen Energien verstärkt. Bei einer eingeschalteten Wechselwirkung U zwischen den Quasiteilchen kann die renormalisierte Spinsuszeptibilität $\chi^{\mathrm{RPA}}(\boldsymbol{q},\omega) = \chi_0(\boldsymbol{q},\omega)/[1 - U\chi_0(\boldsymbol{q},\omega)]$ eine Polstelle bei ω_r erhalten, wenn die Resonanzbedingung $U\chi_0(\boldsymbol{Q}_{\mathrm{sf}},\omega_r) = 1$ erfüllt ist. Gleichzeitig verschwindet die Dämpfung $\mathrm{Im}\,\chi_0(\boldsymbol{Q}_{\mathrm{sf}},\omega_r) = 0$, was die scharfe Anregung im Spektrum bei $\boldsymbol{Q}_{\mathrm{sf}}$ erzeugt.

[2] Diese wurde mittels Punktkontaktspektroskopie zu $\Delta_{\mathrm{AFM}} = 1{,}2\,\mathrm{meV}$ bestimmt.

Im Fall der Eisenpniktide und der Kuprate wird die Resonanz als Spin-1 Anregung aus dem supraleitenden Kondensat angesehen [6]. In CeB_6 ist die Energielücke die Summe aus AFM-Lücke, AFQ-Lücke und der Hybridisationsaufspaltung. Letztere wird durch die Hybridisation von Leitungs-und f-Elektronenbändern erzeugt, welche dem System die Schwerfermionen-Eigenschaften verleiht. Die konkrete Schlussfolgerung aus der Beobachtung der Resonanzmode, beziehungsweise des Exzitons, ist im jeweiligen Fall unterschiedlich. Dies soll im Folgenden knapp erläutert werden.

Zentrales Element der Eisenpniktid Verbindungen sind Ebenen aus $[FeAs]^-$ Einheiten, die mit Ladungsdonatoren interkaliert sind. Supraleitung wird induziert, wenn man die antiferromagnetische Ausgangsverbindung, wie $BaFe_2As_2$ oder LaOFeAs, dotiert, zum Beispiel durch Substitution von Kobalt für Eisen. Hierbei tragen fast ausschließlich die $3d$ Elektronen des Eisens zur Fermifläche bei, die aus drei lochartigen Flächen um den Γ-Punkt und zwei elektronenartigen Flächen um den $X(\frac{1}{2}\ 0)$ Punkt besteht. Hingegen bestehen die $A_xFe_{2-y}Se_2$ Supraleiter aus FeSe Ebenen, das heißt, dass interkalierte Alkaliatome zu einer starken Elektronendotierung führen. *Angle-resolved photoemission spectroscopy* (ARPES) Messungen [4, 7–14] zeigten das Fehlen der Lochbänder am Γ-Punkt und die Existenz großer Elektronenbänder am $X(\frac{1}{2}\ 0)$ Punkt. Die Nesting-Eigenschaft entlang $\boldsymbol{Q}_{\mathrm{AFM}} = (\pi\, 0)$ der Fermifläche für die Eisenpniktide, welche vermutlich den Magnetismus bestimmt und somit die unkonventionelle Cooper-Paarung vermittelt [15], ist für die FeSe122 nicht mehr vorhanden. Stattdessen gibt es ein Quasinesting zwischen den benachbarten Elektronenbändern entlang $\boldsymbol{Q}_{\mathrm{sf}} = (\frac{1}{2}\ \frac{1}{4})$, dass die für die Supraleitung notwendigen Spinfluktuationen erzeugt. Diese wurden zunächst theoretisch vorhergesagt [3] und in dieser Arbeit an zwei verschiedenen Proben, $Rb_{0,8}Fe_{1,6}Se_2$ und $K_{0,77}Fe_{1,85}Se_2$, experimentell beobachtet.[3] Dieses Resultat bestätigt in überzeugender Weise die rein itinerante Beschreibung der Eisenbasierten Supraleiter, deren Magnetismus von der Fermifläche abgeleitet werden kann.

Die Beobachtung der Resonanzmode bei $\boldsymbol{Q}_{\mathrm{sf}}$ unterhalb T_c kann auch als Beweis für einen vorzeichenwechselnden supraleitenden Ordnungsparameter $\Delta(\boldsymbol{q})$ angesehen werden. Dieses Resultat liefert wertvolle Schlüsse für die Diskussion über die Symmetrie von $\Delta(\boldsymbol{q})$, für die momentan s^{++}, d und $s^{\pm}$ Wellen vorgeschlagen werden. Des Weiteren zeigten die Messungen eine anomale Unterdrückung der Spinfluktuationen bei kleinen Energien im Normalzustand, sowie ein spektrales Gewicht der Resonanzmode, das 2–3 Mal stärker ist als bei den Eisenpniktiden. Dies lässt den Schluss zu, dass die FeSe122 Supraleiter phänomenologisch den Kupraten ähneln und möglicherweise stärker korreliert sind als die Eisenpniktide.

In CeB_6 spiegelt das Erscheinen des Exzitons ein interessantes Wechselspiel zwischen itineranten Quasiteilchen und lokaler Ordnung wider. Das Exziton ist eine Eigenschaft der AFM Phase, welche durch Anlegen eines magnetischen Feldes und durch

[3] Die Fehlstöchiometrie in den Proben geht auf die Präsenz einer starken antiferromagnetischen und isolierenden $A_{0,8}Fe_{1,6}Se_2$ Phase zurück ($T_N = 530$ K), die makroskopisch separiert von der supraleitenden $A_xFe_2Se_2$-Phase in allen Proben vorhanden ist. Der Alkaligehalt x der supraleitende Phase kann nur indirekt bestimmt werden. Kernspinresonanz Messungen des ^{87}Rb Nuklids gaben ein Abschätzung von $x = 0.3$ [16].

chemische Substitution des Cers durch Lanthan unterdrückt werden kann. Bestandteil dieser Arbeit war daher auch die Messung der Abhängigkeit des Exzitons von diesen zwei Parametern. In $Ce_{1-x}La_xB_6$ wird mit zunehmender La-Konzentration die Energie des Exzitons unterdrückt und verbreitert. Diese Entwicklung geht einher mit der Unterdrückung der AFM Energielücke, welche essentiell für die Existenz des Exzitons ist.

Im Gegensatz dazu bleibt die Energie des Exzitons im magnetischen Feld konstant. Es wird eine Verbreiterung aufgrund der zunehmenden Dämpfung durch Einteilchenanregungen registriert, jedoch kann eine Zeeman-Aufspaltung ausgeschlossen werden. Oberhalb der kritischen Magnetflussdichte $B_c = 1,7\,\mathrm{T}$ bleibt die Linienbreite konstant und die Energie steigt linear *vs.* B an. Dieses Verhalten entspricht der Erwartung für multipolare Anregungen, die im AFQ Modell vorhergesagt wurde. Daher kann vermutet werden, dass das Exziton und auch die ferromagnetische Mode aus Fluktuationen der zugrundliegenden AFQ Ordnung resultieren. Jedoch sind die Spinanregungen in der AFQ Phase oberhalb von T_N *im Nullfeld* rein quasielastisch mit Maxima in der Intensität bei Γ, $R(\frac{1}{2}\ \frac{1}{2}\ \frac{1}{2})$ und $X(0\ 0\ \frac{1}{2})$. Diese Beobachtungen entsprechen nicht den Erwartungen im Modell der multipolaren Anregungen, sondern gleichen eher itineranten Spinfluktuationen von Schwerfermionensystemen. Ein weiterer ungeklärter Aspekt ist das Erscheinen eines schwachen magnetischen Bragg Reflexes bei $R(\frac{1}{2}\ \frac{1}{2}\ \frac{1}{2})$ unterhalb von T_Q im *Nullfeld*. Antiferroquadrupolare Ordnung kann diesen nicht erzeugen, so dass eine Spindichtewelle vermutet wird.

Die Schlussfolgerung dieser Arbeit lautet, dass der Mechanismus, der zur Resonanzmode führt, auch auf andere Systeme und Phasen, wie die antiferromagnetische Phase in CeB_6, übertragen werden kann. Hierbei werden Fluktuationen einer zugrundeliegenden Ordnung durch das Öffnen einer Ladungslücke offenbart. Diese Beobachtungen können einen wertvollen Beitrag zur Enträtselung des Mechanismus der unkonventionellen Supraleitung in Schwerfermionensystemen, wie $CeCoIn_5$, UPd_2Al_3 und $PrOs_4Sb_{12}$, liefern. In diesen Systemen wurden ebenfalls exzitonartige Moden entdeckt, die als mögliche Paarungsbosonen diskutiert werden.

Abstract

Itinerant Spin Dynamics in Iron-based Superconductors and Cerium-based Heavy-Fermion Antiferromagnets

This thesis contains a comprehensive study of the spin excitations by inelastic neutron scattering (INS) in two different correlated electron systems: the alkali-metal iron selenide superconductors (FeSe122) $A_xFe_{2-y}Se_2$ (A=K, Rb, Cs) and the heavy-fermion antiferromagnet CeB_6. Both systems exhibit intense modes in their spin-fluctuation spectrum below their respective transition temperatures that can be derived from the spin dynamics of the itinerant quasiparticles. However, the implications of these observations, presented here, are different for each particular compound.

The $A_xFe_{2-y}Se_2$ superconductors, with an uniform T_c of 32 K, belong to a qualitative new family of superconductors. They possess a distinctly different Fermi surface compared to the iron-arsenide-based analogues XFe_2As_2 (X=Ca, Sr, Ba). Instead of the central hole pockets at Γ and the electron pockets at $X(\frac{1}{2}\ 0)$, which are nested by the $\boldsymbol{Q}_{\mathrm{AFM}} = (\frac{1}{2}\ 0)$ vector, there exist only large electron pockets at $X(\frac{1}{2}\ 0)$, which render the FeSe122 as strongly electron overdoped variants of the iron arsenides (FeSC). Therefore, the magnetic instability along $\boldsymbol{Q}_{\mathrm{AFM}}$ that presumably provides the pairing glue for the superconductivity in the shape of spin fluctuations is absent in the FeSe122. The search for spin fluctuations by INS was motivated by a theoretical analysis that predicted their presence at an incommensurate wave vector $\boldsymbol{Q} = (0.5\ \delta)$, $\delta = 0.3125$, which results from a quasinesting by $\boldsymbol{Q}$ between the flat parts of the electron pockets. Two samples, namely $Rb_{0.8}Fe_{1.6}Se_2$ and $K_{0.77}Fe_{1.85}Se_2$, were prepared and both showed a sizable anisotropic magnetic response at $\boldsymbol{Q}_{\mathrm{sf}} = (\frac{1}{2}\ \frac{1}{4})$ in the normal state. Furthermore, upon entering the superconducting (SC) state a strong excitation appears at $\hbar\omega_{\mathrm{res}} = 14$ meV in the spectrum at $\boldsymbol{Q}_{\mathrm{sf}}$, which is referred to as *magnetic resonant mode*. This mode is interpreted as a bound spin-1 exciton below the SC charge gap. Its presence implies an unconventional order parameter, which changes the sign between the electron pockets. Moreover, it has a two-dimensional reciprocal-space structure, with an in-plane wave vector $\boldsymbol{Q}_{\mathrm{sf}}$ that is independent of the composition. These results support the current understanding that all FeSe122 contain a unique SC phase with $A_xFe_2Se_2$ stoichiometry and an alkali content of $x = 0.36$. This phase is embedded in a matrix of an insulating and strongly antiferromagnetic $A_{0.8}Fe_{1.6}Se_2$ phase, which explains the iron deficiency. Secondly, the spectral weight of the resonance peak and the suppression of the normal-state intensity towards small energies is similar to the phenomenology in underdoped cuprates, rendering this family stronger correlated than

the FeSC analogues.

CeB_6 is considered as a dense Kondo system that exhibits a peculiar antiferroquadrupolar (AFQ) phase below $T_Q = 3.2\,K$ and an antiferromagnetic (AFM) phase below $T_N = 2.3\,K$. Its magnetic phase diagram has been so far described by a purely localized multipolar mean-field model. However, reports on experimental studies in zero or low magnetic field provide a number of conflicting results that prevented a consistent description till now. These include the indication of heavy-fermion quasiparticles by transport measurements, the observation of a charge gap in the AFM phase and the revelation of ferromagnetic correlations by electron-spin resonance studies in the *antiferroquadrupolar* phase. In this thesis the spin excitations in the AFM and the AFQ state of CeB_6 have been comprehensively mapped out in reciprocal space for the first time. Contrary to the expectations an intense and energetically sharp exciton mode appears at 0.5 meV below T_N, which is restricted to the AFQ wave vector $R(\frac{1}{2}\ \frac{1}{2}\ \frac{1}{2})$. This exciton is created, because a gap opens in the spin and charge excitation spectrum of the interacting heavy-fermion quasiparticles below T_N. This phenomenology is similar to the resonant modes in heavy-fermion superconductors below T_c. The gap is constituted by the AFM and AFQ ordering of the localized f-spins as well as by the hybridization of the f-and conduction electrons. In addition, a strong ferromagnetic mode at 0.25 meV appears at the Γ point below T_N, which broadly disperses across the Brillouin zone. Both the exciton and the ferromagnetic mode are thereby much more intense than the conventional spin waves associated with the AFM order. Both excitations transform into purely quasielastic intensity upon entering the AFQ phase above T_N, where the theoretically proposed multipolar excitations could not be detected. Therefore, the experimental observations here manifest an intriguing interplay of itinerant and localized quasiparticles, which renders the consideration of the heavy-fermion contribution to the magnetic properties as indispensable for the discussion of this model compound.

Further elucidation of the exciton is provided by the study of its evolution upon application of a magnetic field and the substitution of the Ce^{3+} with non-magnetic La^{3+}, which are both known to suppress the AFM phase. In the former case the exciton transforms into a multipolar mode above the critical field B_c. In the latter case the exciton gets reduced in energy and vanishes together with the AFM charge gap at the critical doping level of $x_c = 0.3$. These results imply that the exciton may originate from the fluctuations of the AFQ order parameter.

1 Introduction

Max Planck's famous derivation of the black-body radiation law in 1900 marked the beginning of quantum mechanics [17]. Its subsequent development almost 100 years ago had profound impact on the understanding of magnetism and light. It is fascinating how the complexity of a many-particle state, comprising 10^{23} electrons, can be reduced to simple formulae because of their coherent collective behavior, which is determined by the solution of the Schrödinger equation. This advance in physics is also mirrored in a series of technological achievements in the 20th century, which are based on macroscopic quantum coherence effects. These include the laser, which is used as a readout device for compact discs and DVDs and as an experimental tool in research itself as well as the electron microscope. Based on the wave nature of the electron, it can resolve structures in the sub-nanometer range that were not accessible by conventional light microscopy.

The macroscopic quantum phenomenon of superconductivity (SC) in condensed matter, observed much earlier in 1911 by Heike Kamerlingh Onnes, engages researchers until today in three respects. First, the observation of a non-resistant flow of electrical current below a critical temperature T_c provides obvious routes of technical applications. The use in electric power transmission, energy storage, magnetic levitation shall be mentioned. But also the possibility of creating high magnetic fields, which can be applied in research and in medicine, underlines the importance of this effect. However, an obstacle on the road towards large-scale industrial applications is the restriction of this effect to very low temperatures, which in order to be reached require the consumption of liquid nitrogen and helium. The second line of research therefore focuses either on the discovery of new superconductors or on the optimization of T_c in known families of superconductors. There is a great variety of systems that exhibit superconductivity. First of all, most of the elements superconduct under ambient or high pressure [18]. However the transition temperature is quite low, e.g. a T_c of 7.2 K in lead is among the highest at ambient pressure. A major advance was the observation of $T_c = 30$ K in cuprates by J. G. Bednorz and K. A. Müller in 1986. These are layered systems, which are based on square lattices of CuO_2 units [19]. The critical temperature could be raised to 135 K in $HgBa_2Ca_2Cu_3O_{8+x}$ [20], which represents the current record.

Another line of research effort that concentrates on $4f$ and $5f$ compounds was spurred by the discovery of superconductivity below $T_c = 1.5$ K in $CeCu_2Si_2$ (Steglich *et al.*, 1979 [21]). Since the characteristic temperatures are two orders of magnitude smaller than the ones for the cuprates, the interest in these compounds is based on scientific reasons. The SC quasiparticles were found to be as heavy as 10^3 times of the free

electron mass. Another family of high-T_c superconductors, which is of main concern in this thesis, are the iron-pnictide-based superconductors. After the initial report in 2008 by Kamihara *et al.* in $LaO_{1-x}F_xFeAs$ [2], the T_c could be maximized to a current record of $T_c = 65\,K$ in single layer FeSe [22].

The route towards room temperature superconductivity via the "random" synthesis of new systems would be analogous to the search of the needle in a haystack. This task is rather unsatisfying and early on efforts were put into the realization of a theory of superconductivity, which not only explains the mechanism, but also enables the quantitative analysis of T_c based on the structural, electronic and magnetic properties of the material. A milestone was reached in 1957 when Bardeen, Cooper and Schrieffer (BCS) proposed a microscopic theory, where the macroscopic superconducting wave function is described as a coherent state of Cooper pairs. It was realized in this concept that the exchange of a phonon between a pair of quasiparticles at the Fermi surface, having the momentum and spin $\boldsymbol{k}\uparrow$ and $\boldsymbol{k}'\downarrow$, can mediate an attractive interaction [23]. The condensation of all such pairs into the collective ground state leads to the opening of an isotropic BCS gap 2Δ on the Fermi surface. Extending the theory to the case of strong electron-phonon coupling ($\lambda = 0.2-0.5$) provided a quantitative estimate for T_c, based on material specific parameters like the Debye temperature ω_D and the electron-phonon coupling constant λ [24]. Though the theory can explain the elementary superconductors quite well, it fails to explain the technologically more beneficial high-T_c materials [25]. The cuprates and the iron pnictides possess unconventional order parameters, which have d or $s^{\pm}$ symmetry [26–28], respectively, and which undergo a sign-change across the Fermi surface. Another generic property, shared by all iron pnictides, cuprates and heavy-fermion superconductors, is the proximity to a magnetic phase. More specifically, most of the superconductors are obtained by doping or pressurizing a stoichiometric parent compound, e.g. $BaFe_2As_2$ for iron pnictides and $YBa_2Cu_3O_6$ for cuprates. These compounds show static antiferromagnetic (AFM) ordering with the propagation vector $\boldsymbol{Q}_{AFM}$. Upon variation of an external parameter the order disappears, but spin fluctuations persist, which are conjectured to mediate the Cooper pairing [29]. For detecting these spin excitations with high reciprocal-space and energy resolution inelastic neutron scattering (INS) is the most suitable technique. It is able to map out the complete energy dispersion of the spin waves up to high energy transfers of 200 meV in both the parent compound [30] and the superconducting compounds [31, 32]. It is proposed that the full spin-excitation spectrum may provide the pairing glue for superconductivity [32–34], which could resolve the mystery around the mechanism of the high-temperature superconductivity. However, the theory does not provide the means to predict new high-T_c compounds.

The recent discovery of the iron-based superconductors must appear as a fortunate coincidence, as one is in the position to identify the key ingredients of high-T_c superconductivity by the consideration of two seemingly different families of materials. Iron-pnictide parent compounds are bad metals, where the Fermi surface is composed of five bands, derived from the electronic orbitals of the Fe^{2+} ions. The magnetism

results from an instability towards a spin-density wave (SDW) ordering [15]. In contrast, undoped cuprate compounds are Mott insulators, where the localized spins of Cu^{2+} order. The theoretical description of the superconducting quasiparticles, in terms of an itinerant or a more localized model, is currently under debate [35, 36]. Furthermore, cuprates show a more complicated phase diagram in the underdoped region, where charge-density wave order [37, 38], SDW order [39] and a mysterious pseudogap phase [40] are coexisting or competing with the superconducting phase.

An important commonality between both systems is the intriguing interplay between superconductivity and spin fluctuations that is revealed by the appearance of the resonant mode - a sharp collective mode that forms in the spin excitation spectrum below T_c [6, 41, 42]. This mode not only serves as an indicator for an unconventional superconducting order parameter, but also describes a feedback effect of the SC gap opening on the spin-fluctuation spectrum. An universal scaling of its energy $\hbar\omega_{res}$ with $k_B T_c$, assessed for both pnictides and cuprates [5, 43], is understood as an indication that superconductivity is spin fluctuation mediated and that $\hbar\omega_{res}$ is related to the energy scale of the pairing boson [5].

In this respect, heavy-fermion compounds provide substantial experimental evidence for unconventional pairing scenarios. Heavy superconducting quasiparticles are found to coexist with localized moments, which may show antiferromagnetic order as in the case of UPd_2Al_3 [44] and $Ce(Rh_{1-x}Co_x)In_5$ [45] and, thus, can act as a source of pairing glue [46]. Moreover, superconductivity is found in proximity to phases, whose order parameter is hidden to conventional scattering probes. URu_2Si_2 is of current interest as it exhibits hidden order below $T_0 = 17.5$ K and superconductivity below $T_c = 1.5$ K [47]. In $PrOs_4Sb_{12}$ ($T_c = 1.75$ K) it is believed that an antiferro-coupling of the quadrupole moments, observed in nonzero magnetic fields at $\boldsymbol{q}_{AFQ}$, may also drive Cooper-pairing. Neutron scattering proved to be crucial in observing an excitation at $\boldsymbol{q}_{AFQ}$ that similar to the resonant mode in high-T_c compounds undergoes a clear modification below the critical temperature [48].

1.1 Scope of the thesis

This thesis deals with INS experiments on two different systems - i) the alkali-metal iron selenide family $A_xFe_{2-y}Se_2$ (A=K, Rb, Cs) of superconducting compounds (T_c = 32 K) and ii) the heavy-fermion antiferromagnet CeB_6 ($T_N = 2.3$ K). CeB_6 is also known for displaying antiferro-ordering of the Ce^{3+} quadrupole moments below T_Q = 3.2 K, which is considered as a prototypical example for multipolar phases in f-electron compounds [49]. In both compounds the emergence of a sharp and intense resonant mode in the low-energy spin-excitation spectrum below the respective transition temperature is reported. The explanation of this mode, referred to as resonant mode (exciton), in these seemingly distinct compounds is almost analogously interpreted as a collective mode of interacting quasiparticles that forms because of the opening of a

charge gap below T_c (T_N). However, the implications of these results are different in each particular case.

Chapter 2 introduces the physics of the iron-based superconductors. Special attention is given to the first-principles studies of the electronic structure and the spin dynamics. The close relationship between the Fermi surface and the reciprocal-space structure of the spin fluctuations will be worked out. Afterwards the properties of the alkali-metal iron selenide $A_xFe_{2-y}Se_2$ superconductors (T_c = 32 K) will be discussed. It will be shown that the Fermi surface is distinctly different to the iron-arsenide-based analogues. This motivated the study by INS to search for possible spin fluctuations and to clarify the order parameter symmetry in these compounds.

The second part of Chapter 2 introduces the peculiar compound CeB_6, which is a textbook example for exhibiting an antiferroquadrupolar phase [50]. Its magnetic phase diagram, which was studied in detail in literature, will be presented. The purpose of this review is to introduce the purely localized multipolar model of CeB_6, which explains the magnetic properties in high magnetic field on the one hand, but neglects the presence of the heavy-fermion quasiparticles and fails to explain a number of experimental studies in the low-field range on the other hand. Pointing out this existing controversy will be important, since the INS data in this thesis observes strong itinerant modes that are not captured by the localized model. Furthermore, the evolution of the phase diagram upon substitution with lanthanum in $Ce_{1-x}La_xB_6$ will be mentioned. The introduction of La suppresses both AFM and AFQ ordering and, thus modifies the spin dynamics. At higher doping an enigmatic phase IV appears, whose order parameter has remained unidentified until today.

Chapter 3 will introduce the physics of heavy-fermion compounds, which can simultaneously contain both localized and itinerant quasiparticles. This dual nature will be important in reconciling both the presence of localized magnetic and antiferroquadrupolar order (AFQ) in CeB_6 on the one hand, and the itinerant spin excitations on the other hand. Following this, basic formulae of the spin response for nearly antiferromagnetic and ferromagnetic metals, which can be applied to both iron-based superconductors and CeB_6, will be derived.

Chapter 4 focuses on the experimental techniques employed in this thesis. These include the sample preparation of single-crystalline $A_xFe_{2-y}Se_2$ and CeB_6 as well as the functional principle of neutron scattering. Formulae that can relate the INS cross section to the intrinsic spin correlation function $S(\boldsymbol{Q}, \omega)$ will be given.

The main results of the INS experiments on the $A_xFe_{2-y}Se_2$ (A=K, Rb) superconductors will be presented in **Chapter** 5. The observation of sizeable normal-state spin fluctuations at $\boldsymbol{Q}_{res} = (\frac{1}{2}\ \frac{1}{4})$ as well as the formation of a resonant mode in the superconducting state will be reported. However, the wave vector of the spin fluctuations is distinctly different from the value in the iron pnictides, but consistent with the strong electron-doped Fermi surface in this family of compounds. It will be shown that $\boldsymbol{Q}_{res}$ can be related to the nesting vector of the Fermi surface by calculations of the static spin susceptibility $\chi'(\boldsymbol{q})_{\omega\to 0}$ and the dynamical susceptibility $\chi''(\boldsymbol{q}, \omega)$. These results

confirm the capability of the purely itinerant approach to explain the low-energy spin dynamics in Fe-based superconductors.

Chapter 6 is concerned mainly with the INS study of the itinerant spin dynamics of $Ce_{1-x}La_xB_6$ ($x = 0$, $x = 0.18$, $x = 0.23$ and $x = 0.28$). Parallel to the INS experiments the magnetic phase diagrams of all $Ce_{1-x}La_xB_6$ samples have been reinvestigated by neutron diffraction, which was motivated by the appearance of a weak Bragg peak at $\boldsymbol{q}_{\mathrm{AFQ}} = (\frac{1}{2}\,\frac{1}{2}\,\frac{1}{2})$ below the AFQ transition temperature T_{Q} in zero magnetic field. This Bragg peak is not expected for the ordering of quadrupoles and might indicate a previously overlooked SDW order in this compound.

The main result is provided by the observation of an intense excitation at $\boldsymbol{q}_{\mathrm{AFQ}} = (\frac{1}{2}\,\frac{1}{2}\,\frac{1}{2})$ and $\hbar\omega_R = 0.5\,\mathrm{meV}$ below the antiferromagnetic transition temperature $T_{\mathrm{N}} = 2.3\,\mathrm{K}$. In initial considerations, this mode was interpreted as an exciton in the itinerant spin-fluctuation channel, which forms below the charge gap Δ_{AFM}. Later, a complete mapping of the spin excitation for the whole Brillouin zone led to the discovery of an intense and broadly dispersing ferromagnetic mode at $\hbar\omega_\Gamma = 0.25\,\mathrm{meV}$ below T_{N}. The AFM order itself is constituted by the localized f-spins and conventional spin waves connected with the antiferromagnetic ordering could be observed as well. However, the appearance of the ferromagnetic correlations and the exciton inside an antiferromagnetic phase are a surprising result and will be discussed in the light of the twofold contributions of the f-spins to the spin dynamics both as heavy-fermion quasiparticles and as localized moments. Moreover, further evidence for the itinerant origin of the exciton is given by the measurements of its dependence on an external magnetic field and on the dilution of the f-spins upon La substitution. Especially the magnetic-field dependence allows us to trace how the exciton evolves into a collective multipolar mode, when crossing the magnetic-field boundary between the AFM and the AFQ phase at B_{q}. The spin dynamics in zero field for both AFM and AFQ phase will be described within Moriya's theory of nearly antiferromagnetic heavy-fermion metals [51]. These results strongly call for a rethinking of the persisting localized multipolar order of CeB_6 and motivates a consideration of the heavy-fermion quasiparticles for a consistent description of this simple system, which has model character for a broad class of heavy-fermion compounds.

Finally, **Chapter 7** summarizes the outcome of the INS experiments for both systems. In case of the alkali-metal iron selenide superconductors $A_xFe_{2-y}Se_2$, details of the resonance spectrum that distinguishes it from one of the iron pnictides will be worked out. In line with the recent experimental findings in literature this family seems to be more correlated, lying close to a Mott insulating phase [52]. The ratio of the resonant mode energy $\hbar\omega_{\mathrm{res}}$ with $k_{\mathrm{B}}T_{\mathrm{c}}$ is compared with the universal scaling plot valid for the pnictides [43]. A similar analysis will be done for the exciton in CeB_6. Though phenomenologically similar to the resonant mode in heavy-fermion superconductors, the exciton is observed within an *antiferromagnetic* phase, extending the range of correlated materials, where such modes can be observed.

2 The phase diagram of correlated electron systems

2.1 The family of iron arsenide superconductors

A new class of unconventional superconductors was discovered in 2006 [53], when a critical temperature of T_c = 3.2 K was reported for LaOFeP. In the following the T_c could be raised to 26 K in the $LaO_{1-x}F_xFeAs$ series [2], establishing the Fe-based superconductors (FeSC) as a new class of high-T_c superconductors. Ever since a multitude of superconducting variants were reported, which can be classified according to the stoichiometry. Central element of all compounds is the square lattice of Fe tetrahedrally coordinated by As atoms [see Fig. 2.1 (a)]. The density of states at the Fermi level is almost completely derived from Fe 3*d* orbitals with a small contribution of As 4*p* orbitals [54–56]. The iron and arsenic are covalently bonded to $[FeAs]^{1-}$. The required electron is provided by the intercalated layer. In case of the 1111 family, to which $LaO_{1-x}F_xFeAs$ belongs, this layer comprises units of *RE*O (*RE*= rare earth atom). In the "122" family this is replaced by a single alkaline earth metal. Figure 2.1 (a) shows the body-centered unit cell (I4/mmm symmetry) of the representative $BaFe_2As_2$, which is commonly used in literature [28].[1] Further stoichiometries include 111 (e.g. LiFeAs and NaFeAs) as well as compounds with more complex blocking layers like $(Sr_4V_2O_6)Fe_2As_2$ [59] or $Ca_{10}(Pt_3As_8)(Fe_2As_2)_5$ [60]. Superconductivity was also observed when replacing arsenic with selenium, which constitutes the 11 family of iron chalcogenides. The speciality of this system is the absence of a buffer layer between the FeSe planes. The critical temperature ranges from T_c = 8 K in FeSe [61] to T_c = 14 K in $FeTe_{1-x}Se_x$ (x = 0.5) [62]. Intercalating FeSe with an alkali element results in non-stoichiometric $A_xFe_{2-y}Se_2$ (A =K, Rb, Cs, Tl), which exhibits superconductivity below $T_c \approx 32$ K [1, 63–66]. The experimental data within this thesis on FeSC focuses exclusively on this family of "122" iron chalcogenides (FeSe122). Characteristic for this class of superconductors is the chemical phase separation into a metallic/SC and an insulating/AFM phase, which will be discussed in detail in Section 2.2.2. The superconducting phase of these compounds does not only share the chemical structure with the iron-arsenide-based analogues, but also has a similar electronic structure and magnetic properties. In the following, the most important experimental and theoretical studies on the iron arsenides will be briefly presented, before discussing the FeSe122 superconductors.

[1] This family is particularly well studied, since large single crystals could be grown [57, 58].

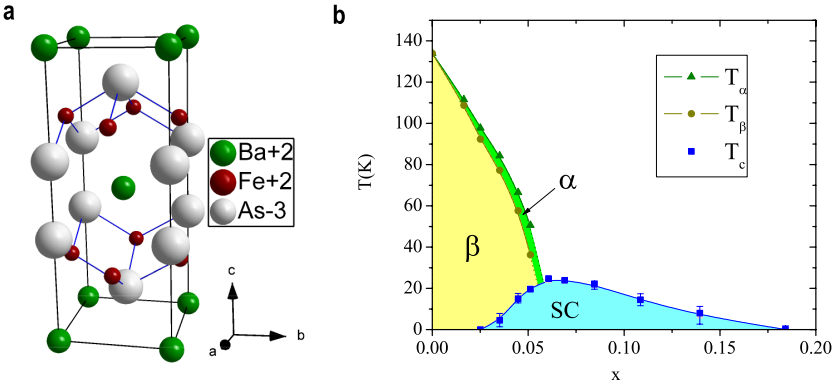

Fig. 2.1: (a) Body-centered I4/mmm unit cell of $BaFe_2As_2$. **(b)** Electronic phase diagram of $Ba(Fe_{1-x}Co_x)_2As_2$, as determined by measurements of specific heat, electrical resistivity and Hall effect. (reproduced from Ref. 67).

Almost all parent compounds of the different iron arsenide families are antiferromagnetic below a Neel temperature T_N. The ordering wave vector is $\boldsymbol{q} = (\frac{1}{2}\ \frac{1}{2}\ 1)_T$ with respect to the paramagnetic/tetragonal unit cell as denoted by the subscript "T" [68, 69]. The spins are collinear and ordered in stripes [see also Fig. 2.3 (c)] [68, 69]. The magnetic transition is accompanied by a structural distortion of the in-plane lattice parameters with orthorhombic symmetry [70]. In contrast to the cuprates, the ground state is not insulating. There is a sharp drop at T_N in the resistivity *vs.* temperature, followed by a gradual decrease that accompanies the increase of the magnetic order parameter [67, 70–72]. A superconducting ground state can be produced by either chemical substitution or by applying pressure [27]. Figure 2.2 (a) shows the evolution of the magnetic susceptibility *vs.* T upon Co-doping in $Ba(Fe_{1-x}Co_x)_2As_2$ [73]. The anomaly, connected to the magnetic/structural phase transition, becomes suppressed to lower temperatures. Near $x = 0.03$ superconductivity appears below the critical temperature T_c, which increases with further doping. The optimal doping with the highest T_c is reached near the offset of the antiferromagnetic/orthorhombic (β/α) phase as shown in the electronic phase diagram in Fig. 2.1 (b). The proximity of the superconducting phase to the magnetic phase is reminiscent of the situation in the cuprates [74], which led to early conjectures that the superconducting pairing is possibly mediated by spin fluctuations [15]. Different theories have been brought forward in order to elucidate the origin of the magnetism in the iron pnictides. First-principles calculations can reproduce the stripe antiferromagnetic order, but they generally overestimate the magnetic moment [75, 76]. Fig. 2.2 (e) shows the level scheme for the six d electrons of Fe^{2+}, published in Ref. 75. The Hund's rule coupling J_H favors a $S = 2$ state. However, the experimentally observed moment is much smaller, being $\mu \approx 0.4\,\mu_B$ for

LaOFeAs [68] and $\mu = 0.87(3)\mu_B$ for $BaFe_2As_2$ [69]. Furthermore, it was pointed out that the iron arsenides must be strongly correlated. The high resistivity is characteristic of the "bad metal" behavior of strongly correlated systems [2]. Also LaOFeAs shows an upturn in the low-temperature resistivity, which indicates a localization of charge carriers [77, 78]. In a strong coupling approach the parent compound is believed to be close to a Mott insulating phase [79, 80]. The stripe antiferromagnetic order can also be reproduced in a localized Heisenberg-model. Here, the lattice of ordered moments can be decomposed into two sublattices with checkerboard antiferromagnetic order, where the order within each sublattice is mediated by the next-nearest-neighbor (NNN) superexchange interaction J_2. Both sublattices are then coupled via the nearest-neighbor (NN) interaction J_1. The stripe order is realized for $J_2 > J_1/2$, which frustrates the NN interaction, and explains the reduced moment [79, 80].

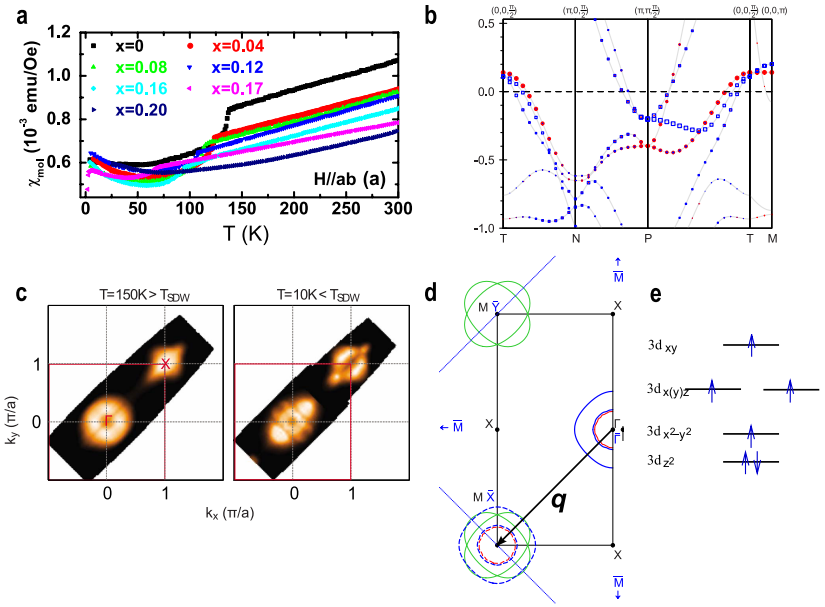

Fig. 2.2: **(a)** Temperature dependence of the magnetic susceptibility χ for different doping levels in $Ba(Fe_{1-x}Co_x)_2As_2$, taken from Ref. 73. **(b)** Band structure of $BaFe_2As_2$, calculated by linear muffin-tin orbital approximation (LMTO) in the paramagnetic state of $BaFe_2As_2$. The different colors denote a different orbital character of the bands. The figure is taken from Ref. 81. **(c)** FS intensity map, as measured by ARPES, in the paramagnetic state and SDW state of $BaFe_2As_2$, taken from Ref. 82. **(d)** Schematic of the FS cross section for LaOFeAs, calculated by the LMTO approximation. A downward correction of the d_{xy}- orbital in energy by 150 meV has been applied (adapted from Ref. 81). **(e)** Level scheme of the Fe^{2+} d-electrons (taken from Ref. 79).

Another magnetic characteristic of the iron pnictides is the unusual T-linear increase of the static susceptibility above T_N, shown in Fig. 2.2 (a). The slope is found to be a generic property irrespective of the doping level or the structural variant of the FeSC [58, 73, 83, 84]. The temperature range of the linear magnetic susceptibility has been explained by a fluctuation regime of local moments [85] and a temperature dependent admixture of the intermediate-spin ($S = 1$) state of the Fe ions [86].

In contrast to that, the linear term has also been related to the enhanced interband coupling of the hole and electron bands at the Fermi surface because of nesting [87]. In fact, a number of theoretical and experimental studies point out the relevance of an itinerant description of the magnetism in iron pnictides.

2.1.1 Electronic structure and Fermi surface of FeSC

First-principles calculations for LaOFeAs [15, 55, 75, 76, 80, 81] provide a similar result for the band structure of the parent compound, shown in Fig. 2.2 (b). Three hole bands are crossing the Fermi level near the Γ point. They are derived from the d_{yz}/d_{zx} (blue) and the d_{xy} orbitals (red) of the Fe^{2+} ion. Furthermore, two electron pockets are centered at the $M(\frac{1}{2}\,\frac{1}{2}\,0)_T$ point, which have d_{yz}/d_{zx} character. The band structure and the Fermi surface in the paramagnetic phase was experimentally confirmed by a number of angle-resolved photoemission spectroscopy studies (ARPES) for the parent compounds [82, 88–100] as well as for the doped superconducting compounds [101–112]. The Fermi surface for $BaFe_2As_2$ is shown in Fig. 2.2 (c). In the paramagnetic state the intensity around the Γ point is made of three barrel-shaped hole pockets that show a slight warping along the k_z direction. Furthermore, there are two elliptical electron pockets at the $M(\frac{1}{2}\,\frac{1}{2}\,0)_T$ point, in agreement with first-principles calculations [81]. These bands have a three-dimensional character, however, they possess also flat sections along k_z [92, 94].

It has been pointed out that this Fermi surface is strongly nested along $\boldsymbol{q} = (\frac{1}{2}\,\frac{1}{2}\,0)$, where $\boldsymbol{q}$ is the translation vector that brings the hole and electron pockets to overlap [see Fig. 2.2 (d)] [15, 76, 113]. Calculations of the real part of the Lindhard susceptibility $\mathrm{Re}\,\chi_0(\boldsymbol{q},\omega)$ show a sharp peak at $M(\frac{1}{2}\,\frac{1}{2}\,0)_T$ [15, 81, 113, 114]. Therefore, the magnetic order can be interpreted as a spin-density wave (SDW), since the in-plane projection of the magnetic Bragg peak $\boldsymbol{Q}_{AFM} = (\frac{1}{2}\,\frac{1}{2}\,1)_T$ coincides with the nesting vector $\boldsymbol{q}$. The out-of-plane component arises from an antiferromagnetic interlayer coupling J_z of the Fe^{2+} spins. The formation of the SDW is accompanied by a charge gap, which is observed by optical-spectroscopy [115] and Hall-effect measurements [67, 116]. Figure 2.2 (c) shows the Fermi surface in the SDW state, which becomes highly reconstructed compared to the paramagnetic state, but still contains parts that are not gapped. A breakup into smaller three-dimensional pockets is also in agreement with the investigation of the Fermi surface by quantum oscillation measurements [117–119]. One way to explain the gap structure is to relate it to the hybridization of the hole bands that are downfolded to the $M(\frac{1}{2}\,\frac{1}{2})_T$ point with the electron bands at $M(\frac{1}{2}\,\frac{1}{2})_T$. This

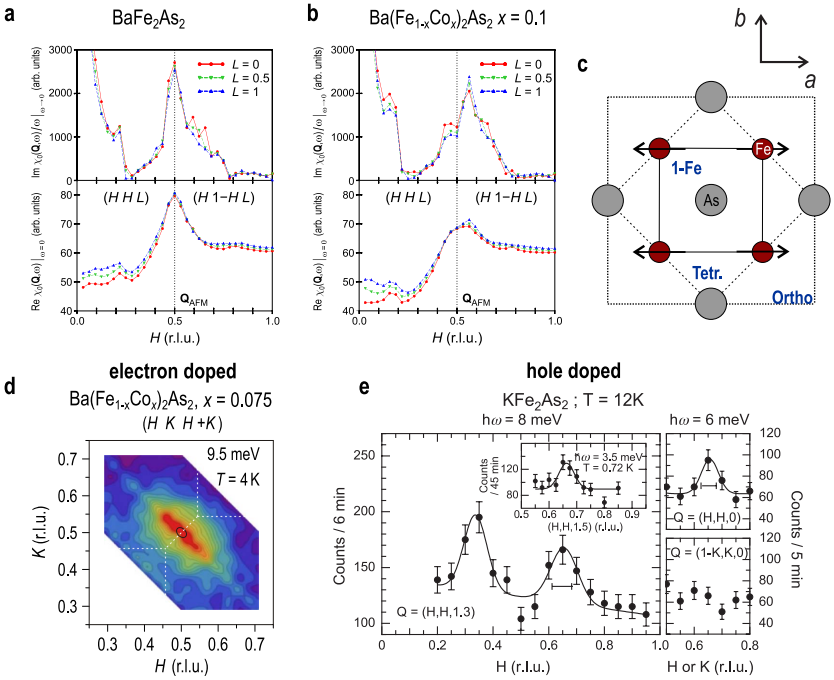

Fig. 2.3: Static limit ($\omega \to 0$) of the imaginary part $\mathrm{Im}\chi_0(\boldsymbol{q},\omega)/\omega$ (upper panel) and real part $\mathrm{Re}\chi_0(\boldsymbol{q},\omega)$ (lower panel) of the Lindhard susceptibility along a longitudinal and transverse trajectory through $\boldsymbol{Q}_{\mathrm{AFM}} = (\frac{1}{2}\ \frac{1}{2}\ 1)_{\mathrm{T}}$ for **(a)** $BaFe_2As_2$ and **(b)** 10 % doped $Ba(Fe_{1-x}Co_x)_2As_2$. **(c)** Sketch of the in-plane projection of the unit cell. The orthorhombic/magnetic (O) unit cell boundaries are indicated by a dotted line, the tetragonal (T) by a dashed line and the iron sublattice (1-Fe) by a solid line. **(d)** Contour map of the in-plane projected inelastic intensity around $\boldsymbol{Q}_{\mathrm{AFM}}$ in the superconducting state of optimally doped $Ba(Fe_{1-x}Co_x)_2As_2$ ($x = 0.075$). **(e)** Momentum cut along $(H\,H\,1.3)$, at $\hbar\omega = 8$ meV, measured in KFe_2As_2, showing incommensurate spin fluctuations at $H = 0.5 \pm 0.16$ r.l.u. Panels (a),(b) and (d) are reproduced from Ref. 120. Panel (e) is reproduced from Ref. 121.

mechanism creates hole pockets near the $M(\frac{1}{2}\ \frac{1}{2})_{\mathrm{T}}$ point. It has been argued that filling these pockets upon electron doping (e.g. Co for Fe) will lead to a Lifshitz transition at $x = 0.038$ [101, 107], accompanied by pronounced changes in the electronic structure at the onset of superconductivity. It also provides the picture that Co doping has a charge effect shifting the chemical potential with respect to the rigid bands.

2.1.2 Reciprocal-space structure of the spin fluctuations in FeSC

Upon doping with Co (or K in the hole doped case) the SDW in $BaFe_2As_2$ state is weakened [67, 71, 122]. The nesting property of the Fermi surface is conditional for the formation of a spin-density wave. It is fulfilled best in the parent compound if one regards the hole and electron pockets as two-dimensional cylindrical sheets. Since the holes and electrons are compensated, the cross-sectional area should be equal for both pockets according to the Luttinger theorem [shown in Fig. 2.2 (d)]. Electron doping with Co or Ni has a charge effect and shifts the Fermi level up with respect to the bands [101, 104, 123]. The imbalance between electrons and holes is mirrored in a shrinking of the cross section for the hole pocket and an increase for the electron pocket [101, 104], which weakens the nesting between them. In the case of electron doping the flat parts of the small hole pocket at Γ and the electron pocket at $M(\frac{1}{2}\ \frac{1}{2}\ 0)_\mathrm{T}$ can still be brought to overlap by a translation with vector $\boldsymbol{q}_1 = (\frac{1}{2}+\delta\ \frac{1}{2}-\delta\ 0)_\mathrm{T}$. This vector now acquires a transverse component $(\delta\ -\delta\ 0)$ with respect to the nesting vector of the parent compound $\boldsymbol{q}_0 = (\frac{1}{2}\ \frac{1}{2}\ 0)_\mathrm{T}$.

An incommensurability of the nesting vector for the electron-doped $Ba(Fe_{1-x}Co_x)_2As_2$ compounds was also quantitatively derived from density-functional-theory (DFT) calculations of the (static) Lindhard-function $\chi_0(\boldsymbol{q},\omega)$, $\omega \to 0$ [81, 120]. As shown in Fig. 2.3 (b) for a 10 % doped doped $Ba(Fe_{1-x}Co_x)_2As_2$ compound, the maximum of the real part $\mathrm{Re}\,\chi_0|_{\omega\to 0}$ is shifted away from $\boldsymbol{Q}_\mathrm{AFM}$ in transverse direction [along $(H\ 1-H\ 0)$], but remains commensurate in longitudinal direction [120]. The same applies to the imaginary part $\mathrm{Im}\,\chi_0/\omega|_{\omega\to 0}$. In another approach, where the DFT calculated band structure is parametrized with a 3D tight-binding (TB) model, electron correlations are taken into account [113, 120, 124].[2] Under consideration of the Coulomb repulsion $\overline{U}$ and the Hund's rule coupling $\overline{J}$ the renormalized RPA susceptibility $\chi_\mathrm{RPA}(\boldsymbol{q})_{\omega\to 0}$ was calculated, and confirmed the result of the Lindhard-function qualitatively in terms of the incommensurability in the transverse direction [120].

Experimentally, the reciprocal-space structure of the spin fluctuations $\mathrm{Im}\,\chi(\boldsymbol{q},\omega)$ can be mapped out by inelastic neutron scattering. Figure 2.3 (d) shows the in-plane projected intensity at $E = 9.5$ meV around $\boldsymbol{Q}_\mathrm{AFM}$ in the superconducting state of optimally doped $Ba(Fe_{1-x}Co_x)_2As_2$ [120]. The pronounced anisotropy, showing an elongation in transverse direction, cannot be explained by an inherent anisotropy of the spin wave excitations in the parent compound, as indicated by the black ellipse. Therefore, the evolution of the nesting vector must be invoked as the primary reason. For higher energies the ellipse transforms into two transversely propagating modes [125, 126], which resemble the observation for the itinerant antiferromagnet chromium [127].

Furthermore, the anisotropy of the ellipse is preserved upon changing the out-of-plane component L. This implies that the observed spin excitations do not follow the symmetry of the tetragonal $I4/mmm$ unit cell [see Fig. 2.3 (c)], which would constitute a $4_2/m$ screw symmetry along the $(\frac{1}{2}\ \frac{1}{2}\ L)_\mathrm{T}$ axis [120]. A subsequent theoretical analy-

[2] Doping with Co was implemented by a rigid-band shift of the electronic structure.

sis showed that this absence of the screw symmetry is to be expected when taking the matrix elements of the Lindhard-function calculations into account. With the moment localized at the iron atoms [128, 129] the symmetry of the spin excitations follows the symmetry of the smaller unit cell, containing one iron atom [solid line in Fig. 2.3 (c)], while the As atoms only create a weak superstructure [120]. Though many theoretical papers follow this unfolded notation [15, 81, 120, 124], the literature has mostly adopted the body-centered tetragonal ("folded") unit cell for the description of the reciprocal space.[3] For the further discussion the unfolded notation, with respect to the iron sublattice, shall be used. This reduces the c lattice parameter by a factor of two and the in-plane lattice parameter by a factor of $\sqrt{2}$. The wave vector of the antiferromagnetic Bragg peak $\boldsymbol{Q}_{\mathrm{afm}} = (\frac{1}{2}\ \frac{1}{2}\ 1)_{\mathrm{T}}$ is thus written in unfolded notation as $(\frac{1}{2}\ 0\ \frac{1}{2})_{1\mathrm{Fe}}$. The subscript will henceforth be left away.

2.1.3 Unconventional order parameter in the superconducting phase of FeSC

Upon destabilizing the spin-density wave phase, the static magnetic order is transformed into a paramagnetic phase with strong spin fluctuations close to the wave vector of the AFM Bragg peak $\boldsymbol{Q}_{\mathrm{sf}} = (\frac{1}{2}\,0\,L)$. The out-of-plane component L is not specified, since it was shown that in the optimally doped samples the spin fluctuations are quasi-two-dimensional with a short correlation length ξ out of the planes [130, 131]. The intensity *vs.* L is then only determined by the Fe^{2+} magnetic form factor, peaking at $L = 0$. Nuclear magnetic resonance (NMR) studies on underdoped and optimally doped $BaFe_2As_2$ [132–135] as well as $LaO_{1-x}F_xFeAs$ [136, 137] found an increase of the spin-lattice relaxation rate (SLRR) $(T_1T)^{-1}$ upon cooling towards T_c, signifying the slowing down of spin fluctuations. The SLRR *vs.* T has been fitted with a Curie-Weiss law (CW)

$$(T_1T)^{-1} = a + b(T + \theta)^{-1} \tag{2.1}$$

where the CW parameter $|\theta|$ lies close to the AFM transition temperature T_N for the underdoped compounds and is crossing zero for the optimally doped compound [133–135]. The full spin-fluctuation spectrum in the normal state $\mathrm{Im}\chi(\boldsymbol{q},\omega)$ at $\boldsymbol{Q}_{\mathrm{sf}} = (\frac{1}{2}\,0\,L)$, observed by inelastic neutron scattering experiments, can be correspondingly fitted with the Moriya-formula, which describes paramagnons in the paramagnetic state $T > T_N$ both for antiferromagnets and nearly antiferromagnetic Fermi liquids [see Fig. 2.4 (b)] [138, 139]. The latter situation applies to the normal state of the optimally doped compounds.

However, upon entering the superconducting state the spin-fluctuation spectrum changes drastically, revealing not only a coexistence, but also an intriguing interplay of superconductivity and spin fluctuations below T_c. A clear peak appears at $\hbar\omega_r = 9.5\,\mathrm{meV}$

[3] The corresponding Miller indices were assigned with the subscript "T".

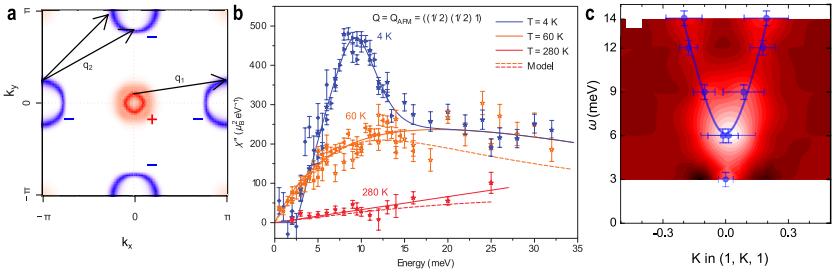

Fig. 2.4: (a) In-plane wave vector dependence of the superconducting gap $\Delta(k)$ for $s^{\pm}$-symmetry. The thickness of the line corresponds to the size and the color corresponds to the sign of $\Delta(k)$ (reproduced from Ref. 140). **(b)** Normal-state and SC-state spectrum at $\boldsymbol{Q}_{\mathrm{AFM}}$ for optimally doped $Ba(Fe_{1-x}Co_x)_2As_2$ ($x = 0.075$, $T_c = 25$ K), reproduced from Ref. 139. **(c)** Contour plot, showing the dispersion of the difference of SC and normal-state intensity in transverse direction to $\boldsymbol{Q}_{\mathrm{AFM}}$ in underdoped $Ba(Fe_{1-x}Ni_x)_2As_2$ ($x = 0.037$, $T_c = 17$ K), reproduced from Ref. 141.

in the superconducting state of optimally doped $Ba(Fe_{1-x}Co_x)_2As_2$ ($x = 0.075$), as shown in Fig. 2.4 (b). The related spectral weight $S(\boldsymbol{q},\omega)$ is deducted from the lower energy range $\omega < \omega_r$, which is completely depleted below 3 meV [139]. This range of zero intensity is termed as spin gap, while the peak is called magnetic resonant mode.[4] This excitation has been observed in the superconducting state for almost all FeSC that have an appreciable T_c, e.g. in $Ba_{1-x}K_xFe_2As_2$ [121, 142–144], $Ba(Fe_{1-x}Co_x)_2As_2$ [125, 126, 130, 139, 145–148], $Ba(Fe_{1-x}Ni_x)_2As_2$ [131, 141, 149–154], $Ba(Fe_{1-x}Ru_x)_2As_2$ [155], $BaFe_2(As_{1-x}P_x)_2$ [156, 157], the 111-family of iron-arsenide-based SC [158–160] and the 11 family of iron-chalcogenide-based SC (e.g. $FeTe_{1-x}Se_x$) [161–173].

Theoretically this mode is well understood as a feedback exciton, formed below the onset of the particle-hole continuum 2Δ. Early on it has been argued that the strong AFM fluctuations along $(\frac{1}{2}\,0\,L)$ lead to a repulsive interaction of the quasiparticles originating from the electron and the hole pockets [15]. This situations would favor a $s^{\pm}$ symmetry for the superconducting wave functions $\Delta(\boldsymbol{q})$

$$\Delta(\boldsymbol{q}) = \Delta_0 \cos(q_x)\cos(q_y) \tag{2.2}$$

which constitutes different signs for $\Delta(\boldsymbol{q})$ on the hole and electron pockets [see Fig. 2.4 (a)]. Thus, the spin fluctuations that can be derived from the normal-state Lindhard-function $\chi_0(\boldsymbol{q},\omega)$ provide the pairing glue for the superconductivity. However, the formation of an isotropic gap on both the hole and the electron pockets suppresses the particle-hole scattering along $\boldsymbol{Q}_{\mathrm{AFM}}$, which stipulates $\mathrm{Im}\,\chi_0(\boldsymbol{Q}_{\mathrm{AFM}},\omega) = 0$ below the onset of the continuum at $\Omega_c = \min(|\Delta_{\boldsymbol{q}}| + |\Delta_{\boldsymbol{q}+\boldsymbol{Q}_{\mathrm{AFM}}}|)$ [113, 120, 124, 140, 174–176].

[4] This follows the terminology in the discussion of cuprates, where an equivalent feature was observed in the SC state [6, 42].

In the RPA-formalism, outlined in Section 3.3, the interaction between the quasiparticles leads to the formation of a collective mode ω_r below Ω_c. Because of the superconducting coherence factors, this mode is only observed by neutron scattering if the SC order parameter carries a different sign on the parts of the Fermi surface that are connected by $\boldsymbol{Q}_{\mathrm{AFM}}$. Furthermore, it was found that the resonance energy exhibits a dispersion for wave vectors $\boldsymbol{q} = \boldsymbol{Q} - \boldsymbol{Q}_{\mathrm{AFM}}$ away from the antiferromagnetic wave vector [see Fig. 2.4 (c)] [141], which can be described by the dispersion relation of a gapped magnon. In conclusion, the observation of a resonant mode in the superconducting state not only serves as a hallmark for a sign-changing order parameter, but also reveals a feedback effect of the superconducting ground state on the magnetic spectrum at $\boldsymbol{Q}_{\mathrm{AFM}}$. It strongly supports the viewpoint of a spin-fluctuation mediated superconductivity in the iron-based superconductors.

2.2 The family of alkali-metal iron selenide superconductors

Within this thesis, most of the experiments regarding FeSC were done on the "122"-type family of iron selenide superconductors, e.g. $A_xFe_{2-y}Se_2$ (A = K, Rb, Cs), $Tl_{1-x}K_xFe_{2-y}Se_2$ and $Tl_{1-x}Rb_xFe_{2-y}Se_2$, which represent a new class of iron chalcogenide compounds. They differ from the known "11" iron chalcogenides $FeTe_{1-x}Se_x$ [61, 62] in that they have an intercalated layer of alkali atoms, which not only separates the FeSe planes, but also introduces additional electron doping in the system. The structure is very similar to the one of the XFe_2As_2 (X = Ca, Sr, Ba) iron arsenide compounds, displayed in Fig. 2.1 (a). Only here the arsenic is replaced by selenium and the alkaline earth metal is replaced by an alkali metal. After the first report of superconductivity in $K_xFe_2Se_2$ by Guo *et al.* in 2010 [1] ($T_c \approx 30$ K) it was soon realized that the real composition exhibits a significant deficiency $y \approx 0.4$ of iron compared to the nominal composition of $A_{0.8}Fe_2Se_2$ [63, 65, 66, 177]. Furthermore, different compositions of x and $2-y$ generate different electronic behavior. As shown in Fig. 2.5 (a), a high amount of alkali-metal atoms results in an insulating ground state, whereas superconducting samples are obtained for $x < 0.8$ [64, 178]. There are a number of characteristics that are uniquely observed for this family of FeSC.

1. The crystals grow to non-stoichiometric composition with a varying content in alkali-metal atoms and iron atoms.

2. Systematic studies of the phase diagram in dependence on either the valence of iron [178] or the iron content $2-y$ [64] showed no variation of T_c for the superconducting samples, which produces a rather rectangular SC dome in Fig. 2.6 (a).

3. The specific-heat anomaly at T_c is weak and hardly discernible [179]. The jump height $\Delta C/T|_{T_c}$ is only a fraction of the corresponding values observed for optimally doped $Ba(Fe_{1-x}Co_x)_2As_2$ and $Ba_{1-x}K_xFe_2As_2$, despite the considerably large T_c [179].

4. The superconducting dome in Fig. 2.6 (a) is bordered by insulating and antiferromagnetic phases, which is contrary to the metallic parent compounds observed for XFe$_2$As$_2$ (X=Ca, Sr, Ba).

5. The normal-state resistivity *vs.* temperature features a broad hump, centered at $T_{\max}$ [1, 63, 65, 66, 180]. The $T_{\max}$ varies for different compositions.

6. Measurements of the magnetic susceptibility [63], μSR [181] and the Mössbauer effect [182] in high temperatures found an antiferromagnetic transition above $T = 500\,\mathrm{K}$ in the superconducting samples. Initially this led to a great astonishment, since such strong magnetism is expected to exclude the occurrence of superconductivity [183].

The transition temperature T_N does not vary much upon changing from the insulating regime to the metallic/superconducting regime [64, 178] [see Fig. 2.6 (a)], which means that the magnetic phase and the superconducting phase are not directly correlated. In fact, a multitude of experiments, which will be discussed in Section 2.2.2, pointed out that the majority part of each superconducting sample is made of the insulating A_2Fe$_4$Se$_5$ phase that is also responsible for the antiferromagnetism. The metallic/SC phase is the minority phase, which can form under certain growth conditions, but has not been obtained in pure form yet. The fact that it occurs only together with the insulating/magnetic phase explains the anomalous properties 1, 3 – 6.

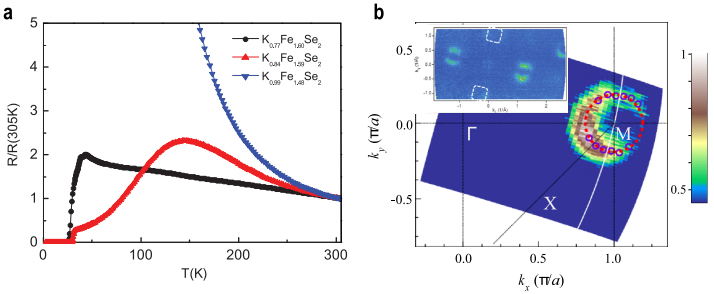

Fig. 2.5: (a) Electrical resistivity *vs.* temperature for various compositions of K$_x$Fe$_{2-y}$Se$_2$, taken from Ref. 180. **(b)** In-plane Fermi surface in the normal state of K$_{0.8}$Fe$_{1.7}$Se$_2$ at $T = 40\,\mathrm{K}$ (reproduced from Ref. 184). The inset shows the Fermi surface, measured on a Rb$_{0.77}$Fe$_{1.61}$Se$_2$ sample, taken from Ref. 14.

2.2.1 Electronic structure of the superconducting phase

Despite the phase separation, a number of ARPES studies were able to determine the Fermi surface of the metallic/SC phase of A_xFe$_{2-y}$Se$_2$ [4, 7–14, 184], which provided

always the same result, given in Fig. 2.5 (b). The central hole pocket at the Γ point vanishes below the Fermi surface, with its top lying 90 meV below the Fermi level E_F. At the $X(\frac{1}{2}\,0\,0)$-point reside two large electron pockets, which are nearly degenerate [4, 7–12, 14, 184]. This electronic structure matches qualitatively with a strongly electron-doped variant of the FeAs-based superconductors. A similar Fermi surface has been observed for overdoped $Ba(Fe_{1-x}Co_x)_2As_2$ ($x = 0.3$) [104], where superconductivity is already suppressed [67, 71]. For this case the absence of the superconducting ground state is expected, since the removal of the hole pocket also disables the nesting between hole and electron pockets and, thus, diminishes the spin fluctuations that are presumably responsible for Cooper pairing. However, the presence of superconductivity with a T_c of 32.4 K [64] observed in $Rb_xFe_{2-y}Se_2$, is then not understandable in this scenario. Therefore, another pairing mechanism must be at hand. A closer inspection of the Fermi surface by polarized ARPES, which can separately observe the two different electron pockets because of the different orbital symmetry, is given in the inset of Fig. 2.5 (b). A rather squarish shape of the pockets [14] is revealed. The quasi-nesting between the flat parts of the contour could act as a source of enhanced spin fluctuations. Calculations of the Lindhard-function will be presented in Chapter 5 in conjunction with the experimentally determined spin-fluctuation spectrum.

Another important input from the ARPES studies is the reciprocal-space structure of the superconducting order parameter $\Delta(\boldsymbol{q})$. It was found that the gap opens isotropically on the electron pocket [4, 7–14]. The gap size Δ varies between different samples. Specifically for $K_xFe_{2-y}Se_2$ a size of 9 meV and 10.3 meV was reported [4, 7].

It was also possible to probe the low-energy spin fluctuations by NMR on the ^{77}Se nuclei in the normal state of the superconducting phase [16, 185–190]. In contrast to the iron pnictides, no Curie-Weiss-like upturn was observed in the temperature dependence of the spin-lattice relaxation rate $(TT_1)^{-1}$, which indicates that spin fluctuations might be weak [16, 185–190]. Nevertheless, the absence of a coherence peak in $(TT_1)^{-1}$ *vs.* T upon transition into the SC state, similar to the iron arsenides, indicates an unconventional pairing mechanism. However, the determination of the nature and the strength of the spin fluctuations requires a $\boldsymbol{Q}$-resolved study like inelastic neutron scattering, which will be provided within Chapter 5.

2.2.2 $A_xFe_{2-y}Se_2$: Phase separation into insulating $A_2Fe_4Se_5$ and superconducting $A_xFe_2Se_2$

The strongly antiferromagnetic and insulating phase, displayed in the unusual phase diagram of the $A_xFe_{2-y}Se_2$ superconductors in Fig. 2.6 (a), could be ascribed to a $A_2Fe_4Se_5$ structure. This phase is stoichiometric, explaining the scattering of the experimentally determined compositions around the $A_{0.8}Fe_{1.6}Se_2$-stoichiometry for FeSe122. The 20% vacancies in the iron sublattice were found to order into a $\sqrt{5} \times \sqrt{5}$ superstructure at very high temperatures ($T_S = 578$ K for $K_{0.8}Fe_{1.6}Se_2$ [192]) by neutron and X-ray diffraction [192–196]. At a somewhat lower temperature antiferromagnetic order sets

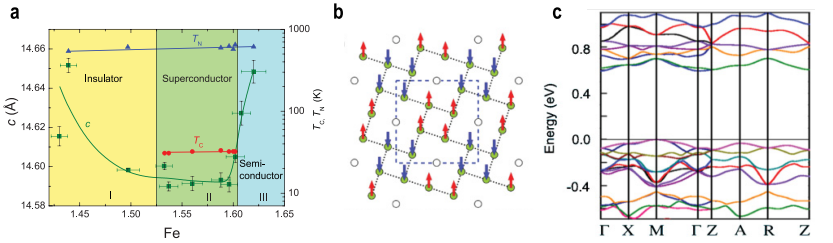

Fig. 2.6: (a) Phase diagram of $Rb_xFe_{2-y}Se_2$ in dependence of the Fe content (reproduced from Ref. 64). **(b)** In-plane crystal and magnetic structure of $A_2Fe_4Se_5$, describing the ordering of the Fe-vacancies and the Fe-spins in a blocked checkerboard antiferromagnetic state ("block-AFM"). **(c)** Band structure from first-principles calculations for the block-AFM state in $K_{0.8}Fe_{1.6}Se_2$. Both panels (b) and (c) are reproduced from Ref. 191.

in (T_N = 559 K). The spin structure was refined to a "block-AFM", following the nomenclature of Dagotto *et al.* [52]. As shown in Fig. 2.6 (b), the iron vacancies group the iron atoms into plaquettes of four ferromagnetically aligned moments. The moment size was found to be as large as $\mu = 3.4\,\mu_B$ [192, 194, 195]. Band structure calculations [191, 197] for this configurations, shown in Fig. 2.6 (c), reveal a band gap of 594 meV, which explains the insulating behavior for this compound.

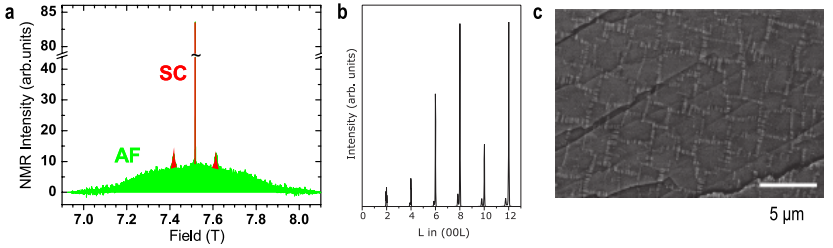

Fig. 2.7: (a) ^{87}Rb NMR spectrum on $Rb_{0.74}Fe_{1.6}Se_2$, measured by Y. Texier. The red intensity stems from nuclei, belonging to the SC phase. The broad green background is related to the antiferromagnetic $Rb_2Fe_4Se_5$ phase. The figure is similarly published in Ref. 16. **(b)** Intensity distribution along $\boldsymbol{c}^*$, determined in a single-crystal X-ray diffraction on $Cs_{0.8}Fe_{1.6}Se_2$ by synchrotron radiation (reproduced from Ref. 198). **(c)** Back-scattered electron images of scanning electron microscopy measurements on $K_xFe_{2-y}Se_2$, showing a network of filaments, which can be identified with the superconducting phase (reproduced from Ref. 199).

The $A_2Fe_4Se_5$ variant obviously is not able to carry superconductivity. A number of experiments revealed a mesoscopic phase separation into a majority vacancy-ordered $A_2Fe_4Se_5$ structure and a minority structure, where vacancies are either disordered [200, 201] or completely absent [16, 202, 203]. The latter phase is the metallic/SC phase, since it remains paramagnetic down to T_c and shows the formation of a vortex

lattice as observed by μSR [204–206]. The volume fraction of the SC phase was determined to lie between 12 % and 20 % [204–206], which renders a structural refinement of the SC phase difficult [207]. All experimental studies, investigating the phase separation, are reviewed in References 52, 208, 209. One of them was an NMR study by our collaborators in the group of J. Bobroff on a $Rb_{0.74}Fe_{1.6}Se_2$ sample that was taken from the same batch used for inelastic neutron scattering. The spectrum of the ^{87}Rb nuclei in Fig. 2.7 (a) shows a sharp component, stemming from the Rb atoms in the SC phase. This is only consistent with a vacancy free iron lattice. Secondly, the spectral weight of the ^{87}Rb line would correspond to a composition of $Rb_{0.3}Fe_2Se_2$. This implies a doping level of 0.15 e^- / Fe, if each Rb donates one electron. Furthermore, single crystal X-ray diffraction with synchrotron radiation resolved Bragg peaks from the SC phase, which appear as satellites to the Bragg peaks of the AFM phase [198]. The relatively sharp width of the satellites along the $(0\,0\,L)$ direction in Fig. 2.7 (b) signifies the bulk character of the SC phase. The real space micro structure of single crystalline $A_xFe_{2-y}Se_2$ has been elucidated by scanning electron microscopy [199, 210], transmission electron microscopy [200, 201] and near-field optical microscopy [205]. These studies all reveal that the superconducting phase condenses into droplets, which are arranged such that they form a spiderweb-like three-dimensional network [199], as shown in Fig. 2.7 (c). On the one hand, this enables long-range coherence of the superconducting condensate, which explains the 100 % shielding fraction as measured by magnetization [64]. On the other hand, the fact that the SC phase is embedded in the bulk $A_2Fe_4Se_5$ matrix, and possibly stabilized by it, also provides structural long-range correlations for the SC phase [198], which is an essential condition for $\boldsymbol{Q}$-resolved experiments with a bulk sensitive technique like neutron scattering.

2.3 Unconventional superconductivity in heavy-fermion compounds

Another important class of superconductors is based on rare-earth elements. Here, the spin and charge degrees of freedom are essentially provided by the f-electrons. Intensive research activity was spurred by the discovery of superconductivity in $CeCu_2Si_2$ ($T_c = 1.5\,K$) by Steglich *et al.* in 1979 [21]. The large specific-heat anomaly of $\Delta C/T_c = 1000\,mJ/mol\,K^2$ correlates with the large linear specific-heat coefficient $\gamma = 1270\,mJ/mol\,K^2$ in the normal state, signalling that strongly renormalized quasiparticles participate in the superconducting pairing [211].[5] The unconventional nature of superconductivity was suggested by the proximity to an antiferromagnetic order [213]. As shown in the phase diagram of $CeCu_2Si_2$ *vs.* hydrostatic pressure [Fig. 2.8 (a)], the superconducting dome encompasses the quantum critical point (QCP) of the bordering antiferromagnetic phase [214].[6] A qualitatively similar picture is provided by the antiferromagnets $CeIn_3$ and $CePd_2Si_2$, which can be tuned towards superconductivity upon application of hydrostatic pressure [46, 215]. The observation of non-Fermi-liquid properties in the normal-state transport can be attributed to the emergence of critical spin fluctuations, which may also provide the pairing glue for the Cooper pairs [46, 215, 216].

The multipolar degrees of freedom in the crystal-field ground state of the f-electron system led to the discovery of multipol-ordered phases in several heavy-fermion compounds, which are reviewed in Ref. 49 and 217. A quite intriguing example is provided by the filled skutterudite $PrOs_4Sb_{12}$, which exhibits superconductivity below $T_c = 1.85\,K$ within a heavy-fermion state ($\Delta C/T_c = 500\,mJ/mol\,K^2$) [218]. Here, superconductivity lies in proximity to an antiferroquadrupolar (AFQ) ordered phase, which is stabilized in an external magnetic field as shown in Fig. 2.8 (b) [219]. The antiferroquadrupolar order gives rise to an antiferromagnetic moment $\boldsymbol{\mu}_{AF}$ along $\boldsymbol{q} = (1\,0\,0)$, which can be detected by neutron diffraction [220]. Fluctuations of the antiferroquadrupolar order in zero field are revealed by the observation of a dispersing quadrupolar exciton at $\boldsymbol{q}$ in the superconducting phase [48]. Therefore, it has been proposed that the excitonic quadrupolar fluctuations are mediating the pairing in $PrOs_4Sb_{12}$ [219], in contrast to the spin-fluctuation mediated superconductivity in other heavy-fermion (HF) systems and transition metal compounds. It is of current interest not only to understand the nature of the exotic superconducting state, but also to clarify the coexistence of HF superconductivity and the purely localized AFQ order in this compound [219]. The recent discovery of a superconducting phase enclosed by a ferroquadrupolarly ordered phase in $PrTi_2Al_{20}$ [221] further highlights the relevance of this topic. The prototypical antiferroquadrupolar ordered system CeB_6 is thereby in the center of interest, since it exhibits an interplay of itinerant spin dynamics and localized

[5] For comparison, specific-heat measurements on optimally doped $Ba_{1-x}K_xFe_2As_2$ found $\gamma = 50\,mJ/mol\,K^2$ and $\Delta C/T_c = 125\,mJ/molK^2$ [212].

[6] A second superconducting dome at higher pressures was identified in $CeCu_2(Si_{1-x}Ge_x)_2$ ($x = 0.1$).

multipolar ordering, which will be the subject of this thesis.

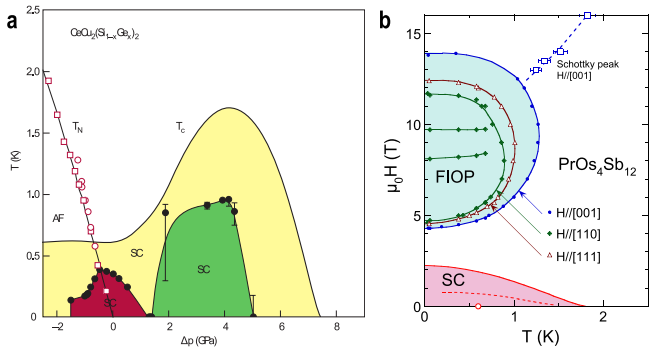

Fig. 2.8: **(a)** Pressure phase diagram of the heavy-fermion compound $CeCu_2(Si_{1-x}Ge_x)_2$ ($x = 0$ and $x = 0.1$) showing the AFM transition temperature T_N and the superconducting transition temperature T_c *vs.* pressure. The thin solid line for T_c corresponds to $x = 0$, the points belong to $x = 0.1$ (reproduced from Ref. 222). **(b)** Magnetic phase diagram of the unconventional superconductor $PrOs_4Sb_{12}$, featuring the superconducting phase in the ground state and an antiferroquadrupolar ordered phase (FIOP) at nonzero fields (reproduced from Ref. 219).

2.4 The magnetic phase diagram of CeB_6

2.4.1 Crystal structure and ground state of CeB_6

CeB_6 is a well studied three-dimensional f-electron compound, which has a simple crystallographic structure. It is composed of a cubic lattice of Ce^{3+} ions, which are surrounded by B_6 octahedra [see Fig. 2.9 (a)]. It orders antiferromagnetically (phase III) below $T_N = 2.4\,K$ as evidenced by a sharp peak in the specific heat in zero field [see Fig. 2.9 (b)] [223]. More interesting is a second weaker feature in c_p at $T_Q = 3.2\,K$, preceding the AFM phase [223]. For a long time, it remained unclear what kind of long-range order is established in the phase below T_Q (phase II). Magnetic field can stabilize this phase, as evidenced by the shift of the c_p anomaly to higher temperatures [see Fig. 2.9 (b)]. The ground state of CeB_6 is the Γ_8 quartet, which is separated by $E = 46\,meV$ from the higher lying Γ_7 doublet, as determined by Raman and neutron spectroscopy [224, 225]. The fourfold degenerate ground state comprises two spin and two orbital degrees of freedom. The eigenstates, expressed in eigenstates of the total

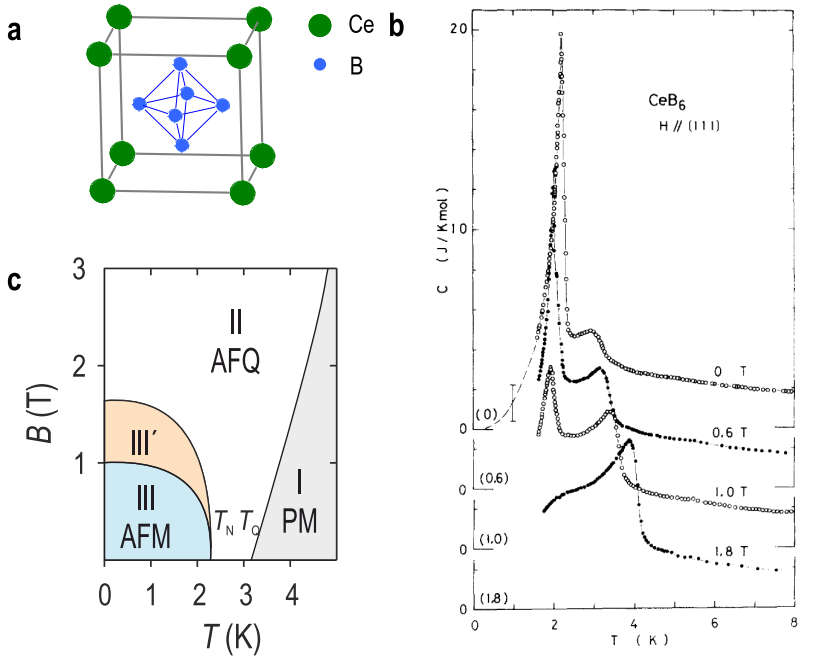

Fig. 2.9: **(a)** Sketch of the chemical unit cell of CeB_6. **(b)** Specific heat *vs.* temperature in different magnetic fields. This figure has been reproduced from Ref. 223. **(c)** Sketch of the (low-field) magnetic phase diagram of CeB_6 for $\boldsymbol{B} \parallel (1\,1\,0)$, comprising paramagnetic, AFQ and AFM phases.

angular moment of $J = 5/2$ for the Ce^{3+} ion, are:

$$|+,\uparrow\rangle = \sqrt{\frac{5}{6}}|\frac{5}{2}\rangle + \sqrt{\frac{1}{6}}|-\frac{3}{2}\rangle \tag{2.3a}$$

$$|+,\downarrow\rangle = \sqrt{\frac{5}{6}}|-\frac{5}{2}\rangle + \sqrt{\frac{1}{6}}|\frac{3}{2}\rangle \tag{2.3b}$$

$$|-,\uparrow\rangle = |\frac{1}{2}\rangle, \quad |-,\downarrow\rangle = |-\frac{1}{2}\rangle \tag{2.3c}$$

Here, the eigenvalues $\sigma = \uparrow\downarrow$ refer to the spin and $\tau = \pm$ to the pseudospin (orbital) component of the wave function. Consequently, an antiferro-orbital ordering has been proposed as the mechanism for phase II, which would lift the orbital degeneracy [226]. Since it does not break time-reversal symmetry, it was related to an ordering of the

electric quadrupoles, which is why phase II is also referred to as an antiferroquadrupolar (AFQ) phase in literature. In zero field, the experimental proof for AFQ ordering was delivered later by resonant X-ray scattering (RXS) at the AFQ ordering wave vector $\boldsymbol{Q}_{\mathrm{AFQ}} = R(\frac{1}{2}\,\frac{1}{2}\,\frac{1}{2})$ [227].[7]

This phase can be stabilized up to very high laboratory fields of 60 T [228, 229]. In low fields the system enters the AFM phase, which upon application of a magnetic field changes to an intermediate phase (phase III′) before entering the phase II.[8]

2.4.2 Magnetic structure in the antiferromagnetic and antiferroquadrupolar phase of CeB_6

In zero magnetic field the ordering of the quadrupoles is generally hidden to neutrons [49, 233].[9] AFQ order has been observed first by resonant X-ray diffraction [227]. However, in magnetic field ordered spins can be induced at the Ce^{3+} site [234], which are modulated according to the underlying AFQ structure, described by the propagation vector $\boldsymbol{q}_{\mathrm{AFQ}} = R(\frac{1}{2}\,\frac{1}{2}\,\frac{1}{2})$. This follows from the Zeeman interaction of the Γ_8-quartet in a magnetic field $\boldsymbol{B}$.

$$\mathcal{H}_{\mathrm{Z}} = g\mu_{\mathrm{B}}\boldsymbol{J}\boldsymbol{B} \tag{2.4}$$

Here the Landé factor is $g = \frac{6}{7}$. The total angular momentum $\boldsymbol{J}$ can be expressed via the orbital operator $\boldsymbol{\tau}$ and the spin operator $\boldsymbol{\sigma}$ [226], and the Zeeman term becomes:

$$\mathcal{H}_Z = 2\mu_{\mathrm{B}}\left[\sigma_x(1+\frac{8}{7}T^x)B_x + \sigma_y(1+\frac{8}{7}T^y)B_y + \sigma_z(1+\frac{8}{7}T^z)B_z\right] \tag{2.5a}$$

$$T^x = \frac{\sqrt{3}}{2}\tau^x - \frac{1}{2}\tau^z, \quad T^y = -\frac{\sqrt{3}}{2}\tau^x - \frac{1}{2}\tau^z, \quad T^z = \tau^z \tag{2.5b}$$

In case of a O_{xy}-type quadrupolar order ($\tau \neq 0$) with the magnetic field applied along $(1\,1\,0)$ an antiferromagnetic dipolar moment J_z is induced [235]. For low enough fields the moment increases linearly with the magnetic field and vanishes in zero field, which has been experimentally observed, as shown in Fig. 2.10 (b) [231, 234, 236]. At the same time a ferromagnetic moment is induced, which can be determined from magnetization measurements [237]. However, because of the underlying quadrupolar order $\tau_z = \pm\tau$ the Landé-factor g is different for lattice sites with different quadrupole moments. For a magnetic field that is applied along a high-symmetry direction, diagonal-

[7] An intensity is observed at the $2p \rightarrow 5d$ edge, which shows an order-parameter-like increase below T_{Q} [227].
[8] The opposite behavior of both AFM and AFQ phases under magnetic field suggests a competition, which will be discussed in Section 2.4.3.
[9] However, neutrons can detect AFQ order indirectly via associated lattice distortions.

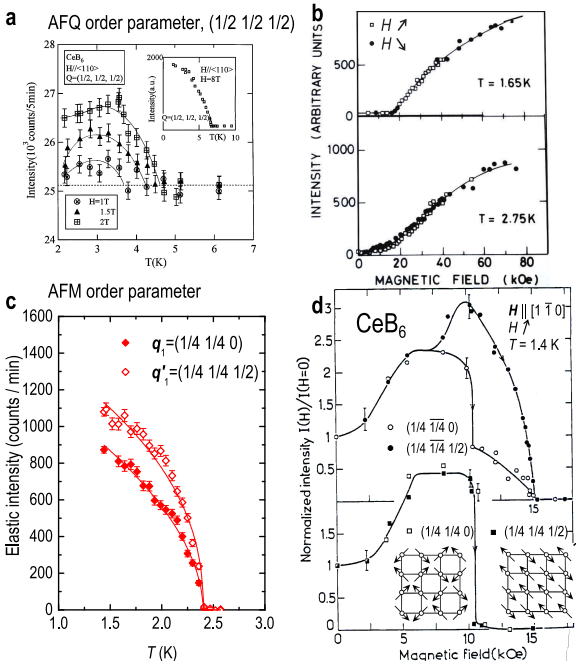

Fig. 2.10: **(a)** Temperature dependence of the AFQ Bragg intensity at $R(\frac{1}{2}\ \frac{1}{2}\ \frac{1}{2})$ in different magnetic fields (reproduced from Ref. 230). **(b)** Magnetic-field dependence of the AFQ Bragg intensity at $R(\frac{1}{2}\ \frac{1}{2}\ \frac{1}{2})$. For $T = 1.65$ K (upper panel) the sample is initially in the AFM state in zero field, for $T = 2.75$ K (lower panel) it is in the AFQ state. The figure is reproduced from Ref. 231. **(c)** Temperature dependence of the AFM Bragg intensity at the ordering wave vectors $\boldsymbol{q}_1 = \Sigma(\frac{1}{4}\ \frac{1}{4}\ 0)$ and $\boldsymbol{q}_1' = S(\frac{1}{4}\ \frac{1}{4}\ \frac{1}{2})$, measured at IN3 (ILL, Grenoble). **(d)** Magnetic-field dependence of the AFM Bragg peaks originating from the K_{xy} domain: $\boldsymbol{q}_1 = \Sigma(\frac{1}{4}\ \frac{1}{4}\ 0)$, $\boldsymbol{q}_1' = S(\frac{1}{4}\ \frac{1}{4}\ \frac{1}{2})$ and $\boldsymbol{q}_2 = \Sigma_2(\frac{1}{4}\ \overline{\frac{1}{4}}\ 0)$, $\boldsymbol{q}_2' = S_2(\frac{1}{4}\ \overline{\frac{1}{4}}\ \frac{1}{2})$ (reproduced from Ref. 232). The sketches depict the ordering of the spins in phase III and phase III′ in the $(0\,0\,1)$ plane.

ization of the Zeeman-term gives the Landé factor [235, 238]:

$$g_{\pm} = 2 \pm \frac{8}{7}, \quad \text{for } \boldsymbol{B} \parallel (0\,0\,1) \tag{2.6a}$$

$$g_{\pm} = \frac{2(\sqrt{61} \pm 2)}{7}, \quad \text{for } \boldsymbol{B} \parallel (1\,1\,0) \tag{2.6b}$$

$$g_{\pm} = 2\frac{8}{7} \pm \frac{1}{7}, \quad \text{for } \boldsymbol{B} \parallel (1\,1\,1) \tag{2.6c}$$

This anisotropic Zeeman splitting is mirrored in the anisotropy of the phase diagram regarding the phase III-II boundary line $B_c^{\langle 001\rangle} > B_c^{\langle 110\rangle} > B_c^{\langle 111\rangle}$, and the AFQ transition line $T_Q^{\langle 001\rangle} < T_Q^{\langle 110\rangle} < T_Q^{\langle 111\rangle}$ [239, 240]. The temperature dependence of the field-induced AFQ intensity in different magnetic fields is shown in Fig. 2.10 (a). It exhibits an anomalous behavior with an order-parameter-like increase below T_Q and a suppression to almost zero towards lower temperatures [230]. The reduction of intensity can be attributed to the transition into the antiferromagnetic phase III, suggesting that both AFQ and AFM phases are competing.

The magnetic structure of the AFM phase in zero field has been studied by elastic neutron scattering experiments [232, 234, 241, 242]. The ordering can be described by a non-collinear $2\boldsymbol{q}_1 - \boldsymbol{q}_1'$ structure, with $\boldsymbol{q}_1 = \Sigma(\frac{1}{4}\,\frac{1}{4}\,0)$, $\boldsymbol{q}_2 = \Sigma_2(\frac{1}{4}\,\frac{\overline{1}}{4}\,0)$ and $\boldsymbol{q}_1' = S(\frac{1}{4}\,\frac{1}{4}\,\frac{1}{2})$, $\boldsymbol{q}_2' = S_2(\frac{1}{4}\,\frac{\overline{1}}{4}\,\frac{1}{2})$ [241, 242]. The corresponding moments $\boldsymbol{m}_{\boldsymbol{q}_1}$ and $\boldsymbol{m}_{\boldsymbol{q}_2}$ were found to be orthogonal, pointing along the $[1\,\overline{1}\,0]$ and $[1\,1\,0]$ directions, respectively, which creates the non-collinear structure as depicted in Fig. 2.10 (d). The assumption of equal moments is conflicting with zero-field μSR measurements, which found eight frequencies instead of the expected three [243]. A neutron powder diffraction study revealed that the spins are additionally modulated in and out of the (001)-plane: $\mu = 0.01\mu_B$, $0.136(7)\,\mu_B$ for $z = 0$ and $\mu = 0.744(16)\mu_B$, $0.543(16)\mu_B$ for $z = 1$ [242]. It was discussed that this structure results from a competition of dipolar, quadrupolar and octupolar interactions [242]. In fact, the AFQ order, which is constituted by the f-electrons only, has impact on the conduction electron system. Muon-spin relaxation studies also found an anisotropic Knight shift, which strongly changes below T_Q [see Fig. 2.11 (c)] [244]. From this an anisotropic contact hyperfine coupling term A_{con} of the muons was inferred, which follows the temperature dependence of the AFQ order parameter for different fields [244].[10]

The temperature dependence of the AFM Bragg peaks at $\boldsymbol{q}_1$ and $\boldsymbol{q}_1'$, presented in Fig. 2.10 (c), shows an order-parameter-like increase below T_N with a critical exponent of $2\beta = 0.44 \pm 0.02$:

$$I(\boldsymbol{q}_1) \sim I(\boldsymbol{q}_1') \sim (1 - \frac{T}{T_N})^{2\beta} \tag{2.7}$$

The exponent $\beta = 0.22 \pm 0.01$ for the magnetic order parameter lies between the $\beta = 0.125 \pm 0.01$ and $\beta = 0.325 \pm 0.01$, which are the solutions for the $d = 2$ and $d = 3$ Ising model.

The field dependence of the AFM Bragg peaks is shown in Fig. 2.10 (d) for $\boldsymbol{B} \parallel [1\,\overline{1}\,1]$ [232]. One must keep in mind that there exist three magnetic domains K_{yz}, K_{zx} and K_{xy}, where the indices denote the plane of the ordered spins for each domain [232, 241]. They are selected by the magnetic field such that the AF moments are aligned perpendicular to the field, which ensures the largest Zeeman-energy gain [232, 245].

[10] It was qualitatively explained by the anisotropic RKKY interaction because of the aspherical charge distribution induced by the AFQ order below T_Q [244].

In Fig. 2.10 (d) the intensity at $\boldsymbol{q}_1^{xy} = \Sigma^{xy}(\frac{1}{4}\,\frac{1}{4}\,0)$ and $\boldsymbol{q}_2^{xy} = \Sigma_2^{xy}(\frac{1}{4}\,\frac{\overline{1}}{4}\,0)$ is increasing in magnetic field $\boldsymbol{B} \parallel [1\,\overline{1}\,1]$, which can be attributed to domain selection. At $B_c = 1.1\,\mathrm{T}$ the abrupt vanishing of the $\boldsymbol{q}_1^{xy} = \Sigma^{xy}(\frac{1}{4}\,\frac{1}{4}\,0)$ and $\boldsymbol{q}_1'^{xy} = S^{xy}(\frac{1}{4}\,\frac{1}{4}\,\frac{1}{2})$ Bragg peaks signals a change of the magnetic structure [232]. The magnetization curve exhibits a step-like increase [see Fig. 2.11 (b)] at B_c, marking the entrance into phase III′. The remaining $\boldsymbol{q}_2^{xy} = \Sigma_2^{xy}(\frac{1}{4}\,\frac{\overline{1}}{4}\,0)$ and $\boldsymbol{q}_2'^{xy} = S_2^{xy}(\frac{1}{4}\,\frac{\overline{1}}{4}\,\frac{1}{2})$ Bragg peaks vanish at $B_{c2} = 1.5\,\mathrm{T}$, accompanied by another anomaly in the magnetization curve [232, 245]. This double-step feature is observed for every field direction in Fig. 2.11 (b), most clearly for $\boldsymbol{B} \parallel [1\,1\,0]$[11] [245]. Since only that set of Bragg peaks $\boldsymbol{q}_2^{xy}$, $\boldsymbol{q}_2'^{xy}$ survives, where the moments point along $\boldsymbol{m} \parallel [1\,1\,0]$, the spin structure of phase III′ is inferred to be collinear [232] [see inset of Fig. 2.10 (d)].

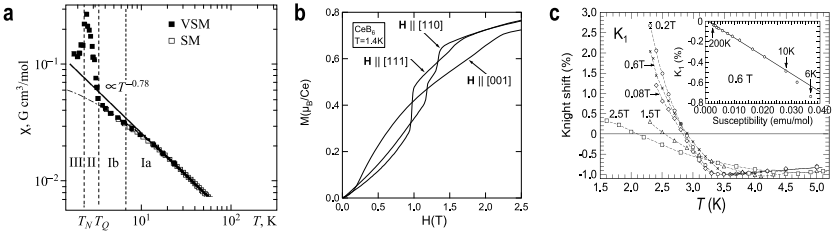

Fig. 2.11: (a) Temperature dependence of the magnetic susceptibility, measured with $\boldsymbol{B} \parallel [1\,1\,1]$ (reproduced from Ref. 237). **(b)** Field dependence of the magnetization in the AFM state for $\boldsymbol{B} \parallel \langle 0\,0\,1\rangle, \langle 1\,1\,0\rangle$ and $\langle 1\,1\,1\rangle$ (reproduced from Ref. 245). **(c)** μSR-Knight shift *vs.* temperature for different magnetic fields (reproduced from Ref. 244).

Above B_{c2} the system enters the AFQ phase, signified by the onset of the AFQ $(\frac{1}{2}\,\frac{1}{2}\,\frac{1}{2})$ Bragg intensity at $B_Q = 1.7\,\mathrm{T}$ [as shown in Fig. 2.10 (b)] [231]. This clearly shows that the RKKY-mediated magnetic order at $\boldsymbol{q}_1$ and $\boldsymbol{q}_1'$ and the AFQ spin-modulations along $\boldsymbol{q}_{\mathrm{AFQ}} = R(\frac{1}{2}\,\frac{1}{2}\,\frac{1}{2})$ are competing. This competition reaches into the AFQ phase at $T = 2.75\,\mathrm{K}$ in Fig. 2.10 (b), where an onset of the Bragg intensity is still discernible because of the convex shape in the low-field range [230, 231]. This motivated a description of the magnetic phase diagram in a localized, mean-field-like model, discussed in the next section.

2.4.3 Mean-field description of the phase diagram

The $B-T$–phase diagram of CeB_6 has been calculated for a mean-field Hamiltonian comprising the Zeeman term [Eq. (2.5)] and the interaction terms for all 15 allowed multipole operators of the Γ_8 quartet (dipolar, quadrupolar and octupolar) [235, 248].

[11] Here at $B_{c1} = 1.2\,\mathrm{T}$ and $B_{c2} = 1.4\,\mathrm{T}$.

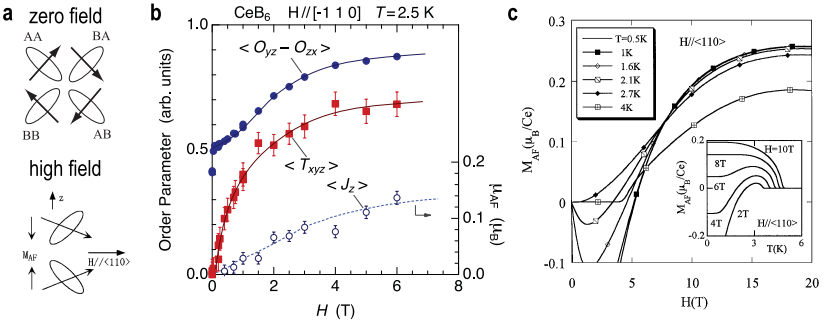

Fig. 2.12: (a) Schematic of the site indexing in the 4 sublattice model. The first index describes the quadrupole sublattice the second index the spin sublattice. Lower panel: spin configuration in high fields $B > B_Q$ (the figures has been reproduced from Ref. 246). **(b)** Field dependence of the induced dipolar moment J_z and the octupolar moment T_{xyz} as well as the quadrupole moment $\langle O_{yz} - O_{zx} \rangle$, which were determined from resonant X-ray diffraction (reproduced from Ref. 247). **(c)** Calculated field dependence of the $(\frac{1}{2}\ \frac{1}{2}\ \frac{1}{2})$ Bragg peak in the multipolar mean-field model (reproduced from Ref. 246).

It was found that the most stable quadrupolar order in the AFQ state is of the O_{xy}-type [235].[12] A subsequent study employed a Hamiltonian consisting of a Zeeman term $\mathcal{H}_Z$, an exchange term $\mathcal{H}_{ex}$, a quadrupole term $\mathcal{H}_Q$ and an octupole term $\mathcal{H}_{oct}$ [246]:

$$\mathcal{H} = \mathcal{H}_Z + \mathcal{H}_{ex} + \mathcal{H}_Q + \mathcal{H}_{oct} \tag{2.8a}$$

$$\mathcal{H}_Z = -\sum_i g_j \mu_B \boldsymbol{B} \boldsymbol{J}(i) \tag{2.8b}$$

$$\mathcal{H}_{ex} = -\sum_{i,j} K_{ex} \boldsymbol{J}(i) \boldsymbol{J}(j) \tag{2.8c}$$

$$\mathcal{H}_Q = -\sum_{i,j} K_{quad} O_\gamma(i) O_\gamma(j), \quad \gamma = (yz, zx, xy) \tag{2.8d}$$

$$\mathcal{H}_{oct} = -\sum_{i,j} K_{oct} T_{xyz}(i) T_{xyz}(j) \tag{2.8e}$$

$$\text{with } O_{xy} = \frac{\sqrt{3}}{2} \overline{J_x J_y}, \quad T_{xyz} = \frac{\sqrt{15}}{6} \overline{J_x J_y J_z} \tag{2.8f}$$

The lattice was divided into 4 sublattices (AA, AB, BA, BB) in regard of the consecutive ordering of quadrupoles and spins [see Fig. 2.12 (a)]. The Hamiltonian is considered in mean-field approximation, where on each sublattice the multipoles are interacting with

[12] Furthermore, the consideration of a field-induced T_{xyz}-type $(\frac{1}{2}\ \frac{1}{2}\ \frac{1}{2})$ antiferrooctupolar ordering was found to be crucial in order to explain the angle dependent hyperfine field at the ^{11}B nucleus [248].

the mean field originating from the neighboring sites.[13]

$$\mathcal{H}^{MF} = \sum_{i\in AA} h_i^{AA} + \sum_{i\in AB} h_i^{AB} + \sum_{i\in BA} h_i^{BA} + \sum_{i\in BB} h_i^{BB} \tag{2.9}$$

The constant interaction terms K_{ex}, K_{quad} and K_{oct} have been chosen such that the transition temperatures $T_{\mathrm{N}} = 2.3\,\mathrm{K}$ and $T_{\mathrm{Q}} = 3.2\,\mathrm{K}$ are reproduced [246]. From this simple model several properties of CeB_6 can already be understood qualitatively. The field induced octupolar moments T_{xyz} stabilize the AFQ phase, which explains the increase of the transition temperature T_{Q} in magnetic field . Experimentally octupolar moments were inferred from the field dependence of the resonant X-ray diffraction at $\boldsymbol{q}_{\mathrm{AFQ}} = R(\frac{1}{2}\ \frac{1}{2}\ \frac{1}{2})$ [247, 249] [see Fig. 2.12 (b)]. The octupolar moment can be expressed as:

$$T_{xyz} \propto J_x O_{yz} + J_y O_{zx} + J_z O_{xy} \tag{2.10}$$

Thus, for O_{xy}-type AFQ order, established for $\boldsymbol{B} \parallel [001]$, it can be approximated as $\langle T_{xyz}\rangle \propto \langle J_z\rangle\langle O_{xy}\rangle$, where the antiferro-ordering of the O_{xy} quadrupoles and T_{xyz} octupoles favors a ferromagnetic spin alignment [246]. This directly competes with the antiferromagnetic exchange K_{ex}, that may explain subtle features of the low-field phase diagram, e.g. the convex shape of the AFQ-Bragg intensity *vs.* B in Fig. 2.12 (b). Furthermore, ferromagnetic spin correlations have been observed above T_{Q} by magnetization measurements [250] and it has been argued that these might be induced via the short-range ordering of the quadrupoles and octupoles [250].[14]

Another experimental test of the model is the observation of the collective multipolar modes associated with the ordering of the quadrupoles. Thalmeier *et al.* considered the mean-field model with symmetric interaction term $D = K_{\mathrm{ex}} = K_{\mathrm{quad}} = K_{\mathrm{oct}}$ and calculated the dipolar scattering function in random-phase approximation (RPA) approach from the local multipolar susceptibility [251, 254] and in an Holstein-Primakoff (HP) approach [252]. The dispersion of the multipolar excitations is given in Fig. 2.13 (a) for zero field $B = 0$. A Goldstone mode can be found at the Γ point, belonging to a dispersion branch that extends across the whole Brillouin zone [251, 254]. In magnetic field all modes increase linearly with field in first approximation [254]. Previous inelastic neutron scattering experiments in the AFQ state by Bouvet *et al.* [253] and Regnault *et al.* [255] revealed dispersing excitations along lines of high symmetry in a magnetic field of $B = 6\,\mathrm{T}$ and $B = 4\,\mathrm{T}$, respectively ($\boldsymbol{B} \parallel [001]$). On the one hand, the theory captures the "leading" mode in the spectrum as shown in Fig. 2.13 (b) [252]. On the other hand, the *zero field* spectra exhibit a featureless, quasielastic response [253],

[13] e.g. for $i \in AA$ $\langle O_y\rangle^{BA}, \langle T_{xyz}\rangle^{BA}, \langle J_x\rangle^{AB}, \langle J_x\rangle^{BA} + \langle J_x\rangle^{BB}$, and so on [246].

[14] The model also captures the anisotropy of the B_{c}-line as well as the T_{Q}-line in the phase diagram and reproduces the high-field magnetization of the ferromagnetic and antiferromagnetic spin component [246].

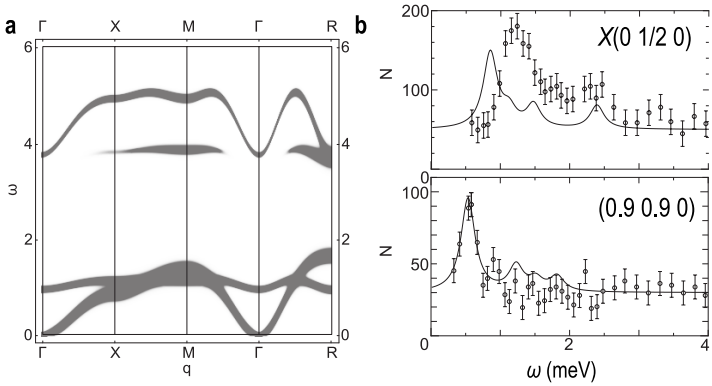

Fig. 2.13: (a) Dispersion plot along $\Gamma XMR\Gamma$ of the multipolar excitations calculated for the mean-field Hamiltonian within a RPA approach in the AFQ phase at zero field [251]. The thickness of the lines corresponds to the dipolar scattering function $S(\boldsymbol{q}, \omega)$. The y-axis is given in units of $k_B T_0 = 0.41\,\text{meV}$. T_0 is the energy scale of the multipolar interaction K_{quad}, $T_0 = 2zD$, $z = 6$ (reproduced from Ref. 252). **(b)** Comparison of the calculated and the measured spectra (see Ref. 253) at $\boldsymbol{B} = 6\,\text{T}$ and $\boldsymbol{B} \parallel [001]$ for the $X(0\ \frac{1}{2}\ 0)$ point (upper panel) and the $(0.9\ 0.9\ 0)$ point (lower panel). Both panels are reproduced from Ref. 252.

clearly disagreeing with the calculations in Fig. 2.13 (a).[15]

Further shortcomings of the model are revealed when describing static quantities like the low-field magnetization. Calculations in Fig. 2.12 (c) suggest a zero crossing of the field induced antiferromagnetic moment in the temperature and field dependence, which has not been observed [230, 231]. Second, the metamagnetic-like double step in the low-temperature magnetization, most pronounced for $\boldsymbol{B} \parallel [1\,1\,0]$ [see Fig. 2.11 (b)] is not explained by the model. Moreover, the model neglects the formation of heavy-fermion quasiparticles in the ground state of CeB_6, which are observed by transport. It will be shown in this thesis that the itinerant electrons contribute significantly to the spin dynamics in CeB_6. This finding was not expected by any of the model calculations published in the literature.

2.4.4 Electronic properties of CeB_6

The transport properties of CeB_6 are summarized in Fig. 2.14. Panel (a) shows that the resistivity *vs.* temperature for $T > 10\,\text{K}$ evolves continuously from the one observed for $Ce_{1-x}La_xB_6$ ($x = 0.97$). At intermediate temperatures all concentrations exhibit the logarithmic scaling $\rho(T) \sim \ln(T/T_K)$ expected for the single-ion Kondo effect [256].

[15] In Ref. 253 the zero-field spectrum at some points suggests the existence of damped modes. But the reinvestigation with higher energy resolution, which will be presented in this thesis, revealed that the spin-response is purely quasielastic for the whole Brillouin zone. Further discussion is passed to Section 6.2.

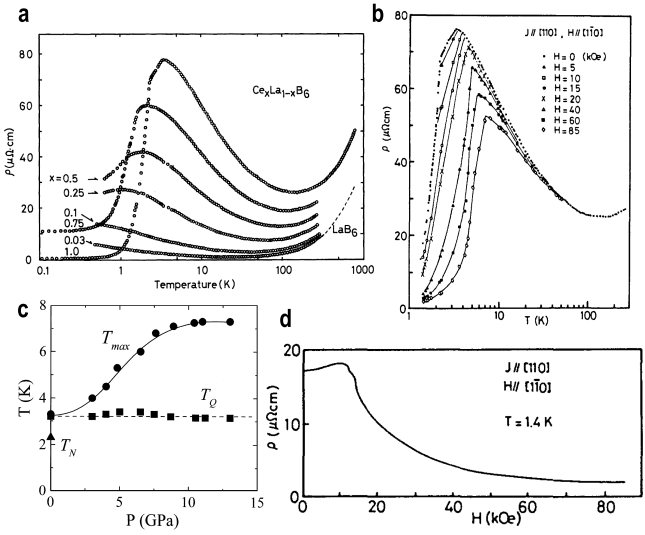

Fig. 2.14: **(a)** Temperature dependence of the electrical resistivity for $Ce_xLa_{1-x}B_6$, spanning concentrations from the highly diluted ($x = 0.03$) to the dense ($x = 1$) regime (reproduced from Ref. 256). **(b)** Resistivity *vs.* T in different magnetic fields (reproduced from Ref. 257). **(c)** Pressure dependence of the temperature $T_{\max}$, where the resistivity takes a maximum, and of the AFQ transition temperature T_Q (reproduced from Ref. 258). **(d)** Magnetoresistance in the AFM phase ($T = 1.4$ K) (reproduced from Ref. 257).

The Kondo temperature for the dilute samples was determined as $T_K \sim 1$ K [256]. For higher concentrations the resistivity drops at low temperatures, signalling the onset of a coherent Kondo state [256]. For CeB_6 the decrease of resistivity is coupled to T_Q. This is nicely demonstrated by measurements in nonzero fields in Fig. 2.14 (b), where the temperature of the maximum in resistivity $T_{\max}$ increases, since T_Q increases. At lowest temperatures the resistivity exhibits a Fermi-liquid-like T dependence $\rho(T) \sim T^2$ [256]. Also measurements of the magnetoresistance $\rho(B)$ in Ref. 237 show that upon crossing into the AFQ phase the resistivity shows a rapid decrease above $B = B_Q$ [237, 257]. A negative magnetoresistance is typical for the incoherent Kondo-effect, since it suppresses the scattering of the conduction electrons from the f-electrons. However, the rapid decrease in resistivity upon entering the AFQ phase for $B > B_Q$ and $T < T_Q$ signals the removal of scattering upon the ordering of the quadrupoles. In the AFM phase the magnetoresistance is weakly positive [see Fig.2.14 (d)] and then shows kinks at the transition fields $B_c = 1.05$ T and $B_Q = 1.7$ T to phase III′ and phase II, respectively. The magnetoresistance in heavy-fermion systems is usually positive in the ground state, but changes sign when the coherence is destroyed. The system changes then to the inco-

herent Kondo regime.[16]

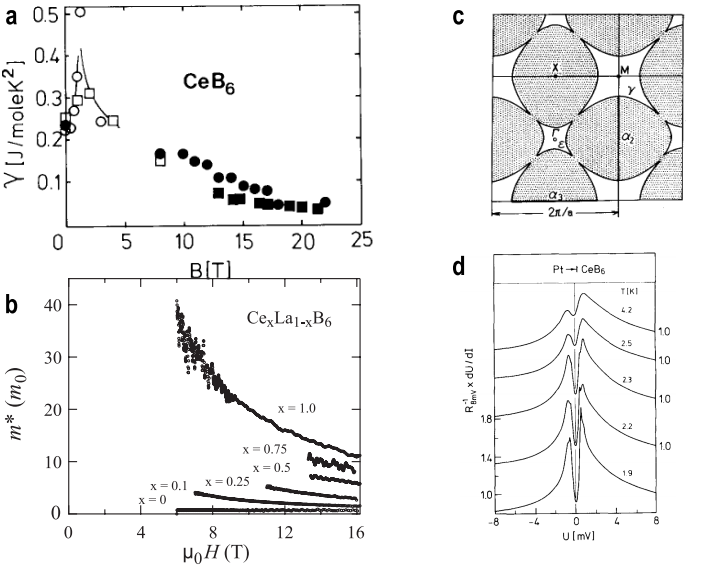

Fig. 2.15: (a) Magnetic-field dependence of the linear specific-heat coefficient γ (reproduced from Ref. 260). **(b)** Magnetic-field dependence of the quasiparticle effective mass m^*, determined from dHvA measurements of the α_3 orbit. (reproduced from Ref. 261). **(c)** Outline of the Fermi surface along the (001) plane (reproduced from Ref. 262). **(d)** Dependence of the effective mass on the Ce concentration in $Ce_{1-x}La_xB_6$ (reproduced from Ref. 263). **(e)** dU/dI characteristic, determined by point-contact spectroscopy (reproduced from Ref. 264).

This poses the question, whether the electronic properties of CeB_6 are governed by heavy-fermion quasiparticles. The Sommerfeld coefficient ($\gamma_0 = 250\,\mathrm{mJ/mole\,K^2}$), determined from the zero-temperature extrapolation of the specific heat $c_p(T)$, is strongly enhanced compared to the non-magnetic LaB_6 ($\gamma_0 = 2.6\,\mathrm{mJ/mole\,K^2}$) [260], which signals correlated quasiparticles. Since the decrease in resistivity is connected to T_Q, it is difficult to define a coherence temperature T^*. However, experiments under pressure up to $p = 13\,\mathrm{GPa}$ showed that the maximum temperature T_{max} of the resistivity increases and exceeds T_Q [Fig. 2.14 (c)] [258]. First, this is expected, since pressure increases hybridization between f-electrons and conduction electrons and, therefore, promotes the development of coherence between the f-states. Second, it shows that the coherent HF ground state is not necessarily connected to the AFQ phase, whose

[16] This is observed, for example, in $CeCu_6$ which has a comparable Kondo-temperature of $T_K = 2\,\mathrm{K}$ [259].

transition temperature T_Q is nearly pressure independent [258].[17]

The Fermi surface of the $Ce_{1-x}La_xB_6$ in dependence of the Ce concentrations has been determined by the observation of quantum oscillations [261–263, 267–272]. These studies employed high magnetic fields for which CeB_6 is in the AFQ state. Here, the Fermi surface was found to be quite similar to the one of the other hexaborides, such as LaB_6 and PrB_6 [262, 268], where it consists of ellipsoidal electron pockets centered at the $X(0\,0\,\frac{1}{2})$ points, as shown in Fig. 2.15 (c).[18] The corresponding quasiparticle mass was found to decrease with increasing magnetic field [Fig. 2.15 (b)] [269]. On the low-field side the effective mass diverges towards B_Q, reaching $m^* = 30m_0$ [261]. That this mass enhancement is related to the DOS of the f-electrons was revealed by a systematic study of $Ce_xLa_{1-x}B_6$ alloys, which revealed a continuous increase of m^* when increasing the cerium concentration x in Fig. 2.15 (d) [263]. Furthermore, the carrier density n was found to increase with x, suggesting a (partial) contribution of the f-electrons to the Fermi surface [261]. The field dependence of the linear specific-heat coefficient γ_0, which is proportional to m^* for a Fermi liquid, seems to exhibit a similar field dependence in Fig. 2.15 (a), taking a maximum at B_Q [260].[19]

The dHvA experiments could not access the phase III or phase III′ because of the low critical field of $B_c = 1.1\,T$ or $B_Q = 1.7\,T$, respectively. However, the related compounds PrB_6 and NdB_6 have higher Néel temperatures of $T_N = 7\,K$ and $T_N = 8.3\,K$ and correspondingly higher critical fields ($B_c = 30\,T$ for NdB_6) [273, 274]. Across B_c the Fermi surface changes drastically, resembling the Fermi surface of LaB_6 in the paramagnetic state [274, 275]. The effective masses in the paramagnetic state are comparable to CeB_6 [274, 275]. However, for both compounds no divergence of the quasiparticle mass towards the critical field B_c was found. The low mass across the whole measured field range was rather related to the weaker hybridization between conduction and f-electrons with the f-electrons being essentially localized [274, 275]. However, magnetic order apparently reconstructs the Fermi surface for CeB_6. Point contact spectroscopy measurements [264] [see Fig. 2.15 (e)] and scanning-tunneling spectroscopy measurements [276] found a charge gap of $2\Delta_{AFM} \approx 1.2\,meV$ opening below T_N. Unfortunately, little is known about the shape of the reconstructed Fermi surface. For PrB_6 and NdB_6 the main sheet of the Fermi surface is spherical [275], but whether the same applies to CeB_6 is speculative.

In conclusion, CeB_6 shows Fermi-liquid like behavior in the transport at low temperatures in both AFM and AFQ phases. On the one hand, the large linear specific-heat coefficient in low fields and the large effective mass of the charge carriers, determined

[17] Other studies observed a decrease of the antiferromagnetic transition temperature T_N under pressure [265, 266]. This is characteristic for RKKY-mediated order, since the localized f-moment is reduced because of the larger Kondo screening.

[18] The ellipsoids slightly overlap forming necks.

[19] When comparing the quasiparticle density of states $N_{qp}(E_F)$ derived from the Fermi surface according to dHvA-measurements and density of states $N_{sh}(E_F)$, determined from specific heat there is a discrepancy by a factor 3 [270]. It was found that only one-spin ($m = -J$) contributes to the dHvA-signal [271], while the minority spin quasiparticles ($m = J$) are either incoherent or removed from the Fermi surface.

by dHvA measurements, suggest that heavy fermions are contributing to the transport. On the other hand, the localized f-spins magnetically order to a low-temperature antiferromagnetic phase, analogously to the observations for PrB_6 and NdB_6. This apparent dichotomy can be described in a phenomenological two-fluid model, where local-moment order in the presence of heavy quasiparticles may set in [277, 278]. In this thesis the interplay between both competing ground states is investigated, where magnetic field and substitution of Ce by non-magnetic La is used as external parameters to tune the system.

2.4.5 Alternative approach to phase II

On the one hand, the commonly accepted model of the interacting multipoles treats the f-electrons as purely localized quasiparticles. On the other hand, transport measurements signal a coherent HF fermion ground state at low temperatures. In the two-fluid description of the Kondo lattice (KL) [277, 278], both localized and HF quasiparticles contribute to the magnetic properties below the intersite coherence temperature T^*. One consequence is the deviation from the linear scaling between the spin part of the Knight shift and the susceptibility $K_{\mathrm{spin}} \propto \chi$, since the local response χ_{KL} and the response of the hybridized quasiparticles χ_{HF} contribute differently to the susceptibility χ and to K_{spin} below T^* [279]. This loss of scaling between K_{spin} and χ has also been observed for CeB_6 below $T^* \approx 10\,\mathrm{K}$ [see Fig. 2.11 (c)] [244], indicating that the contribution of the heavy fermions cannot be neglected. This temperature also roughly coincides with the onset of Bragg scattering at $R(\frac{1}{2}\,\frac{1}{2}\,\frac{1}{2})$, shown in Fig. 2.16 (a). It will be shown later that this intensity mainly originates from fluctuating spins. Simultaneously, the longitudinal muon-spin relaxation rate $\lambda(T)$ increases below $T \approx 30\,\mathrm{K}$ in zero-field and $B = 0.6\,\mathrm{T}$ [see Fig. 2.16 (d)] [280, 281]. The $\boldsymbol{Q}$-averaged quasielastic linewidth Γ, measured on polycrystals, decreases with $\sqrt{T}$ for the whole temperature range [see Fig. 2.16 (b)] [282]. Below roughly the same temperature a Raman scattering study found that the Γ_8 ground state splits into two doublets, separated by $E_{8,1} - E_{8,2} \approx 30\,\mathrm{K}$ [224]. Such a splitting in the paramagnetic state for $T > T_{\mathrm{Q}}$ could not be observed by inelastic neutron scattering measurements [225, 253], which can be due to a vanishing matrix element for the particular transition. If the splitting is related to the short-range order of the quadrupoles, then one would expect an additional splitting into two transitions upon application of a magnetic field. This follows from the different g-factors for two Ce^{3+}-sites, given in Equation (2.6). Electron spin resonance (ESR) measurements observe only one resonance in a field of $B_{\mathrm{res}} = 2.8\,\mathrm{T}$, which appears below $T_{\mathrm{Q}}(B_{\mathrm{res}}) = 4.7\,\mathrm{K}$ [284, 285].[20] The existence of only *one* resonance was attributed to the hybridization of conduction and f-electrons, which essentially averages both g-factors to *one* uniform g-factor [238] that was experimentally determined to $g = 1.6$ [284, 285]. Not only the presence of ferromagnetic correlations were shown

[20] Its confinement to the AFQ phase was related to the enhancement of the susceptibility below T_{Q} [see Fig. 2.16 (e)], which reduces the relaxation rate and thus makes it observable [238].

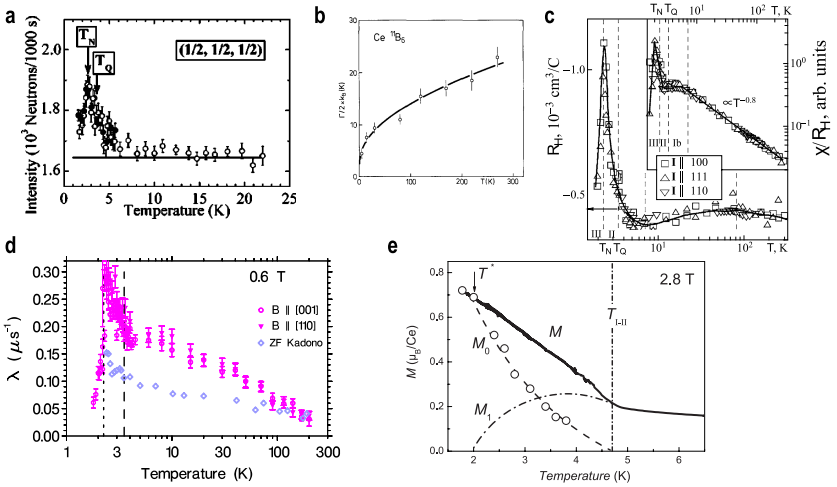

Fig. 2.16: **(a)** Neutron spin-flip scattering intensity *vs.* temperature at the $R(\frac{1}{2}\,\frac{1}{2}\,\frac{1}{2})$ Bragg peak in zero field (reproduced from Ref. 283). The horizontal line denotes the background intensity. **(b)** Temperature dependence of the quasielastic linewidth Γ for polycrystalline CeB_6 (reproduced from Ref. 282). **(c)** Hall constant R_H *vs.* temperature. The inset shows the ratio of magnetic susceptibility χ and Hall constant (reproduced from Ref. 237). **(d)** Longitudinal muon-spin relaxation rate *vs.* temperature in zero field (reproduced from Ref. 280) and $B = 0.6\,\mathrm{T}$ (reproduced from Ref. 281). **(e)** Temperature dependence of the fluctuating moment M_0 and the total magnetization M, determined from the ESR measurements for $B_{res} = 2.8\,\mathrm{T}$ and $\boldsymbol{B} \parallel (1\,\bar{1}\,0)$ (reproduced from Ref. 284).

in the ESR-study, but also the magnitude of the oscillating moment M_0 was found to increase from below T_Q down to T^*, where it accounted completely for the total magnetization [see Fig. 2.16 (e)] [284]. For $T > T^*$ the magnetization is the sum of an oscillating moment M_0 and a non-oscillating moment M_1: $M(B,T) = M_0(B,T) + M_1(B,T)$. Assigning the resonance to hybridized quasiparticles is in line with the observation of a similar resonance in a wide class of HF compounds (e.g. $YbRh_2Si_2$, CeRuPO) featuring ferromagnetic correlations [286]. However, this interpretation is clearly at odds with the multipolar mean-field model.

An alternative explanation was developed in a detailed transport and magnetization study of CeB_6 [237]. The authors pointed out that in the temperature regime $T_Q < T < 7\,\mathrm{K}$ the susceptibility χ and the Hall coefficient are proportional and show an activated behavior [see Fig. 2.16 (c) and inset] [237]:

$$\chi(T) \propto R_H(T) \propto e^{\frac{E_{sp}}{k_B T}} \tag{2.11}$$

The corresponding energy of $E_{sp}/k_B \approx 3.3\,K$ was associated with the formation of local polarons ("ferrons") [237]. Below T_Q, a transition to a SDW state of the conduction electrons frees the local moments, which leads to the observed enhancement of the magnetic response [237]. In low fields the transition to the AFM state would then be competing with a SDW because of the antiferromagnetic coupling of the localized spins, which polarize the conduction electrons via the RKKY-interaction [$\chi_c(\boldsymbol{q}) \propto J(\boldsymbol{q})$]. Inelastic neutron scattering would be a useful probe, since it is able to resolve charge gaps associated with the SDW ordering at a wave-vector $\boldsymbol{q}_{SDW}$. One way to investigate the interplay between AFM and AFQ (SDW) order is the dilution of the Ce^{3+} ions with non-magnetic La^{3+}, which should weaken the long-range order of localized spins. The phase diagram of $Ce_{1-x}La_xB_6$ will be discusses briefly in the next sections.

2.4.6 Appearance of phase IV in $Ce_{1-x}La_xB_6$

Upon substitution of cerium with lanthanum in $Ce_{1-x}La_xB_6$ the spins get diluted and the transition temperatures T_Q and T_N get suppressed [290]. Although the lanthanum introduces chemical disorder, its scattering potential is negligible, as demonstrated by the observation of dHvA oscillations across the whole doping series [263]. For low doping ($x < 0.2$), the transition temperature to the AFQ phase (phase II) T_Q decreases faster than the transition temperature to the antiferromagnetic state (phase III) [290] [compare with Fig. 2.18 (a)]. When T_Q almost coincides with T_N at $x \approx 0.2$, the temperature dependence of the susceptibility $\chi(T)$ [see Fig. 2.17 (b)] is reversed: first it decreases at $T_{IV} = 1.7\,K$, marking an antiferromagnetic transition, and then rises again at $T = 1.5\,K$ [287, 291].[21] Contrary to expectations, the phase below T_{IV} is not the same AFM phase (phase III) as observed in CeB_6, but an anomalous phase IV. Neutron powder diffraction studies on a $x = 0.25$ sample [293, 294] report the absence of any magnetic Bragg peaks for phase IV. Surprisingly, they revealed phase III as the low-temperature ordered phase below $T_N = 1.1\,K$, exhibiting the same magnetic structure as in CeB_6 [293, 294]. Measurements of the magnetic phase diagram [291, 292], given in Fig. 2.17 (a), establish the picture that phase IV precedes phase III in zero field. The AFQ phase can only be stabilized in finite fields. Further doping suppresses strongly the AFM transition temperature T_N, resulting in the replacement of phase III by phase IV as the ground state at $x_c = 0.3$ (see also Fig. 2.18 (a)].

A characteristic of phase IV is an anomalously large softening of the C_{44} elastic constant [291, 292]. The associated order parameter has remained elusive. Resonant X-ray scattering experiments on a $x = 0.3$ sample ($T_{IV} = 1.5\,K$) observed dipolar and octupolar symmetry for the E1 and E2 transitions of the L_2 absorption edge of Ce [289]. Both intensities have an onset at T_{IV} in Fig. 2.17 (d), with some residual dipolar intensity persisting to even higher temperatures [289]. The $\boldsymbol{Q}$-width of the octupolar peak indicates a long-range ordered state (LRO), whereas the broader dipolar intensity can be

[21] Specific heat confirms the reversal, showing a strong and sharp peak at T_{IV} and a shallow bump at T_N [292].

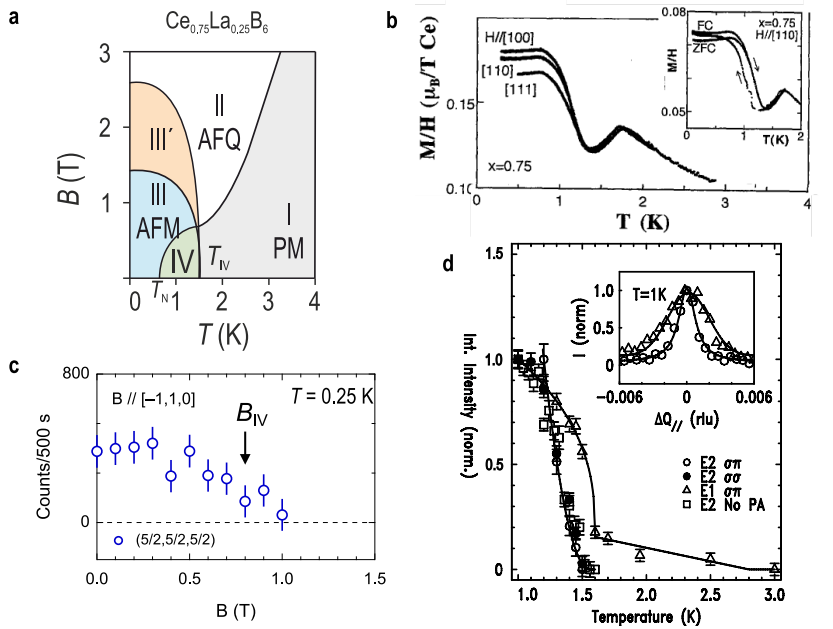

Fig. 2.17: **(a)** Sketch of a representative magnetic phase diagram of $Ce_{1-x}La_xB_6$ in the Fermi liquid regime ($x < 0.3$). It is adapted from Ref. 240. **(b)** Magnetic susceptibility M/H of a $x = 0.25$ sample, obtained for $B = 0.1$ T after field-cooling (reproduced from Ref. 287). **(c)** Magnetic-field dependence of the Bragg intensity at $R(\frac{1}{2}\,\frac{1}{2}\,\frac{1}{2})$ for $x = 0.3$, measured by ENS at $T = 0.25$ K (reproduced from Ref. 288). **(d)** Temperature dependence of RXS intensity at $R(\frac{3}{2}\,\frac{3}{2}\,\frac{3}{2})$ of the E1 (dipolar symmetry) and E2 (octupolar symmetry) transitions at the L_2 absorption edge, measured for $Ce_{0.7}La_{0.3}B_6$ (reproduced from Ref. 289).

associated with a short-range ordered state (SRO) [289]. The different temperature dependencies of both OP's Fig. 2.17 (d) suggest an order parameter segregation [289]. An elastic neutron study confirmed the presence of weak Bragg intensity appearing below T_{IV} at $R(\frac{1}{2}\,\frac{1}{2}\,\frac{1}{2})$ and at equivalent higher order wave vectors [288]. Its field dependence for $\boldsymbol{B} \parallel (1\,\bar{1}\,0)$ shows a suppression towards $B_{III} = 0.8$ T [see Fig. 2.17 (c)], which marks the entrance into phase III. Thus, the $(\frac{1}{2}\,\frac{1}{2}\,\frac{1}{2})$-Bragg intensity must be associated with phase IV [288]. Another important result of the study was the observation of an increase of the Bragg intensity *vs.* the modulus of the wave-vector $|\boldsymbol{Q}|$ [288], suggesting a non-dipolar magnetic form factor. This is interpreted as evidence for octupolar order as the "hidden" order parameter for phase IV [49, 217]. However, μSR studies, though not sensitive to octupolar order [281], provide a different picture of the spin structure of phase IV. The exponential relaxation rate λ, mirroring the fluctuations, diverges at

T_{IV}, but shows no anomaly across T_N [295].[22] It was therefore suggested that phase IV is the SRO state of the AFM phase [295].

Furthermore, it was found that phase III can be stabilized against phase IV. Doping with neodymium in $Ce_{0.3}Nd_yLa_{0.7-y}B_6$ stabilizes phase III and smallest amounts of Nd-atoms are sufficient ($y = 0.03$) to completely replace phase IV by phase III [296]. A metamagnetic-like transition is observed in the magnetization at the transition field B_{III} between phase IV and III, which shows a small hysteresis [287]. Thus, the transition of phase IV to phase III is of first order and phase IV was interpreted as an itinerant ordered phase [287].

In higher fields, the system enters phase III′ and then phase II [see Fig. 2.17 (a)], as signaled by kinks in the $M(B)$-curve at the respective fields [287, 291].[23] Whereas B_c is slightly enhanced compared to CeB_6, B_Q is strongly enhanced. Thus, phase III′ seems to be stabilized against phase II by doping with lanthanum. This correlates with the stronger decrease of T_Q, compared to T_N upon La doping [290].

2.4.7 Non-Fermi-liquid regime of $Ce_{1-x}La_xB_6$

Extrapolating the evolution of T_N *vs.* x, as shown in Fig. 2.18 (a), a QCP is expected in zero field for the AFM phase close to $x_c = 0.3$. Therefore, one would expect the appearance of critical fluctuations near x_c, which might induce non-Fermi-liquid behavior (NFL) in the transport. A resistivity study over the whole concentration range in $Ce_{1-x}La_xB_6$ found Fermi liquid (FL) behavior ($\rho = \rho_0 + AT^2$) at low temperatures [299] up to a doping of $x = 0.35$, which lies beyond the critical concentration. However, the transport coefficient A, which scales with the effective mass as $A \sim m^{*2}$, diverges upon approaching x_c [see Fig.2.18 (c)] [299]. Above x_c, where the ground state of $Ce_{1-x}La_xB_6$ is constituted by phase IV, the A coefficient seems to take a finite value and does not change at least up to $x = 0.5$. The mass enhancement on the one hand and the Fermi-liquid behavior on the other hand [299] would be understandable in a 3D-SDW quantum critical scenario. Then only a fraction of the quasiparticles are scattered from critical fluctuations $M_{\boldsymbol{Q}}$, located at hot-spot wave vectors $\boldsymbol{Q}$ [300]. But the results above suggest that the mass enhancement is a property of phase IV rather than a property of the critical doping x_c. Further doping leads to a unusual magnetic phase diagram shown in Fig. 2.18 (c), where the AFM (phase III) becomes detached from the $B = 0$ line and can only be stabilized by magnetic field.

The transition temperature T_{IV}, which can be inferred from the peak in magnetization *vs.* temperature [287], decreases with La concentration.[24] For $x > 0.4$ non-Fermi-liquid behavior has been observed in resistivity $\rho(T) \sim T^n$ with an exponent n that decreases

[22] A Gaussian-relaxing component a_1 is present as well, revealing randomly oriented moments [295].

[23] For $x = 0.25$ they are determined to $B_c^{\langle 110\rangle} = 1.5\,\mathrm{T}$, and $B_Q^{\langle 110\rangle} = 2.5\,\mathrm{T}$.

[24] However, specific heat $c_p(T)$ does not show a phase transition for $x \geq 0.4$ (for $x = 0.35$ it does) [301]. Instead it exhibits a broad bump, which was related to the Kondo-singlet formation rather than a long-range ordered state [301].The critical doping level x_{c2} for the suppression of phase IV has been put close to $x = 0.4$ [301].

vs. x and reaches $n = 1.5$ at $x = 0.5$ [299, 302]. At the same time, the temperature dependence of the specific heat c_p takes the form

$$c_p = \alpha T^{\delta} \tag{2.12}$$

with $\delta = 1.6$ for $x = 0.4$. Though the law deviates from the FL behavior ($\delta = 1$), it is not understandable in any quantum critical scenario discussed in Section 3.1.2, where one would expect in any case an increasing specific heat upon lowering the temperature.[25]

In order to understand the origin of the NFL behavior one would first need to understand the nature of the ordering behind phase IV. In this thesis phase IV will be investigated by elastic and inelastic neutron scattering. One sample with a doping of $x = 0.28$ is dedicated for this purpose, as it exhibits phase IV in its ground state. Looking at the phase diagram in Fig. 2.18 (a) this doping level is close to the point where T_N vanishes in zero-field. However, in contrast to typical phase diagrams of heavy-fermion superconductors like $Ce(Rh_{1-x}Co_x)In_5$ or $CeCu_2Si_2$ under pressure, the QCP of the AFM phase does not coincide with a superconducting dome. Instead, phase IV is playing the role of the competing phase in $Ce_{1-x}La_xB_6$. Therefore, the disclosure of its order parameter is crucial not only for the understanding of the $Ce_{1-x}La_xB_6$ phase diagram, but also for clarifying the leading interaction that distinguishes CeB_6 from the heavy-fermion superconductors.

2.4.8 Status of the CeB_6 problem at the outset of the thesis

CeB_6 is considered to be a model compound for exhibiting antiferroquadrupolar order. Although the mean-field multipolar model [226, 230, 235, 246] provides a good ansatz for explaining the high-field magnetic phase diagram of CeB_6, it fails to describe the low-field magnetic properties of CeB_6 even qualitatively. In particular, the following problems remained open at the outset of the thesis.

- A weak magnetic Bragg scattering at $R(\frac{1}{2}\ \frac{1}{2}\ \frac{1}{2})$ appears below T_Q upon cooling. It is not expected from the quadrupole ordering, since it does not break time-reversal symmetry. The onset of the scattering is also accompanied by a splitting of the Γ_8-quartet [224], a slowing down of the spin fluctuations, observed by μSR [281] and INS [282], the appearance of ferromagnetic fluctuations [250] and a localization regime of the charge carriers [237]. There is no consistent microscopical understanding for all of these properties yet.

- Previous INS studies of the spin dynamics failed to detect clear excitations in the AFQ state in *zero field* [253]. This is contrary to the observation at finite fields [253, 255] and to the calculated spectra of the multipolar modes [251, 254].

[25] Not included in the phase diagram, displayed in Fig. 2.18 (a), is a superconducting phase with $T_c = 5.7$ K in LaB_6 [303]. However, it must be spurious since it has not been further discussed in literature. Simple metallic behavior is reported for the resistivity down to lowest temperatures in later studies [304].

- ESR reports only one transition in the AFQ state [284], although two are expected for AFQ order [238].
- The purely localized description on the one hand, and the existence of a heavy-fermion ground state on the other hand are contradicting.
- A divergence of the effective mass was reported upon approaching the boundary between the AFM phase and the AFQ phase at B_Q in magnetic field. Although this could be due to critical fluctuations, the transport shows only Fermi-liquid-like behavior.
- The AFM phase has not been investigated by inelastic neutron scattering in literature. Such a study would provide important parameters like the dipolar exchange constant J, which could be compared with the model.
- The order parameter of phase IV, observed in $Ce_{1-x}La_xB_6$ (for $x > 0.2$) remains elusive. Although octupolar ordering has been discussed [288, 289, 305], it remains an open issue because of a number of conflicting experimental reports [295, 306–308].

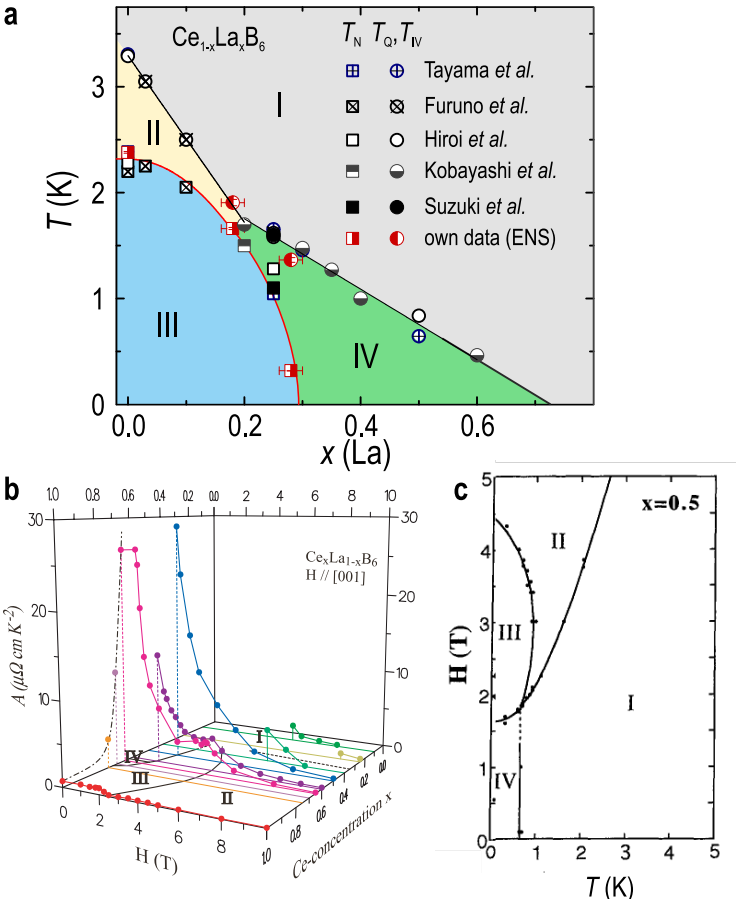

Fig. 2.18: (a) Electronic phase diagram *vs.* La concentrations in $Ce_{1-x}La_xB_6$. The data points were mainly taken from measurements of the magnetization and specific heat, published in Ref. 239, 287, 290–292, 297, 298. **(b)** Dependence of the transport coefficient A on magnetic field and Ce concentration in $Ce_{1-x}La_xB_6$ (reproduced from Ref. 299). Magnetic phase diagram for $Ce_{0.5}La_{0.5}B_6$, as determined from susceptibility measurements $\chi(T)$ (reproduced from Ref. 287).

3 Magnetism and spin dynamics in metals: theoretical considerations

3.1 The physics of heavy-fermion systems

Starting point for describing the electronic properties of a lattice comprising f-electrons is the periodic Anderson model. It contains terms, which accommodate the dispersive band (band width W) of the conduction electrons $\epsilon_{\boldsymbol{k}}$ and the flat band $\epsilon^f_{\boldsymbol{k}}$ of the f-electrons, which are essentially localized on the atoms. The hybridization term accounts for the coupling of both bands via the matrix element $v_{\boldsymbol{k}}$. In addition, two or more electrons localized on the f-site are interacting via Coulomb repulsion described by the energy term U_f.

$$\hat{H} = \sum_{\boldsymbol{k},\sigma} \epsilon_{\boldsymbol{k}} c^\dagger_{\boldsymbol{k}\sigma} c_{\boldsymbol{k}\sigma} + \sum_{\boldsymbol{k},\sigma} \epsilon^f_{\boldsymbol{k}} f^\dagger_{\boldsymbol{k}\sigma} f_{\boldsymbol{k}\sigma} - \sum_{\boldsymbol{k},\sigma} v_{\boldsymbol{k}} (c^\dagger_{\boldsymbol{k}\sigma} f_{\boldsymbol{k}\sigma} + f^\dagger_{\boldsymbol{k}\sigma} c_{\boldsymbol{k}\sigma}) + U_f \sum_j \hat{n}^f_{j\uparrow} \hat{n}^f_{j\downarrow} \tag{3.1}$$

The non-interacting part of this Hamiltonian can be diagonalized, yielding hybridized bands:

$$\lambda_{\boldsymbol{k}} = \frac{1}{2}(\epsilon_{\boldsymbol{k}} + \epsilon_f \pm \sqrt{(\epsilon_{\boldsymbol{k}} - \epsilon_f)^2 + 4v^2_{\boldsymbol{k}}}) \tag{3.2}$$

A first feature arising from this approximative derivation is the hybridization gap [50]

$$\Delta(U_f = 0) \approx v^2 (\frac{1}{W - \epsilon_f} + \frac{1}{\epsilon_f}) \tag{3.3}$$

This gap corresponds to the indirect gap in the band structure of Fig. 3.1 (a) and can be experimentally observed by tunneling spectroscopy. Figure 3.1 (b) shows the spectrum for $CeCoIn_5$, which exhibits two peaks corresponding to the lower and the upper hybrid band edge [309]. The theoretical value for Δ needs to be modified when taking into account the Coulomb interaction term. Electrons in the same f-state feel Coulomb repulsion. Therefore, conduction electrons can only hop into empty f-states, for which the probability is proportional to $r^2 = 1 - n_f$. The matrix element for hybridization $v_{\boldsymbol{k}}$ becomes renormalized:

$$\tilde{v}_{\boldsymbol{k}} = \sqrt{1 - n_f} v_{\boldsymbol{k}} \tag{3.4}$$

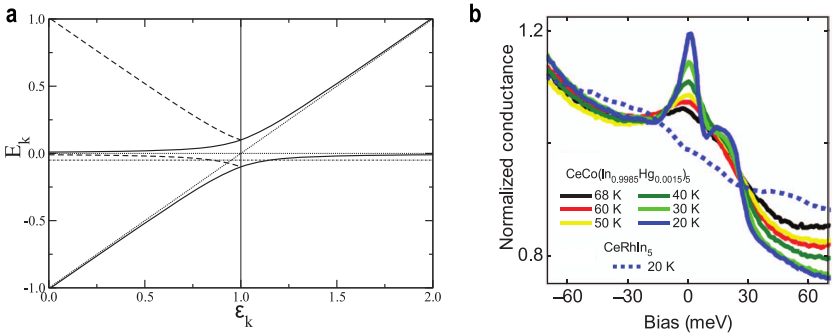

Fig. 3.1: (a) The hybridized bands in the Anderson model [formula 3.1] are shown as solid lines. The dashed lines are the folded bands. The bare f-derived and the conduction bands are shown by dotted lines. The Fermi level, indicated by dash-dotted line, is lying below the edge of the lower hybridized band (reproduced from Ref. 238). **(b)** Tunneling spectra of $CeCoIn_5$ for different temperatures, showing the opening of the indirect hybridization gap (reproduced from Ref. 309).

When performing a mean-field treatment of the Hamiltonian (3.1) one can obtain the renormalized f-level energy and the occupation number n_f [310]:[1]

$$\tilde{\epsilon}_f = \mu\left(1 + e^{-\frac{\Lambda}{\nu_f D(E_\mathrm{F}) V^2}}\right) = \mu + k_\mathrm{B} T^* \tag{3.5}$$

$$n_f = 1 - \frac{k_\mathrm{B} T^*}{\nu_f D(E_\mathrm{F}) V^2} \tag{3.6}$$

Here, ν_f denotes the orbital degeneracy of the f-orbital and $D(E_\mathrm{F})$ is the density of states at the Fermi energy. The temperature T^* can be thought of as a coherence temperature below which the conduction and the f-electrons hybridize. It also gives the energy gain for hybridization. Above this temperature the f-electrons are decoupled from the Fermi sea and localized. Depending on the parameters, it may happen that the deviation of the occupation number from unity $1 - n_f$ is exponentially small according to Eq. (3.6). This case is called nearly integral valent. From Eq. (3.5) follows that the energy of the f-orbital ϵ_f gets renormalized to the value $\tilde{\epsilon}_f$, which lies slightly above the chemical potential μ. Thus, the chemical potential cuts the lower hybridized band in a region, where it is almost flat *vs.* $\boldsymbol{k}$, which brings about a large DOS at the Fermi level. Another consequence is the large enhancement of the effective mass [50], which led to the term "heavy fermion" to classify these compounds.

$$\frac{m^*}{m} \propto \frac{n_f}{1 - n_f} \tag{3.7}$$

[1] with consideration of the condition (3.4) by the Lagrangian parameter Λ. Furthermore, $v_{\boldsymbol{k}} = V$.

The hybridization gap Δ is exponentially small, being in the range of 5–10 K [50]. The renormalized density of states $\tilde{\rho}(\mu) = \frac{m^*}{m}\rho(\mu)$ can be accessed via the measurement of the linear coefficient γ of the specific heat *vs.* temperature. Early classification termed compounds with $\gamma > 400\,\mathrm{mJ/mol\,K^2}$ as heavy fermions, which were mainly restricted to Ce, Yb, U and Np based systems [211].

In the case of weak correlations or intermediate valence, the hybridization gap takes a larger value and the chemical potential might be situated in the indirect gap. In that case, the transport shows semiconducting behavior according to the activation law. Well studied representatives are SmB_6 and YbB_{12}, which show a gap of 14 meV and 25 meV, respectively [311].

3.1.1 Kondo lattice systems

The Kondo lattice model describes a system of localized f-electrons immersed into a sea of conduction electrons. Here, the f-electrons are localized at each lattice site and the interaction with the conduction electrons can be expressed via their respective spins similar to the Heisenberg spin exchange model for strongly correlated d-electrons.

$$\hat{H} = \sum_{\boldsymbol{k},\sigma} \epsilon_{\boldsymbol{k}} c^\dagger_{\boldsymbol{k}\sigma} c_{\boldsymbol{k}\sigma} + \frac{J}{2} \sum_{\boldsymbol{j}} \sum_{\sigma\sigma'} \boldsymbol{S_j} (c^\dagger_{\boldsymbol{j}\sigma} \vec{\sigma}_{\sigma\sigma'} c_{\boldsymbol{j}\sigma'}) \tag{3.8a}$$

$$J = v^2 \sum_{\boldsymbol{k}} \left[\frac{\Theta(\epsilon_{\boldsymbol{k}} - \mu)}{\epsilon_{\boldsymbol{k}} - \epsilon_f} + \frac{\Theta(\mu - \epsilon_{\boldsymbol{k}})}{\epsilon_f + U_f - \epsilon_{\boldsymbol{k}}} \right] \tag{3.8b}$$

This Hamiltonian can be derived from the periodic Anderson Hamiltonian by means of the Schrieffer-Wolff-Transformation [50]. The exchange coupling J is antiferromagnetic. Equation (3.8) essentially describes localized f-electron spins, which are locally coupled to the conduction electron spins by the Kondo term. Many Kondo-lattice systems behave like dilute systems, where the f-atom (e.g. Ce) is substituted by non-magnetic ions (e.g. La for the $4f$ systems), and is thus treated as a single impurity. In this case the Hamiltonian would be:

$$\hat{H}_{\mathrm{imp}} = \sum_{\boldsymbol{k},\boldsymbol{q}} J_{\boldsymbol{k},\boldsymbol{q}} \left(S^+ c^\dagger_{\boldsymbol{k},\downarrow} c_{\boldsymbol{q},\uparrow} + S^- c^\dagger_{\boldsymbol{k},\uparrow} c_{\boldsymbol{q},\downarrow} + S_z (c^\dagger_{\boldsymbol{k},\uparrow} c_{\boldsymbol{q},\uparrow} - c^\dagger_{\boldsymbol{k},\downarrow} c_{\boldsymbol{q},\downarrow}) \right) \tag{3.9}$$

Because of the antiferromagnetic coupling between the conduction electrons and the f-electrons, both will form a singlet at low temperatures. An ansatz for obtaining the energy gain for such a coupling can be made with a variational trial state, involving all possible $c - f$ singlets:

$$|\Phi_0\rangle = \sum_{\boldsymbol{k}} a(\boldsymbol{k})(f_\uparrow^\dagger c_{\boldsymbol{k},\uparrow} + f_\downarrow^\dagger c_{\boldsymbol{k},\downarrow})|\Phi_{\mathrm{FS}}\rangle \tag{3.10}$$

Here $|\Phi_{\mathrm{FS}}\rangle$ is the Fermi surface, formed by the conduction electrons. Solving the Schrödinger equation with regard to an infinite number of particle-hole excitations, Eq. (3.9) gives an energy for the singlet of:

$$E_s = -We^{1/2J\rho_0} \tag{3.11}$$

$\rho_0 = \rho(\varepsilon)$ is the DOS under assumption that it is constant over the whole band width. The associated temperature T_{K}

$$k_{\mathrm{B}}T_{\mathrm{K}} \sim We^{-1/2J\rho_0} \tag{3.12}$$

is the Kondo temperature.

When calculating the susceptibility of the impurity applying perturbation theory to the Hamiltonian (3.9), one obtains [50]:

$$\chi_{\mathrm{imp}}(T) = \frac{(g\mu_{\mathrm{B}})^2}{4k_{\mathrm{B}}T}\left(1 - \frac{1}{\ln T/T_{\mathrm{K}}}\right) \tag{3.13}$$

The Kondo impurity causes a deviation in the magnetic susceptibility from the high-temperature Curie-like behavior. However, this approximation is not true for $T \approx T_{\mathrm{K}}$, since the term diverges logarithmically in this region. With increasing concentration x of f-electrons (e.g. in $\mathrm{Ce}_x\mathrm{La}_{1-x}$-type alloys) the interactions between f-spins take place and the system can order magnetically or form a coherent heavy-fermion ground state.

RKKY interaction

The antiferromagnetic coupling between f-electrons and conduction electrons creates a polarization cloud, which, for dense Kondo systems, extends over several other f-sites and thus leads to an indirect exchange[2] between them.

$$\mathcal{H}_{\mathrm{RKKY}} = \sum_{\boldsymbol{k},\sigma} \epsilon_{\boldsymbol{k}} c_{\boldsymbol{k}\sigma}^\dagger c_{\boldsymbol{k}\sigma} + \frac{1}{2}\sum_{i\neq j} \mathcal{I}(\boldsymbol{R}_i - \boldsymbol{R}_j)\boldsymbol{S}_i\boldsymbol{S}_j \tag{3.14}$$

[2] also called Rudermann-Kittel-Kasuya-Yosida-Interaction (RKKY)

The interaction constant depends on the free electron susceptibility $\chi_0(\boldsymbol{p})$ [50]:

$$\mathcal{I}(\boldsymbol{R}_i - \boldsymbol{R}_j) = -\frac{J^2}{L}\sum_{\boldsymbol{p}}\chi_0(\boldsymbol{p})\cos\boldsymbol{p}(\boldsymbol{R}_i - \boldsymbol{R}_j) \tag{3.15}$$

The right-hand side of Eq. (3.15) can be explicitly evaluated for a free electron gas:

$$\mathcal{I}(\boldsymbol{R}_i - \boldsymbol{R}_j) = -J^2 k_{\mathrm{F}}^3 \frac{3n}{8\pi\epsilon_{\mathrm{F}}} F(2k_{\mathrm{F}}R_{ij}) \tag{3.16}$$

$$\text{with} \quad F(x) = \frac{\sin x - x\cos x}{x^4} \tag{3.17}$$

Here, k_{F} is the Fermi momentum. The interaction decays with R_{ij}^4, where R_{ij} is the distance of the rare-earth ion sites $R_{ij} = |\boldsymbol{R}_i - \boldsymbol{R}_j|$. The interaction energy in Eq. (3.14) scales with second order in J. The ordering temperature T_{RKKY} should scale as

$$T_{\mathrm{RKKY}} \sim \frac{J^2}{W k_{\mathrm{B}}} \tag{3.18}$$

3.1.2 Itinerant *vs.* localized behavior

So far, three different temperature scales, crucial for f-electron systems, have been discussed: T_{coh} as the crossover temperature into a coherent HF state,[3] T_{K} as the Kondo temperature describing the transport and the susceptibility in the incoherent single-ion Kondo regime and T_{RKKY}, as the temperature scale, where the f-spins start interacting. The Kondo effect by virtue of the coupling between f-electrons and conduction electrons, competes with magnetic ordering, since it effectively screens the f-spins. Depending on which energy scale is larger one would expect the ground state of the dense Kondo-system to be either non-magnetic or magnetically ordered. Since both T_{K} [see Eq. (3.12)] and T_{RKKY} [see Eq. (3.18)] depend essentially on the product $J/D \sim J\rho_0$, both energy scales can be simultaneously varied in dependence of this product [312]. As a result one obtains the Doniach phase diagram in Fig. 3.2 (a), which describes the transition from a local moment magnetic state to a heavy Fermi liquid. Consequently, near the point, where $T_{\mathrm{K}} > T_{\mathrm{RKKY}}$, the tendency towards magnetic ordering is suppressed and T_{N} should approach continuously zero. The investigation of the electronic properties close to such a quantum critical point (QCP) is a hot topic in contemporary research on heavy-fermion systems.

[3] exhibiting Fermi-liquid-like behavior

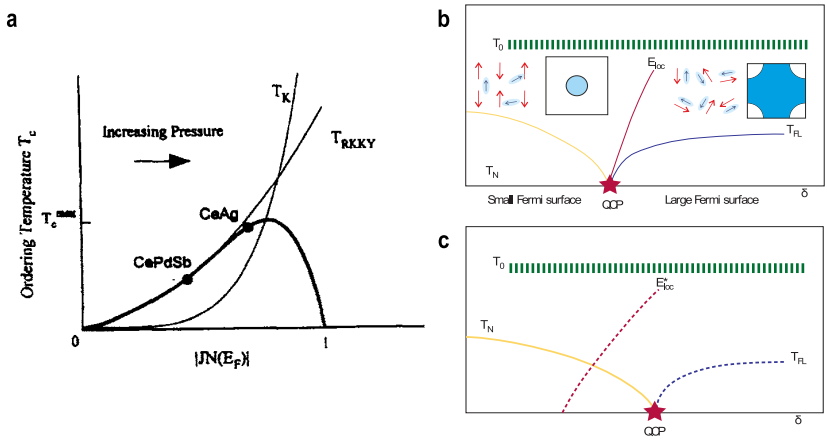

Fig. 3.2: **(a)** The Doniach phase diagram, which describes the evolution of a transition into a localized, RKKY-mediated antiferromagnetic state at T_{RKKY} and into a Kondo-singlet state at T_{K}, both in dependence on the parameter $JN(E_{\mathrm{F}}) \triangleq J\rho_0$. The figure is reproduced from Ref. 50. **(b)** Energetic phase diagram of a magnetically ordered f-electron system, tunable towards a QCP via an external parameter δ. T_0 marks the temperature, where the Kondo-interaction operates. E_{loc} is the energy scale, separating a state where the f-electrons via Kondo coupling delocalize and a state, where the f-electrons localize and magnetically interact via the conduction electrons. The drawings sketch the antiferromagnetic ordering of the localized f-spins and the small conduction electron Fermi surface on the left side of E_{loc} as well as the $f-c$ coupling and the large FS on the right side of E_{loc}. Here, $T_{\mathrm{N}} = 0$ and $E_{\mathrm{loc}} = 0$ coincide at the same critical value δ_{c}. T_{FL} is the temperature below which Fermi liquid-like behavior is observed. **(c)** QCP in a spin-density-wave scenario, where the E_{loc} line intersects the AFM dome. Both panels (b) and (c) are reproduced from Ref. 222.

Itinerant Quantum critical point

Different to the strong coupling picture, the Fermi surface in the paramagnetic state can also be unstable against magnetism along "hot" lines, sheets of the Fermi surface that can be brought to overlay by a shift with vector $\boldsymbol{Q}$. In that case, tuning the system by an external parameter δ, can lead to the formation of a spin-density wave (SDW) at the critical point δ_{c}.

$$\boldsymbol{M}(\boldsymbol{r}) = \boldsymbol{M}_{\boldsymbol{Q}} \exp(-i\boldsymbol{Q}\boldsymbol{r}) \tag{3.19}$$

The electronic spin density of the quasiparticles $\boldsymbol{\sigma}$ couples to the fluctuations of the spin-density wave [313]:

$$\boldsymbol{\sigma}_{-\boldsymbol{q}} = \sum_{\boldsymbol{k}} c^{\dagger}_{\boldsymbol{k}-\boldsymbol{q}} \boldsymbol{\sigma} c_{\boldsymbol{k}} \tag{3.20}$$

$$L_F = g \sum_{\boldsymbol{k},\boldsymbol{Q}} \boldsymbol{\sigma}_{-\boldsymbol{Q}} \boldsymbol{M}_{\boldsymbol{Q}} \tag{3.21}$$

Thus, only quasiparticles scattered by a wave vector $\boldsymbol{Q}$ interact with the fluctuations. In contrast, quasiparticles from "cold" regions of the Fermi surface are unaffected. The effective mass, averaged over the whole Fermi surface, therefore, remains finite. The Sommerfeld coefficient and the resistivity *vs.* T reveal a certain temperature scaling

$$\Delta\rho(T) \sim T^n, \quad n = 1.5 \tag{3.22}$$

$$\gamma(T) = \gamma_0 - \sqrt{T} \tag{3.23}$$

According to the Hertz-Millis theory for a critical spin-density wave in three dimensions the dynamical response function will exhibit a different E/T-scaling compared to the local criticality [313]:

$$F(E,T) = \frac{1}{E^\alpha} f(E/T^{3/2}) \tag{3.24}$$

This behavior has been reported for a number of HF systems. A notable example is $CeCu_2Si_2$, which magnetically orders at the incommensurate wave vector $\boldsymbol{Q}_{\mathrm{AF}} = (0.22\ 0.22\ 0.53)$. $\boldsymbol{Q}_{\mathrm{AF}}$ can be related to a nesting vector of the Fermi surface [314]. For the superconducting S-type $CeCu_2Si_2$, where the SDW is critical, it has been found that the dynamical susceptibility follows the scaling according to Eq. (3.24) (here: $\alpha = 3/2$) [315], while the spin susceptibility $\chi(\boldsymbol{Q}_{\mathrm{AF}})$ and the relaxation rate $\Gamma(\boldsymbol{Q}_{\mathrm{AF}})$ are proportional to $T^{3/2}$ [315].

3.2 Itinerant ferro- and antiferromagnetism

The simplest model to describe correlated d-electron systems is the Hubbard model.

$$\mathcal{H} = t \sum_{jl} \sum_{\sigma} c^\dagger_{j\sigma} c_{l\sigma} + U \sum_j \hat{n}_{j\uparrow} \hat{n}_{j\downarrow} \tag{3.25}$$

The first term ($= \mathcal{H}_0$) is the kinetic term describing the hopping of the electrons with spin σ between lattice sites $\boldsymbol{j}$ and $\boldsymbol{l}$. The second term is the interaction term with the parameter U, which accounts for the Coulomb repulsion of $\hat{n}_j$ electrons, being localized on the site $\boldsymbol{j}$. The kinetic term $\mathcal{H}_0$ alone would describe Bloch states $\phi(\boldsymbol{k})$ with momentum $\boldsymbol{k}$ and energy $\varepsilon(\boldsymbol{k})$. It can be expressed for a grand canonical ensemble with the total particle operator $\hat{N} = \sum_{j\sigma} \hat{n}_{j\sigma}$:

$$\mathcal{H}_0 = \sum_{\boldsymbol{k}\sigma} (\varepsilon(\boldsymbol{k}) - \mu) \hat{n}_{\boldsymbol{k}\sigma} \tag{3.26}$$

The interaction term in equation (3.25) favors a single occupation of the Wannier-state at site $\boldsymbol{j}$, which in the theoretical case of an infinitely narrow band would result in the

equal population of spin-up and spin-down states:

$$\langle n_{j\sigma}\rangle = \langle n_\sigma\rangle = \langle n_{-\sigma}\rangle = \frac{1}{2}n \tag{3.27}$$

For ferromagnetic order the occupation for both spin states is different leading to a local effective spin S_j^z or magnetization m:

$$S_j^z = m = \frac{1}{2}(\langle n_\uparrow\rangle - \langle n_\downarrow\rangle) \tag{3.28}$$

$$\langle \hat{n}_{j\uparrow}\rangle = \frac{1}{2}n + m, \quad \langle \hat{n}_{j\downarrow}\rangle = \frac{1}{2}n - m \tag{3.29}$$

In the mean-field approximation (MFA) the fluctuations of the quantities $n_\uparrow$ and $n_\downarrow$ are assumed to be small. The interaction term can thus be simplified:

$$\hat{n}_{j\uparrow}\hat{n}_{j\downarrow} \sim \hat{n}_{j\uparrow}\langle \hat{n}_{j\downarrow}\rangle + \hat{n}_{j\downarrow}\langle \hat{n}_{j\uparrow}\rangle + \langle \hat{n}_{j\uparrow}\rangle\langle \hat{n}_{j\downarrow}\rangle \tag{3.30}$$

The MFA-Hamitonian can now be written in an accessible form:

$$\mathcal{H}_{\mathrm{MFA}} = \sum_{\boldsymbol{k}}(E_\uparrow(\boldsymbol{k})\hat{n}_{\boldsymbol{k}\uparrow} + E_\downarrow(\boldsymbol{k})\hat{n}_{\boldsymbol{k}\downarrow}) - U(\frac{n^2}{4} - m^2) \tag{3.31a}$$

$$E_\uparrow(\boldsymbol{k}) = \varepsilon_{\boldsymbol{k}} + \frac{Un}{2} - Um \tag{3.31b}$$

$$E_\downarrow(\boldsymbol{k}) = \varepsilon_{\boldsymbol{k}} + \frac{Un}{2} + Um \tag{3.31c}$$

As result, the degenerate quasiparticle band $\varepsilon(\boldsymbol{k})$ splits now into spin-↑ and spin-↓ bands, which are separated by an exchange splitting $\Delta E_{\mathrm{ex}} = 2Um$.

In case of antiferromagnetic ordering the spin changes from site to site, which can be described by a modulation with wave vector $\boldsymbol{Q}$:

$$\langle \hat{n}_{j\downarrow}\rangle = \frac{n}{2} + \eta(\sigma)me^{i\boldsymbol{Q}j} \tag{3.32}$$
$$\text{with } \eta = \pm 1, \quad \text{for } \sigma = \uparrow, \downarrow$$

The ordering wave vector $\boldsymbol{Q}$ is determined by the divergence of the spin susceptibility. The spin operators are conveniently expressed in $\boldsymbol{q}$-space:

$$\boldsymbol{S}(\boldsymbol{q}) = \frac{1}{2}\sum_{\boldsymbol{p}}\sum_{\alpha\beta} c^\dagger_{\boldsymbol{p}+\boldsymbol{q},\alpha}\boldsymbol{\sigma}_{\alpha\beta}c_{\boldsymbol{p},\beta} \tag{3.33a}$$

$$S^+(\boldsymbol{q}) = \sum_{\boldsymbol{p}} c^\dagger_{\boldsymbol{p}+\boldsymbol{q},\uparrow}c_{\boldsymbol{p},\downarrow} \tag{3.33b}$$

$$S^-(\boldsymbol{q}) = \sum_{\boldsymbol{p}} c^\dagger_{\boldsymbol{p}+\boldsymbol{q},\downarrow}c_{\boldsymbol{p},\uparrow} \tag{3.33c}$$

Here, the $\sigma_{\alpha\beta}$ represents the vector of the Pauli matrices. If the spin is modulated with the wave vector $\boldsymbol{q}$, $\langle S_j \rangle = S\cos(\boldsymbol{qj})$, and an external field is applied in x-direction, the Hamiltonian becomes:

$$\mathcal{H}' = \left(\frac{g\mu_B H^x}{2} + US\right)[S^x(\boldsymbol{q}) + S^x(-\boldsymbol{q})] \tag{3.34}$$

This term, treated as a perturbation to the system of band electrons, describes a process, where a quasiparticle is scattered under a spin flip and a momentum transfer of $\boldsymbol{q}$ or $-\boldsymbol{q}$. One can calculate the expectation value of $S^x(\boldsymbol{q})$, which corresponds to the magnetization, and obtain the spin susceptibility:

$$\chi(\boldsymbol{q}) = \frac{\chi_0(\boldsymbol{q})}{1 - U\chi_0(\boldsymbol{q})} \tag{3.35}$$

Here, χ_0 is the static Lindhard susceptibility of the non-interacting quasiparticles. It can be calculated for finite temperatures with the Fermi function $f_{\boldsymbol{p}}$.

$$\chi_0(\boldsymbol{q}) = \sum_{\boldsymbol{p}} \frac{f_{\boldsymbol{p}} - f_{\boldsymbol{p}+\boldsymbol{q}}}{\varepsilon_{\boldsymbol{p}} - \varepsilon_{\boldsymbol{p}+\boldsymbol{q}}} \tag{3.36}$$

The Stoner criterion for magnetic order is thus

$$\chi_0(\boldsymbol{q}) U^{\boldsymbol{q}}_{\mathrm{cr}} = 1 \tag{3.37}$$

For $\boldsymbol{q} = 0$ the system is unstable against ferromagnetism. For $\boldsymbol{q} \neq 0$ a spin-density wave (SDW) can form [316]. This condition selects the critical wave vector such that $U^{\boldsymbol{q}}_{\mathrm{cr}}$ is minimal or $\chi_0(\boldsymbol{q})$ is maximal [50].

$$U_{\mathrm{cr}} = \left(\max_{\boldsymbol{q}} \chi^{(0)}(\boldsymbol{q})\right)^{-1} \tag{3.38}$$

$\chi_0(\boldsymbol{q})$ depends on the particular band structure. Magnetic instabilities occur on Fermi surfaces that fulfill the nesting condition ($\varepsilon_{\mathrm{F}} = 0$):

$$\epsilon_{\boldsymbol{k}+\boldsymbol{Q}} = -\epsilon_{\boldsymbol{k}} \quad \forall \boldsymbol{k} \in FS \tag{3.39}$$

In this case the Lindhard susceptibility diverges logarithmically for a finite density of states at the Fermi level ($\rho(\varepsilon_{\mathrm{F}}) \neq 0$) [50, 317]:

$$\chi_0(\boldsymbol{Q}) \sim \int_{\varepsilon_u}^{\mu} d\epsilon \frac{\rho(\epsilon)}{\epsilon} \tag{3.40}$$

Here, ε_u is the bottom edge of the conduction band.

3.2.1 Spin fluctuations in nearly ferro-and antiferromagnetic materials

A quantity that describes the fluctuation of the spin density $\boldsymbol{s}(\boldsymbol{r},t)$ is the space-time correlation function

$$S(\boldsymbol{r},\boldsymbol{r}',t-t') = \langle \boldsymbol{s}(\boldsymbol{r},t)\boldsymbol{s}(\boldsymbol{r}',t')\rangle \tag{3.41a}$$

$$\boldsymbol{s}(\boldsymbol{r}) = \sum_j \delta(\boldsymbol{r}-\boldsymbol{r}_j)\boldsymbol{S}_j \tag{3.41b}$$

Inelastic neutron scattering is a conventional technique to measure the Fourier transform $S(\boldsymbol{q},\omega)$ of the spin-flip part $\sim \langle s_-(\boldsymbol{q},t)s_+(-\boldsymbol{q},0)\rangle$ [see equation (3.33)] of the correlation function. It is related to the imaginary part of the transverse dynamical susceptibility $\chi''_{-+}(\boldsymbol{q},\omega)$ via the fluctuation-dissipation theorem [138]. The real-and imaginary part of the dynamical susceptibility χ_0 are first derived for the Hamiltonian that describes the non-interacting electrons [318]:

$$\chi'_{0-+}(\boldsymbol{q},\omega) = \sum_{\boldsymbol{k}} \frac{f_{\boldsymbol{k},\downarrow}(1-f_{\boldsymbol{k}+\boldsymbol{q},\uparrow})}{\varepsilon_{\boldsymbol{k}+\boldsymbol{q},\uparrow}-\varepsilon_{\boldsymbol{k},\downarrow}-\hbar\omega} \tag{3.42a}$$

$$\chi''_{0-+}(\boldsymbol{q},\omega) = \sum_{\boldsymbol{k}} f_{\boldsymbol{k}}(1-f_{\boldsymbol{k}+\boldsymbol{q},\uparrow})\delta(\hbar\omega-\varepsilon_{\boldsymbol{k}+\boldsymbol{q},\uparrow}+\varepsilon_{\boldsymbol{k},\downarrow}) \tag{3.42b}$$

With the interaction switched on, the renormalized susceptibility can be determined from the equation of motion [138, 319]. In the random-phase approximation (RPA) the oscillating molecular field is treated as a mean field.

$$\chi^{+-}_{\mathrm{RPA}}(\boldsymbol{q},\omega) = \frac{\chi_0^{+-}(\boldsymbol{q},\omega)}{1-U\chi_0^{+-}(\boldsymbol{q},\omega)} \tag{3.43}$$

This is analogous to the static result, which in this case is the limiting result for $\omega \to 0$.

However, the MFA-RPA approximation is insufficient for describing real systems. For ferromagnets it predicts a constant static susceptibility $1/\chi = 1/\chi_0 - 2U$ above the Curie temperature T_{C}, whereas real systems are described by the Curie-Weiss law at high temperatures $T \gg T_{\mathrm{C}}$:

$$\chi(T) = \frac{C}{T-T_{\mathrm{C}}} \tag{3.44}$$

An improvement is the self-consistent renormalization (SCR) theory, where a temperature dependent correction term $\lambda(\delta,T)$ [138] is added to the static susceptibility.

$$\frac{\chi_0}{\chi(0,0)} = 1-\alpha+\lambda(T,\delta) \tag{3.45}$$

$$\alpha = U\chi_0(0,0)$$

$$\lambda(T,\delta) \sim S_L^2$$

For weakly or nearly ferromagnetic metals applies $\alpha \simeq 1$ as stipulated by the Stoner criterium. Here, S_L^2 is the mean square local amplitude of spin fluctuations. In a metal this quantity is temperature dependent, increasing linearly for $T > T_c$, whereas in a local moment insulator it is temperature independent. For an antiferromagnetic instability at $\boldsymbol{Q}$ correspondingly holds [138]:

$$\frac{\chi_{0Q}}{\chi_0(\boldsymbol{Q},0)} = 1 - \alpha_Q + \lambda_Q(T,\delta) \tag{3.46}$$
$$\alpha = U\chi_0(\boldsymbol{Q},0)$$

The dynamic susceptibility above T_c for weakly ferro-and antiferromagnetic metals is appropriately modified in order to be consistent with the static susceptibility [138]:

$$\chi(\boldsymbol{q},\omega) \simeq \frac{\chi_0(\boldsymbol{q},\omega)/\alpha}{\delta + 1 - \chi(\boldsymbol{q},\omega)/\chi_0(0,0)} \tag{3.47}$$
$$\delta = \chi_0(0,0)/\alpha\chi(0,0)$$

It can be approximated for small q and ω/q [138].

$$\chi(\boldsymbol{q},\omega) = \frac{\chi(\boldsymbol{q})}{1 - \mathrm{i}\omega/\Gamma_{\boldsymbol{q}}} \tag{3.48a}$$
$$\chi(\boldsymbol{q}) = \frac{\chi(0)}{1 + q^2/\kappa^2} \tag{3.48b}$$
$$\Gamma_{\boldsymbol{q}} = \Gamma_0 q(\kappa^2 + q^2) \tag{3.48c}$$
$$\chi''(\boldsymbol{q},\omega) = \chi(\boldsymbol{q})\frac{\omega\Gamma_{\boldsymbol{q}}}{\omega^2 + \Gamma_{\boldsymbol{q}}^2} \tag{3.48d}$$

The parameter $\Gamma_{\boldsymbol{q}}$ is the relaxation rate. The $\kappa \propto \delta$ has a temperature dependence derived from the Curie-Weiss law:

$$\kappa = \kappa_0\sqrt{T - T_c} \tag{3.49}$$

For a nearly antiferromagnetic metal, with the critical wave vector $\boldsymbol{Q} = \boldsymbol{q}_{\mathrm{AFM}}$, similar formulae hold for $T > T_N$ [138].

$$\chi(\boldsymbol{Q} + \boldsymbol{q}) = \frac{\chi(\boldsymbol{Q})}{1 + q^2/\kappa_Q^2} \tag{3.50a}$$
$$\Gamma_{\boldsymbol{Q}+\boldsymbol{q}} = \Gamma_{0Q}(\kappa_Q^2 + q^2) \tag{3.50b}$$

The constants Γ_0, κ_0 and Γ_{0Q} have to be determined by the experiment. Equation (3.50)

together with (3.48d) can be cast into a simpler form [139].

$$\chi''(\boldsymbol{Q}+\boldsymbol{q},\omega) = \frac{\chi_0 \Gamma_T \omega}{\omega^2 + \Gamma_T^2(1+\xi_T^2 q^2)^2} \tag{3.51a}$$

$$\Gamma_T = \Gamma_0(T+\Theta) \tag{3.51b}$$

$$\xi_T = 1/\kappa = \frac{\xi_0}{\sqrt{T+\Theta}} \tag{3.51c}$$

The constant Θ corresponds to the Curie-Weiss temperature of the antiferromagnet. At the critical wave vector, where $\boldsymbol{q} = 0$, this ω-dependence takes a quasielastic lineshape. The relaxation function Γ_T takes a minimum at $\boldsymbol{q}_{\mathrm{AFM}}$ and decreases with temperature. This corresponds to a slowing down of the spin fluctuations and an accumulation of spectral weight at low energies.

3.2.2 Dynamical susceptibility in nearly antiferromagnetic heavy-fermion systems

In contrast to the itinerant antiferro- and ferromagnets, the local dynamic susceptibility is considered first. In the paramagnetic state the fluctuations of the spin originate from the Kondo-coupling [51].

$$\chi_{\mathrm{L}}(\omega) = \frac{\chi_{\mathrm{L}}}{1 - \mathrm{i}\omega/\Gamma_{\mathrm{L}}} \tag{3.52}$$

This term has to be modified because of the RKKY interaction $\sum_{jl} J_{jl}\boldsymbol{S}_j\boldsymbol{S}_l = \sum_q J_q |S_{\boldsymbol{q}}|^2$ and intersite hoppings via sf-coupling. Similar to the derivations above, mean-field approximation delivers a $\boldsymbol{q}$-dependent susceptibility. The antiferromagnetic wave vector be $\boldsymbol{Q}$ [51].

$$\chi(\boldsymbol{Q}+\boldsymbol{q},\omega) = \frac{\chi_{\mathrm{L}}(\omega)}{1 - J_{Q+q}\chi_{\mathrm{L}}(\omega)} \tag{3.53}$$

The imaginary part of the dynamical susceptibility *vs.* ω can again be cast into a quasielastic lineshape [51, 320]

$$\chi''(\boldsymbol{Q}+\boldsymbol{q},\omega) = \chi_{Q+q}\Gamma_{Q+q}\frac{\omega}{\omega^2 + \Gamma_{Q+q}^2} \tag{3.54a}$$

$$\chi_{Q+q} = \frac{1}{1/\chi_L - J_{Q+q}} \tag{3.54b}$$

$$\Gamma_{Q+q} = \frac{\chi_L \Gamma_L}{\chi_{Q+q}} \tag{3.54c}$$

This model enables direct comparison with the experiment, which can provide the adjustable parameters χ_L, Γ_L and J_{Q+q}. J_{Q+q} is expanded around the antiferromagnetic

wave vector [51]

$$J_Q - J_{Q+q} = Aq^2 + ... \tag{3.55}$$

With equation (3.54) it becomes clear that χ_{Q+q} takes its maximum and Γ_{Q+q} takes its minimum at the antiferromagnetic wave vector $\boldsymbol{q} = 0$. The exchange constant $J(\boldsymbol{q})$, according to Equation (3.15), is related to the susceptibility of the conduction electrons. Therefore, for a quantitative description of the spin fluctuations the band structure needs to be taken into account. Experimentally the intersite exchange interactions can be determined via:

$$J(\boldsymbol{q}) = \sum_{\boldsymbol{r}\neq 0} J_{\boldsymbol{r},0} e^{i\boldsymbol{q}\boldsymbol{r}} \tag{3.56}$$

3.2.3 Spin waves in itinerant ferromagnets

The spin excitations in the ferromagnetically ordered compound are given by the poles of the dynamic spin susceptibility $\chi^{+-}_{\mathrm{RPA}}(\boldsymbol{q},\omega)$, as described by Eq. (3.43). This includes single-particle excitations, where the majority spin electron is excited by flipping the spin and transferring the momentum $\boldsymbol{q}$. The spin bands are given by equation (3.31). These singe-particle or Stoner excitations form a continuum, shown by the shaded area in the dispersion plot in Fig. 3.3:

$$\hbar\omega = \varepsilon_{\boldsymbol{k}+\boldsymbol{q}} - \varepsilon_{\boldsymbol{k}} + E_{\mathrm{ex}} \tag{3.57}$$

Here, E_{ex} is the exchange splitting. The minimum excitation energy is given by the Stoner gap Δ [321]. Beside the Stoner excitations the model also predicts a collective mode below the Stoner-continuum, given by the dashed line in Fig. 3.3 (a), which disperses away from $\boldsymbol{q} = 0$ and merges with the continuum for high enough wave vectors. For parabolic bands its dispersion can be approximated as

$$\hbar\omega_{\boldsymbol{q}} \approx D\boldsymbol{q}^2 \tag{3.58}$$

These spin waves can be experimentally observed via inelastic neutron scattering, which probes the imaginary part of the RPA susceptibility. From equation (3.43) for the RPA susceptibility follows:

$$\chi''_{+-}(\boldsymbol{q},\omega) = \frac{\chi''_{+-0}(\boldsymbol{q},\omega)}{[1 - U\chi'_{+-0}(\boldsymbol{q},\omega)]^2 + [U\chi''_{+-0}(\boldsymbol{q},\omega)]^2} \tag{3.59}$$

The imaginary part of the Lindhard susceptibility $\chi''_{+-0}(\boldsymbol{q},\omega)$ is given by the particle-hole excitations, which in case of a ferromagnet are given by the Stoner continuum.

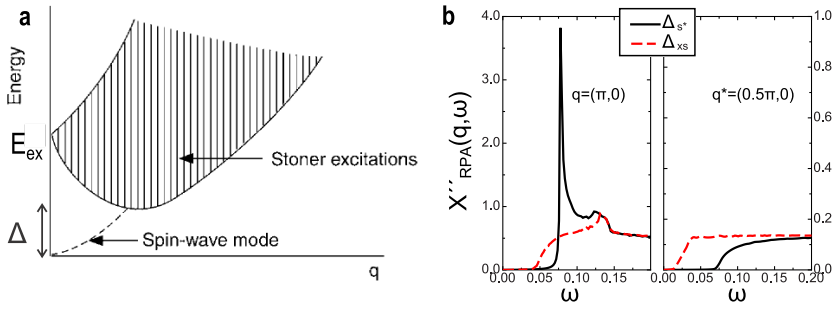

Fig. 3.3: (a) Spin wave dispersion and Stoner continuum (shaded area) for an itinerant ferromagnet. **(b)** RPA dynamic spin susceptibility χ'' versus frequency in the superconducting state for doped LaOFeAs, assuming a $s^{\pm}$-wave gap (solid line) and an extended s-wave gap for $\boldsymbol{q} = (\frac{1}{2}\,0)$ and $\boldsymbol{q}^* = (\frac{1}{4}\,0)$. The figure is reproduced from Ref. 175.

Outside of the continuum holds $\chi''_{+-0}(\boldsymbol{q},\omega) = 0$ and the equation reduces to [318]

$$\chi''_{+-}(\boldsymbol{q},\omega) = \frac{2\mu_B}{U}\delta[1 - U\chi'_{+-0}(\boldsymbol{q},\omega)] \tag{3.60}$$

which describes the sharp spin waves. For energies close to the onset of the continuum at Δ the imaginary part of $\chi_{+-0}(\boldsymbol{q},\omega)$ becomes finite and the delta-function broadens into a Lorentzian shape. In other words, the spin wave is damped because of the decay into particle-hole excitations. Therefore, one would expect an increase of damping for larger wave vectors q.

3.3 The magnetic resonant mode in the superconducting state of unconventional superconductors

Collective modes like the spin waves in the Stoner model arise because of the interaction between the quasiparticles. However, these are only created by the modification of the spin excitation spectrum $\chi''_{+-0}(\boldsymbol{q},\omega)$ upon opening a Stoner gap. In superconductors, the opening of the gap similarly has impact on the itinerant spin excitations. However, unlike a metal the coherence factors of the SC quasiparticles have to be taken into account. The Lindhard function in the superconducting state can be written as [6, 322]

$$\chi_0^{\mathrm{SC}}(\boldsymbol{q},\omega) = -\frac{1}{(2\pi)^3}\int \mathrm{d}\boldsymbol{k} \sum_{\alpha,\beta=\pm} (A_{\boldsymbol{k}}^{\alpha}A_{\boldsymbol{k}+\boldsymbol{q}}^{\beta} + C_{\boldsymbol{k}}^{\alpha}C_{\boldsymbol{k}+\boldsymbol{q}}^{\beta})\frac{f(E_{\boldsymbol{k}+\boldsymbol{q}}^{\alpha}) - f(E_{\boldsymbol{k}}^{\beta})}{E_{\boldsymbol{k}+\boldsymbol{q}}^{\alpha} - E_{\boldsymbol{k}}^{\beta} - \omega + \mathrm{i}\delta} \tag{3.61}$$

with $E_{\boldsymbol{k}}^{\pm} = \pm\sqrt{\epsilon_{\boldsymbol{k}}^2 + \Delta_{\boldsymbol{k}}^2}$ being the well-known SC quasiparticle dispersion, where $\epsilon_{\boldsymbol{k}}$ is the energy difference to the chemical potential μ. The factors $A_{\boldsymbol{k}}^{\pm}$ and $C_{\boldsymbol{k}}^{\pm}$ are derived from the coherence factors and are determined as

$$A_{\boldsymbol{k}}^{\pm} = \frac{1}{2} \pm \frac{\epsilon_{\boldsymbol{k}}}{E_{\boldsymbol{k}}^{+} - E_{\boldsymbol{k}}^{-}} \quad C_{\boldsymbol{k}}^{\pm} = \frac{\Delta_{\boldsymbol{k}}}{E_{\boldsymbol{k}}^{+} - E_{\boldsymbol{k}}^{-}} \tag{3.62}$$

The RPA-susceptibility $\chi_{\mathrm{RPA}}^{\mathrm{SC}}(\boldsymbol{q}, \omega)$ then follows from equation (3.43) under knowledge of the interaction parameter U. In case of the FeSC superconductors U is a combination of the Couloumb repulsion U_{C}, Hund's rule coupling J and the pair hopping energy denoted by J' [120, 176]. The fulfillment of the resonance condition $\chi_0^{\mathrm{SC}\prime}(\boldsymbol{q}, \omega_{\mathrm{res}}) = 1/U$ and the gapping of the particle-hole excitations $\chi_0^{\mathrm{SC}\prime\prime}(\boldsymbol{q}, \omega_{\mathrm{res}}) = 0$ lead to the formation of a bound spin-1 exciton below the superconducting gap Δ in the spectrum at the spin-fluctuation wave vector $\boldsymbol{Q}_{\mathrm{AFM}}$ [6, 322]. The amplitude of the exciton is thereby determined by the prefactor in Eq. (3.43). For the pair-production term it is given as

$$\frac{1}{2}\left(1 - \frac{\epsilon_{\boldsymbol{k}}\epsilon_{\boldsymbol{k}+\boldsymbol{q}} + \Delta_{\boldsymbol{k}}\Delta_{\boldsymbol{k}+\boldsymbol{q}}}{E_{\boldsymbol{k}}E_{\boldsymbol{k}+\boldsymbol{q}}}\right) \tag{3.63}$$

Since $\epsilon_{\boldsymbol{k}}\epsilon_{\boldsymbol{k}+\boldsymbol{q}} \approx 0$ and $E_{\boldsymbol{k}}E_{\boldsymbol{k}+\boldsymbol{q}} \approx \Delta_{\boldsymbol{k}}\Delta_{\boldsymbol{k}+\boldsymbol{q}}$, only a SC order parameter $\Delta_{\boldsymbol{k}}$ that changes the sign on different Fermi surface sheets, connected by $\boldsymbol{q}$, will produce a finite amplitude for the exciton [6, 322]. Figure 3.3 (b) shows the spectrum of the RPA calculated imaginary part of the dynamic susceptibility in the superconducting state of doped LaOFeAs, based on a tight-binding fit of its band structure [175]. A sharp resonant mode is created for $\boldsymbol{q} = (\frac{1}{2}\,0)$ scattering that connects both hole and electron pockets. A necessary condition is that the superconducting gap has different signs on the pockets, which is established under $s^{\pm}$ symmetry. If a sign change is missing (here for extended s-wave symmetry), the peak is absent. The same applies to intra-pocket scattering along $\boldsymbol{q}^{*} = (\frac{1}{4}\,0)$, which does not involve a sign change for both symmetries [see Fig. 3.3 (b)]. The experimental observation of the resonant mode (see Section 2.1.3) in both iron pnictides and cuprates is thus regarded as a hallmark of a sign-changing order parameter and a strong indication for magnetically mediated superconductivity.

4 Experimental Methods

4.1 Preparation of $A_xFe_{2-y}Se_2$ (A = K, Rb) single crystals

Because of the weak interaction between neutrons and matter large samples with a mass of several grams are required for inelastic neutron scattering experiments. For obtaining single crystals of alkali-metal iron selenide superconductors (FeSe122) two different crystal growth techniques were applied.

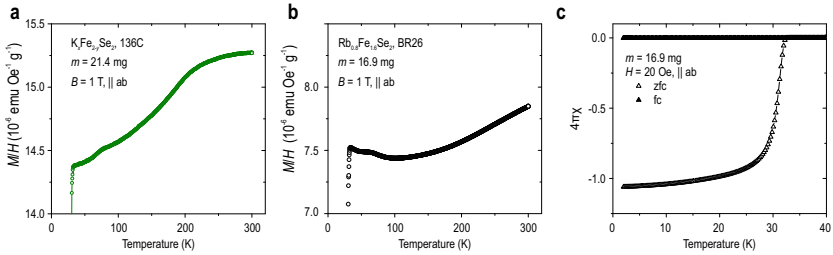

Fig. 4.1: Magnetic susceptibility M/H *vs.* temperature for **(a)** a piece of $K_xFe_{2-y}Se_2$ (batch 136C), grown by the floating zone technique, and **(b)** a piece of $Rb_{0.8}Fe_{1.6}Se_2$ (batch BR16), grown by the Bridgman technique. **(c)** Magnetic susceptibility $4\pi\chi$ in the superconducting state of the $Rb_{0.8}Fe_{1.6}Se_2$ sample, measured under zero-field cooling (zfc) and field cooling of the sample. All measurements have been performed in a SQUID-VSM magnetometer, with the field applied along the *ab* plane.

The $K_xFe_{2-y}Se_2$ single crystals were grown by the optical floating-zone technique in the group of Dr. C. T. Lin (MPI-FKF, Stuttgart). The details of the procedure are described in Reference 323. A nominal composition of $K_{0.8}Fe_2Se_2$ was pre-reacted and grounded into powder, which was pressed into a feed rod of 6–7 mm diameter and 70–80 mm length [323] and subsequently mounted into an optical furnace. The melting temperature was T_m = 889 °C. Unfortunately, during the traveling the crystallized part decomposed into K-poor K–Fe–Se. At the end of the growth the melt was quenched to T = 280 °C by which one could obtain a single-crystalline end [shown in Fig. 4.2 (a)], which was harvested from the batch. The shiny surface, corresponding to the (001) plane in Fig. 4.2 (a), signifies a good quality of the crystals. However, because of the mesoscopic phase separation inherent for these compounds, the crystals had to be checked for the presence of a sufficient volume fraction of the SC phase. The crystals were characterized by the measurement of the DC resistivity [323] and the DC magnetic

susceptibility.[1] The latter technique allows to measure the superconducting shielding fraction in a low magnetic field of $H = 20\,\mathrm{Oe}$. For most of the samples the shielding fraction is close to 100%, but this serves only as an indication. In the literature the real superconducting volume fraction was found to lie between 12% and 20% [204, 205]. The transition temperature of $T_c = (31.5 \pm 0.5)\,\mathrm{K}$ was found not to vary much between the different batches. All batches are summarized in table 4.1. The composition was determined by energy-dispersive X-ray spectroscopy (EDX). The Fe content varied between $1.81 < 2 - y < 1.89$ and the K content varied between $0.74 < x < 0.80$ on the surface of one single crystal. It was found that the composition for different batches scattered in a comparable interval (see table 4.1). The reason for the scattering lies in the different local mixture of the superconducting $K_xFe_2Se_2$ phase and the insulating $K_2Fe_4Se_5$ phase. Therefore, given that T_c is the same for all samples it is justified to combine the batches to one neutron sample. The susceptibility in the normal state, shown in Fig. 4.1 (a), does not reveal any anomalies, apart from the drop at T_c. Thus, the samples do not contain any third phase that corresponds to a different iron vacancy superstructure ordering reported in literature [324].

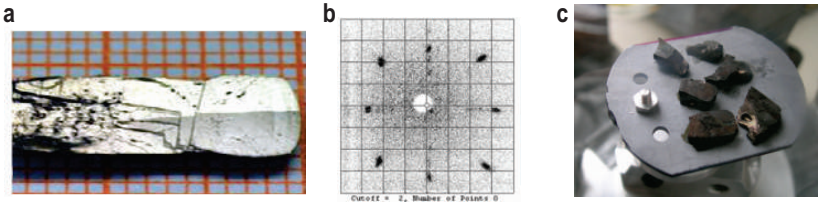

Fig. 4.2: (a) Photograph of a $K_xFe_{2-y}Se_2$ ingot after the floating-zone growth. By courtesy of Dr. C. T. Lin, MPI-FKF, Stuttgart. **(b)** Laue pattern of the $Rb_{0.8}Fe_{1.6}Se_2$ sample, taken in backscattering configuration along the [0 0 1] direction. **(c)** Photograph of the assembled $Rb_{0.8}Fe_{1.6}Se_2$ sample used for the neutron scattering experiments.

Two different batches of $Rb_xFe_{2-y}Se_2$ crystals have been provided by Dr. V. Tsurkan in the group of Prof. Loidl (University of Augsburg). The samples were grown by the Bridgman method with details given in Ref. 64. The composition, as determined by wavelength dispersive X-ray electron-probe microanalysis (WDS EPMA), is given in table 4.1. Characterization by magnetization measurements [see Fig. 4.1 (b)] does not reveal the presence of any impurities. The superconducting transition temperature was determined to $T_c = (32.2 \pm 0.5)\,\mathrm{K}$. The shielding fraction was close to 100%, underlining the good quality of the samples.

The main challenge in sample preparation was the co-alignment of different pieces on one sample holder, thus mimicking a large single crystal. The crystals naturally cleave perpendicular to the c-axis. The single crystals were attached to a silicon wafer

[1] using a PPMS and a SQUID-VSM magnetometer (Quantum Design), respectively.

Table 4.1: Upper table: Batches of $K_xFe_{2-y}Se_2$ that were combined to the INS sample. Given is the real composition determined by EDX. Lower table: batches of $Rb_xFe_{2-y}Se_2$ samples. They were not combined but treated as separate samples. The composition was determined by WDS EPMA (see also Ref. 64).

$K_xFe_{2-y}Se_2$

Batch no.	composition EDX (K:Fe:Se)
KFS 131C	0.75 : 1.85 : 2
KFS 134B	0.74 : 1.89 : 2
KFS 136A	0.77 : 1.85 : 2
KFS 136C	0.80 : 1.86 : 2
BR 2	0.80 : 1.81 : 2
Total	0.77 : 1.85 : 2

$Rb_xFe_{2-y}Se_2$

Batch no	composition WDS (Rb:Fe:Se)
BR 16	0.80 : 1.60 : 2
BR 26	0.74 : 1.60 : 2

Table 4.2: Experimental parameters for the each sample. The lattice parameters refer to the unit cell containing one iron atom.

sample	$K_{0.77}Fe_{1.85}Se_2$	$Rb_{0.8}Fe_{1.6}Se_2$	$Rb_{0.74}Fe_{1.6}Se_2$
T_c (K)	31.5 ± 0.5	32.4 ± 0.5	32.3 ± 0.3
a (Å)	2.75	2.76	2.78
a (Å)	2.75	2.76	2.78
c (Å)	7	7.2	7.3
mass (g)	2.7	1	0.7

or to an aluminium grid.[2] Only the in-plane directions $\boldsymbol{a}^*$ and $\boldsymbol{b}^*$ needed to be corrected with respect to the coordinate frame assigned to the sample holder. This was done by checking the corresponding reflections with a Laue camera.[3] One obstacle was the high air sensitivity compared to the "122" iron arsenide compounds. Pieces that were left in air visibly degraded[4] and lost the superconducting properties. In order to perform the hour-long process of co-alignment, the sample holder with the crystals was loaded into a specially designed air-tight gasket under argon atmosphere.[5] A window pane, made

[2] by glue (IM7031 Insulating Varnish, known as "GE") or by aluminium wire.

[3] Real-time back-reflection Laue camera (*Multiwire Laboratories, Ltd*) in conjunction with a *Seifert* X-ray tube based on a wolfram cathode.

[4] The samples tarnished and the color changed to reddish in case of $K_xFe_{2-y}Se_2$.

[5] Details of this device are given in Ref. 325.

of elastic foil, allowed both to probe the crystals with X-rays and to mechanically align them.

In this mount, the sample plate spans the $(H\,K\,0)$ scattering plane. This configuration was mostly used in the experiment, since the INS signal did not exhibit any L-dependence.

4.2 Preparation of $Ce_{1-x}La_xB_6$ single crystals

Single crystals of $Ce_{1-x}La_xB_6$ were prepared in the group of N. Shitsevalova.[6] This system can be grown by the floating-zone technique. The rods have a diameter of 5–6 mm and are 40–50 mm long, weighting roughly 4 grams. The boron isotope ^{10}B is strongly absorbing. Therefore 99.6% enriched ^{11}B powder was used in the synthesis.

Table 4.3: List of the prepared $Ce_{1-x}La_xB_6$ single crystals, investigated in this thesis. The zero-field AFM and AFQ transition temperatures for each sample were determined from the anomalies in specific heat *vs.* T. The data are published in the literature or were measured by our collaborators. For higher dopings the transition into phase IV at T_{IV} replaces the transition into phase II in zero field.

x	T_N (K)	T_Q (K) or T_{IV} (K)
0	2.28 (Ref. 297)	3.29 (Ref. 297)
0.18	1.7 ± 0.04	2.07 ± 0.2[a]
0.23	1.2 [b]	1.6 (IV)[b]
0.28	–[c]	1.37 ± 0.03 (IV)

[a] hardly discernible anomaly in the zero field heat capacity
[b] from preliminary specific-heat data, measured in the group of M. Brando, MPI-CPFS, Dresden.
[c] not observed

Beside CeB_6, three more lanthanum doped compounds have been prepared: $x = 0.18$, $x = 0.23$ and $x = 0.28$. These dopings span the dome of the antiferromagnetic (AFM) phase in dependence of x up to its vanishing around $x_c = 0.3$ [287]. All La-doped samples have been characterized by measurements of the specific heat $c_p(T)$ in the groups of R. Kremer (MPI-FKF, Stuttgart) and M. Brando (MPI-CPFS, Dresden). The determined transition temperatures for the antiferroquadrupolar (AFQ) and the AFM phase are given in table 4.3. The $x = 0.28$ sample does not show AFM order in zero field.[7] An example of the WDS microanalysis of La concentration along the length of the rod in Fig. 4.3 (c) shows a flat and homogeneous distribution.[8] The cubic lattice constant $a = 4.14$ Å does not change much upon introduction of lanthanum. Rocking

[6] from the I.M. Frantsevich Institute for Problems of Materials Science in Kiev

[7] but can be induced by magnetic field.

[8] The value of the determined average concentration $c(\mathrm{La})$ slightly deviates from the nominal concentration, but the transition temperature in table 4.3 agrees well with the published phase diagram in Fig. 2.18 if plotted *vs.* nominal La content.

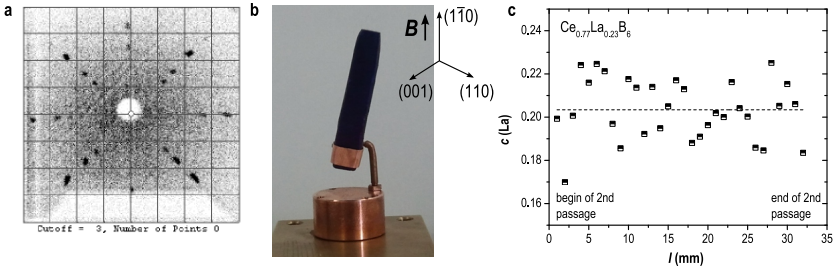

Fig. 4.3: **(a)** Laue pattern of the $Ce_{0.77}La_{0.23}B_6$ sample, taken in backscattering configuration along the $\langle 0\,0\,1\rangle$ direction. **(b)** Photograph of the $Ce_{0.77}La_{0.23}B_6$-single crystal, mounted on the Cu-sample holder. The magnetic field in the INS experiment points along the vertical direction. The scattering plane corresponds to the horizontal plane. **(c)** EDX analysis of the La-concentration along the axial direction of the $Ce_{0.77}La_{0.23}B_6$-crystal.

scans through the Bragg reflections to characterize the mosaicity were measured for all rods. Figure 4.4 (a) and (b) show the $(0\,0\,1)$ and the $(1\,1\,0)$ reflections for the CeB_6 rod. The corrugated lineshape is due to multiple grains in the sample, which are slightly misaligned. The FWHM of the Gaussian fit is $(5.0 \pm 0.4)^\circ$ for $(0\,0\,1)$ and $(2.3 \pm 0.2)^\circ$ for the $(1\,1\,0)$ direction. The $Ce_{0.77}La_{0.23}B_6$ crystal in Fig. 4.4 (c) possesses a better mosaicity of FWHM= $(0.70 \pm 0.02)^\circ$. The angular spread because of the mosaicity will also be reflected in the magnetic Bragg peaks. But such a broadening is an extrinsic effect.

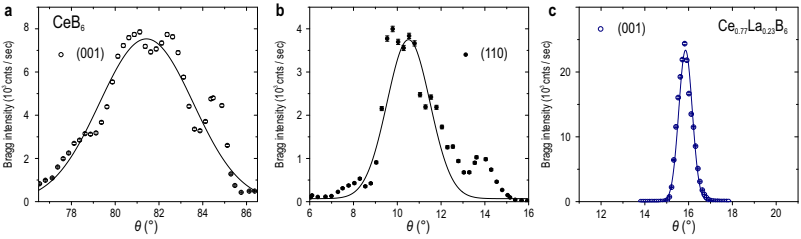

Fig. 4.4: **(a)** and **(b)** Elastic rocking scan through the $(0\,0\,1)$ Bragg peak and the $(1\,1\,0)$ Bragg peak of the CeB_6 crystal. **(c)** Rocking scan through the $(0\,0\,1)$ Bragg peak of the $Ce_{0.77}La_{0.23}B_6$ crystal. The solid lines are Gaussian fits. All measurements were done at the PANDA spectrometer.

The axis of the rods corresponds to the $(1\,\bar{1}\,0)$ direction. Their cross section corresponds to the $(H\,H\,L)$ plane, which is identical to the scattering plane when mounting the crystals vertically, as shown in Fig. 4.3 (b). No other configuration was used. The $(H\,H\,L)$ plane is very convenient as it allows to access the AFM wave vectors at $\boldsymbol{q}_1 = \Sigma(\frac{1}{4}\,\frac{1}{4}\,0)$ and $\boldsymbol{q}_1' = S(\frac{1}{4}\,\frac{1}{4}\,\frac{1}{2})$ as well as the AFQ wave vector at $\boldsymbol{q}_{\mathrm{AFQ}} = R(\frac{1}{2}\,\frac{1}{2}\,\frac{1}{2})$.

The crystals were mechanically mounted on a copper sample holder. Because of the low transition temperatures most experiments were performed in the sub-Kelvin range, which was reached by means of a dilution or a ^{3}He insert. A thin copper thread in Fig. 4.3 (b) does not only fix the crystal away from the copper base, but also establishes the thermal contact between the copper base and the rod. The comparatively good thermal conduction of copper ensures fast thermalization of the sample in those measurements, where the temperature is changed.

4.3 The experimental technique of neutron scattering

Neutron scattering offers several advantages over other scattering techniques, e.g. with X-rays or electrons, which make it a powerful technique in condensed matter research. Thermal neutrons possess a comparatively short de-Broglie wavelength of $\lambda = 1.8\,\text{Å}$, which can be used to resolve periodic structures in solids and liquids. The associated energy of $E = 5$–$100\,\text{meV}$ lies in the range of elementary excitations like phonons and magnons, which can thus be studied with high precision. Moreover, the neutron does not carry a charge. It is considered a bulk probe, as it can illuminate deep into a material. It interacts with the nucleus by nuclear forces. This entails a different cross section compared to X-ray radiation, which makes it complementary probe for structural analysis. Furthermore, it carries a spin, which interacts with the magnetic moment of the electrons. Therefore, it can be used to refine magnetic structures by diffraction. It also enables the determination of the whole energy and $\boldsymbol{Q}$ dependence of the dynamic spin susceptibility $\chi''(\boldsymbol{Q}, \omega)$ by inelastic scattering. The latter characterizes the spin dynamics of the system and thus delivers an important complementary input to the electronic structure investigations, e.g. by ARPES or optical spectroscopy.

One drawback is the small scattering cross section and the low flux,[9] that necessitates long counting times. Second, the production of neutrons is quite costly. Most of the experiments presented in this thesis were conducted at research reactors, e.g. the Insitute Laue-Langevin (ILL) or the Forschungsreaktor Heinz Maier-Leibnitz (FRM II), where neutrons are created from the nuclear fission of ^{235}U cores. Spallation sources produce neutrons by collision of high-energy protons with a target made of heavy nuclei, such as Bi, Pb or Hg. Collecting the protons into pulses with a fixed repetition rate ($\sim$ 10–100 Hz) allows for the generation of short neutron pulses, with a length of $1\,\mu$s, which can be used for time-of-flight spectroscopy.

The kinematics in the neutron scattering process is governed by energy-and momentum conservation. An incident neutron with the wave vector k_i is scattered and becomes

[9] $\Phi = 10^8$ neutrons/cm^{-2}s^{-1} for $k_\text{i} = 2.662\,\text{Å}^{-1}$ at IN8 [326].

an outgoing neutron with the final momentum k_f

$$\hbar \boldsymbol{Q} = \boldsymbol{k}_i - \boldsymbol{k}_f \tag{4.1a}$$

$$\hbar\omega = \hbar\omega_i - \hbar\omega_f = \frac{\hbar^2}{2m_n}\left(k_i^2 - k_f^2\right) \tag{4.1b}$$

In addition, the incident and final neutrons are characterized by their spin state $\boldsymbol{\sigma}_i$, $\boldsymbol{\sigma}_f$. The probability that a neutron is scattered into the solid angle in the direction (θ, φ), $d\Omega = \sin\theta d\theta d\varphi$,[10] and under an energy transfer of $\omega + d\omega$ is described by the partial differential cross section:

$$\frac{d^2\sigma}{d\Omega d\omega} = \frac{\text{no. of neutrons per second scattered into } d\Omega \text{ under an energy transfer of } \omega + d\omega}{\Phi d\Omega d\omega} \tag{4.2}$$

Here, Φ is the neutron flux at the sample. In the two main neutron spectroscopy methods, triple-axis spectroscopy (TAS) and time-of-flight spectroscopy (TOF), the generation of the incoming neutrons and the detection of the final neutrons is differently realized.

4.3.1 Triple-axis neutron spectroscopy

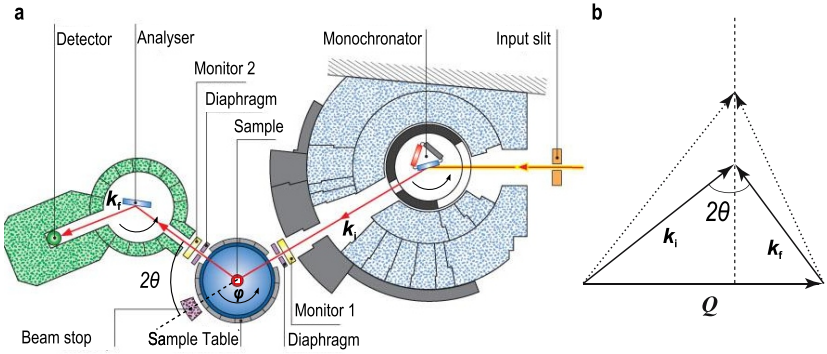

Fig. 4.5: (a) Experimental setup for inelastic neutron scattering in TAS configuration. The incoming wave vector k_i is selected at the monochromator, the outgoing wave vector k_f is selected at the analyzer. The angles $(2\theta, \varphi)$ determine the wave vector $\boldsymbol{Q}$. The figure has been adapted from Ref. 326. **(b)** Scattering triangle in reciprocal space. The dashed line marks the end points of the allowed k_i and k_f wave vectors (dotted vectors) in the scattering plane.

[10] an approximation that is only valid if the dimension of the detector is small compared to the distance between detector and sample.

A typical setup of a TAS experiment is depicted in Fig. 4.5 (a), which is adapted from the configuration at IN8 (ILL, Grenoble), where also most of the experiments were performed. Figure 4.5 (b) shows the scattering triangle in reciprocal space, which fulfils the kinematic constraints of equation (4.1). The wave vectors $\boldsymbol{k}_\mathrm{i}$ and $\boldsymbol{k}_\mathrm{f}$ are confined to the scattering plane, which leaves four degrees of freedom in choosing $(\boldsymbol{k}_\mathrm{i},\ \boldsymbol{k}_\mathrm{f})$. Measuring a certain excitation with energy $\hbar\omega$, e.g. a phonon at $\boldsymbol{Q} = \boldsymbol{q} + \boldsymbol{\tau}$, where $\boldsymbol{\tau}$ is a reciprocal-lattice vector, fixes three degrees. The remaining freedom allows the arbitrary shifting of the mutual endpoint of ($\boldsymbol{k}_\mathrm{i}$ and $\boldsymbol{k}_\mathrm{f}$) along the line in Fig. 4.5 (b). In the experiment, the length of k_f is kept fixed and is changed only in the case that kinematical constraints, e.g. in case of large Q or ω, require this. Different $|\boldsymbol{k}_\mathrm{f}|$ always imply different experimental conditions regarding intensity and resolution, which need to be taken into account.

A detailed description of the TAS method is given in the literature [327–329]. Each triple-axis spectrometer has the following components:

- The term "triple" axis refers to rotatable monochromator, analyzer and sample stages in the setup [see Fig. 4.5 (a)]. The wave vectors $\boldsymbol{k}_\mathrm{i}$ and $\boldsymbol{k}_\mathrm{f}$ are selected by Bragg scattering ($2k \sin\theta = n\lambda$) at the monochromator and analyzer, respectively, after adjusting the proper scattering angle 2θ and the rocking angle φ. Commonly the monochromator and analyzer are made of pyrolytic graphite (PG) or silicon. The angle pair for the sample $(2\theta_s, \varphi_s)$ selects the transferred momentum $\boldsymbol{Q}$. By setting $k_\mathrm{i} = k_\mathrm{f}$, a triple-axis spectrometer can also be used as a diffractometer. The barrel for analyzer and monochromator, except for the openings for incident and outgoing beam, are shielded with polyethylene or paraffin wax and highly neutron absorbing elements such as cadmium, gadolinium or boron.

- The detector is a proportional counter based on ^{3}He gas. The monitor 1 is a detector that estimates the incident flux on the sample. For inelastic scattering this quantity is used to normalize intensities, measured under different conditions, to the same flux. The flux of the incoming neutrons *vs.* the velocity follows approximately the Maxwellian distribution, and is therefore energy dependent. Moreover, during the course of an experiment the flux may fluctuate slightly, which is otherwise not detectable.

- The purpose of the filter is to remove contamination of the neutron beam from higher-order harmonics of the neutron wavelength λ_i/n ($n > 1$) that are selected at the monochromator stage together with the desired first order neutrons. In case of thermal neutrons a PG filter is used. It is placed in the final neutron beam path with its c-axis pointing along $\boldsymbol{k}_\mathrm{f}$. For certain wave numbers $k_\mathrm{f} = 2.662\,\text{Å}^{-1}, 3.84\,\text{Å}^{-1}$ or $4.1\,\text{Å}^{-1}$ only the higher-order wave numbers $2k_\mathrm{f}$, $3k_\mathrm{f}$ are Bragg scattered and thus filtered from the beam. At cold neutron spectrometers a beryllium-filter is used. Here, the larger wavelength of the neutrons is comparable to the largest lattice spacing of the beryllium crystal $2d_\mathrm{max}$. There-

fore, when using polycrystalline Be one can achieve that all wave lengths smaller than the cutoff wavelength $\lambda_{\min} = 2d_{\max}$ are scattered out of the beam. For beryllium applies $\lambda_{\min} = 4\,\text{Å}$, which puts an upper limit of $k_{\max} = 1.57\,\text{Å}^{-1}$ to the usable wave numbers.

- Diaphragm ("slits") are placed in the beam before and after the sample. Their openings are adjusted, so that the beam ideally only illuminates the sample volume. This decreases the scattering from parts of the sample environment, which otherwise would contribute to the background.

There is a subdivision of TAS instruments according the energy range of the incoming neutrons, given in table 4.4.

Table 4.4: Types of TAS instruments, classified according to the energy of the incoming neutrons. The typical range of the final wave vectors k_f as well as of the energy resolution are given. Experiments within this thesis' work were done at the given beam lines.

	Energy E_i (meV)	k_f (Å^{-1})	FWHM (meV)	beam lines
cold	2 – 15	1.2 – 1.55	0.06 – 0.2	IN14, 4F2, PANDA
thermal	15 – 100	2.662 – 4.1	1.4 – 3.7	IN8, IN20, 2T, PUMA
hot	80 – 500	>4.1	–[a]	IN1

[a] not determined

The choice of the particular TAS instrument depends mostly on the energy transfer $\hbar\omega$ of the excitation, and on the requirements for the resolution in $\boldsymbol{Q}$ and ω.

4.3.2 Resolution and background of a triple-axis spectrometer

The cross section is related to the intrinsic scattering function of a material via:

$$\frac{\mathrm{d}^2\sigma}{\mathrm{d}\Omega\mathrm{d}\omega} = \frac{k_f}{k_i} S(\boldsymbol{Q}, \omega) \tag{4.3}$$

The finite resolution smears the intrinsic scattering function measured at $(\boldsymbol{Q}_0, \omega_0)$ over region in reciprocal space and energy. Even with a perfect monochromatic beam the resolution will still be limited by the mosaicity of the sample. Scattering at the monochromator and the analyzer further lowers the resolution. This is described by the transmission coefficient $p(\boldsymbol{k}_i)$ and $p(\boldsymbol{k}_f)$ for the monochromator and the analyzer, which are Gaussian distributions centered at the means $\overline{\boldsymbol{k}}_i$ and $\overline{\boldsymbol{k}}_f$, respectively. Both distributions determine the resolution function $R(\boldsymbol{Q} - \boldsymbol{Q}_0, \omega - \omega_0)$. The convolution of $R(\boldsymbol{Q} - \boldsymbol{Q}_0, \omega - \omega_0)$ with the intrinsic scattering function $S(\boldsymbol{Q}, \omega)$ would then correspond

to the experimentally determined intensity $I(\boldsymbol{Q}_0, \omega_0)$.[11]

$$R(\boldsymbol{Q}-\boldsymbol{Q}_0, \omega-\omega_0) = \int p(\boldsymbol{k}_i)p(\boldsymbol{k}_f)\delta[\boldsymbol{Q}+\boldsymbol{k}_i-\boldsymbol{k}_f] \\ \delta[\hbar\omega - \hbar^2(\boldsymbol{k}_i^2-\boldsymbol{k}_f^2)/2m_n]\mathrm{d}\boldsymbol{k}_i\mathrm{d}\boldsymbol{k}_f \tag{4.4}$$

$$I(\boldsymbol{Q}_0, \omega_0) = N\langle A(\boldsymbol{k}_i)\rangle \int R(\boldsymbol{Q}-\boldsymbol{Q}_0, \omega-\omega_0)S(\boldsymbol{Q}, \omega)\mathrm{d}\boldsymbol{Q}\mathrm{d}\omega \tag{4.5}$$

The integral of $p(\boldsymbol{k}_i)$ and $p(\boldsymbol{k}_f)$ defines volumes in reciprocal space, V_I and V_F, whose product is the norm of the resolution function.

$$V_I = \int p_i(\boldsymbol{k}_i)\mathrm{d}\boldsymbol{k}_i \sim \frac{\overline{\boldsymbol{k}}_i^3}{\tan\theta_m} \tag{4.6a}$$

$$V_F = \int p_f(\boldsymbol{k}_f)\mathrm{d}\boldsymbol{k}_f \sim \frac{\overline{\boldsymbol{k}}_f^3}{\tan\theta_a} \tag{4.6b}$$

The volume V_I, after reflection at the monochromator, is outlined in Figure 4.7 (a).

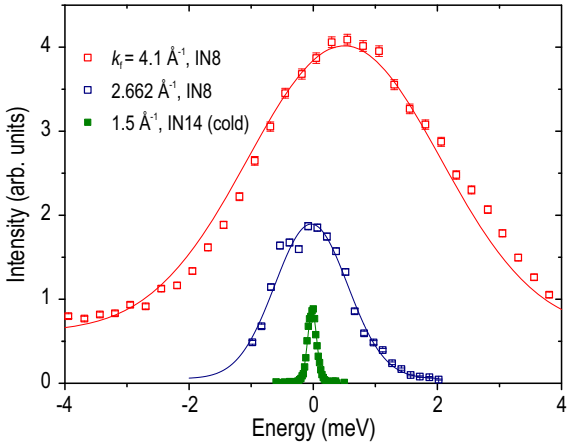

Fig. 4.6: Energy scans at an arbitrary wave vector $\boldsymbol{Q}$ across the elastic position E = 0, performed at the thermal neutron TAS IN8 for k_f = 2.662 Å^{-1} and 4.1 Å^{-1} and at the cold TAS IN14 for k_f = 1.5 Å^{-1}. The rescaling factor between IN14 and IN8 is arbitrary. The solid lines are Gaussian fits.

The incoming beam has a collimation α_0, which translates to a collimation α_1 after scattering. The thickness of V_I is controlled by the mosaic width η_m of the monochromator. The deviation of the incident wave vector $\boldsymbol{k}_i$ from $\overline{\boldsymbol{k}}_i$, $\delta\boldsymbol{k}_i = (\delta k_i^{\parallel}, \delta k_i^{\perp}, \delta k_i^{z})$, is divided into a component $\delta k_i^{\parallel}$ longitudinal to $\overline{\boldsymbol{k}}_i$, a component $\delta k_i^{\perp}$ transverse to $\overline{\boldsymbol{k}}_i$ and a component δk_i^{z} normal to the scattering plane. A similar derivation also holds for the analyzer. How $\delta\boldsymbol{k}_i$ and $\delta\boldsymbol{k}_f$ contribute to the smearing in $\boldsymbol{Q}$-space ($\delta Q^{\parallel}, \delta Q^{\perp}$) and

[11] N is a normalization factor and $\langle A(\boldsymbol{k}_i)\rangle$ is the spectral distribution of the neutrons from the source, which varies slowly around $\overline{\boldsymbol{k}}_i$.

energy $\delta\omega$ is generally quite complicated.[12] However, from simple reasoning one can infer that the spread in energy $\delta\omega$ depends, among other parameters, on the uncertainty in the magnitude of $k_i = k_i^{\parallel}$. It can be roughly estimated from mosaic width of the monochromator:

$$\frac{\delta k_i^{\parallel}}{k_i^{\parallel}} = \eta_m \cot\theta_m \tag{4.7}$$

Since the scattering angle θ_m decreases with larger k_i, choosing a larger k_f and consequently k_i impairs the energy resolution. However, knowing the energy width of an excitation is crucial, since this can give information about its lifetime. An reliable estimate for the energy resolution can be obtained by measuring the *incoherent scattering intensity vs.* energy at an arbitrary wave vector close to the point of interest at $\boldsymbol{Q}_0$, as shown in Fig. 4.6. This intensity is purely elastic ($E = 0$), but is smeared into a Gaussian lineshape by virtue of the resolution function. Its width would then correspond approximately to the resolution limit at $\boldsymbol{Q}$.

From Fig. 4.6 it is clear that the choice of the appropriate k_f and the associated energy resolution depends strongly on the energy of the signal. In CeB_6 the energy of the exciton, which is studied in this thesis, has an energy smaller than 1 meV. Measuring this signal at a thermal spectrometer would be pointless, since the incoherent intensity reaches up to $E = 1$ meV even with the smallest k_f of 2.662 Å^{-1}, which would overwhelm any inelastic signal in this region. Therefore, this compound is exclusively measured at a cold neutron spectrometers (e.g. IN14, Panda). The resonant mode in the $A_xFe_{2-y}Se_2$ family of high-T_c superconductors at $\hbar\omega_\mathrm{res} = 13.6$ meV lies in an energy range, which is covered by thermal neutron spectrometers (e.g. IN8, Puma). The determination of the intrinsic linewidth of a signal with μeV precision can be achieved by neutron spin echo spectroscopy, which is based on the triple-axis technique, but uses polarized neutrons [330].[13]

Background and spurions

The background is a critical quantity in a neutron experiment. The measured intensity, being N counts within a given time t_0, follows the Poisson distribution, since the sample number N_0 of neutrons passing the sample within t_0 is large, but the probability of scattering a neutron is very low. The counts N is an estimate for the expectation value λ. The uncertainty, usually identified with one standard deviation of N, is $\sqrt{N+1}$. This statistical error determines the scattering of the data points around λ. The relative error $\sqrt{N+1}/N$ can be decreased by increasing N, which means counting longer. In reality the intensity is contributed by the desired magnetic signal $I(\boldsymbol{Q}_0, \omega_0)$ and the

[12] However, it is clear the e.g. $\delta k_i^z (\delta k_f^z)$ only couples to δQ^z.

[13] The polarization after an echo sequence that is realized by RF flippers can be used to determine the intrinsic relaxation of the excitations.

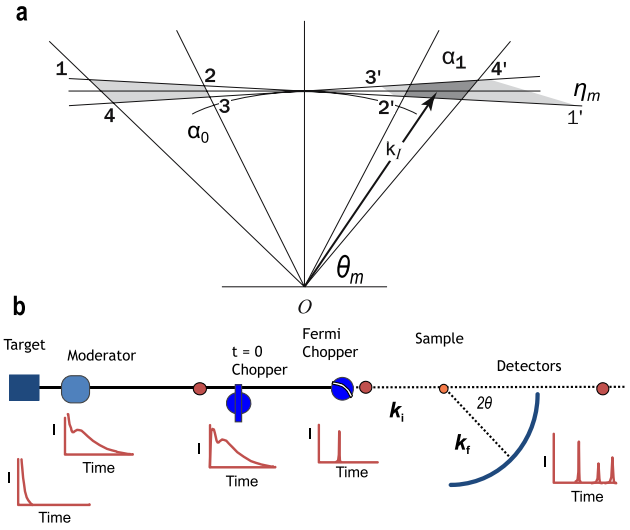

Fig. 4.7: **(a)** Illustration of the $\boldsymbol{Q}$-space volume of the $\boldsymbol{k}_i$ vectors after scattering at the monochromator. The angle α_0 and α_1 are the collimation of the beam before and after the scattering (reproduced from Ref. 329). **(b)** Schematic of the TOF setup. Adapted from Ref. 331.

background intensity N_{bg}.

$$N = I(\boldsymbol{Q}_0, \omega_0) + N_{\mathrm{bg}} \tag{4.8}$$

It might be possible to estimate the background signal N_{bg}, but it will contribute to the error $\sqrt{I(\boldsymbol{Q}_0, \omega_0) + N_{\mathrm{bg}} + 1}$ in any case.

Towards low energies the background increases because of the tail of the incoherent scattering (see Fig. 4.6). Another source of background is the direct beam, which contains all neutrons that are not scattered by the sample. As shown in Fig. 4.5 (a), the detector lies at angle 2θ to the direct beam. The higher the energy transfer E is the smaller the angle 2θ becomes, since k_i increases.[14] As the detector comes closer to the direct beam, more neutrons can leak into the analyzer path and are incoherently scattered into the detector.

Thus, the background intensity has a unknown non-monotonous dependence on the energy transfer. This hampers the measurement of a signal at $\boldsymbol{Q}_0$ by energy scans (constant-$\boldsymbol{Q}$ scans). Usually the background intensity *vs.* energy is assessed at an arbitrary wave vector $\boldsymbol{Q}_{\mathrm{BG}}$ that has the same length as $\boldsymbol{Q}_0$ and that exhibits no signal from the sample. Alternatively, one could measure the $\boldsymbol{Q}$-dependence of the signal at a certain energy (constant-energy scans) along a trajectory in reciprocal space through $\boldsymbol{Q}_0$. This trajectory can be a rocking curve, where the sample is rotated, leaving the magnitude of $\boldsymbol{Q}$ unchanged. But also a straight trajectory, usually transverse to $\boldsymbol{Q}_0$, is used.

[14] At the theoretically highest possible energy transfer holds $2\theta = 0$, with $\boldsymbol{k}_i$, $\boldsymbol{k}_f$ and $\boldsymbol{Q}$ being collinear

Repeating such scans for increasing energy allows to investigate a possible dispersion $\omega(\boldsymbol{q})$ of the signal, e.g. in the case of phonons or spin waves.

Another source of background intensity are scattering processes, where two or more phonons are created. Unlike one-phonon processes the scattering is continuous in $\boldsymbol{Q}$ space. This source of background becomes crucial for higher wave vectors, since the cross section scales with $\sim \boldsymbol{Q}^2$.

Beside the continuous sources of background, discussed above, the appearance of strong spurious signals ("spurions"), which can have a localized structure in $\boldsymbol{Q}$, constitutes another experimental challenge. Such features can be related to accidental Bragg scattering at the sample or the sample holder. For instance, in case of a Al or Cu sample holder, the scattering angle of powder lines $2\theta_{\mathrm{Al/Cu}}$ may coincide with the 2θ of the inelastic scattering process $k_\mathrm{f} < k_\mathrm{i}$ that is investigated. The final wave number $k_{\mathrm{f,el}} = k_i$ of the Bragg scattered neutrons, coming from powder lines, should be filtered out at the analyzer. However, a fraction of these neutrons can still reach the detector via incoherent scattering. The incoherent scattering capability of the sample itself may also become problematic if the spectrometer is set, so that $3k_\mathrm{f} = 2k_\mathrm{i}$ applies. In this case the third harmonic $3k_\mathrm{f}$ will be Bragg scattered at the analyzer.[15]

4.3.3 Time-of-flight spectroscopy

In the TAS method the detector surveys only a small solid angle, which corresponds to a small fraction of the $(\boldsymbol{Q}, \omega)$ space. Thus, it is deployed when a known signal at a certain position $(\boldsymbol{Q}_0, \omega_0)$ (e.g. the resonant mode in the SC state of high-T_c superconductors) is investigated in dependence of an external parameter like temperature, magnetic field and pressure. It also offers the possibility of polarized neutron scattering. However, it is not suitable when the position of the signal is not known beforehand or when its reciprocal-space structure should be determined. In that case the simultaneous detection of all scattered neutrons in a large solid angle would be advantageous. This geometry is realized in a time-of-flight (TOF) spectrometer, schematically shown in Fig. 4.7 (b). The neutron pulse is monochromatized at a Fermi chopper. Position sensitive detectors, surrounding the sample, count the scattered neutrons in histograms in dependence on the time of arrival. The time of flight from the chopper to the detectors allows to calculate the energy $\hbar\omega$, while the scattering angles $(2\theta, \varphi)$ determine the momentum transfer $\hbar\boldsymbol{Q}$. Unlike to TAS, $\boldsymbol{Q}$ and ω are coupled because of the kinematical constraints in Eq. (4.1). In case of a sample with a two-dimensional crystal structure, being aligned such that $\boldsymbol{k}_\mathrm{i}$ is parallel to the c axis, the out-of-plane moment component L in $\boldsymbol{Q} = (H\,K\,L)$ varies when changing ω. This coupling can be lifted by repeating the scans under rotation of the sample. However, TOF is a comparable time consuming technique. For instance, one beam time of 7 days may provide reciprocal-space maps

[15] The suppression of higher harmonics by the PG filter cannot sufficiently remove such effects.

with reasonable statistical certainty for only two different temperatures.[16]

4.4 The theory of neutron scattering

The theory of neutron scattering relates the experimentally determined cross section σ to microscopic properties of the material under study. It is reviewed in detail in literature [332, 333]. Only the most important results shall be given here. The general double differential cross section for neutrons follows from Fermi's golden rule in perturbation theory:

$$\frac{\mathrm{d}^2\sigma}{\mathrm{d}\Omega\mathrm{d}\omega} = \left(\frac{m}{2\pi\hbar^2}\right)^2 \frac{k_\mathrm{f}}{k_\mathrm{i}} \sum_{n_1,\sigma_\mathrm{f}} \sum_{n_0,\sigma_\mathrm{i}} p(n_0)\, |\langle k_\mathrm{f}\sigma_\mathrm{f} n_1|V|k_\mathrm{i}\sigma_i n_0\rangle|^2\, \delta(\varepsilon_1 - \varepsilon_0 - \hbar\omega) \tag{4.9}$$

Here, n_0 and n_1 denote the initial and final states of the system with energies ε_1 and ε_0, while k_i, σ_i and k_f, σ_f describe the spin and momentum states of the incoming and outgoing neutron, respectively. The factor $p(n_0)$ is the thermal occupation of the initial state $|k_\mathrm{i}\sigma_i n_0\rangle$. The interaction potential V between neutron and matter, which will be specified in the following, connects the initial and final state of the system via the matrix element $\langle k_\mathrm{f}\sigma_\mathrm{f} n_1|V|k_\mathrm{i}\sigma_i n_0\rangle$. The thermal average $\sum_{n_0,\sigma_\mathrm{i}} p(n_0)...$ over all initial states and the sum over all final states is then proportional to the cross section.

In case of nuclear scattering a Fermi pseudo potential is used to describe the interaction with the nuclei, which are sitting at the positions $\boldsymbol{R}_j$:

$$V(\boldsymbol{r}) = \frac{2\pi\hbar^2}{m} \sum_j b_j \delta(\boldsymbol{r} - \boldsymbol{R}_j) \tag{4.10}$$

The value b_j is the scattering length of the nucleus. This parameter strongly depends on the element and the isotope. Evaluating equation (4.9) for this potential provides two different forms of nuclear scattering: coherent and incoherent scattering.

$$\begin{aligned}\frac{\mathrm{d}^2\sigma}{\mathrm{d}\Omega\mathrm{d}\omega} =& \frac{k_f}{k_i}\frac{1}{2\pi\hbar}\Big[\overline{b}^2 \sum_{jj'} \int_{-\infty}^{\infty} \mathrm{d}t \langle e^{-i\boldsymbol{Q}\boldsymbol{R}_{j'}(0)} e^{i\boldsymbol{Q}\boldsymbol{R}_j(t)}\rangle e^{-i\omega t} \\ &+ (\overline{b^2} - \overline{b}^2) \sum_j \int_{-\infty}^{\infty} \mathrm{d}t \langle e^{-i\boldsymbol{Q}\boldsymbol{R}_j(0)} e^{i\boldsymbol{Q}\boldsymbol{R}_j(t)}\rangle e^{-i\omega t}\Big]\end{aligned} \tag{4.11}$$

The first term describes coherent scattering, where the scattering lengths for each nucleus is replaced by the average scattering length $\overline{b}$ of all nuclei. The effect of the individual deviation for each nucleus' scattering length b_j from the average $\overline{b}$ causes the

[16] This estimate is based on the TOF experiment on $K_{0.77}Fe_{1.85}Se_2$, which was measured in the superconducting state and in the normal state and which is discussed in Section 5.3.

incoherent scattering, which has no $\boldsymbol{Q}$ dependence and can therefore be measured at any $\boldsymbol{Q}$. For coherent scattering Eq. (4.11) gives the relation between the cross section and the scattering function $S(\boldsymbol{Q},\omega)$, which is the Fourier transform of the pair correlation function $G(\boldsymbol{r},t)$ in both space and time.

$$\frac{\mathrm{d}^2\sigma}{\mathrm{d}\Omega\mathrm{d}\omega} = \frac{k_f}{k_i}\overline{b}^2 S(\boldsymbol{Q},\omega) \tag{4.12a}$$

$$S(\boldsymbol{Q},\omega) = \frac{1}{2\pi\hbar}\int \mathrm{d}\boldsymbol{r}\int_{-\infty}^{\infty}\mathrm{d}t\, G(\boldsymbol{r},t)e^{\mathrm{i}(\boldsymbol{Q}\boldsymbol{r}-\omega t)} \tag{4.12b}$$

$$G(\boldsymbol{r},t) = \int \mathrm{d}\boldsymbol{r}'\langle\rho(\boldsymbol{r}',0)\rho(\boldsymbol{r}'+\boldsymbol{r},t)\rangle_T \tag{4.12c}$$

Here, ρ is the density operator of all N nuclei:

$$\rho(\boldsymbol{r},t) = \sum_{j=1}^{N}\delta[\boldsymbol{r}-\boldsymbol{R}_j(t)] \tag{4.13}$$

The time independent part of the pair correlation function $G(\boldsymbol{r},t)$ is obtained for $t\to\infty$. This provides the elastic scattering part of the cross section, which can be evaluated with Eq. (4.12) to

$$\frac{\mathrm{d}\sigma}{\mathrm{d}\Omega} = N\frac{(2\pi)^3}{V_0}\overline{b}^2\sum_{\boldsymbol{\tau}}\delta(\boldsymbol{Q}-\boldsymbol{\tau}) \tag{4.14}$$

This formula corresponds essentially to the Laue condition, which relates the reflections to the reciprocal-lattice vector $\boldsymbol{\tau}$. The unit cell contains only one atom. The general case of several atoms at positions $\boldsymbol{d}_\alpha$ is provided by multiplying the nuclear structure factor F_τ to the delta-function.

$$F_{\boldsymbol{\tau}} = \sum_{\alpha}\overline{b}_\alpha e^{\mathrm{i}\boldsymbol{\tau}\boldsymbol{d}_\alpha}e^{-W_d} \tag{4.15}$$

The term e^{-W_d} is the Debye-Waller factor, where W_d corresponds to the mean-square displacement of the atom from its lattice site.

4.4.1 Magnetic neutron scattering

In case of magnetic neutron scattering the magnetic moment $\boldsymbol{\mu}_\mathrm{n}$ of the neutron interacts with the magnetic field $\boldsymbol{B}$, which is associated with the spin angular momentum $\hat{\boldsymbol{s}}$ and

the orbital angular momentum $\hat{\boldsymbol{l}}$ of the electron.[17]

$$\hat{V}_{\mathrm{m}} = \hat{\boldsymbol{\mu}}_{\mathrm{n}} \boldsymbol{B} \tag{4.16}$$

$$\hat{\boldsymbol{\mu}}_{\mathrm{n}} = \gamma \mu_{\mathrm{N}} \hat{\boldsymbol{\sigma}} \tag{4.17}$$

The evaluation of the scattering potential with the master equation (4.9) is quite lengthy (see References 318, 332, 333). An important result is that the operator inside the matrix element takes the form $\boldsymbol{\sigma U}(\boldsymbol{Q})$, where $\boldsymbol{U}(\boldsymbol{Q})$ is proportional to the Fourier transform of the total magnetization $\boldsymbol{M}(\boldsymbol{r})$ of the sample. After integrating out the neutron momentum dependent part $\langle \boldsymbol{k}'|\boldsymbol{U}|\boldsymbol{k}\rangle$ only the component $U_\perp$ perpendicular to the scattering vector $\boldsymbol{Q}$ remains. This fact is implemented via the orientation factor in the cross section

$$\boldsymbol{U}_\perp^\dagger \boldsymbol{U}_\perp = \sum_{\alpha\beta} (\delta_{\alpha\beta} - \hat{Q}_\alpha \hat{Q}_\beta) U_\alpha^\dagger U_\beta \tag{4.18}$$

where $\hat{\boldsymbol{Q}} = \boldsymbol{Q}/Q$ denotes the direction of $\boldsymbol{Q}$ and $\delta_{\alpha\beta}$ is the Kronecker delta with $\alpha, \beta \triangleq x, y, z$.

The spin state of the neutron "averages out" for unpolarized neutrons

$$\sum_{\lambda\lambda'} p_\lambda \sum_{\sigma\sigma'} p_\sigma \left|\langle \sigma'\lambda'|\boldsymbol{\sigma U}_\perp|\sigma\lambda\rangle\right|^2 = \sum_{\lambda\lambda'} p_\lambda \left|\langle \lambda'|\boldsymbol{U}_\perp|\lambda\rangle\right|^2 \tag{4.19}$$

Further simplifications can be made when only spin scattering is considered. For a single magnetic ion situated at $\boldsymbol{R}_l$ and carrying p unpaired electrons, the matrix element can be written as

$$\langle \lambda'|\boldsymbol{U}_\perp|\lambda\rangle_l = F(\boldsymbol{Q}) \langle \lambda'|e^{\mathrm{i}\boldsymbol{Q}\boldsymbol{R}_l} \boldsymbol{S}_l|\lambda\rangle \tag{4.20}$$

where $\boldsymbol{S}_l$ is total spin of the ion. The spatial distribution of the spin density $s(\boldsymbol{r})$ is absorbed into the magnetic from factor $F(\boldsymbol{Q})$:

$$F(\boldsymbol{Q}) = \int s(\boldsymbol{r}) e^{\mathrm{i}\boldsymbol{Q}\boldsymbol{r}} \mathrm{d}\boldsymbol{r} \tag{4.21}$$

This function $F(\boldsymbol{Q})$ is tabulated for each magnetic ion (see Ref. 334). Generally it is monotonously decreasing for a dipolar form factor. If the orbital angular momentum is only partially quenched, $F(\boldsymbol{Q})$ is replaced by $\frac{1}{2} g F(\boldsymbol{Q})$, where g is the Landé splitting factor.

[17] The nuclear magneton μ_{N} is a constant, given by $\mu_{\mathrm{N}} = 3.153 \times 10^{-5} \mathrm{meV/T}$ and $\gamma = 1.913$

All of these terms are collected into the cross section for magnetic scattering[18]

$$\frac{\mathrm{d}^2\sigma}{\mathrm{d}\Omega\mathrm{d}\omega} = \frac{(\gamma r_0)^2}{2\pi\hbar}\frac{k_\mathrm{f}}{k_\mathrm{i}}\left|\frac{1}{2}gF(\boldsymbol{Q})\right|^2 e^{-2W_Q}\sum_{\alpha\beta}(\delta_{\alpha\beta}-\hat{Q}_\alpha\hat{Q}_\beta)\sum_{ll'}e^{\mathrm{i}\boldsymbol{Q}(\boldsymbol{R}_l-\boldsymbol{R}_{l'})} \times\int_{-\infty}^{\infty}\langle S_l^\alpha(0)S_{l'}^\beta(t)\rangle e^{-\mathrm{i}\omega t}\mathrm{d}t \tag{4.22}$$

This formula relates the cross section to the magnetic scattering function $S(\boldsymbol{Q},\omega)$ (also known as dynamical form factor), which describes the correlation in space and time for the magnetic moments.

$$S(\boldsymbol{Q},\omega)_{\alpha\beta} = \frac{1}{2\pi\hbar N}\int_{-\infty}^{\infty}\sum_{ll'}e^{\mathrm{i}\boldsymbol{Q}(\boldsymbol{R}_l-\boldsymbol{R}_{l'})}\langle S_l^\alpha(0)S_{l'}^\beta(t)\rangle e^{-\mathrm{i}\omega t}\mathrm{d}t \tag{4.23}$$

N is the number of spins. The evaluation for $t\to\infty$ describes the elastic scattering, while the finite t part represents the inelastic contribution to $S(\boldsymbol{Q},\omega)$. Real transitions in the system are due to perturbations that are constituted by the interaction with the spins of the neutron. Since the energy $\hbar\omega$ is dissipated in the scattering process, it must be related to the imaginary part of the dynamical spin susceptibility $\chi(\boldsymbol{Q},\omega)$.

$$\chi''(\boldsymbol{Q},\omega) = -\pi[S(\boldsymbol{Q},\omega)-S(\boldsymbol{Q},-\omega)] \tag{4.24}$$

Conversely, the $S(\boldsymbol{Q},\omega)$ can be expressed as

$$S(\boldsymbol{Q},\omega) = \frac{1}{\pi}\frac{1}{1-e^{-\hbar\omega/k_\mathrm{B}T}}\chi''(\boldsymbol{Q},\omega) \tag{4.25}$$

which is known as the *fluctuation-dissipation theorem*. The temperature dependent prefactor is the Bose-factor

$$n(T,\omega) = \frac{1}{1-e^{-\hbar\omega/k_\mathrm{B}T}} \tag{4.26}$$

The scattering function $S(\boldsymbol{Q},\omega)_{\alpha\beta}$ and the spin susceptibility $\chi''_{\alpha\beta}$ are tensors. For spin fluctuations without preferred direction, the orientation factor can be evaluated to $\sum_{\alpha\beta}(\delta_{\alpha\beta}-\hat{Q}_\alpha\hat{Q}_\beta)\chi''_{\alpha\beta}(\boldsymbol{Q},\omega) = 2\mathrm{Tr}(\chi''_{\alpha\beta})/3$, where the right side corresponds to the isotropic spin susceptibility $\chi'' = \mathrm{Tr}(\chi''_{\alpha\beta})/3$. There are different conventions in literature on how the scattering function is converted to the imaginary part of the dynamic susceptibility. According to equation (4.25) one obtains[19]

$$S(\boldsymbol{Q},\omega) = \frac{2}{\pi(g\mu_\mathrm{B})^2}n(T,\omega)\chi''(\boldsymbol{Q},\omega) \tag{4.27}$$

[18] The Debye-Waller factor here is e^{-2W_Q}. $(\gamma r_0)^2 = 0.2905$ barn sr^{-1} is a constant.

[19] This is in accord with the convention for neutron scattering experiments on $YBa_2Cu_3O_{6+x}$ (see Ref. 335).

χ'' is usually given in units of $\mu_B^2/\mathrm{eV\,f.u.}$, where μ_B is the Bohr magneton and f.u. means one formula unit. But also more expanded versions of $S(\boldsymbol{Q},\omega)$ including prefactors and the magnetic form factor, can be found in the literature (see Ref. 125, 336).

$$S(\boldsymbol{Q},\omega) = \frac{2(\gamma r_0)^2}{\pi(g\mu_B)^2}|F(\boldsymbol{Q})|^2 n(T,\omega)\chi''(\boldsymbol{Q},\omega) \tag{4.28}$$

The differential cross section is measured in units of barn $\mathrm{meV^{-1}sr^{-1}f.u.^{-1}}$. However, in triple-axis spectroscopy the intensity is not calibrated and is given in "counts". The conversion to "absolute" units is quite complicated, since the intensity depends on the experimental conditions (see previous paragraph). Therefore, from experimental point of view the intensity, corrected for the background, is identified with $S(\boldsymbol{Q},\omega)$ and any prefactors are neglected. When converting it to $\chi''(\boldsymbol{Q},\omega)$ the inclusion of the magnetic form factor and the Bose factor will be explicitly stated.

The exact form of $\chi''(\boldsymbol{Q},\omega)$ depends on the system under study. The expressions for the itinerant spin dynamics are given in Section 3.2. However, an interesting special case is provided by a paramagnet. The spins are randomly oriented and changing the direction of spins does not change the energy of the system. Thus, the spin-spin correlation function is time independent and the spins are not correlated for $l \neq l'$

$$\langle S_l^\alpha(0)S_{l'}^\beta(t)\rangle = \langle S_l^\alpha S_{l'}^\beta\rangle = \begin{cases} 0, & l \neq l' \\ \frac{1}{3}\delta_{\alpha\beta}S(S+1), & l = l' \end{cases} \tag{4.29}$$

The cross section becomes

$$\frac{\mathrm{d}\sigma}{\mathrm{d}\Omega} = \frac{2}{3}(\gamma r_0)^2 N|\frac{1}{2}gF(\boldsymbol{Q})|^2 e^{-2W}S(S+1) \tag{4.30}$$

The scattering is elastic and completely diffuse, where any interference effects are absent. With the onset of interactions between the moments they can order, giving rise to coherent elastic contributions and inelastic contributions. The total spectral weight remains thereby constant, which is stipulated by the *Sum rule* of neutron scattering.

$$\frac{\int_{-\infty}^{\infty}\mathrm{d}\omega\int_{\mathrm{BZ}}\mathrm{d}\boldsymbol{Q}S_{\alpha\beta}(\boldsymbol{Q},\omega)}{\int_{\mathrm{BZ}}\mathrm{d}\boldsymbol{Q}} = \frac{1}{3}S(S+1)\delta_{\alpha\beta} \tag{4.31}$$

The scattering function is integrated over the Brillouin zone and over all energies. This means that the spectral weight can be redistributed in $\boldsymbol{Q}$, e.g. upon formation of long-range order, and redistributed in energy, e.g. from elastic to inelastic.

This thesis is mainly concerned with the inelastic response of the system. Theoretically, a spin wave excitation $\hbar\omega(\boldsymbol{q})$ appears as a δ-function, centered at $\boldsymbol{q}$, in the $\boldsymbol{Q}$ dependence and as a δ-function, centered at $\hbar\omega(\boldsymbol{q})$, in the energy dependence of $S(\boldsymbol{q},\omega)$ [or $\chi''(\boldsymbol{q},\omega)$]. However, in reality the excitation has a finite life time because of the damping by particle-hole excitations and anharmonic processes. Therefore, a

Lorentzian lineshape is applied to analyze the spectrum.

$$\chi''(\omega) = \chi' \left[\frac{\Gamma}{\hbar^2[\omega - \omega(\boldsymbol{q})]^2 + \Gamma^2} - \frac{\Gamma}{\hbar^2[\omega + \omega(\boldsymbol{q})]^2 + \Gamma^2} \right] \tag{4.32}$$

The anti-Stokes term with $-\omega(\boldsymbol{q})$ satisfies the odd symmetry of $\chi''(\omega)$ in the energy dependence. The linewidth $\Gamma(\boldsymbol{q})$ corresponds to the half-width-half-maximum (HWHM) of the peak.

If the signal is resolution limited or broadened by random external parameters like sample inhomogeneities, $S(\boldsymbol{q}, \omega)$ is fitted to a Gaussian lineshape

$$S(\boldsymbol{q}, \omega) = Ae^{-\frac{1}{2}\left(\frac{\hbar\omega - \hbar\omega(\boldsymbol{q})}{\sigma}\right)^2} \tag{4.33}$$

where A is the amplitude and σ corresponds to one standard deviation from the extrema at $\hbar\omega(\boldsymbol{q})$.

Measurement and Results

The following Chapters 5 and 6 contain almost exclusively original data of neutron scattering experiments on $A_xFe_{2-y}Se_2$-superconductors and $Ce_{1-x}La_xB_6$ antiferromagnets that were collected within this thesis. Results of theoretical analyses that were motivated by or that are in close connection with the experimental data will be displayed in these chapters for the convenience of discussion. This external work will be cited explicitly.

Furthermore, parts of the presented figures have been published in identical or similar form prior to the completion of this thesis. The following publications contain original data that emerged in the course of the work on this thesis.

Chaper 5

Parts of the data on $A_xFe_{2-y}Se_2$-superconductors were measured in collaboration with Dr. J. Park and are displayed in his thesis, *Spin dynamics in 122-Type Iron-Based Superconductors* (Universität Stuttgart, 2012).

Furthermore, some figures concerning neutron scattering experiments on $Rb_{0.8}Fe_{1.6}Se_2$ are similarly published in

- J. T. Park, G. Friemel, Y. Li, J.-H. Kim, V. Tsurkan, J. Deisenhofer, H.-A. Krug von Nidda, A. Loidl, A. Ivanov, B. Keimer and D. S. Inosov, *Magnetic Resonant Mode in the Low-Energy Spin-Excitation Spectrum of Superconducting* $Rb_2Fe_4Se_5$ *Single Crystals*, Phys. Rev. Lett. **107**, 177005 (2011). Copyright (2011) by the American Physical Society.

- G. Friemel, J. T. Park, T. A. Maier, V. Tsurkan, Y. Li, J. Deisenhofer, H.-A. Krug von Nidda, A. Loidl, A. Ivanov, B. Keimer and D. S. Inosov, *Reciprocal-space structure and dispersion of the magnetic resonant mode in the superconducting phase of* $Rb_xFe_{2-y}Se_2$ *single crystals* , Phys. Rev. B **85**, 140511 (2012). Copyright (2012) by the American Physical Society.

Some figures concerning neutron scattering experiments on $K_xFe_{2-y}Se_2$ are similarly published in

- G. Friemel, W. P. Liu, E. A. Goremychkin, Y. Liu, J. T. Park, O. Sobolev, C. T. Lin, B. Keimer and D. S. Inosov, *Conformity of spin fluctuations in alkali-metal iron selenide superconductors inferred from the observation of a magnetic resonant mode in* $K_xFe_{2-y}Se_2$, EPL **99**, 67004 (2012). Copyright (2012) EPLA.

Chaper 6

Some figures concerning neutron scattering experiments on CeB_6 are similarly published in

- G. Friemel, Y. Li, A. Dukhnenko, N. Shitsevalova, N. Sluchanko, A. Ivanov, V. Filipov, B. Keimer and D. Inosov, *Resonant magnetic exciton mode in the heavy-fermion antiferromagnet CeB_6*, Nat Commun **3**, 830– (2012). Copyright (2012) Macmillan Publishers Limited.

- H. Jang, G. Friemel, J. Ollivier, A. V. Dukhnenko, N. Y. Shitsevalova, V. B. Filipov, B. Keimer and D. S. Inosov, *Intense low-energy ferromagnetic fluctuations in the antiferromagnetic heavy-fermion metal CeB6*, Nat Mater **13**, 682–687 (2014). Copyright (2012) Macmillan Publishers Limited.

5 Itinerant spin fluctuations in alkali-metal iron selenide superconductors $A_xFe_{2-y}Se_2$ (A=K, Rb)

5.1 Prediction of the magnetic resonant mode in the superconducting phase of $A_xFe_{2-y}Se_2$

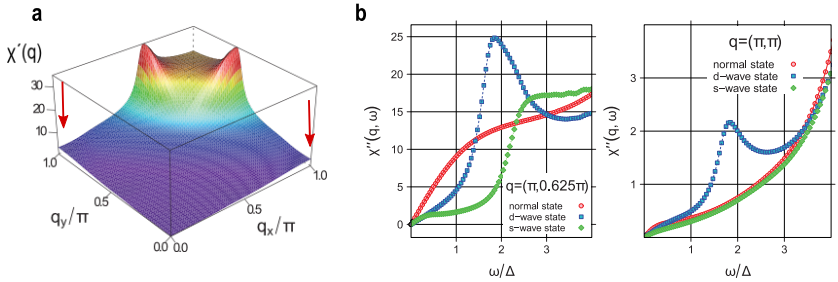

Fig. 5.1: **(a)** In-plane $\boldsymbol{Q}$-dependence of $\mathrm{Re}\,\chi^{\mathrm{RPA}}(\boldsymbol{q},\omega)$, calculated for a shifted band structure of KFe_2Se_2 that matches the experimental one. **(b)** Imaginary part of the RPA spin susceptibility in the normal state and in the superconducting state of KFe_2Se_2, evaluated for different symmetries of the SC order parameter and for certain wave vectors of spin fluctuations. All figures have been reproduced from Ref. 3.

The discovery of superconductivity below T_c = 31 K in $K_xFe_{2-y}Se_2$ [1, 52] provided an intriguing special case of the FeSC. The pure electron-like Fermi surface, observed by ARPES [4, 7, 10, 11, 184], clearly opposes the paradigm of a nesting between hole and electron pockets that facilitates superconductivity for the iron-based compounds. Whether the superconductivity is unconventional and whether it is possibly mediated by spin fluctuations were open questions. The most important theoretical analysis by Maier *et al.* [3] will be outlined in the following. A five orbital tight-binding model has been fitted to the LDA-computed band structure of stoichiometric KFe_2Se_2, which delivers the parameters for intra-and interorbital interaction ($\overline{U}$, $\overline{U}'$, $\overline{J}$, $\overline{J}'$). The Fermi level has been adjusted, so that the calculated Fermi surface fits the experimentally observed one for $K_{0.8}Fe_{1.7}Se_2$ [184]. Evaluation of the real part of the RPA-renormalized spin susceptibility $\mathrm{Re}\,\chi^{\mathrm{RPA}}(\boldsymbol{q},\omega)$ pointed out that there is quasi-nesting between the

electron pockets along $\boldsymbol{q} = (\pi\ 0.625\pi\ 0)$,[1] creating the ridges in Fig. 5.1 (a). These maxima are considerably shifted from the position of the nesting peak in the iron arsenide compounds marked by the arrow. The pairing symmetry has been evaluated within the fluctuation exchange approximation and an instability towards d-wave symmetry was found [3]. This result would impose a sign-change of the SC order parameter for neighboring electron pockets, whose contours are connected by $\boldsymbol{q} = (\pi\ 0.625\pi\ 0)$. In this scenario the formation of a resonant mode at $\boldsymbol{q}$ would be enabled [see Fig. 5.1 (b)] [3].[2]

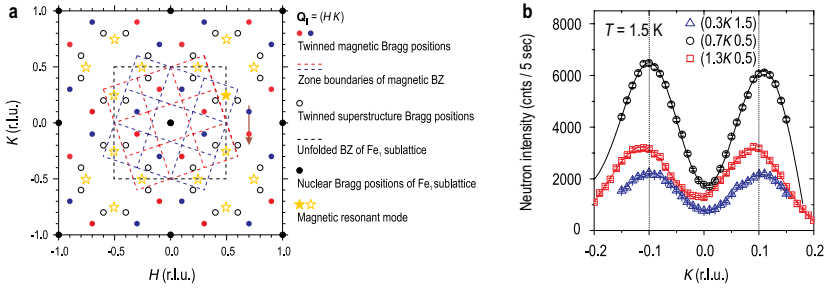

Fig. 5.2: (a) The in-plane projection of the twinned magnetic (red and blue) and nuclear Bragg peak positions (circles) arising from the block-AFM order and the $\sqrt{5} \times \sqrt{5}$ Fe-vacancy superstructure, respectively. The blue and red dots denote the magnetic superstructure Bragg reflections for left and right twin domains, respectively. The dashed lines mark the corresponding magnetic BZ boundaries. **(b)** Elastic scans (along the K direction) through a pair of magnetic Bragg peaks, measured at $T = 1.5$ K, with the two peaks belonging to different twins. The data have been measured at IN8 (ILL, Grenoble) and are published in Ref. 338.

5.2 Report of the magnetic resonant mode in the superconducting phase of $Rb_{0.8}Fe_{1.6}Se_2$

The experimental confirmation of the resonant mode is rendered somewhat complicated because of the presence of the vacancy ordered and strongly antiferromagnetic $Rb_2Fe_4Se_5$ phase, which is mesoscopically separated from the superconducting (SC)

[1] The coordinates are given in '2π' notation in line with Ref. 3. But the notation in this thesis adopts generally the Miller index convention, which drops the 2π-factor.

[2] It should be noted that any sign-changing order parameter would create a resonant mode. Thus, its observation would refute proposals of s^{++} symmetry for the order parameter [337].

phase. The $\sqrt{5} \times \sqrt{5}$ block-AFM order in $Rb_2Fe_4Se_5$ gives rise to Bragg peaks at[3]

$$\boldsymbol{Q}_{\mathrm{AFM,l}} = (\frac{1}{10}\ \frac{3}{10}\ \frac{1}{2})$$
$$\boldsymbol{Q}_{\mathrm{AFM,r}} = (\frac{3}{10}\ \frac{1}{10}\ \frac{1}{2})$$

where the additional subscript denotes the twin with either left or right chirality [193]. The iron vacancy ordering creates superstructure peaks at

$$\boldsymbol{Q}_{\mathrm{v}} = (\frac{4}{10}\ \frac{2}{10}\ 0)$$

The in-plane projection of all superstructure peaks in reciprocal space are schematically shown in Fig. 5.2 (a).[4] The magnetic superstructure peaks were confirmed to be present in the $Rb_{0.8}Fe_{1.6}Se_2$ sample used in this study,[5] as shown in Fig. 5.2. Moreover, the equal intensity for both peaks at $\boldsymbol{Q}_{\mathrm{AFM,l}}$ and at $\boldsymbol{Q}_{\mathrm{AFM,r}}$ implies an equal population of the two twins.

However, goal of the study was to look for spin fluctuations originating from the superconducting phase. The spectra at the commensurate positions $\boldsymbol{Q} = (\frac{1}{2}\ \frac{1}{2}\ 0)$ and $\boldsymbol{Q} = (\frac{1}{2}\ 0\ 0)$, with the latter being the wave vector of the resonant mode in the iron-based superconductors, did not exhibit a resonance peak. Finally, the spectrum at the theoretically proposed wave vector $\boldsymbol{q} = (0.5\ 0.312\ 0.5)$[6] showed an enhancement of intensity around $E = 14\,\mathrm{meV}$. Scanning along $(\frac{1}{2}\ K\ \frac{1}{2})$ at $E = 14\,\mathrm{meV}$ in the normal state revealed a corresponding peak, centered close to $K = 0.25$ in Fig. 5.3 (a), which gets enhanced significantly upon entering the superconducting state. The raw intensity at the peak maximum shows an order-parameter-like temperature dependence below T_c [see Fig. 5.3 (b)]. This not only proofs that the mode originates from the superconducting phase, but also that it can be identified with the predicted resonant mode. In the next steps its energy and reciprocal-space structure were investigated. Fig. 5.3 (d1) shows the energy dependence of the raw INS intensity at $\boldsymbol{Q}_r = (\frac{1}{2}\ \frac{1}{4}\ \frac{1}{2})$ for the normal state and the SC state. Unfortunately, no clear peak is visible, and only by subtracting the normal-state spectrum from the SC-state spectrum produces a peak at $E = 14\,\mathrm{meV}$ that corresponds to the resonant intensity. Neither the energy nor the amplitude of the resonance peak, shown for $L = 1$ and $L = 0.5$ in panel (d2) shows any notable L-dependence beyond the uncertainty of the fit. Moreover, the resonant intensity as a function of the out-of-plane component L, shown in panel (c2), can be described solely

[3] Note that the notation refers to the iron sublattice unit cell.

[4] The AFM Bragg peaks have a out-of-plane component $L = 0.5, 1.5, \ldots$ because of the antiferromagnetic coupling along the $\boldsymbol{c}^*$ direction.

[5] The vacancy superstructure peaks were also observed (not shown).

[6] A nonzero out-of-plane component $L = 0.5$, instead of the theoretical $L = 0$ [3], was chosen for technical reasons.

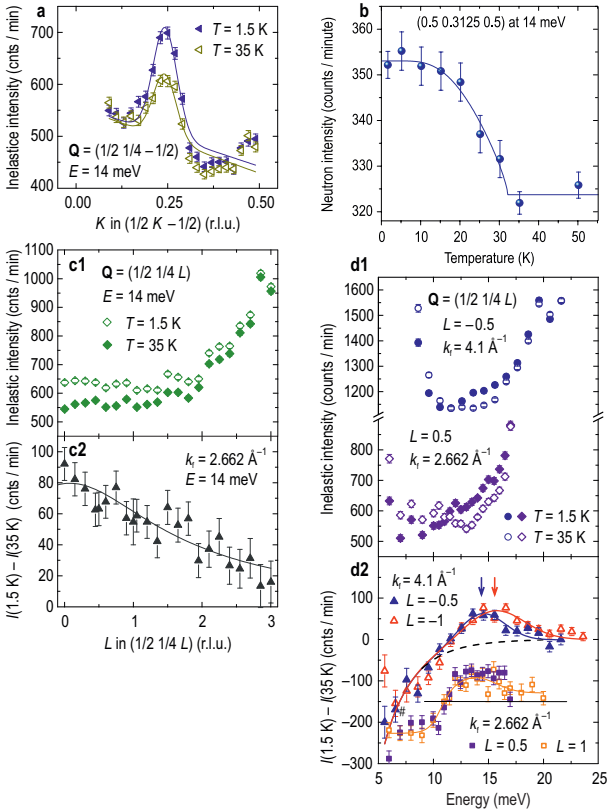

Fig. 5.3: Inelastic neutron scattering data on $Rb_{0.8}Fe_{1.6}Se_2$, collected at IN8, ILL, Grenoble. **(a)** Longitudinal momentum scans through $\boldsymbol{Q}_r = (\frac{1}{2}\ \frac{1}{4}\ \overline{\frac{1}{2}})$ in the normal state at $T = 35$ K and in the SC state at 1.5 K, both at $E = 14$ meV. **(b)** Temperature dependence of the raw INS intensity at $E = 14$ meV, close to the resonant mode wave vector at $\boldsymbol{q} = (0.5\ 0.312\ 0.5)$. **(c1)** L-dependence of the intensity at $E = 14$ meV along $\boldsymbol{Q}_r = (\frac{1}{2}\ \frac{1}{4}\ L)$ at the same temperatures. **(c2)** The difference of the two scans, fitted to the Fe^{2+} magnetic form factor (solid line). **(d1)** Energy scans at the resonance position, measured at $L = 0.5$ for two different final wave vectors $k_f = 4.1$ Å^{-1} and $k_f = 2.662$ Å^{-1} in the normal and in the SC states. **(d2)** Difference of the SC- and normal-state intensities at integer and half-integer L. The solid line through the data points for $k_f = 4.1$ Å^{-1} is a fit with a Gaussian function superposed on the difference of the Bose factors for both temperatures (dashed line). The data points, taken with $k_f = 2.662$ Å^{-1}, are shifted down by 150 counts for clarity. The figures have been similarly published in Ref. 338 and 339.

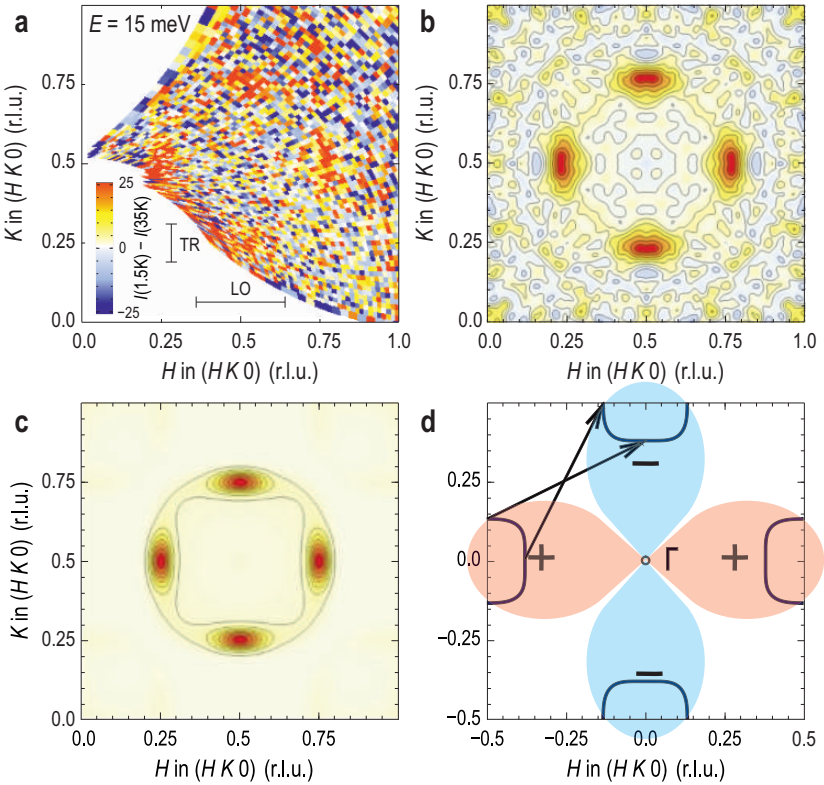

Fig. 5.4: **(a)** Color map of the reciprocal space, showing the intensity difference between the SC and normal states at $E = 15$ meV, measured by the *FlatCone* detector configuration at IN8 (ILL, Grenoble). **(b)** The same map as in (a), rebinned on a 81×81 grid, symmetrized with respect to the mirror planes and smoothed using a Gaussian filter with 1 pixel standard deviation. **(c)** The difference of the calculated imaginary parts of the dynamic spin susceptibility for the SC and normal states, $\chi''_{\mathrm{SC}}(\boldsymbol{Q}, \omega_{\mathrm{res}}) - \chi''_{\mathrm{n}}(\boldsymbol{Q}, \omega_{\mathrm{res}})$, taken at the resonance energy. An isotropic Gaussian broadening with a standard deviation of 0.02 r.l.u. has been applied to mimic the experimental resolution. **(d)** The corresponding Fermi surface in the $(H\,K\,0)$ plane, calculated for a doping level of 0.18 electrons/Fe. The black arrows are the in-plane nesting vectors responsible for the resonance peaks in $Rb_{0.8}Fe_{1.6}Se_2$. Overlayed is the $d_{x^2-y^2}$ wave function for the SC order parameter, which was proposed by Maier *et al.* [3]. The figures have been similarly published in Ref. 339.

by the $\boldsymbol{Q}$ dependence of the Fe^{2+} magnetic form factor, revealing a 2D structure for the signal.[7]

Based on the quasi-2D character of the magnetic intensity, the resonant enhancement at $E = 15$ meV has been mapped out in the $(H\,K\,0)$ scattering plane by means of the *FlatCone* multianalyzer. Figure 5.4 (a) shows the difference of the intensity maps between SC and normal states, covering a section around the BZ corner [$\boldsymbol{Q} = (\frac{1}{2}\ \frac{1}{2})$]. The resonant intensity at all four symmetric positions equivalent to $(\frac{1}{2}\ \frac{1}{4}\ 0)$ can be observed. The contrast of these features can be improved after smoothing and symmetrization with respect to the mirror planes,[8] as shown in Fig. 5.4 (b). One sees that the in-plane shape of the resonant intensity takes an elliptical form, elongated transversely with respect to the vector connecting it to $(\frac{1}{2}\ \frac{1}{2}\ 0)$. The ratio of the peak widths in the transverse and longitudinal directions results in an aspect ratio of 2.1 for the resonance feature.

Qualitatively, the results shown here provide valuable information on the possible chemical structure of the superconducting phase. The in-plane structure, displayed in Fig. 5.4 (b), strictly follows the unit cell of the iron-sublattice, where all iron atoms are filled. Any presence of the vacancy ordering in the SC phase should lead to a strong reconstruction of the signal, with respect to a smaller Brillouin zone. Recent STM measurements also reported a multitude of superstructures, underlying the SC phase: $\sqrt{5}\times\sqrt{2}$, $\sqrt{2}\times\sqrt{2}$ and $\sqrt{8}\times\sqrt{10}$ [199, 203, 340].[9] Even if these structures have an electronic origin, they do not influence the spin dynamics of the system. Therefore, the reciprocal-space structure established here is consistent with the NMR measurements on the same samples [16], which proved the absence of iron vacancies.

In fact, the wave vector of the resonant mode at $\boldsymbol{Q}_r = (\frac{1}{2}\ \frac{1}{4}\ 0)$ is very close to the position $\boldsymbol{q} = (0.5\ 0.312\ 0.5)$ predicted by Maier *et al.*, which has been derived for a AFe_2Se_2 superconductor [3]. Repeating the same analysis can reproduce the experimentally determined in-plane shape of the resonant mode after rigidly shifting the chemical potential. The calculated imaginary part of the RPA-derived susceptibility $\mathrm{Im}\,\chi^{\mathrm{RPA}}(\boldsymbol{q},\omega)$ is shown in Fig. 5.4 (c). The wave vector of the resonant mode $\boldsymbol{Q}_r = (\frac{1}{2}\ \frac{1}{4}\ 0)$ [arrows in Fig. 5.4 (d)] connects the flat parts of the neighboring electron pockets. In principal, shrinking or expanding the pockets by adjusting the doping level can change the K coordinate to any arbitrary and incommensurate value $\boldsymbol{Q}_r = (\frac{1}{2}\ \frac{1}{4} + \delta\ 0)$. The commensurability of the experimentally determined value $K = \frac{1}{4}$ must then be a coincidence.[10]

The pure spin-flip scattering of the resonance intensity was assured by polarized neutron scattering experiments, shown in the Appendix A.1.1. Furthermore, the interpocket scattering is also the source for the normal-state intensity at $\boldsymbol{Q}_r = (\frac{1}{2}\ \frac{1}{4}\ 0)$

[7] This fact is consistent with ARPES measurements, reporting a weak k_z-dispersion of both the electron band and the SC gap [4].

[8] both in order to decrease statistical noise.

[9] It has been argued they are related to charge ordering [203, 340].

[10] The required doping level of ~ 0.18 electrons/Fe is in reasonable agreement with the independent estimate of 0.15 electrons/Fe from the NMR study [16].

as provided by Fig. 5.3 (a). This intensity was found to decrease towards higher temperatures [see Fig. 5.5 (a) and (b)] and is almost indistinguishable at $T = 193$ K. This dismisses the possibility that the peak at $\boldsymbol{Q}_r = (\frac{1}{2}\ \frac{1}{4}\ 0)$ might be a tail of a spin wave arising from the block-AFM order of the $Rb_2Fe_4Se_5$ phase, which vanishes at much higher temperatures $T_N = 527$ K [64].

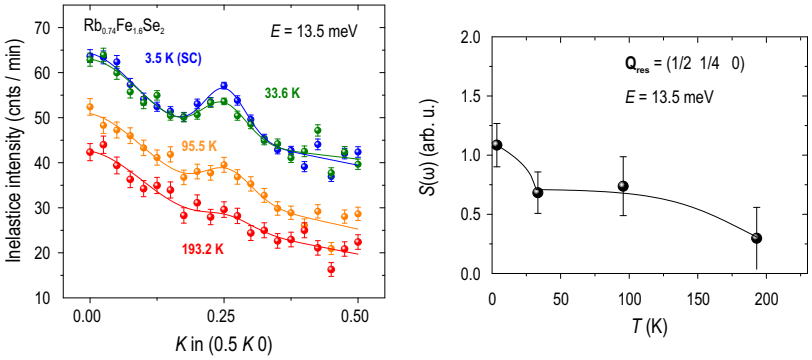

Fig. 5.5: Temperature dependence of the normal-state spin fluctuations. The measurements were performed on a $Rb_{0.74}Fe_{1.6}Se_2$ sample at the 2T spectrometer (Laboratoire Léon Brillouin, Saclay) with $k_f = 2.662$ Å^{-1}. **(a)** Momentum scans along $\boldsymbol{Q}_r = (\frac{1}{2}\ K\ 0)$ at $E = 13.5$ meV for different temperatures. The peak in the middle at $K = 0.25$ is the resonant mode/paramagnon. The curves for $T = 95.5$ K and $T = 193.2$ K have been shifted for clarity. **(b)** Temperature dependence of the spin fluctuations at $\boldsymbol{Q}_r = (\frac{1}{2}\ \frac{1}{4}\ 0)$. The intensity corresponds to the area of the peak in panel (a).

5.3 Conformity of spin fluctuations in alkali-metal iron selenide superconductors

The study of spin excitations in $Rb_{0.8}Fe_{1.6}Se_2$ verified the existence of a resonant mode in the $A_xFe_{2-y}Se_2$ family of superconductors. However, so far only the spectrum of the *resonant* intensity was obtained by subtracting the normal-state intensity from the intensity in the SC state. In order to acquire a measure of intensity on the absolute scale, a time-of-flight (TOF) neutron spectroscopy experiment was performed on a $K_{0.77}Fe_{1.85}Se_2$ sample.[11] In Figs. 5.6 (a) and (b) the in-plane wave vector dependence of the TOF scattering intensity, projected on the $(H\,K\,0)$ plane and integrated over the energy range of $\hbar\omega = (14 \pm 3)$ meV for the SC and normal states, is presented. The strong excitations emerging from $(0.3, \pm 0.1)$, $(0.7, \pm 0.1)$ and equivalent wave vectors are spin wave excitations centered at the magnetic Bragg peak positions

[11] The intensity was normalized to units of the differential cross section $d^2\sigma/d\Omega d\omega$ (mb meV^{-1}sr^{-1}f.u.$^{-1}$) by means of a vanadium standard.

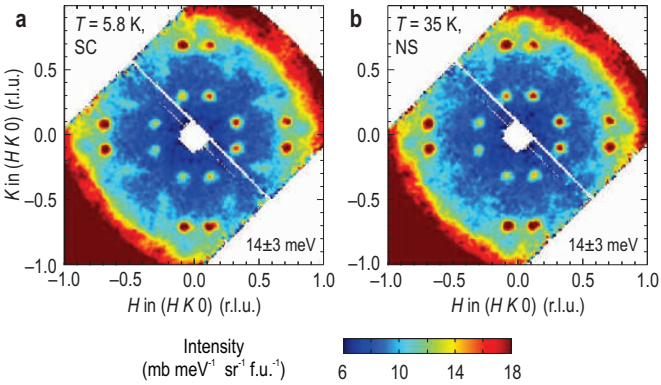

Fig. 5.6: In-plane wave vector dependence of the spin excitations in $K_xFe_{2-y}Se_2$, integrated over the energy range of $\hbar\omega = (14 \pm 3)$ meV, obtained with an incident neutron energy of $E_i = 35$ meV ($k_i = 4.1$ Å^{-1}) in the **(a)** SC state at $T = 5.8$ K and **(b)** normal state at $T = 35$ K. The out-of-plane momentum at $\boldsymbol{Q}_r = (\frac{1}{2}\ \frac{1}{4}\ L)$ is $L = 1.33$. The experiment was carried out at the MERLIN TOF chopper spectrometer (Rutherford-Appleton Laboratory, Oxford). The figure has been similarly published in Ref. 341.

of the insulating/antiferromagnetic phase $K_2Fe_4Se_5$. The weaker feature, centered at $\boldsymbol{Q}_r = (\frac{1}{2}\ \frac{1}{4})$, $(\frac{1}{4}\ \frac{1}{2})$ in Fig. 5.6 (a) and taking the shape of an ellipse, is the resonant mode. In the normal state the intensity is significantly reduced, but still discernible. Figure 5.7 (a) shows the spectra in the SC and normal states.[12] Here, the cross section has been converted into the $\boldsymbol{Q}$-averaged imaginary part of the spin susceptibility $\chi''(\omega)$, after correcting for the Bose factor and the Fe^{2+} magnetic form factor.[13] A peak is visible around $\hbar\omega_r = 14$ meV, which coincides with the energy found for the resonant mode in $Rb_xFe_{2-y}Se_2$. This excitation forms on top of a broad pre-existing normal-state response measured at $T = 35$ K.[14] This peak is created by depleting the low-energy spectral weight as observed in the related iron-based superconductors [125, 139, 143]. Contrary to expectations, the SC spectrum in Fig. 5.7 (a) does not show the full suppression to zero intensity below the resonance energy $E < \hbar\omega_r$, but rather a shoulder or a plateau, which reaches down to 5 meV.[15] Apparently a low-energy (LE) excitation, centered at 7.5 meV, overlays the spin-gap. However, as shown in the Appendix, this additional feature is not magnetic and will not be discussed further. This contamination

[12] The spectrum was obtained by integrating over the region of the ellipse at $H = (0.5 \pm 0.1)$ and $K = (0.25 \pm 0.05)$ and subtracting the background intensity *vs.* energy, which was assessed at $\boldsymbol{Q} = (0.55\ 0.07)$.

[13] Here the averaging is performed by normalizing the total spectral weight, integrated over four resonant peaks at symmetrically equivalent positions, in the unfolded Brillouin zone by the total Brillouin zone area.

[14] The normal-state spectrum in Fig. 5.7 (a) was fitted with the quasielastic lineshape, which describes the spin dynamics for nearly antiferromagnetic metals (see Moriya formula Eq. (3.50)).

[15] Even lower energies $E < 5$ meV were not accessible here because of the strong contamination from incoherent scattering centered at the elastic line.

seems absent in $Rb_{0.8}Fe_{1.6}Se_2$. A reinvestigation of the full spectrum, covering also lower energies, will be presented in the next chapter.

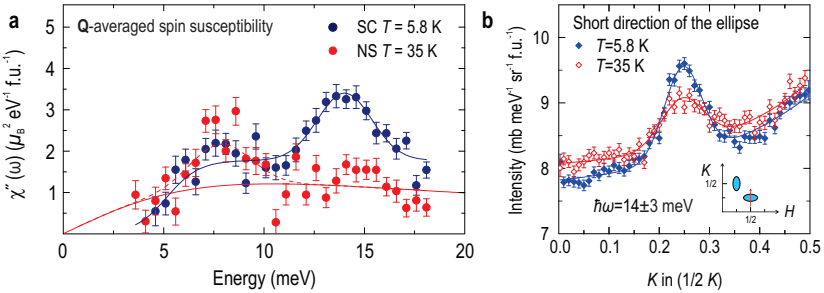

Fig. 5.7: (a) Q-averaged dynamical spin susceptibility $\chi''(\omega)$ of the superconducting phase, in the SC (T = 5.8 K) and normal (T = 35 K) states. **(b)** Momentum cuts through the resonance peak and the corresponding normal-state profile at $\hbar\omega = (14 \pm 3)$ meV along the short direction of its cross section $\triangleq (\frac{1}{2}\,K)$. The figures have been similarly published in Ref. 341.

As discussed for $Rb_{0.8}Fe_{1.6}Se_2$, the K-coordinate of the resonant mode is a direct measure of the electron pocket size, which is determined by the iron valence. Figure 5.7 (b) shows a cut through the resonant mode along $(\frac{1}{2}\,K)$. The resonance peak is situated at $K = (0.247 \pm 0.002)$, i.e. almost perfectly commensurate within the experimental uncertainty. This value almost equals the value of $K = (0.244 \pm 0.002)$ found for $Rb_{0.8}Fe_{1.6}Se_2$. Thus, it seems that the doping level of the superconducting phase in the $A_xFe_{2-y}Se_2$ compounds is pinned to a certain global value (0.18 electrons/Fe as estimated for the $Rb_{0.8}Fe_{1.6}Se_2$ sample). If there were a variation of doping then an additional broadening of the resonance peak along $(\frac{1}{2}\,K)$ should be expected for the $K_{0.77}Fe_{1.85}Se_2$ sample, since it is an assemblage from batches with different composition. However, this broadening is absent, as inferred from the FWHM of the peak in Fig. 5.7 (b). In this respect it is worthwhile to mention that a resonant peak has been observed close to $K = 0.25$ in $Cs_{0.8}Fe_{1.9}Se_2$ [342], which corroborates the conclusion of a unique superconducting phase in all alkali-metal iron selenide superconductors.

A unique SC phase is in line with the observation of an invariable T_c for all superconducting $A_xFe_{2-y}Se_2$ compounds [64, 178]. This stands in contrast to the iron arsenides, where a dome-like variation of T_c in dependence of the charge doping is observed, which is also accompanied by an evolving Fermi surface [101, 104]. Therefore, the picture that the FeSe122 family constitutes a second dome on the strong electron-doped side [343] is not fully correct. Yet, the FeSe122 compounds manifest a qualitative different Fermi surface, which in the FeAs compounds could be accessed only by strong charge doping. The latter approach is not feasible because of the introduced chemical disorder, which is detrimental to superconductivity.

The chemical structure of the SC phase is not fully established yet, since it is embedded in the coexisting $A_2Fe_4Se_5$ phase, which makes crystallographic refinement difficult. It appears that the $A_2Fe_4Se_5$ matrix does not only stabilize the SC phase, but also facilitates one particular structure that realizes the unique superconducting phase. Since the experimental studies suggest the absence of Fe-vacancies (in a $A_xFe_2Se_2$ composition) for the SC phase, it can be conceived that the alkali-metal atoms may be ordered in the *ab*-plane [198], so that $x = 0.3$ is naturally selected [16]. Understanding the microstructure of the SC phase is important in the light that the intrinsic doping level determines the nesting vector to be at a commensurate wave vector $\boldsymbol{Q}_r = (\frac{1}{2}\ \frac{1}{4}\ 0)$. It would be interesting to investigate, whether the nesting vector can be tuned away from $\boldsymbol{Q}_r$ upon further charge doping and how the T_c would react to this. Such a study would elucidate the question, whether a commensurate nesting is an important ingredient for the high-T_c superconductivity in the iron-based compounds.

5.4 The full spin-fluctuation spectrum of $A_xFe_{2-y}Se_2$ superconductors

Determining the full spin-fluctuation spectrum $S(\omega)$ at $\boldsymbol{Q}_r = (\frac{1}{2}\ \frac{1}{4}\ 0)$ was not possible previously because of a contamination by a phonon mode in the spin gap region. In a second approach the intensity was determined by momentum scans along $(\frac{1}{2}\ K\ L)$, which enable to extract the magnetic intensity at the center $K = \frac{1}{4}$ reliably, by fits to a Gaussian lineshape. In order to avoid contaminations from phonons the L-coordinate was left free to choose. This does not change the result, since the signal does not depend on the out-of-plane wave vector q_z. The experiments were performed on several spectrometers on both the $Rb_{0.8}Fe_{1.6}Se_2$ and the $K_{0.77}Fe_{1.85}Se_2$ samples. Most importantly, it was possible to measure the response in the low-energy range $E < 6\,\text{meV}$ by means of cold neutrons ($k_f = 1.55\,\text{Å}^{-1}$). Figure 5.8 (a) shows the amplitude of the signal *vs.* energy for both the normal state (at $T = 35\,\text{K}$) and the superconducting state (at $T = 1.5\,\text{K}$). The corresponding data points for both samples agree within statistical certainty, which justifies the combined presentation in one plot. The spectrum confirms the resonant peak at $\hbar\omega_r = 14\,\text{meV}$. In Fig. 5.8 (b) only the resonant intensity is plotted, which was obtained from the difference between the momentum scans in the normal and in the SC state at each energy. There are new details that have not been resolved previously.

- The resonance peak has a very sharp edge towards low energies, which defines a clear boundary at $\Delta_s = (11.1 \pm 0.07)\,\text{meV}$ between the spin gap and the resonance peak. The width of the edge can be estimated to $\delta\Delta_s \approx 2.5\,\text{meV}$, which is much smaller than the one observed for pnictides ($\delta\Delta_s = 6.5\,\text{meV}$ for optimally doped $Ba(Fe_{1-x}Co_x)_2As_2$ [139] and $Ba_{1-x}K_xFe_2As_2$ [142]). This could be explained by the weak chemical disorder present in the $A_xFe_2Se_2$-type SC phase due the absence of any dopants and iron vacancies. On the high energy side the resonance

peak shows a rather extended tail [HWHM= (5.2 ± 0.8) meV], which can be explained by the onset of particle-hole scattering at the gap edge of $2\Delta \approx 20.6$ meV, determined by ARPES [4].

- The spin gap region $E < \Delta_s$ is completely depleted of intensity in the SC state, in line with the theoretical expectation. The points that are above the baseline might be contaminated by a phonon. Such contamination is canceled out in the difference between SC and normal-state intensity in Fig. 5.8 (b).

- Benefitting from the conversion into absolute units in the TOF experiment, the spectral weight of the resonance peak, which is a measure of the fluctuating moment, can be estimated to $\int(\chi''_{SC} - \chi''_{NS})d\omega = (0.011 \pm 0.003)\mu_B^2$/f.u. This value compares with the one observed in optimally doped $Ba(Fe_{1-x}Co_x)_2As_2$ [125, 139]. However, taking into account a volume fraction of only 20% for the SC phase puts the result very close to the resonant spectral weight of $0.069\,\mu_B^2$/f.u., found in underdoped $YBa_2Cu_3O_{6+x}$ [335].

- In the normal state the scattering function is monotonically decreasing towards lower energies. No normal-state intensity could be detected in the momentum scan at $E = 1$ meV. Thus, it is possible that it even reaches zero at lowest energies, as suggested by the dashed line in Fig. 5.8 (a).[16] Such low-energy suppression of the normal-state spin-fluctuation spectrum is a familiar phenomenon in underdoped cuprates (e.g. $YBa_2Cu_3O_{6+x}$ at $x = 0.6$ [344]). It is correlated with the emergence of a pseudogap below T^*. However, it is not observed in the iron arsenides, where $S(\boldsymbol{Q}_{AFM}, \omega)$ stays constant *vs.* energy [126, 139, 162].

The last property for the FeSe122 agrees with the absence of an increase in the NMR spin-lattice relaxation rate (SLRR) above T_c [16, 185–190], which probes the spin fluctuations in the corresponding energy range. Instead, the behavior of the SLRR *vs.* temperature in the normal state has been attributed to a pseudogap with a size of $\Delta/k_B \sim 435$ K [189]. It has been argued that the alkali-metal iron selenide superconductors are stronger correlated than the iron arsenide superconductors, being close to a Mott transition [52, 345, 346], which is based on the observation of an orbital-selective Mott phase by ARPES [8] and optical spectroscopy [347]. The former study observed a strongly renormalized d_{xy} band at the $X(\frac{1}{2}\ 0)$ point, which quickly loses spectral weight upon heating above 100 K, while the itinerant d_{yz} band remains [8]. The second study similarly found an increase in the optical conductivity below $T_{met} = 90$ K, which reaches its maximum at $T_{gap} = 61$ K [347]. For lower temperatures the response is suppressed for energies smaller than 3.2 meV [347]. This could be related to a precursor of the superconducting gap, which may explain the suppression of the low-energy spin

[16] The possibility that the low-energy spin fluctuations become incommensurate along $(\frac{1}{2} \pm \delta, \frac{1}{4})$ or along $(\frac{1}{2}, \frac{1}{4} \pm \delta)$ was excluded by means of the TOF data

[17] In the IN8 experiment, using $k_f = 4.1$ Å^{-1}, a $(H\ H/2\ L)$ scattering plane was chosen.

fluctuations in the normal state. In order to confirm this scenario an investigation on how the spectrum evolves across $T_{met} = 90\,K$ and $T_{gap} = 61\,K$ is required.

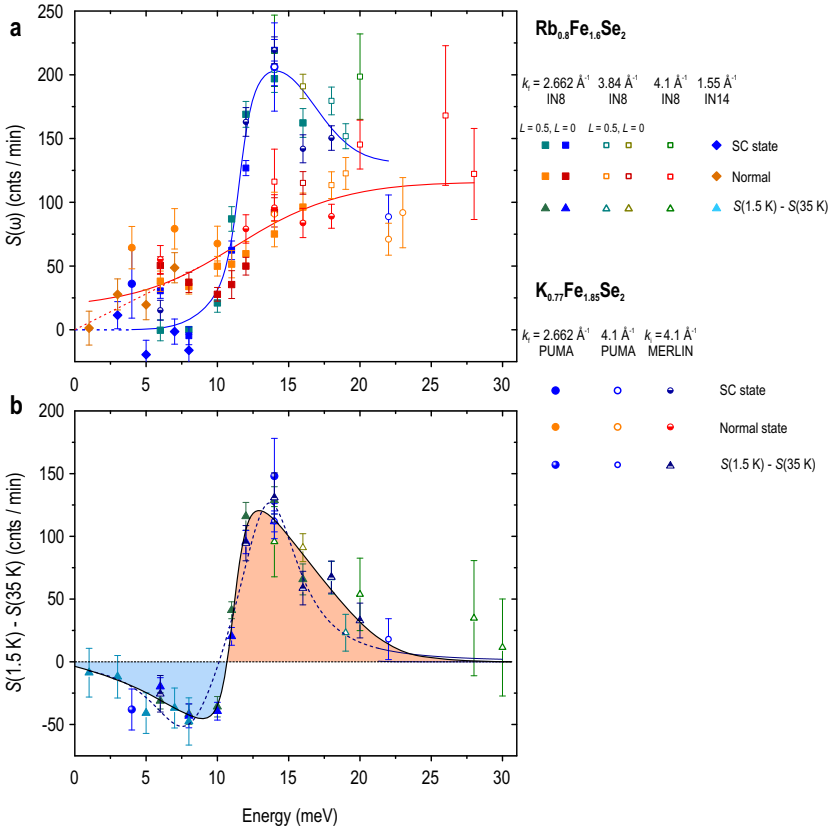

Fig. 5.8: **(a)** Amplitude of the SC and normal-state peak *vs.* energy at $\boldsymbol{Q}_r = (\frac{1}{2}\ \frac{1}{4})$, determined from Gaussian fits to the momentum scans along $\boldsymbol{Q}_r = (\frac{1}{2}\ K)$. The data, which were obtained from the two different samples, $Rb_{0.8}Fe_{1.6}Se_2$ and $K_{0.77}Fe_{1.85}Se_2$, are shown on the same plot. Moreover, the symbol's shape and color distinguishes individual experiments, performed at the spectrometers given in the legend. In the IN8 experiment, the out-of-plane component $L = 0.5$, beside $L = 0$, was chosen to enable higher energy transfers.[17] **(b)** Difference in intensity *vs.* energy between the SC and the normal state, $S(1.5\,\mathrm{K}) - S(35\,\mathrm{K})$. The data points are determined from Gaussian fits to the resulting momentum scan, after subtracting the normal-state intensity from the SC-state intensity. The dashed line is a fit with two Lorentzians peaks, which approximate the spin gap region and the resonance peak region. All solid lines in (a) and (b) are guides to the eyes.

6 Neutron scattering studies on CeB_6

6.1 Temperature and field dependence of the AFM and AFQ order parameters in $Ce_{1-x}La_xB_6$

6.1.1 Observation of a zero-field SDW order parameter in $Ce_{1-x}La_xB_6$

The ordering of quadrupoles in zero magnetic field along $\boldsymbol{q}_{\mathrm{AFQ}} = R(\frac{1}{2}\,\frac{1}{2}\,\frac{1}{2})$ in phase II should be hidden to the neutron scattering probe, since the neutrons can only scatter from time-reversal symmetry breaking fields [233]. Dipolar spin ordering on top of the AFQ-pattern can only be induced in magnetic field. Surprisingly, a small intensity was detected at $\boldsymbol{q}_{\mathrm{AFQ}}$ in *zero field*, which appears below $T \approx 7\,\mathrm{K}$ [283]. The scattering is mainly diffusive with a correlation length of only $\xi \sim 10\,\text{Å}$ [283]. It correlates with the onset of the antiferromagnetic phase (phase III) at T_{N}, showing a strong decrease in its width in momentum space [283]. The intensity is very weak, and the estimated moment is an order of magnitude smaller than the AFM moments, ordered along $\boldsymbol{q}_1 = \Sigma(\frac{1}{4}\,\frac{1}{4}\,0)$ and $\boldsymbol{q}_1' = S(\frac{1}{4}\,\frac{1}{4}\,\frac{1}{2})$ [242, 283]. It is also not clear how this intensity is related to the magnetic-field-induced spin modulation at $\boldsymbol{q}_{\mathrm{AFQ}}$ that appears below T_{Q} [234] in *nonzero* fields.

As part of the thesis the temperature dependencies of the AFQ and AFM order parameters at $\boldsymbol{q}_{\mathrm{AFQ}}$ and $\boldsymbol{q}_1'$, respectively, have been investigated by means of cold neutrons at IN14 (ILL, Grenoble) and by thermal neutrons at IN3 (ILL, Grenoble). In the first experiment the smaller final wave vector of $k_{\mathrm{f}} = 1.4\,\text{Å}^{-1}$ provides a better energy resolution compared to the wave vector $k_{\mathrm{f}} = 2.662\,\text{Å}^{-1}$ of thermal neutrons. The temperature dependence of the Bragg scattering at $R(\frac{1}{2}\,\frac{1}{2}\,\frac{1}{2})$ for CeB_6 is shown in Fig. 6.1 (a). The data points for $k_{\mathrm{f}} = 2.662\,\text{Å}^{-1}$ agree with the literature showing an onset of intensity near $T = 7\,\mathrm{K}$. However, near $T_{\mathrm{Q}} = 3.2\,\mathrm{K}$ another onset can be resolved. Below T_{N} the intensity decreases. Measurements with $k_{\mathrm{f}} = 1.4\,\text{Å}^{-1}$ show a different curve, which has an onset near $T = 3.8\,\mathrm{K}$, and no clear suppression can be resolved below T_{N}. The $(\frac{1}{2}\,\frac{1}{2}\,\frac{1}{2})$-intensity has a comparable $\boldsymbol{Q}$-width as the AFM Bragg peak (not shown), implying a long-range magnetic ordered state already below T_{Q}. The lower curve must then be a superposition of this long-range static magnetic contribution and a diffuse scattering contribution. The latter contribution causes the high temperature tail and is broadly distributed in momentum space. It originates from the quasielastic intensity that has also been detected by μSR [281] and which will be discussed together with the

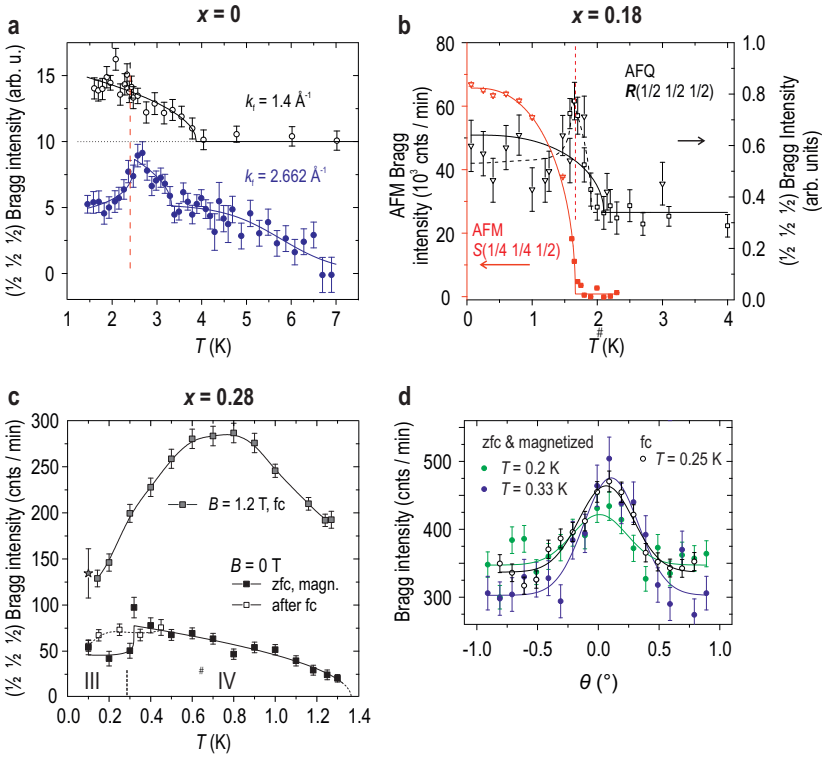

Fig. 6.1: **(a)** Temperature dependence of the $(\frac{1}{2}\ \frac{1}{2}\ \frac{1}{2})$-Bragg peak for CeB_6 in zero field. The data points have been measured by three-point scans for two different final wave vectors: $k_f = 2.66\,\text{Å}^{-1}$ (measured at IN3) and $k_f = 1.4\,\text{Å}^{-1}$ (measured at IN14), with the latter data being shifted by 10 counts for clarity. The dashed line marks T_N, which has been determined from the temperature dependence of the AFM Bragg peaks. **(b)** $Ce_{0.82}La_{0.18}B_6$: Temperature dependence of the AFM-Bragg peak intensity, at $\boldsymbol{q}_1' = S(\frac{1}{4}\ \frac{1}{4}\ \frac{1}{2})$, and the $R(\frac{1}{2}\ \frac{1}{2}\ \frac{1}{2})$-Bragg peak intensity. The intensity corresponds to the area of the Gaussian-fits to the momentum scans through S and R, respectively. **(c)** $Ce_{0.72}La_{0.28}B_6$. Here, the ground state is in phase IV. Shown is the $R(\frac{1}{2}\ \frac{1}{2}\ \frac{1}{2})$-Bragg intensity *vs.* T in zero field after the sample was field-cooled (fc) (hollow points) and zero-field cooled (filled points). In the latter case the sample was cycled in magnetic field, which stabilizes phase III in the ground state. A field-cooled curve in a field of $B = 1.2\,\text{T}$ has also been measured. All lines in panels (a)–(c) are guides to the eyes. **(d)** Selected rocking scans through $(\frac{1}{2}\ \frac{1}{2}\ \frac{1}{2})$ for $x = 0.28$, fitted with a Gaussian. The area of the Gaussian corresponds to the intensity that is plotted in panel (c).

inelastic neutron scattering data in Section 6.2.1.

Table 6.1: Zero-field transition temperatures for $Ce_{1-x}La_xB_6$, determined from the T-dependence of the respective order parameters. T_Q denotes the transition temperature into phase II, T_{IV} denotes the transition temperature into phase IV and T_N denotes the transition into phase III.

x	T_N (K)	T_Q (K) or T_{IV} (K)	2β
0	2.38 ± 0.05	3.9 ± 0.2	0.44 ± 0.02
0.18	1.66 ± 0.05	1.9 ± 0.1	0.43 ± 0.09
0.23	1.2 [a]	1.6 [a](IV)	n.d. [b]
0.28	0.32 ± 0.02 [c]	1.37 ± 0.03 (IV)	–

[a] from specific-heat measurements (M. Brando, MPI-CPFS, Dresden)

[b] n.d. $\hat{=}$ not determined

[c] Phase IV is the ground state, but phase III can be stabilized in zero field after cycling the sample in a high magnetic field.

The intensity of the elastic contribution is quite small, in agreement with Ref. 283, where an associated magnetic moment of $\mu < 0.03\mu_B$ was estimated.

A similar observation was made in $x = 0.18$ doped CeB_6, shown in Fig. 6.1 (b). A weak intensity appears at $R(\frac{1}{2}\,\frac{1}{2}\,\frac{1}{2})$ below $T_Q = (1.9 \pm 0.1)$ K.[1] The antiferromagnetic Bragg intensity (red curve) at $\boldsymbol{q}_1' = S(\frac{1}{4}\,\frac{1}{4}\,\frac{1}{2})$ was detected below $T_N = (1.66 \pm 0.05)$ K. It seems that the $(\frac{1}{2}\,\frac{1}{2}\,\frac{1}{2})$ ordering and the AFM ordering are competing, since the former becomes slightly suppressed below T_N. This resembles the anomalous suppression of the $(\frac{1}{2}\,\frac{1}{2}\,\frac{1}{2})$-intensity $I_{(\frac{1}{2}\,\frac{1}{2}\,\frac{1}{2})}(T)$ for *nonzero* fields at low temperatures, observed in the parent compound [230]. Only here, the suppression appears sharply at T_N.

For the $x = 0.28$ sample the AFQ phase has been replaced by phase IV in zero field. Still a $(\frac{1}{2}\,\frac{1}{2}\,\frac{1}{2})$-Bragg peak can be observed below $T_{IV} = (1.37 \pm 0.03)$ K in Fig. 6.1 (c).[2] No AFM Bragg peak could be observed in zero field, but a remnant zero field magnetic order can be induced by magnetizing the sample in a high magnetic field. Only upon warming the magnetized sample, the $I_{(\frac{1}{2}\,\frac{1}{2}\,\frac{1}{2})}(T)$ curve has a jump to higher intensity at $T_N = (0.32 \pm 0.02)$ K, presumably related to the collapse of the remnant AFM order.[3] Figure 6.1 (c) also shows a temperature scan for a field of $B = 1.2$ T, where phase II is stabilized. Analogous to the observation in the parent compound [230] an anomalous suppression of $I_{(\frac{1}{2}\,\frac{1}{2}\,\frac{1}{2})}$ towards low temperatures is shown.

[1] The intensity for $T > T_Q$ is a contamination related to the second order Bragg scattering from the (1 1 1) reflex.

[2] This Bragg peak has also been previously reported for $x = 0.3$ [288].

[3] When field cooling the sample and then measuring the temperature dependence, the jump is absent.

For the $x = 0.28$ sample the $I_{(\frac{1}{2}\,\frac{1}{2}\,\frac{1}{2})}(T)$ intensity can be associated with long-range order, since the FWHM of the corresponding rocking scans [shown in Fig. 6.1 (d)] is $(0.53 \pm 0.016)^\circ$, which equals the value of $(0.54 \pm 0.008)^\circ$ observed for the structural Bragg peaks $(0\,0\,1)$ and $(1\,1\,0)$. In Ref. 288 octupolar order in phase IV with $\boldsymbol{q}_{\mathrm{IV}} = (\frac{1}{2}\,\frac{1}{2}\,\frac{1}{2})$ was proposed. However, as pointed out here the weak $(\frac{1}{2}\,\frac{1}{2}\,\frac{1}{2})$-Bragg peak is not special to phase IV, but is observed in phase II, phase III and phase IV. Therefore, the $(\frac{1}{2}\,\frac{1}{2}\,\frac{1}{2})$-Bragg peak might be related to a spin-density wave (SDW) ordering, as suggested in Ref. 237, which would explain the opening of a charge gap in transport below T_{Q} [237]. The suppression of its amplitude upon entering the antiferromagnetic phase III might then be a result of the competition about the same density of states, since another charge gap opens below T_{N} [264]. Small moment antiferromagnetism is occasionally observed among heavy-fermion compounds, such as $CeRu_2Si_2$ [348], $CeCu_2Si_2$ [314] and UPt_3 [349]. For the former two, a SDW scenario has been put forward to explain the magnetic order, since the ordering of localized moments would constitute much higher moment values.

6.1.2 Field dependence of the SDW and AFQ Bragg peaks in CeB_6

The B-T-phase diagram of CeB_6 has been previously determined by elastic neutron scattering experiments [230, 231, 234]. However, these studies did not detect the weak SDW in zero field. For this reason the magnetic-field dependence of the $(\frac{1}{2}\,\frac{1}{2}\,\frac{1}{2})$ intensity has been reinvestigated and is shown in Fig. 6.2 (a) (green curve). The intensity remains constant up to a field of $B_{\mathrm{Q}} = 1.7\,\mathrm{T}$. Above B_{Q} the intensity grows linearly up to at least $B = 5\,\mathrm{T}$. This confirms the G-type antiferroquadrupolar model, where the application of a magnetic field induces dipoles with the same $\boldsymbol{Q}$-modulations as the AFQ order [226, 246]. However, the linear scaling is an approximation, which is only valid for small fields $B_{\mathrm{Q}} < B < 5\,\mathrm{T}$ as confirmed here. In higher fields the ferromagnetic coupling, induced by the octupolar order, dominates. Though the localized multipolar ordering model may explain the $(\frac{1}{2}\,\frac{1}{2}\,\frac{1}{2})$ intensity for $B > B_{\mathrm{Q}}$, it fails to explain the dependence for $B < B_{\mathrm{Q}}$. Calculations within the mean-field multipolar model expect that a $(\frac{1}{2}\,\frac{1}{2}\,\frac{1}{2})$-moment is induced within phase III, which reverses its direction at B_{Q} [230, 246]. This is clearly not observed. Instead, the $(\frac{1}{2}\,\frac{1}{2}\,\frac{1}{2})$ intensity remains constant *vs.* B and is also not perturbed by the critical field of the AFM phase and phase III$'$ at $B_{\mathrm{c1}} = 1.1\,\mathrm{T}$ and $B_{\mathrm{c2}} = 1.4\,\mathrm{T}$, respectively. This again corroborates the notion that it might be a SDW, formed by itinerant quasiparticles rather than localized f-electrons. The term SDW is henceforth used to distinguish the weak low-field $(\frac{1}{2}\,\frac{1}{2}\,\frac{1}{2})$-intensity from the field-induced spin modulation above B_{Q} related to AFQ order.

A study of the field evolution of phase III is more difficult, since the scattering plane $(H\,H\,L)$ contains only the Bragg peaks $\boldsymbol{q}_1^{xy} = \Sigma^{xy}(\frac{1}{4}\,\frac{1}{4}\,0)$, $\boldsymbol{q}_1'^{xy} = S^{xy}(\frac{1}{4}\,\frac{1}{4}\,\frac{1}{2})$, which belong to the K_{xy} domain and which are quickly suppressed for a field $\boldsymbol{B} \parallel (1\,\bar{1}\,0)$ by

selection as visible in Fig. 6.2 (a).[4] However, recent preliminary measurements, collected at E4 [350], allowed to access the out-of-plane peak $\boldsymbol{q}_1^{zx} = \Sigma^{zx}(0\ \frac{1}{4}\ \frac{1}{4})$ belonging to the K_{zx} domain. First, there is an increase of intensity up to $B_{c1} = 1.1\,\mathrm{T}$ and then an abrupt decrease, reaching zero at $B_{c2} = 1.4\,\mathrm{T}$ [350]. The fields B_{c1} and B_{c2} correspond to the step seen in the magnetization curve [245] and they are delimiting a range that is related to phase III′ [232, 245]. Further studies should investigate, how the size and the direction of the spin changes in phase III′ compared to phase III.[5]

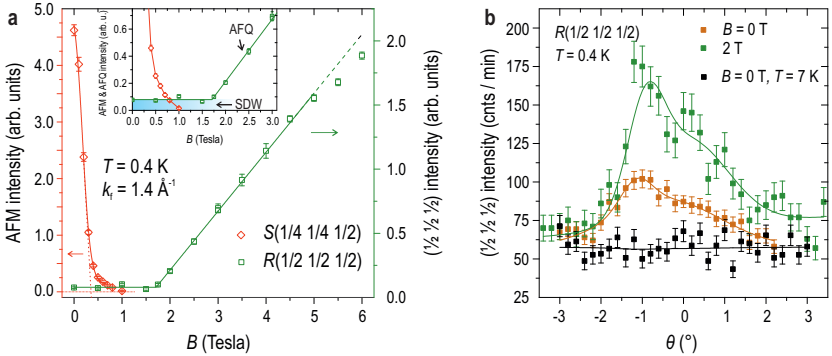

Fig. 6.2: **(a)** Magnetic-field dependence of the AFM Bragg intensity (red), measured at $\boldsymbol{q}_1' = S(\frac{1}{4}\ \frac{1}{4}\ \frac{1}{2})$ and the SDW/AFQ intensity at $\boldsymbol{q}_{\mathrm{AFQ}} = R(\frac{1}{2}\ \frac{1}{2}\ \frac{1}{2})$ at $T = 0.4\,\mathrm{K}$. The inset shows an enlarged view of the low-field region. The data have been obtained at PANDA (FRMII, Garching). **(b)** Rocking scans through $R(\frac{1}{2}\ \frac{1}{2}\ \frac{1}{2})$, representatively shown for $B = 0\,\mathrm{T}$ and $B = 2\,\mathrm{T}$. The non-Gaussian shape of the peak profile is related to the imperfect mosaicity of the sample. The solid lines are guides to the eyes. The rocking scan at $T = 7\,\mathrm{K}$ signals the absence of any Bragg scattering in the paramagnetic state.

6.1.3 The magnetic phase diagram of $Ce_{0.82}La_{0.18}B_6$

The first lanthanum doping level of $x = 0.18$ has been selected, so that it lies close to the doping level $x_{\mathrm{IV}} = 0.2$, where phase IV appears in the phase diagram (see Fig. 2.18) [291]. Elastic neutron studies on single crystals are scarcely available for the lanthanum-doped compounds (see e.g. Ref. 236). Thus, parallel to the measurements of the field dependent spin dynamics it was necessary to map out the phase boundaries in the $B - T$- phase diagram to reach a consistent description. Analogous to CeB_6 Fig. 6.3 (a) shows the magnetic-field dependence of the AFM $[\boldsymbol{q}_1' = S(\frac{1}{4}\ \frac{1}{4}\ \frac{1}{2})]$ and the $(\frac{1}{2}\ \frac{1}{2}\ \frac{1}{2})$ Bragg peak. The AFM Bragg peak is suppressed because of domain

[4] An extrapolated offset field of only $B_{\mathrm{off}} = 0.35\,\mathrm{T}$ for the $\boldsymbol{q}_1'^{xy}$ Bragg peak and a tail extending up to the critical field of $B_c = 1.1\,\mathrm{T}$ speaks in favor of this.

[5] In this respect it would also be crucial to investigate the magnetic structure of a possible phase III″ for the fields $B_{c2} = 1.4\,\mathrm{T} < B < B_Q = 1.7\,\mathrm{T}$. So far, no magnetic Bragg peak seems to be present in this range except for the weak intensity at $(\frac{1}{2}\ \frac{1}{2}\ \frac{1}{2})$.

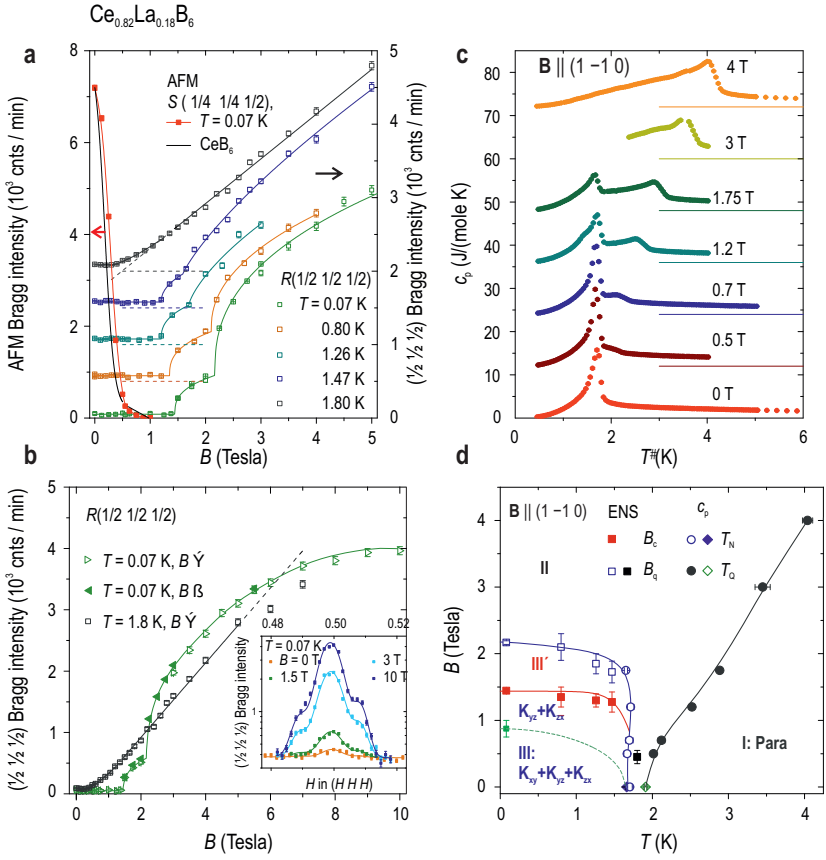

Fig. 6.3: **(a)** Field dependence of the AFM Bragg intensity at $\boldsymbol{q}_1' = S(\frac{1}{4}\ \frac{1}{4}\ \frac{1}{2})$ and the SDW/AFQ intensity at $\boldsymbol{q}_{\mathrm{AFQ}} = R(\frac{1}{2}\ \frac{1}{2}\ \frac{1}{2})$. The latter has been investigated for different temperatures. The intensity was determined by integrating the rocking scans through S and the longitudinal scans through R, respectively. The lines are guides to the eyes. **(b)** Field dependence of the $(\frac{1}{2}\ \frac{1}{2}\ \frac{1}{2})$ intensity up to the highest possible field of $B = 10\,\mathrm{T}$, in the AFM phase at $T = 0.07\,\mathrm{K}$ and in the AFQ phase at $T = 1.8\,\mathrm{K}$. The inset shows selected longitudinal momentum scans through $(\frac{1}{2}\ \frac{1}{2}\ \frac{1}{2})$, fitted with Gaussians. The area of the fit corresponds to the intensity plotted in the main panel. The data in panels (a) and (b) have been measured at IN14 (ILL, Grenoble). **(c)** Temperature dependence of the specific heat in various magnetic fields $\boldsymbol{B} \parallel (1\ \bar{1}\ 0)$. The measurements were provided by the group of R. Kremer (MPI-FKF, Stuttgart). **(d)** $B-T$-phase diagram for $Ce_{0.82}La_{0.18}B_6$, compiled with the transition fields B_c and B_Q [see panel (a)], and the transition temperatures T_N and T_Q [see panel (c)]. The solid lines mark the phase boundaries. The dashed lines marks the transition from a three domain state into a two domain state for the AFM phase, observed by the vanishing of the K_{xy} domain.

selection. The $(\frac{1}{2}\ \frac{1}{2}\ \frac{1}{2})$-intensity *vs.* field, measured for different temperatures, shows a more subtle behavior, compared to CeB_6. First of all the small and constant intensity in low magnetic fields can be related to the SDW as discussed in Section 6.1.1. At $B_c = (1.45 \pm 0.13)$ T the intensity increases in step-like manner. This step coincides with the critical field of the AFM phase.[6] Above B_c the system enters phase III′. Another onset in the $(\frac{1}{2}\ \frac{1}{2}\ \frac{1}{2})$-intensity is observed at $B_Q = (2.17 \pm 0.25)$ T, which marks the transition to phase II. The $(\frac{1}{2}\ \frac{1}{2}\ \frac{1}{2})$ intensity reaches saturation at $B = 10$ T [Fig. 6.3 (b)] in agreement with the theoretical prediction [246]. This supports the viewpoint that it is a fingerprint of the AFQ order, rather than the AFQ order parameter itself.

The field interval of phase III′, delimited by the two steps, decreases with increasing temperature [Fig. 6.3 (b)]. At $T = 1.8$ K, where AFQ order is established in zero field, linear field scaling of the $(\frac{1}{2}\ \frac{1}{2}\ \frac{1}{2})$ intensity is recovered. Thus, the discrete jumps in $I_{(\frac{1}{2}\ \frac{1}{2}\ \frac{1}{2})}$ *vs.* B are property of the AFM phase and could be interpreted as the transitions into a spin-flop phase. However, in contrast to a conventional spin-flop phase, where the spins cant towards the applied field, the spin canting here must be modulated with $\boldsymbol{q} = (\frac{1}{2}\ \frac{1}{2}\ \frac{1}{2})$, giving rise to the observed Bragg peak. Therefore, the Zeeman-term, which induces the $(\frac{1}{2}\ \frac{1}{2}\ \frac{1}{2})$ modulation of the spins on top of the AFQ order, must be already active. This is in contrast with CeB_6, where the stronger antiferromagnetic exchange presumably inhibits the observation of the $(\frac{1}{2}\ \frac{1}{2}\ \frac{1}{2})$-modulation in phase III′.

Further transition points for the $B - T-$ phase diagram have been provided by the measurements of the temperature dependent specific heat $c_p(T)$.[7] As shown in Fig. 6.3 (c), the transition to the AFM phase is signified by a sharp anomaly at T_N in zero field. An anomaly, associated with the AFQ transition, is not visible in zero field, but can be discerned as a shoulder that grows and moves to higher temperature as soon as a magnetic field is applied. The obtained transition temperatures T_N and T_Q *vs.* B as well as the transition fields B_c and B_Q *vs.* T, provided by the neutron scattering data, are plotted in the phase diagram Fig. 6.3 (d). It is similar to the phase diagram of CeB_6, except that the AFM dome is almost rectangular shaped. In fact, it seems that the $T_N(B)$ slightly bends to the right, following $T_Q(B)$, which starts to increase for the same field region. This effect is even more pronounced when phase IV is present in the phase diagram for $x > x_{IV} = 0.2$ [291]. There, phase III bends over phase IV in nonzero fields [291].

6.1.4 The magnetic phase diagram of $Ce_{0.77}La_{0.23}B_6$

The second lanthanum doped sample with $x = 0.23$ lies intermediate between x_{IV} and $x_c = 0.3$. Thus, it still features the AFM phase at low temperatures. The field dependence of the AFM Bragg peak is displayed in Fig. 6.4 (a). It becomes suppressed as

[6] Though the out-of-plane AFM Bragg peaks were not measured in this compound, the assignment of the onset for the $(\frac{1}{2}\ \frac{1}{2}\ \frac{1}{2})$-intensity to B_c is motivated by the similar observation in the $x = 0.28$ sample (see Section 6.1.5).

[7] conducted by the Kremer group in MPI-FKF, Stuttgart

expected from the domain formation. The $(\frac{1}{2}\,\frac{1}{2}\,\frac{1}{2})$ intensity *vs.* B shows similar to the $x = 0.18$ sample a double-step, which provides the boundaries $B_c = (1.50 \pm 0.13)\,\mathrm{T}$ and $B_Q = (2.3 \pm 0.2)\,\mathrm{T}$ of phase III′. However, a new quality is observed concerning the $(\frac{1}{2}\,\frac{1}{2}\,\frac{1}{2})$-intensity. It is suppressed in low fields by a factor of two [see inset Fig. 6.4 (a)]. This observation is supported by the rocking scans through $R(\frac{1}{2}\,\frac{1}{2}\,\frac{1}{2})$ in Fig. 6.4 (b), which show a genuine decrease of intensity upon going from $B = 0\,\mathrm{T}$ to $B = 1.25\,\mathrm{T}$. At B_c the intensity increases because of the induction of the $(\frac{1}{2}\,\frac{1}{2}\,\frac{1}{2})$ spin modulation as previously discussed. Therefore, since the $(\frac{1}{2}\,\frac{1}{2}\,\frac{1}{2})$ Bragg reflection is related to a SDW, the reduction of the amplitude must arise because of the competition with the Zeeman-energy. For lower dopings this intensity was quite robust *vs.* field, but for the $x = 0.23$ sample the SDW must be weakened enough, so that this competition is active already in low fields.[8]

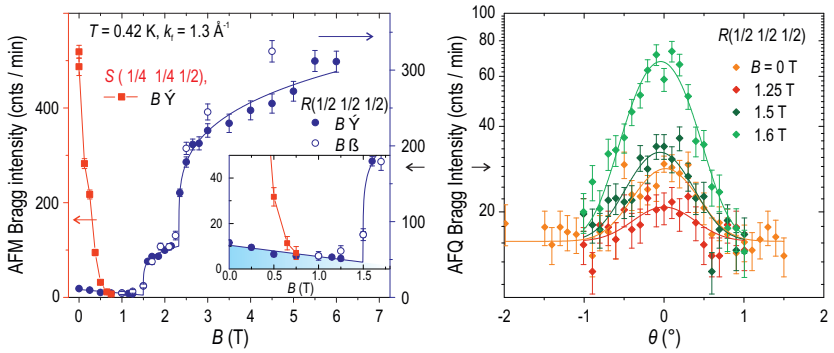

Fig. 6.4: (a) Field dependence of the AFM Bragg intensity at $\boldsymbol{q}_1' = S(\frac{1}{4}\,\frac{1}{4}\,\frac{1}{2})$ and of the SDW/AFQ intensity at $\boldsymbol{q}_{AFQ} = R(\frac{1}{2}\,\frac{1}{2}\,\frac{1}{2})$ for $Ce_{0.77}La_{0.23}B_6$, $T = 0.4\,\mathrm{K}$. The intensity corresponds to the integrated rocking scan through the respective Bragg peak. The inset shows a zoom-in of the low-field data. The $(\frac{1}{2}\,\frac{1}{2}\,\frac{1}{2})$ Bragg intensity has also been checked for hysteresis, when decreasing the field. **(b)** Selected rocking scans through $(\frac{1}{2}\,\frac{1}{2}\,\frac{1}{2})$ in the low magnetic-field regime, fitted with a Gaussian. All data have been obtained at PANDA (FRMII, Garching).

6.1.5 The magnetic phase diagram of $Ce_{0.72}La_{0.28}B_6$

The $Ce_{0.72}La_{0.28}B_6$ sample has a composition close to the QCP at $x_c = 0.3$, where the antiferromagnetic ordering vanishes in zero field [see Fig. 2.18 (a)]. The neutron diffraction experiments were carried out at IN14 (ILL, Grenoble) and at E2 (Helmholtz-Zentrum Berlin). In the ground state ($T = 0.1\,\mathrm{K}$) the AFM Bragg peaks at $\boldsymbol{q}_1^{xy} = \Sigma^{xy}(\frac{1}{4}\,\frac{1}{4}\,0)$ and $\boldsymbol{q}_1'^{xy} = S^{xy}(\frac{1}{4}\,\frac{1}{4}\,\frac{1}{2})$ that originate from the K_{xy} domain are absent and

[8] Irrespective of its interpretation as a SDW, the experimental results here unequivocally point out the completely opposite behavior below and above B_c for the $(\frac{1}{2}\,\frac{1}{2}\,\frac{1}{2})$ intensity.

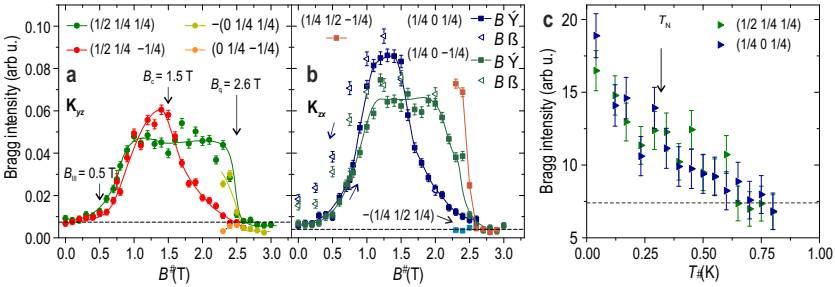

Fig. 6.5: AFM Bragg peaks in $Ce_{0.72}La_{0.28}B_6$. **(a)** Magnetic-field dependence of the out-of-plane Bragg peaks for the K_{yz} domain in $Ce_{0.72}La_{0.28}B_6$. **(b)** Field dependence of the Bragg peaks for the K_{zx} domain. Hollow triangles denote the respective Bragg intensity, measured in decreasing field. **(c)** Temperature dependence of two selected remanent Bragg peaks in zero field after the magnetic field has been cycled. The data have been obtained at the E2 single crystal diffractometer, equipped with a Flatcone detector. All lines are guides to the eyes. The dashed lines indicate the level of the background intensity. It consists mainly of contaminations because of fourth order Bragg scattering from a nuclear reflection.

can not be induced by an applied field along the $(1\,\bar{1}\,0)$ direction. For checking, whether the AFM phase can be induced by magnetic field it is necessary to measure the out-of-plane Bragg peaks [e.g. $S^{yz}(\frac{1}{2}\,\frac{1}{4}\,\frac{1}{4})$ and $S^{zx}(\frac{1}{4}\,\frac{1}{2}\,\frac{1}{4})$], originating from the K_{yz} and the K_{xz} domains, respectively, since these are favored for the magnetic field along $\boldsymbol{B} \parallel (1\,\bar{1}\,0)$.[9] The panels (a) and (b) in Fig. 6.5 are dedicated to K_{yz} and K_{xz}, respectively. These domains, are equivalent for the given magnetic-field configuration. All four Bragg peaks of the $2\boldsymbol{q} - \boldsymbol{q}'$ structure are recovered when applying a magnetic field $B > B_{III} = (0.55 \pm 0.05)$ T. However, there is no sharp onset of intensity, but rather a gradual increase. Saturation is reached for a field of $B_0 = (1.1 \pm 0.1)$ T.

Above $B_c = (1.5 \pm 0.1)$ T a change in magnetic structure occurs, since the pairs $S_2^{yz}(\frac{1}{2}\,\frac{1}{4}\,\overline{\frac{1}{4}})$, $\Sigma_2^{yz}(0\,\frac{1}{4}\,\overline{\frac{1}{4}})$ and $S^{zx}(\frac{1}{4}\,\frac{1}{2}\,\frac{1}{4}), \Sigma^{zx}(\frac{1}{4}\,0\,\frac{1}{4})$ of Bragg peaks vanish. This new phase must be phase III′. As already pointed out in Section 2.4.2, the observation of only a single $\boldsymbol{q}_1 - \boldsymbol{q}_1'$ structure ($\boldsymbol{q}_1 = \langle\frac{1}{4}\,\frac{1}{4}\,0\rangle$ and $\boldsymbol{q}_1' = \langle\frac{1}{4}\,\frac{1}{4}\,\frac{1}{2}\rangle$) resembles the structure found for phase III′ in CeB_6 [232]. While $\boldsymbol{q}_2'^{yz} = S_2^{yz}(\frac{1}{2}\,\frac{1}{4}\,\overline{\frac{1}{4}})$ vanishes, the intensity of $\boldsymbol{q}_1'^{yz} = S^{yz}(\frac{1}{2}\,\frac{1}{4}\,\frac{1}{4})$ seems to be constant through the transition [panel (a) in Fig. 6.5]. The same applies to the wave vector pair $\boldsymbol{q}_2^{yz} = \Sigma_2^{yz}(0\,\frac{1}{4}\,\overline{\frac{1}{4}})$ and $\boldsymbol{q}_1^{yz} = \Sigma^{yz}(0\,\frac{1}{4}\,\frac{1}{4})$. The Bragg peaks $\boldsymbol{q}_1^{yz}$ and $\boldsymbol{q}_1'^{yz}$ originate from the Ce spins of one AFQ - sublattice, pointing along $[0\,\bar{1}\,1]$, and the Bragg peaks $\boldsymbol{q}_2^{yz}$ and $\boldsymbol{q}_2'^{yz}$ originate from spins on the other Ce sublattice, pointing along $[0\,1\,1]$. The vanishing of the latter pair above $B_c = 1.5$ T implies that the moment rotate away from the $[0\,1\,1]$ direction and become collinear with the spins of the other sublattice. An analogous discussion can be made for the K_{zx} domain.

[9] The out-of-plane reflections were detected by means of a vertical detector array in combination with a Flatcone setup, employed at E2 (Helmholtz-Zentrum Berlin)

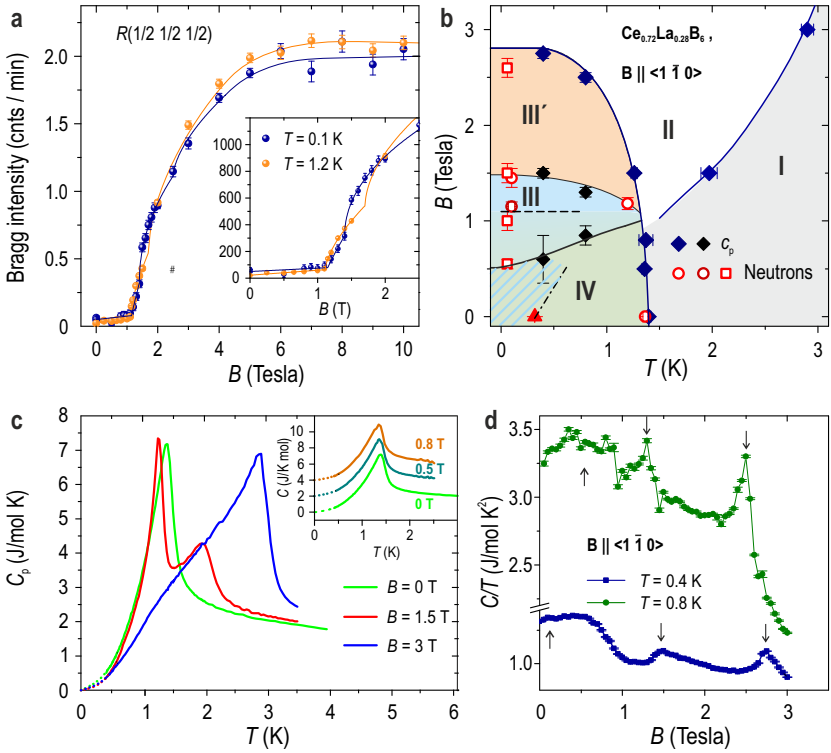

Fig. 6.6: The magnetic phase diagram of $Ce_{0.72}La_{0.28}B_6$. **(a)** Field dependence of the $(\frac{1}{2}\ \frac{1}{2}\ \frac{1}{2})$ intensity up to highest possible field of $B = 10\,\mathrm{T}$, at low temperature ($T = 0.1\,\mathrm{K}$) and at a higher temperature (phase IV) ($T = 1.2\,\mathrm{K}$). The data have been obtained at IN14. The inset shows an enlarged view of the low-field region. **(b)** $B-T$-phase diagram for $Ce_{0.72}La_{0.28}B_6$, compiled with the transition fields, B_c and B_Q, and the transition temperatures T_N and T_Q. They were determined from the field dependence of the AFM Bragg peaks [see figure 6.5 (a) and (b)] and the $(\frac{1}{2}\ \frac{1}{2}\ \frac{1}{2})$ intensity [panel (a)]. T_N and T_Q were derived from specific-heat measurements *vs.* temperature [see panel (c)] and *vs.* field [see panel (d)]. The solid lines denote phase boundaries. The boundary between phase IV and III (B_{IV}) is not sharply defined because of the gradual onset of the AFM Bragg peaks in field. This is indicated by the color gradient between B_{III} and the dashed line, which marks the field above which the AFM Bragg peaks have reached full intensity. The hatched area corresponds to the mixed phase that can been induced via hysteresis at low temperature. **(c)** Temperature dependence of the specific heat $c_p(T)$ in various magnetic fields $\boldsymbol{B} \parallel (1\,\bar{1}\,0)$. The inset shows $c_p(T)$ for selected, low magnetic-field values, shifted for clarity. **(d)** Magnetic-field dependence of the specific heat for two different temperatures. The data in (c) and (d) have been measured by the Kremer group, MPI-FKF, Stuttgart. The magnetic field was always applied along $\boldsymbol{B} \parallel (1\,\bar{1}\,0)$.

The field boundary B_c is also mirrored in the $(\frac{1}{2}\,\frac{1}{2}\,\frac{1}{2})$ intensity in Fig. 6.6 (a) exhibiting an onset at $B_c = (1.5 \pm 0.1)$ T.[10] Further increase of the field leads finally to a sharp suppression of the $\boldsymbol{q}_1^{yz} = \Sigma^{yz}(0\,\frac{1}{4}\,\frac{1}{4})$ and $\boldsymbol{q}_1'^{yz} = S^{yz}(\frac{1}{2}\,\frac{1}{4}\,\frac{1}{4})$ reflections, reaching zero intensity at $B_Q = (2.6 \pm 0.1)$ T. This marks the transition into the AFQ phase (phase II), accompanied by another kink in the $(\frac{1}{2}\,\frac{1}{2}\,\frac{1}{2})$-Bragg intensity *vs.* B in Fig. 6.6 (a) (blue curve).[11] All transition fields B_{III}, B_c, B_Q are plotted as red circles in the $B-T$ phase diagram, shown in Fig. 6.6 (b). The phase boundary lines agree quite well with the phase boundaries T_{IV} and T_Q (blue points) determined from specific-heat measurements, which will be discussed below.

To check for a hysteresis of the AFM Bragg peaks, the reflections $\boldsymbol{q}_1^{zx} = \Sigma^{zx}(\frac{1}{4}\,0\,\frac{1}{4})$ and $\boldsymbol{q}_2^{zx} = \Sigma^{zx}(\frac{1}{4}\,0\,\overline{\frac{1}{4}})$ have been measured when decreasing the external magnetic field [see Fig. 6.5 (b)]. The downward curve deviates from the upward curve below $B_0 = (1.1 \pm 0.1)$ T.[12] Although the Bragg peaks lose intensity upon further decrease of the field, they can still retain intensity down to zero field. This is in contrast to the initial state of the sample, where no AFM Bragg peaks could be detected. Such a mixed state naturally raises the question, whether phase III and phase IV are microscopically coexisting or macroscopically phase separated. Phase III (see Section 2.4.6), unlike in CeB_6, exhibits a ferromagnetic moment, when entering it from phase IV *vs.* temperature. Therefore, it could be conceived that remanent ferromagnetic domains survive in the mixed state. These domains would be embedded in a phase-IV matrix, which is a singlet state without net moment [287]. The investigation of such a scenario is suitable for local-probes like NMR or μSR in future. Fig. 6.5 (c) shows the temperature dependence of the remanent Bragg intensity at $\boldsymbol{q}_1'^{yz} = S^{yz}(\frac{1}{2}\,\frac{1}{4}\,\frac{1}{4})$ and $\boldsymbol{q}_1^{zx} = \Sigma^{zx}(\frac{1}{4}\,0\,\frac{1}{4})$. There is a quick decrease of intensity upon warming to $T \approx 0.35$ K. This temperature coincides with a jump in the $(\frac{1}{2}\,\frac{1}{2}\,\frac{1}{2})$ intensity at $T_N^* = (0.32 \pm 0.001)$ K, shown earlier in Fig. 6.1. Presumably it signifies the change to a pure phase IV. T_N^* is part of a new phase boundary line (dash-dotted) in Fig. 6.5 (b), which is only valid when the mixed state has been induced in the sample via hysteresis. The change at T_N^* can be understood as resulting from the disappearance of the AFM domains within a macroscopic phase separation scenario. In case of a microscopic phase coexistence scenario it seems that phase III and phase IV are competing for the same density of states of the conduction electrons.

Another piece of information is given by a closer inspection of the low-field $(\frac{1}{2}\,\frac{1}{2}\,\frac{1}{2})$-intensity, given in the inset of Fig. 6.6 (a). For $T = 0.1$ K it first shows a suppression at $B = 0.5$ T, but with the formation of phase III above $B_{III} = (0.55 \pm 0.05)$ T, the intensity reenters fully and remains constant until the step at $B_0 = (1.1 \pm 0.1)$ T. In conclusion,

[10] This is the field induced spin-modulation $\mu_z \cos(2\pi \boldsymbol{q} \boldsymbol{j})$ in z-direction, characteristic for the AFQ order [236] and in line with the observations for the lower dopings.

[11] The intensity of the $(\frac{1}{2}\,\frac{1}{2}\,\frac{1}{2})$-Bragg peak becomes saturated above $B = 5$ T, similar to the observations for $x = 0.18$, $x = 0.23$.

[12] This field also delimits the broad crossover region between phase IV and phase III [see phase diagram in Fig. 6.6 (b)].

the weak $(\frac{1}{2}\,\frac{1}{2}\,\frac{1}{2})$ Bragg peak exhibits a rather complex interplay with the underlying ordered phase. It is observed both in phase IV and phase III, but takes a minimum at the boundary field B_{III} between both phases. Second, it is possible to induce a mixed state of phase III and phase IV in zero field via an hysteresis loop at low temperatures. Whether this state shows phase separation or coexistence has to be investigated in the future.

It should be mentioned that the zero-field μSR time spectrum exhibited only a depolarization in phase III for a similar La concentration $x = 0.25$ [295]. In the $x = 0.28$ sample here, preliminary analysis reveals that the Q-width of the magnetic Bragg peaks at $\boldsymbol{q}_1^{zx}$, $\boldsymbol{q}_1'^{zx}$ etc. in phase III is much broadened compared to the structural Bragg peaks. This could be either due to short-range order or due to a slightly incommensurate magnetic order. Both scenarios would produce the inhomogeneous internal field distribution that quickly depolarizes the spin of the muons.

Figure 6.6 (c) displays the temperature dependent specific heat for different magnetic fields $\boldsymbol{B} \parallel (1\,\bar{1}\,0)$.[13] The specific heat $c_p(T)$ in fields up to $B = 0.8\,\mathrm{T}$ shows a strong peak at T_{IV} associated with the phase transition to phase IV. This agrees with the observation for the $x = 0.25$ sample in Ref. 292, where the main entropy release is connected to T_{IV} and not to T_{N}. According to the phase diagram in Fig. 6.6 (b) one would expect to observe a transition into phase III at low temperatures for $B = 0.8\,\mathrm{T}$, in addition to the transition of T_{IV}. However, no second anomaly can be discerned in the specific heat $c_p(T)$ for this field, shown in the inset of Fig. 6.6 (c). In the c_p *vs.* B data in Fig. 6.6 (d), the IV-III boundary is signified by a step (see arrow) in the $T = 0.4\,\mathrm{K}$ and $T = 0.8\,\mathrm{K}$ curves, and not a peak. In contrast to that, the boundaries B_{c} and B_{Q} are visible as clear peaks. Therefore, the boundary between phase IV and phase III resembles a crossover, rather than a sharp phase transition.[14]

In higher fields phase II can be induced and an associated second peak at T_{Q}, preceding the antiferromagnetic phase transition, appears in the specific heat [see Fig. 6.6 (c)].

[13] Data provided by the Chemical service group of MPI-FKF, Stuttgart.

[14] This was also realized from the gradual increase of the AFM Bragg peaks in magnetic fields.

Table 6.2: Transition fields for the low-temperature phases of $Ce_{1-x}La_xB_6$. B_{c} is the transition field from phase III to phase III′. B_{Q} is the transition field from phase III′ to phase II and B_{III} marks the onset of transition from phase IV to phase III. The latter is only observed in the $x = 0.28$ sample, where phase IV defines the ground state.

x	B_{c} (Tesla)	B_{Q} (Tesla)	B_{III} (Tesla)
0	1.10 ± 0.05	1.71 ± 0.024	–
0.18	1.45 ± 0.13	2.17 ± 0.25	–
0.23	1.50 ± 0.13	2.30 ± 0.2	–
0.28	1.45 ± 0.1	2.60 ± 0.1	0.55 ± 0.05

T_Q increases with magnetic field, in line with the observations for the $x = 0.18$ sample.

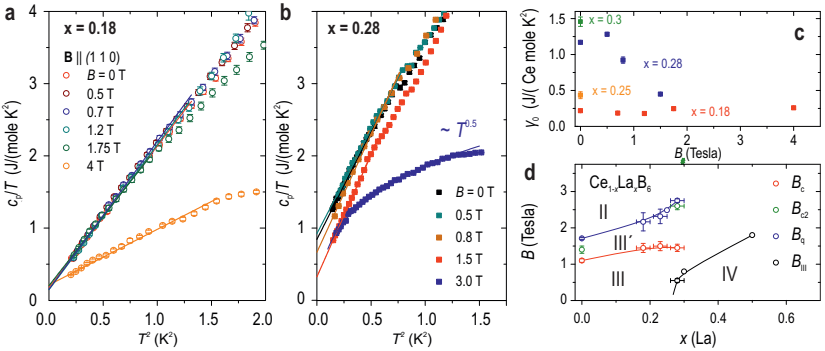

Fig. 6.7: **(a)** Low-temperature part of the specific heat c_p/T *vs.* T^2 for $x = 0.18$ and **(b)** $x = 0.28$ in different magnetic fields $\boldsymbol{B} \parallel (1\,1\,0)$. The solid lines are linear fits. **(c)** Linear specific-heat coefficient γ *vs.* magnetic field, determined for $x = 0.18$ and $x = 0.28$ from the data in panel (a) and (b), respectively. **(d)** Doping dependence of the transition fields B_c, B_Q and B_{III}. The data for $x = 0.25$ and $x = 0.3$ have been taken from Ref. 288 and 351, respectively.

In order to understand the enhancement of the specific heat in phase IV, the low-temperature region of $c_p(T)$ has been fitted according to the formula

$$c_p(T) = \gamma T + \delta T^3 \tag{6.1}$$

The first part accounts for the contribution of the Fermi liquid and the second part accounts for the contribution of the antiferromagnetic spin waves [223, 290].[15] The low-temperature specific heat is conveniently plotted as c_p/T *vs.* T^2 in Fig. 6.7 (a) for the $x = 0.18$ sample and in Fig. 6.7 (b) for the $x = 0.28$ sample. The linear curve for all fields in both compounds confirms the applicability of the law (6.1). An exception is the curve at $B = 3\,\mathrm{T}$ in panel (b), where the specific heat follows a $c_p \sim T^{3/2}$ law, which is indicative of a ferromagnetic spin-wave contribution [318]. The fits for the other fields provide a linear specific-heat coefficient γ, which is plotted in Fig. 6.7 (c), together with the data points for the $x = 0.25$ and $x = 0.3$ samples, taken from Ref. 292 and Ref. 298. The value for $x = 0.18$ does not deviate much from the parent compound CeB_6 ($\gamma = 0.250\,\mathrm{J/mole\,K^2}$), and is nearly field-independent. For $x = 0.28$, where the ground state is constituted by phase IV, γ jumps to a much higher value. This is in agreement with the observation of a strong increase of the transport coefficient A for the low-temperature resistivity [299], since both scale with the enhancement of the

[15] Contributions from phonons ($\sim \beta T^3$) can be estimated from the heat capacity of non-magnetic LaB_6, but were found to contribute significantly only for $T > 10\,\mathrm{K}$ [223].

effective mass, according to the Kadowaki-Woods-relation [352].

$$A \propto \gamma^2 \propto \left(\frac{m^*}{m}\right)^2 \tag{6.2}$$

For higher fields, $\gamma(x = 0.28)$ is suppressed to the level of $\gamma(x = 0.18)$. Therefore, the enhanced mass must be restricted only to phase IV. Since phase III and phase IV are supposed to be closely related, it is difficult to understand this finding. The magnetoresistance was found to be constant for phase IV [239], followed by a step when changing to phase III. Thus, it could be conjectured that phase IV is close to a magnetic instability and the charge carriers are scattered by the associated fluctuations. The absence of any non-Fermi-liquid behavior in transport and specific heat could be related to the concentration of the fluctuations around hot spots, which do not affect the whole Fermi surface [300].

6.1.6 Summary of the neutron diffraction studies of $Ce_{1-x}La_xB_6$

An investigation of the $B - T$- phase diagrams for $Ce_{1-x}La_xB_6$ ($x = 0$, $x = 0.18$, $x = 0.23$, $x = 0.28$) by elastic neutron scattering has been presented. They agree with the phase diagrams in literature, determined by other probes. In the $x = 0.28$ sample the AFM phase can only be induced in magnetic field.[16] In addition, a change of magnetic structure, upon entering phase III$'$ was observed, which stands in contrast to the claim of Ref. 236 that phase III$'$ is just the single domain state of phase III.

The magnetic Bragg peak at $R(\frac{1}{2}\ \frac{1}{2}\ \frac{1}{2})$ reveals an interesting interplay between the AFM phase and the AFQ phase. On the one hand, the $(\frac{1}{2}\ \frac{1}{2}\ \frac{1}{2})$ intensity has an onset at B_Q and then saturates in high-fields, which confirms the prediction from the localized multipolar mean-field model [230, 246]. On the other hand, a weak intensity in *zero field* appears below T_Q, which is not expected, since the antiferroquadrupolar order does not break time-reversal symmetry. Furthermore, this intensity is constant *vs.* B up to B_c, disagreeing with the same theoretical model [246]. Therefore, the $R(\frac{1}{2}\ \frac{1}{2}\ \frac{1}{2})$ Bragg peak is preliminarily related to a SDW, which forms in the subspace of the conduction electrons and could explain the charge gap observed by Hall-effect measurements [237]. It would be worthwhile to examine the existence of a similar Bragg peak in PrB_6 and NdB_6, since these compounds possess a similar Fermi surface as CeB_6 [262, 274]. In phase III$'$ the $(\frac{1}{2}\ \frac{1}{2}\ \frac{1}{2})$ intensity shows a step-like increase, which can be regarded as a fingerprint of the underlying AFQ order. Only CeB_6 does not exhibit this interplay, where the onset of $(\frac{1}{2}\ \frac{1}{2}\ \frac{1}{2})$ at B_Q is quite shifted from the critical field $B_{c2} = 1.4\,\mathrm{T}$ of phase III$'$. The evolution of the transition fields B_c and B_Q *vs.* doping x is shown in Fig. 6.7 (d). Interestingly both boundaries get enhanced, although T_N is suppressed by

[16] Phase III was observed via the detection of the out-of-plane Bragg peaks at $\boldsymbol{q}_1^{yz} = \Sigma^{yz}(0\ \frac{1}{4}\ \frac{1}{4})$ and $\boldsymbol{q}_1^{zx} = \Sigma^{zx}(\frac{1}{4}\ 0\ \frac{1}{4})$ etc., belonging to the K_{yz} and K_{zx} domains, respectively.

doping. This signifies that the AFQ phase is more sensitive against doping with La than the AFM phase.

In the $x = 0.28$ sample phase IV persists down to lowest temperatures. Only the weak $(\frac{1}{2}\ \frac{1}{2}\ \frac{1}{2})$ Bragg peak could be observed, which seems to be present irrespective of whether the system is in the AFM, AFQ or phase IV. No order parameter of phase IV could be unveiled, but it was pointed out that the effective mass within phase IV is strongly enhanced. This property might be related to a SDW criticality that scatters only a fraction of carriers at certain wave vectors of the Brillioun zone. The effective mass returns to "normal" values as soon as the system enters phase III for $B > B_{\mathrm{III}}$.

6.2 The spin dynamics in the AFM and AFQ states of $Ce_{1-x}La_xB_6$

6.2.1 The observation of a resonant spin exciton in the AFM phase of CeB_6

The theoretically proposed spin excitation spectrum in the AFQ state of CeB_6 [254], discussed in Section 2.4.3, has been previously measured in high magnetic fields $B = 6\,\mathrm{T}$ and at low temperatures $T < 3.2\,\mathrm{K}$. Spin excitations have been observed at selected wave vectors in the Brillouin zone [253]. A complete mapping of the spin excitation for all wave vectors $\boldsymbol{Q}$ was missing, which prevented a convincing comparison with the theoretical calculations. In *zero field*, the theory proposed branches of multipolar spin excitations [254]. However, the few experimentally measured spectra could not confirm these [253]. Furthermore, the low temperature AFM phase was scarcely studied in the literature by inelastic neutron scattering. By this, important parameter like the antiferromagnetic exchange interaction could be determined by measuring the associated collective modes. Second, no study of the spin dynamics was available for lanthanum doped compounds. Especially, the enigmatic phase IV is in the focus of interest, where an identification of the order parameter is still pending.

First, the CeB_6 has been reinvestigated under improved energy resolution and by the means of the recently developed *FlatCone*-technique.[1] Figure 6.8 (a)–(c) shows a map at constant energy ($E = 0.5\,\mathrm{meV}$) for the AFM state, the AFQ state and the paramagnetic state. The spin excitations in the AFQ and in the paramagnetic state exhibit a weak intensity at the AFQ wave vector $\boldsymbol{q}_{\mathrm{AFQ}} = R(\frac{1}{2}\ \frac{1}{2}\ \frac{1}{2})$. However, upon entering the AFM phase a strong excitation emerges at $R(\frac{1}{2}\ \frac{1}{2}\ \frac{1}{2})$, dominating the spin excitations in the $(H\,H\,L)$ scattering plane. This is completely unexpected, since one would expect the spin dynamics to be constituted by collective modes emerging from the AFM ordering wave vectors, e.g. $\boldsymbol{q}_1 = \Sigma(\frac{1}{4}\ \frac{1}{4}\ 0)$ and $\boldsymbol{q}_1' = S(\frac{1}{4}\ \frac{1}{4}\ \frac{1}{2})$.

The spectrum at $R(\frac{1}{2}\ \frac{1}{2}\ \frac{1}{2})$ [Fig. 6.9 (a)] shows the appearance of a strong and sharp peak in the AFM state near $\hbar\omega_R = (0.480 \pm 0.008)\,\mathrm{meV}$, while in the AFQ state it

[1] which allows to simultaneously measure a large 2θ angle range of 70° and allows to effectively map out the spin excitations for many $\boldsymbol{Q}$.

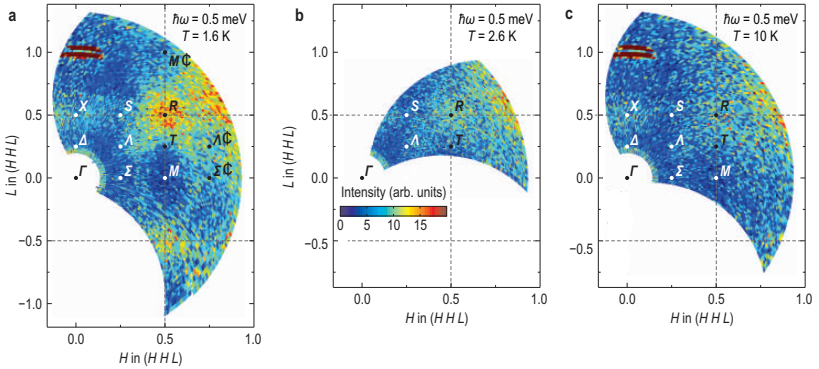

Fig. 6.8: Inelastic intensity distribution in the (HHL) scattering plane at $E = 0.5$ meV, measured in **(a)** the AFM phase at $T = 1.5$ K, **(b)** the AFQ phase at $T = 2.5$ K and **(c)** the paramagnetic phase at $T = 10$ K of CeB_6. The data were collected at IN14 (ILL) equipped with the FlatCone detector. These figures are similarly published in Ref. 353.

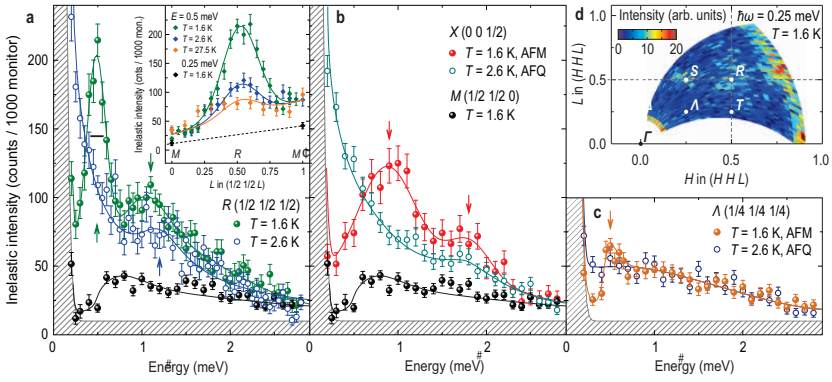

Fig. 6.9: (a) INS spectrum at $R(\frac{1}{2}\,\frac{1}{2}\,\frac{1}{2})$ in the AFM state ($T = 1.5$ K) and in the AFQ state ($T = 2.5$ K). The shoulder in the AFQ-curve around $E = 1.2$ meV in panel (a) is an artefact, since it could not be reproduced in later experiments. The inset shows momentum scans along $(\frac{1}{2}\,\frac{1}{2}\,L)$ at $E = 0.5$ meV for different temperatures. **(b)** AFM and AFQ spectra for the $X(0\,0\,\frac{1}{2})$ point and **(c)** the $\Lambda(\frac{1}{4}\,\frac{1}{4}\,\frac{1}{4})$ point. **(d)** Inelastic intensity map of the (HHL) scattering plane in the spin gap region at $E = 0.25$ meV. The lines are guides to the eyes. The data were obtained at IN14 and are similarly published in Ref. 353.

exhibits the familiar quasielastic lineshape expected for Kondo lattice systems. The enhancement of intensity at $\hbar\omega_R$ below T_N goes parallel with a suppression of intensity for energies below 0.35 meV, establishing a spin gap in this range. Thus, the transition into the AFM phase has the strongest impact on the spin dynamics. It might be tempting to relate this excitation to a branch of spin waves extending to the $R(\frac{1}{2}\,\frac{1}{2}\,\frac{1}{2})$ point. However, no dispersion of the mode for wave vectors away from $R(\frac{1}{2}\,\frac{1}{2}\,\frac{1}{2})$ can be seen, when doing a similar map at lower energies [see Fig. 6.9 (d)]. Also its width in $\boldsymbol{Q}$-space is very large, extending from $M(\frac{1}{2}\,\frac{1}{2}\,0)$ to $M'(\frac{1}{2}\,\frac{1}{2}\,1)$ [see inset of Fig. 6.9 (a)], which is much broader than the $\boldsymbol{Q}$-width of the actual spin waves emerging from the antiferromagnetic Bragg peaks $\boldsymbol{q}_1$ and $\boldsymbol{q}_1'$ and which will be discussed in detail in Section 6.2.3. Given its almost resolution limited energy width and strong intensity, this mode has a striking similarity to the resonant mode, observed in a number of heavy-fermion and high-T_c superconductors [41, 139, 354, 355]. This mode is understood as an exciton that form below the onset of the particle-hole continuum, marked by 2Δ.[2]

In the case of CeB_6 a charge gap in the AFM state with a size of $\Delta_{AFM} \approx 1.2$ meV has been observed by point-contact spectroscopy [264]. This justifies to term the $\hbar\omega_R$ mode as *resonant mode* or *exciton*, since it lies inside the charge gap. However, unlike to the high-T_c superconductors, where the resonant mode is confined to the wave vector of the magnetic Bragg peak, an exciton-like feature is observed for a number of wave vectors, e.g. at $X(0\,0\,\frac{1}{2})$ in Fig. 6.9 (b) and $\Lambda(\frac{1}{4}\,\frac{1}{4}\,\frac{1}{4})$ in Fig. 6.9 (c). Even the $M(\frac{1}{2}\,\frac{1}{2}\,0)$-point, where the intensity is minimal, a spin gap can be observed at $E < 0.6$ meV. The map in Fig. 6.9 (d) measured at an energy $E = 0.25$ meV inside the spin gap, shows that the intensity is suppressed throughout the (HHL) scattering plane. The weak dispersion of the spin gap and of the resonant mode, at least within the scattering plane, could also be explained by a localized crystal-field excitation. It would be overdamped by particle-hole excitations in the AFQ state,[3] but is observable once the damping is removed by the opening of the AFM charge gap. This scenario can be checked by measuring the temperature evolution of the spectrum upon warming from the AFM state to the AFQ state, as shown in Fig. 6.10 (a). Here, the energy position of the peak clearly decreases and the width increases because of the closing of the AFM charge gap. At $T_N = 2.4$ K, where $\Delta_{AFM} = 0$ holds, one obtains the quasielastic lineshape. This is in contrast to the observations in some HF superconductors, e.g. $PrOs_4Sb_{12}$ and UPd_2Al_3. A sharp crystal-field excitation has been observed in the superconducting state [48, 356], which hardens or softens when crossing T_c, but which is still observed in the normal state [48, 356]. When looking at the temperature dependence of the exciton energy $\hbar\omega_R$ in CeB_6 [inset of Fig. 6.10 (b)], the data points show an order-parameter-like increase below T_N, signifying its linkage to the AFM charge gap. Since the existence of the exciton is strongly coupled to the existence of the AFM charge, it would be crucial for consistency to observe the gap by inelastic neutron scattering,

[2] Its theoretical assessment in the RPA formalism has been discussed in Section 3.3.

[3] As documented by the observation of a quasielastic lineshape for all wave vectors in Fig. 6.9 (a)–(c) in the AFQ state.

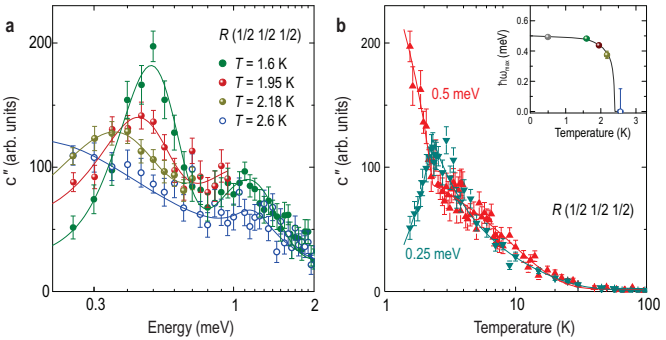

Fig. 6.10: (a) Evolution of the spectrum at $R(\frac{1}{2}\,\frac{1}{2}\,\frac{1}{2})$ for different temperatures upon warming from the AFM to the AFQ state through $T_N = 2.4\,\mathrm{K}$. **(b)** Temperature dependence of the inelastic intensity at $E = 0.5\,\mathrm{meV}$ (exciton) and $E = 0.25\,\mathrm{meV}$ (spin gap). The inset shows the temperature dependence of the exciton energy $\hbar\omega_R$, extracted from the fits in panel (a). Both panels have been similarly published in Ref. 353.

especially since this technique allows a $\boldsymbol{Q}$-resolved determination of Δ_{AFM}. Indications for an observation of the AFM charge gap will be discussed in Section 6.2.4.

The temperature dependence of the spin fluctuations at $E = 0.5\,\mathrm{meV}$ and $E = 0.25\,\mathrm{meV}$ in the paramagnetic state are shown in Fig. 6.10 (b). For both energies the spin fluctuation have an onset around $T_0 \approx 30\,\mathrm{K}$, which coincides with the increase of the relaxation rate $\lambda(T)$ probed by μSR [280, 281]. Especially the curve for $E = 0.25\,\mathrm{meV}$ seems to diverge to lower temperatures, suggesting an instability to static order. However, this progress is halted by the opening of the spin gap in the AFM state and the consequent suppression of the spin fluctuations. The origin of these spin fluctuations will be discussed in Section 6.2.5.

6.2.2 The observation of ferromagnetic correlations in the AFM phase of CeB_6

The spin dynamics in the AFM phase of CeB_6 have also been reinvestigated by the time-of-flight technique of neutron scattering.[4] Figures 6.11 (a) and (b) show energy-momentum profiles along high-symmetry directions in the AFM and AFQ state, respectively. The exciton at $R(\frac{1}{2}\,\frac{1}{2}\,\frac{1}{2})$ is reproduced in panel (a), revealing itself as a spot of intensity at the R point, localized in energy ($\hbar\omega \approx 0.5\,\mathrm{meV}$). Even more pronounced is a previously unobserved, intense and dispersive mode at $\hbar\omega_0 = 0.25\,\mathrm{meV}$ originating from the $\Gamma(1\,1\,0)$ and $\Gamma'(0\,0\,1)$ points. The dispersion follows the one expected for ferromagnetic spin waves and the intensity is much stronger than the AFM spin

[4] This technique allows to conveniently cover the whole $(\boldsymbol{Q}, E)$-space, only limited by kinematical restrictions and the direct beam.

waves. The black points follow the maxima in the spectrum, revealing that the ferromagnetic mode and the exciton at $R(\frac{1}{2}\,\frac{1}{2}\,\frac{1}{2})$ are possibly connected. The dispersion of the ferromagnetic mode, spanning the whole Brillouin zone, would also explain why an exciton-like peak has been previously observed by TAS for a number of wave vectors (see Fig. 6.9). Closer inspection of Fig. 6.11 (a) reveals that the exciton forms a local minimum and, thus, cannot be considered simply as the extension of the ferromagnetic branch to the zone boundary. Rather one would need to take into account the hybridization with the antiferromagnetic spin waves, originating from the magnetic zone centers [e.g. $S(\frac{1}{4}\,\frac{1}{4}\,\frac{1}{2})$].

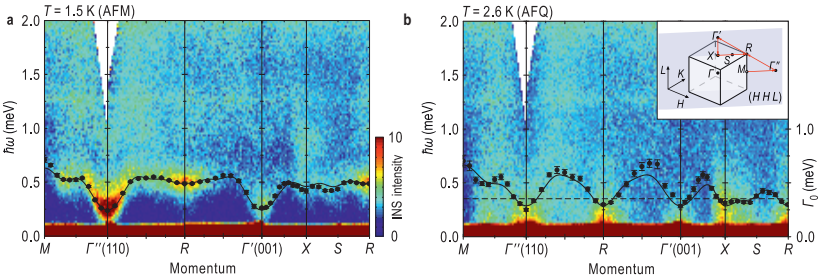

Fig. 6.11: This figure shows part of the TOF data measured at the IN5 spectrometer at ILL. The data were analyzed by H. Jang and is reproduced from Ref. 357. It shows $E-\boldsymbol{Q}$ cuts along crystallographic high symmetry lines as sketched in the inset of panel (b). **(a)** AFM state at $T = 1.5$ K and **(b)** the AFQ state at $T = 2.5$ K. The black points denote the energy of the intensity maxima in panel (a). In the panel (b) they correspond to the relaxation rate Γ that was determined from quasielastic lineshape fits to the spectrum. The dashed line shows the powder-averaged line width from Ref. 282, taken at the same temperature

The AFM magnons are sharper defined in momentum than the exciton and the ferromagnetic mode. Furthermore, in the AFQ state for $T > T_N$ in Fig. 6.11 (b) the scattering becomes quasielastic throughout the Brillouin zone, with the intensity peaked at the Γ, $X(0\,0\,\frac{1}{2})$ and $R(\frac{1}{2}\,\frac{1}{2}\,\frac{1}{2})$ points and not at the AFM ordering wave vectors $\boldsymbol{q}_1 = \Sigma(\frac{1}{4}\,\frac{1}{4}\,0)$ and $\boldsymbol{q}_1' = S(\frac{1}{4}\,\frac{1}{4}\,\frac{1}{2})$. Therefore, the intense dispersing modes in the AFM phase of CeB_6 should be rather associated with the itinerant quasiparticles, where the scattering function in $\boldsymbol{Q}$-space is defined by the nesting vectors of the paramagnetic Fermi surface. A similar case has been observed in the hidden-order compound URu_2Si_2, where spin excitations preexist as paramagnons in the paramagnetic state and become visible as dispersing modes upon transition into the hidden-order state below $T_0 = 17.5$ K [358].[5] Indications for ferromagnetic correlations in CeB_6 were provided by the observation of an enhanced magnetization in the AFQ state [250]. In zero field, the proposed

[5] Here, the local extremum ($\hbar\omega^* = 4$ meV) of the dispersion is at the incommensurate wave vector $\boldsymbol{Q}^* = (1 \pm 0.4, 0, 0)$, where the spin fluctuations are peaked for $T > T_0$ [358]. Subsequent analysis has interpreted the wave vector $\boldsymbol{Q}^*$ as a nesting vector of the Fermi surface and the excitation $\hbar\omega^*$ as a resonant mode below a charge gap, opening below T_0 [359–361].

AFQ ordering of the O_{xy} quadrupole moments together with the antiferro-coupling of the T_{xyz} octupolar moments favor a ferromagnetic alignment of the dipoles, since $\langle T_{xyz}\rangle = \langle O_{xy}\rangle \langle J_z\rangle$. However, in that case it is difficult to understand why the dispersing magnon modes are not already observable in the AFQ state, as proposed theoretically [251, 254]. This is similar to the exciton at $R(\frac{1}{2}\,\frac{1}{2}\,\frac{1}{2})$, which becomes quasielastic in the AFQ state, instead of remaining a damped crystal-field-like multipolar excitation as expected in the same theory [251, 254].

6.2.3 Spin waves in the AFM state

In search of the spin waves that are associated with the $2\boldsymbol{q}_1 - \boldsymbol{q}_1'$ antiferromagnetic ordering, energy-momentum cuts through the AFM propagation vector ($T = 1.5\,\mathrm{K}$) [$S(\frac{1}{2}\,\frac{1}{4}\,\frac{1}{4})$ and $S'(\frac{1}{2}\,\frac{3}{4}\,\overline{\frac{1}{4}})$ points] were exctracted, as shown in Fig. 6.12 (e). A cone-shaped dispersion is revealed, satisfying the relation for an Heisenberg-antiferromagnet. The intensity becomes critical upon changing to the AFQ state ($T = 2.5\,\mathrm{K}$). The spectrum, measured at the magnetic zone center $S(\frac{1}{4}\,\frac{1}{4}\,\frac{1}{2})$ in Fig. 6.12 (c), shows a peak at low energies marking the onset of the spin-wave cone. The upper boundary for the spin anisotropy gap can be estimated to $\Delta_A < 0.25\,\mathrm{meV}$.

In Fig. 6.12 (e), one can follow the dispersion up to an energy of $E = 0.5\,\mathrm{meV}$, which appears to be the upper limit for the zone boundary spin waves. This value is close to the energy of the exciton at $R(\frac{1}{2}\,\frac{1}{2}\,\frac{1}{2})$ and, consequently, it can be conjectured that the exciton is the undamped zone boundary spin wave mode [362]. The streaks of intensity at $E = 0.5\,\mathrm{meV}$ in the map of Fig. 6.8 (a), connecting the R points [$R(\frac{1}{2}\,\frac{1}{2}\,\frac{1}{2})$ and $R^*(\frac{1}{2}\,\frac{1}{2}\,\overline{\frac{1}{2}})$],[6] can be linked to spin-wave branches originating from the equivalent AFM Bragg peaks lying outside the (HHL) scattering plane, namely $S'(\frac{1}{2}\,\frac{1}{4}\,\frac{1}{4})$ and $S''(\frac{1}{2}\,\frac{1}{4}\,\overline{\frac{1}{4}})$ [357]. Figures 6.12 (a) and (b) show momentum cuts at various energies through this ellipse, crossing the $T(\frac{1}{2}\,\frac{1}{2}\,\frac{1}{4})$ and $M(\frac{1}{2}\,\frac{1}{2}\,0)$ points, respectively. One can see incommensurate peaks, symmetrically displaced from the center at $H = 0.5$ r.l.u. The absence of excitations at $E = 0.8\,\mathrm{meV}$ in Fig. 6.12 (b) implies that the spin-wave band is restricted to lower energies. For each peak the full-width-half-maximum (FWHM) of the Gaussian fit is given in the panel, ranging from 0.15 r.l.u. to 0.26 r.l.u. This is different to the exciton, which has a much larger spread in $\boldsymbol{Q}$-space with a FWHM= (0.33 ± 0.02) r.l.u., taken from the momentum scan in the inset of Fig. 6.9 (a). The exciton at the X-point ($\hbar\omega_X = 0.8\,\mathrm{meV}$) is similarly extended, having a FWHM of (0.314 ± 0.05) r.l.u. along the $(HH0)$ direction. This observation resembles the case for the resonant mode in the $A_xFe_{2-y}Se_2$ superconductors, where the broad distribution in $\boldsymbol{Q}$-space was related to a quasi-nested Fermi surface. In conclusion, there is a clear distinction in spin excitations between the broad and isolated itinerant modes at Γ, $X(00\frac{1}{2})$ and $R(\frac{1}{2}\,\frac{1}{2}\,\frac{1}{2})$ and the more finely structured and dispersing spin-wave modes, emanating from the AFM Bragg peaks.

[6] together forming an elliptical shape

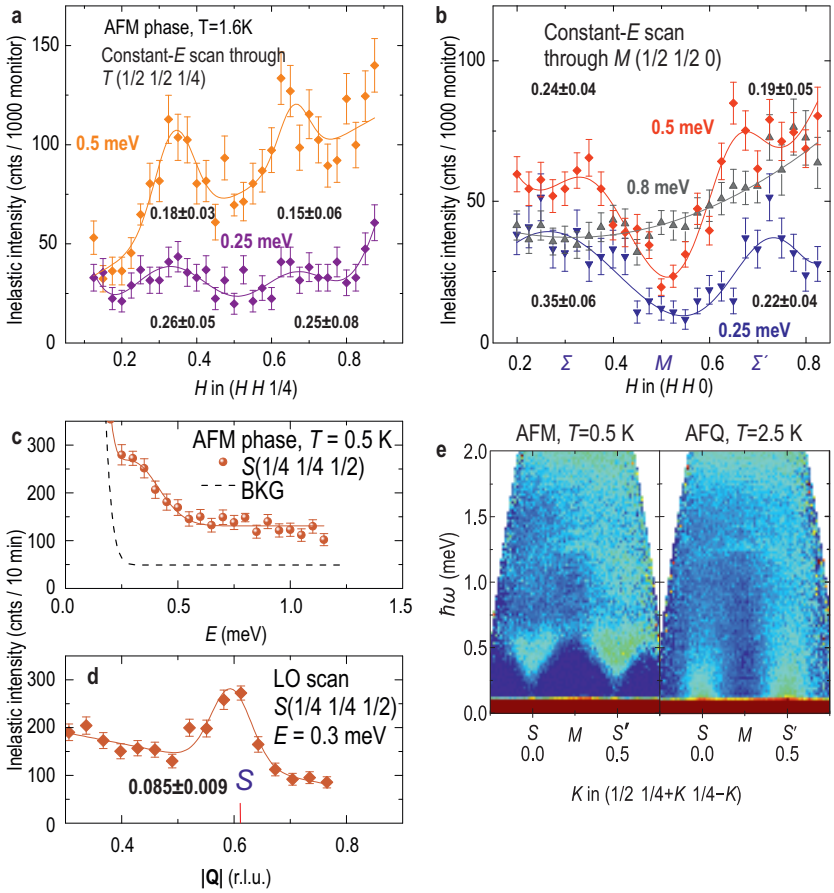

Fig. 6.12: **(a)**–**(b)** Momentum scans through the "ellipse" for different energies in the AFM phase ($T = 1.6$ K): **(a)** through the $T(\frac{1}{2}\ \frac{1}{2}\ \frac{1}{4})$ point and **(b)** through the $M(\frac{1}{2}\ \frac{1}{2}\ 0)$ point (center). All peaks were fitted with a Gaussian profile (solid lines). The small number denotes the Gaussian FWHM. Panels (a) and (b) have been similarly published in Ref. 353. **(c)** Spectrum at the AFM ordering wave vector $S(\frac{1}{4}\ \frac{1}{4}\ \frac{1}{2})$ ($T = 0.5$ K). **(d)** Longitudinal momentum scan through S for $E = 0.3$ meV. The solid line is a Gaussian fit. The data of panels (a)–(d) have been measured at IN14. **(e)** $\hbar\omega - \boldsymbol{Q}$ cuts of the TOF data along the connection line of the AFM ordering wave vectors $S(\frac{1}{2}\ \frac{1}{4}\ \frac{1}{4})$ and $S'(\frac{1}{2}\ \frac{3}{4}\ \frac{1}{4})$. Panel (e) has been similarly published in Ref. 357.

6.2.4 Observation of a charge gap in the AFM state

The interpretation of the sharp mode at $R(\frac{1}{2}\,\frac{1}{2}\,\frac{1}{2})$ as an exciton below the onset of the particle-hole continuum at Δ_{AFM} naturally gives rise to the question, whether the AFM gap can also be observed by neutron spectroscopy. In this respect, a second broad peak at $\hbar\omega_2 = 1.05\,\mathrm{meV}$ in the spectrum at $T = 0.5\,\mathrm{K}$ for the $R(\frac{1}{2}\,\frac{1}{2}\,\frac{1}{2})$ point [marked by the arrow in Fig. 6.13 (b)] appears to be a promising candidate. Such a second peak is also observed in the spectra in Fig. 6.13 (a), taken at wave vectors along the crystallographic symmetry line $(H\,\frac{1}{2}\,0)$.[7] All spectra have been fitted with two Lorentzians, to account for the narrow exciton mode at low energies ($\hbar\omega \approx 0.5\,\mathrm{meV}$) and the broad high-energy mode at $\hbar\omega_2$. For the latter the center $\hbar\omega_2$ is indicated by the grey box, which slightly disperses upon changing the wave vector. On the one hand, the value of $\hbar\omega_2$ varies between 0.95 meV and 1.05 meV for the analyzed spectra, putting it very close to the $\boldsymbol{Q}$-averaged value of $\Delta \approx 1.2\,\mathrm{meV}$ for the charge gap that was determined by point-contact spectroscopy [264]. On the other hand, it could also be assigned to a crystal-field excitations (CEF) of Ce^{3+}, which slightly disperses because of the intersite interaction J_{ff}.[8]

In order to distinguish, whether a CEF excitation scenario or a charge gap scenario can serve as the explanation for the $\hbar\omega_2$-mode, the spectrum for $R(\frac{1}{2}\,\frac{1}{2}\,\frac{1}{2})$ and $\boldsymbol{q} = (\frac{7}{8}\,\frac{1}{2}\,0)$ has also been measured in the AFQ state at $T = 2.5\,\mathrm{K}$ [shown in Fig. 6.13 (b)]. For both wave vectors the spectra show the familiar quasielastic lineshape, which exhibits no high-energy mode. The same observation applies also for the $X(0\,0\,\frac{1}{2})$ point and $\Lambda(\frac{1}{4}\,\frac{1}{4}\,\frac{1}{4})$ point in Fig. 6.9 (b) and (c).[9] Thus, the $\hbar\omega_2$-mode can be associated with the AFM charge gap Δ_{AFM}, since it is clearly connected with the AFM state.[10] A similar direct observation of the charge gap by inelastic neutron scattering has been discussed for the HF superconductor $CeCu_2Si_2$ ($T_c = 0.6\,\mathrm{K}$) [355].[11] However, unlike $CeCu_2Si_2$, where the spin fluctuations are concentrated at one particular wave vector [314], the spin fluctuations in CeB_6 are observable throughout the Brillioun zone. As a consequence, the charge gap is observable at all wave vectors by virtue of the coupling

[7] which connects $M(\frac{1}{2}\,\frac{1}{2}\,0)$ and $X^{\star}(1\,\frac{1}{2}\,0)$ points [see also inset of Fig. 6.13 (b)].

[8] The spectrum with the two modes shows intriguing similarity to the spectrum at the antiferromagnetic Bragg peak $\boldsymbol{Q} = (0\,0\,\frac{1}{2})$ in UPd_2Al_3 [356]. There, the ground state of the compound is superconducting and a low-energy resonant mode appears upon cooling below T_c, whereas the high energy mode continues to exist above T_c [356]. Consequently, the high-energy peak was interpreted as a crystal-field excitation of the localized f-electrons, which creates the low-energy resonance peak upon opening of the SC gap because of the strong coupling with itinerant electrons [44].

[9] The AFQ-spectrum at $R(\frac{1}{2}\,\frac{1}{2}\,\frac{1}{2})$ in Fig. 6.9 (a), measured in another beam time, was similarly published in Ref. 353 with a guide to the eyes suggesting a shoulder around $E \approx 1.2\,\mathrm{meV}$. However, a clear shoulder could not be reproduced in all subsequent beam times (at IN14, IN5 and 4F2) and, therefore, will not be discussed.

[10] Further evidence is provided by the magnetic-field dependence of $\hbar\omega_2$ that is shown in Fig. 6.17. It decreases quadratically *vs.* B and vanishes upon crossing the critical field B_c of the AFM phase.

[11] There, the spectrum at the spin-fluctuation wave vector $\boldsymbol{Q}_{\mathrm{AF}} = (0.215\ 0.215\ 1.458)$ develops a spin gap of $\hbar\omega = 0.2\,\mathrm{meV}$ in the SC state, which follows the SC density of states $Z(\omega) = \frac{\hbar\omega}{\sqrt{\hbar^2\omega^2-(2\Delta)^2}}$ (for $\hbar\omega > 2\Delta$) [363].

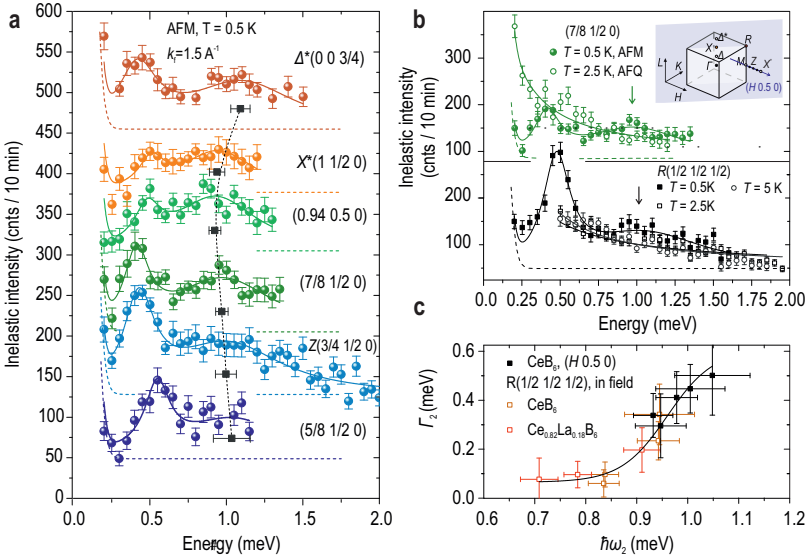

Fig. 6.13: **(a)** Spectra at various wave vectors $(H\ \frac{1}{2}\ 0)$ in the AFM state ($T = 0.5$ K), where a broad high-energy peak $\hbar\omega_2$ was observed in the spectrum. The $\Delta'(0\,0\,\frac{3}{4})$ point has been added for completeness. Each spectrum has been shifted for clarity and the corresponding dashed line marks the background baseline. The solid lines are Lorentzian-fits. The black box marks the energy of the high energy mode $\hbar\omega_2$. **(b)** Spectrum at $\boldsymbol{Q} = (\frac{7}{8}\ \frac{1}{2}\ 0)$ and $R(\frac{1}{2}\ \frac{1}{2}\ \frac{1}{2})$ in the AFM and in the AFQ state ($T = 2.5$ K). For the R point the spectrum in the paramagnetic state at $T = 5$ K has been added as well. The solid lines represent fits according to the text. The inset shows a sketch of the Brillouin zone illustrating the position of the spectra for panels (a) and (b). **(c)** Half-width-half-maximum Γ_2 of the high-energy peak *vs.* $\hbar\omega_2$ (black points). Data that were obtained from spectra in different magnetic fields for CeB_6 (brownish boxes) and for $Ce_{0.82}La_{0.18}B_6$ (red boxes) have been added. The corresponding spectra are shown in Section 6.2.6. The experiment was performed at IN14, using a dilution insert to reach lowest temperatures.

between spin and charge for the itinerant quasiparticles. The origin of the AFM charge gap is discussed in the next section.

Another parameter, which is provided by the Lorentzian fits to the spectrum, is the HWHM Γ_2 of the peak at $\hbar\omega_2$. In Fig. 6.13 (c) it is plotted *vs.* $\hbar\omega_2$ for all measured wave vectors (black points).[12] Irrespective of how the points were obtained, by either applying magnetic field, doping with La (to be discussed later) or by changing $\boldsymbol{Q}$, the points seem to fall on an universal curve. For energies below $\hbar\omega < 0.9$ meV the Γ_2 is almost resolution limited, whereas it starts increasing for $\hbar\omega > 0.9$ meV. Such energy dependent damping term is typical for itinerant spin dynamics and will be discussed in

[12] Data points that have been taken from evolution of the spectrum in magnetic field (see Section 6.2.6) are added.

the next section.

6.2.5 Itinerant description of the spin dynamics in CeB_6

The presented comprehensive zero-field study of the spin excitations in CeB_6 is clearly at odds with the expected spin dynamics for the multipolar order in this compound. In the AFQ state only a quasielastic intensity is observed, instead of the dispersive collective modes expected in the multipolar model [254]. Spin excitations only appear below T_N and seem to reveal a twofold character: i) spin waves emanating from the antiferromagnetic Bragg peaks and ii) a strongly dispersing ferromagnetic mode at Γ plus exciton-like modes at $R(\frac{1}{2}\,\frac{1}{2}\,\frac{1}{2})$ and $X(0\,0\,\frac{1}{2})$. Such excitons are occasionally occurring phenomena, not only observed in the superconducting state of HF superconductors [354, 355], but also observed in so-called Kondo insulators like SmB_6 [364] and YbB_{12} [365, 366] as well as inside the hidden-order phase of URu_2Si_2 [358, 361]. An interesting case is provided by the "1-2-10" family CeT_2Al_{10} (T=Fe, Ru). $CeRu_2Al_{10}$ is a antiferromagnet below $T_0 = 27.3\,\mathrm{K}$, while $CeFe_2Al_{10}$ is a Kondo insulator with the hybridization gap forming below $T^* = 50\,\mathrm{K}$. Both compounds display the formation of an exciton at $\boldsymbol{Q} = (1\,0\,0)$ below their characteristic temperatures, with an energy of $\hbar\omega = 4.8\,\mathrm{meV}$ and $8\,\mathrm{meV}$, respectively [367–369]. Thus, it seems that the appearance of the spin gap is independent of the exact ground state of the compound. For the Kondo-insulators YbB_{12} and $CeFe_2Al_{10}$ the spin gaps are understood as collective modes that form below the onset of the particle-hole continuum, determined by the indirect hybridization gap at $\boldsymbol{Q}$ [370, 371].

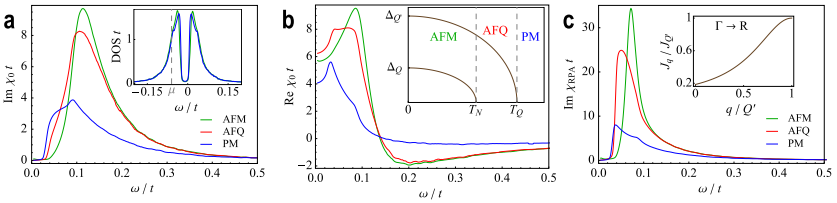

Fig. 6.14: **(a)** Imaginary part and **(b)** real part of the Lindhard susceptibility at the R point. The inset of (a) shows the quasiparticle density of states in the paramagnetic state. **(c)** The imaginary part of the RPA susceptibility. All figures have been reproduced from Ref. 372.

The exciton at $\hbar\omega_R = 0.5\,\mathrm{meV}$ and $\boldsymbol{q}_{\mathrm{AFQ}} = R(\frac{1}{2}\,\frac{1}{2}\,\frac{1}{2})$ in CeB_6 has been similarly interpreted as a feedback spin exciton in the work of Akbari *et al.* [372, 373]. Basis for the following theoretical analysis, which follows Akbari *et al.* [372], is the microscopic fourfold (Γ_8-type) degenerate Anderson lattice model, which describes the heavy-fermion ground state. The on-site Coulomb repulsion is assumed to be infinitely large ($U_{ff} \to \infty$) to ensure single occupation of the f-orbitals. Here, the main effect

of the AFQ and AFM ordering on the conduction electron spectrum is to create charge gaps at their respective ordering wave vectors $\boldsymbol{Q}' = R(\frac{1}{2}\ \frac{1}{2}\ \frac{1}{2})$ and $\boldsymbol{Q} = \boldsymbol{q}_1,\ \boldsymbol{q}'_1$, which are included in the Hamiltonian as mean-field terms:

$$\mathcal{H}_{\mathrm{AFQ}} = \sum_{\boldsymbol{k},\sigma} \Delta_{\boldsymbol{Q}'} \left(f^{\dagger}_{\boldsymbol{k},+\sigma} f_{\boldsymbol{k}+\boldsymbol{Q}',-\sigma} + f^{\dagger}_{\boldsymbol{k},-\sigma} f_{\boldsymbol{k}+\boldsymbol{Q}',+\sigma} \right) \tag{6.3a}$$

$$\mathcal{H}_{\mathrm{AFM}} = \sum_{\boldsymbol{k},\tau} \Delta_{\boldsymbol{Q}} \left(f^{\dagger}_{\boldsymbol{k}\tau\uparrow} f_{\boldsymbol{k}+\boldsymbol{Q}\tau\downarrow} + f^{\dagger}_{\boldsymbol{k}\tau\downarrow} f_{\boldsymbol{k}+\boldsymbol{Q}\tau\uparrow} \right) \tag{6.3b}$$

The chemical potential has been fixed close to the upper edge of the lower hybridization band [see inset of Fig. 6.14 (a)]. The susceptibility of the non-interacting quasiparticles $\chi_0(\boldsymbol{q}, \omega)$ at the AFQ ordering wave vector in the paramagnetic, antiferroqadrupolar and the antiferromagnetic phase is given in Fig. 6.14 (a) for the imaginary part and (b) for the real part. The dynamic susceptibility for the interacting quasiparticles $\chi_{\mathrm{RPA}}(\boldsymbol{q}, \omega)$ has been assessed via the RPA formalism:

$$\chi_{\mathrm{RPA}}(\boldsymbol{q}, \omega) = \frac{\chi_0(\boldsymbol{q}, \omega)}{1 - J_{\boldsymbol{q}} \chi_0(\boldsymbol{q}, \omega)} \tag{6.4}$$

The interaction term $J_{\boldsymbol{q}}$ is assumed to be a Lorentzian function peaked at the wave vector of the exciton $\boldsymbol{Q}' = R(\frac{1}{2}\ \frac{1}{2}\ \frac{1}{2})$ [372]. The opening of the gaps in both AFQ and AFM phases in the spectrum of the quasiparticles pushes the response to higher values. If the resonance condition $J(\boldsymbol{Q}')\chi_0(\boldsymbol{Q}', \omega_R) = 1$ is met, the RPA susceptibility gains a pole at $\omega = \omega_R$. This would manifest itself as the sharp exciton feature observed experimentally by inelastic neutron scattering. Apparently this condition is reached inside the AFM state, which explains why the exciton can *only* be observed there.[13] In the AFQ state the size of the gap is too small to sufficiently enhance $\chi'_0(\boldsymbol{Q})$.[14]

A shortcoming of the model is the uncertainty about the interaction $J_{\boldsymbol{q}}$, which leaves open, whether it originates from the direct exchange term, or from RKKY-mediated dipolar or quadrupolar interaction. Second, there is a different theoretical approach that interprets excitons, such as the resonant mode in unconventional superconductors, as localized magnon-like excitations. Those appear at the antiferromagnetic wave vector only upon the opening of the SC gap, which removes the damping by particle-hole excitations [362].[15] In case of CeB_6 the charge gap is generated by the AFM order and the localized soft mode could be of the multipolar type, as predicted by Thalmeier *et al.* [254], or a crystal-field excitation. This alternative description was not addressed in the itinerant description by Akbari *et al.* [372]. There the exciton is regarded as an excitation out of the heavy-quasiparticle ground state. Analogously to the resonant

[13] The temperature dependence of the energy ω_R, following the opening of the AFM gap Δ_{AFM}, and the small dispersion of the exciton away from $\boldsymbol{Q}'$ [see Ref. 372] are likewise captured by the theory.

[14] Since $\Delta_{\boldsymbol{Q}'}$ is stabilized in magnetic field, it has been predicted that the resonance should already appear in the AFQ state for a sufficiently large field [372].

[15] Such a scenario was proposed to the explain the resonant mode in the 3D compound $CeCoIn_5$ below T_c [354, 362].

modes iron-based superconductors and cuprates it would correspond to a singlet-triplet transition [6]. Furthermore, in Ref. 372 the $\boldsymbol{Q}$-dependence of $J_{\boldsymbol{q}}$ is designed such that it creates an exciton only at the $R(\frac{1}{2}\,\frac{1}{2}\,\frac{1}{2})$ point. However, the spin dynamics, determined for the whole Brillouin zone in Fig. 6.11, exhibit a more complex structure.

A theoretical analysis of the complete spin dynamics is still awaited, but several properties can already be understood phenomenologically with the theories, discussed in Chapter 3. First of all, when looking at the inelastic intensity in the AFQ phase in Fig. 6.11 (b), where the intensity *vs.* energy displays a quasielastic lineshape for all wave vectors

$$\chi''(\boldsymbol{q},\omega) = \chi_{\boldsymbol{q}}\Gamma_{\boldsymbol{q}}\frac{\hbar\omega}{(\hbar\omega)^2+\Gamma_{\boldsymbol{q}}^2} \tag{6.5}$$

one can assign the maxima of intensity rather to the Γ, R and X points, than to the antiferromagnetic Bragg peaks at $\boldsymbol{q}_1$ and $\boldsymbol{q}_1'$. Furthermore, the relaxation rate $\Gamma_{\boldsymbol{q}}$ seems to behave inversely to the intensity, taking a local minimum at Γ, R and X. This encourages to describe the spin-fluctuations in the self-consistent renormalization (SCR)-theory for heavy-fermion systems [51].[16] A modulated relaxation rate Γ_q and response χ_q is expected, according to

$$\chi_q = \frac{1}{1/\chi_L - J_q} \tag{6.6a}$$

$$\Gamma_q = \frac{\chi_L\Gamma_L}{\chi_q} \tag{6.6b}$$

where χ_L corresponds to the local dynamical susceptibility and J_q to the intersite interaction. This term is composed of exchange interactions involving intermediate states of high-energy excitations (e.g. RKKY interaction) as well as low-energy excitations of the quasiparticles, becoming significant at the nesting vectors $\boldsymbol{Q}$ of the Fermi surface [320]. Therefore, the *hot spots* of χ_q at $R(\frac{1}{2}\,\frac{1}{2}\,\frac{1}{2})$ and $X(0\,0\,\frac{1}{2})$ represent maxima of the intersite interaction $J(\boldsymbol{q})$. $J(\boldsymbol{q})$ can only be evaluated theoretically under knowledge of the band structure and the Fermi surface, which has been determined so far only by quantum oscillations in high magnetic fields (Section 2.4.4) or by angle-resolved photoemission spectroscopy at a relatively high temperature of $T = 30\,\mathrm{K}$ [374]. The RKKY interaction $I(\boldsymbol{q})$ has been calculated on the basis of the reported Fermi surface [375], which yielded maxima at $R(\frac{1}{2}\,\frac{1}{2}\,\frac{1}{2})$, close to $X(0\,0\,\frac{1}{2})$ as well as at the antiferromagnetic zone center $\boldsymbol{q}_1' = (\frac{1}{4}\,\frac{1}{4}\,\frac{1}{2})$ [375]. However, a detailed knowledge of the Fermi surface in the HF ground state of CeB_6 is conditional for a more advanced analysis.

[16] The theory successfully describes the spin dynamics of other weakly antiferromagnetic itinerant HF compounds, such as $CeRu_2Si_2$ [320].

6.2.6 Magnetic-field dependence of the spin exciton in CeB_6

As discussed in the previous section, there are two opposite descriptions of the exciton: scenario A explains it as an itinerant excitation out of the heavy-fermion ground state following Akbari *et al.* [372], scenario B relates it to a localized excitation that becomes visible upon the removal of the damping within the AFM state. To differentiate between these scenarios, the evolution of the exciton mode has been studied upon the suppression of the AFM state by (i) application of an external magnetic field, and by (ii) dilution with non-magnetic La^{3+} in $Ce_{1-x}La_xB_6$. Especially the magnetic-field study should provide valuable information about the final state of the excitation. Were it a triplet, then the degeneracy should be lifted in magnetic field and the mode should split into three excitations.[17]

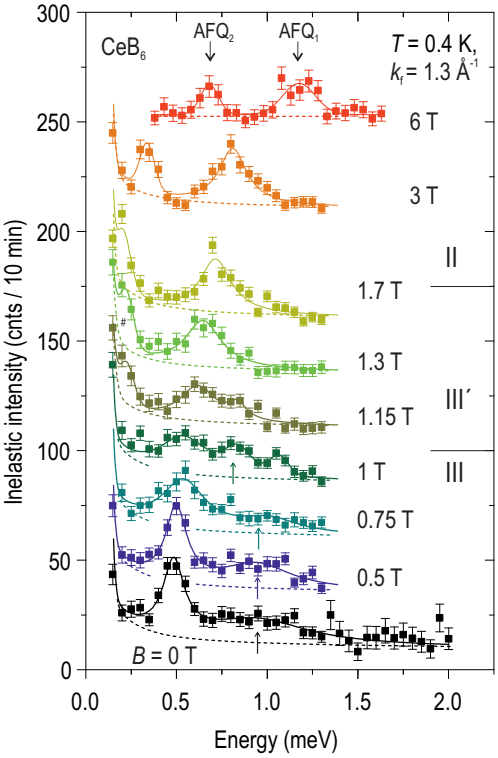

Fig. 6.15: Spectra at the exciton wave vector $R(\frac{1}{2}\ \frac{1}{2}\ \frac{1}{2})$ in different magnetic fields in the AFM state of CeB_6 at a low temperature ($T = 0.4$ K). The data have been measured at the PANDA spectrometer (FRMII, Garching). The sample environment comprised a ^{3}He insert in combination with a vertical-field magnet with the field pointing along the $[1\,\bar{1}\,0]$ direction, perpendicular to the scattering plane. The spectra have been shifted for clarity, and the dashed line in each panel indicates the background baseline for each spectrum. The solid lines are fits consisting of multiple Lorentzian functions.

[17] It would also clarify how the spectrum in zero field evolves to the spectrum at high fields showing multipolar excitations [253].

Figure 6.15 shows the evolution of the spectrum at $R(\frac{1}{2}\,\frac{1}{2}\,\frac{1}{2})$ upon application of a magnetic field $\boldsymbol{B} \parallel (1\,\bar{1}\,0)$. The spectrum at zero field exhibits the spin exciton at $\hbar\omega_R = (0.484 \pm 0.008)$ meV and a broad shoulder at $\hbar\omega_2 = (0.94 \pm 0.07)$ meV, which can be tentatively ascribed to the onset of the continuum because of the AFM charge gap. Each excitation is fitted with a Lorentzian-function. The broadening of the peak because of the instrumental resolution is negligible (HWHM = 0.04 meV). Upon increasing the field towards the critical field $B_c = 1.1$ T of the AFM phase, the exciton mode decreases in amplitude and broadens. In contrast, the $\hbar\omega_2$ mode decreases in energy and gets sharper. Upon crossing over to phase III′ the behavior changes distinctly. The amplitude of the exciton seems to increase, whereas the $\hbar\omega_2$-mode vanishes. In addition, another excitation appears at low energies, which has a very sharp linewidth. There is no qualitative change of the spectrum upon changing to the AFQ phase at $B_Q = 1.7$ T. Therefore, for the purpose of discussion the broader peak at $\hbar\omega_{II1} = (0.72 \pm 0.01)$ meV is assigned as the AFQ_1 mode and the sharp low energy peak at $\hbar\omega_{II2} = (0.21 \pm 0.01)$ meV is assigned as AFQ_2 mode. For higher fields $B > B_Q$ these energies are increasing.[18]

6.2.7 Evolution of the spin exciton in $Ce_{1-x}La_xB_6$

Analogously to CeB_6, the spin excitation for all La-doped samples ($x = 0.18$, $x = 0.23$ and $x = 0.28$) have been mapped for a series of fields. Figure 6.16 shows the spectrum at $R(\frac{1}{2}\,\frac{1}{2}\,\frac{1}{2})$ for (a) $x = 0.18$, (b) $x = 0.23$ and (c) $x = 0.28$. The insertion of non-magnetic lanthanum suppresses the AFM transition temperature. Considering only the zero-field spectra for $Ce_{1-x}La_xB_6$ (black data points in Fig. 6.15 and Fig. 6.16), the impact of La-doping alone is to broaden the spin exciton and to suppress its energy. For the $x = 0.28$ sample only a quasielastic line shape is visible in zero magnetic field.[19] Qualitatively, the spectrum of the $x = 0.18$ sample is similar to the spectrum of CeB_6, exhibiting also a second peak at $\hbar\omega_2 = (0.91 \pm 0.04)$ meV. A $\hbar\omega_2$-peak could not be resolved for the higher doping levels.

The field dependence of the spectra is as complex as the field dependence in CeB_6. For the purpose of an overview, Fig. 6.17 presents colormaps of the scattering function $S(\hbar\omega)$ of the measured $\hbar\omega$-B parameter space, where the background intensity, as given by the dashed lines for each spectrum in Fig. 6.15, has been subtracted. The field ranges of phase III, III′ and II are indicated at the bottom of each panel. The spectra in Fig. 6.15 and 6.16 have been fitted to a Lorentzian line shape, after taking into account the Bose factor $n(T,\hbar\omega)$ [$\chi''(\hbar\omega) = n(T,\hbar\omega)S(\hbar\omega)$].

$$\chi''(\hbar\omega) = \chi' \left[\frac{\Gamma}{\hbar^2(\omega-\omega_0)^2 + \Gamma^2} - \frac{\Gamma}{\hbar^2(\omega+\omega_0)^2 + \Gamma^2} \right] \tag{6.7}$$

[18] The AFQ_1 mode has also been previously reported for the $R(\frac{1}{2}\,\frac{1}{2}\,\frac{1}{2})$ point in a field of $B = 6$ T [253].

[19] This effect resembles the doping effect on the resonant mode in $Ce_{1-x}La_xCoIn_5$, where the resonant mode energy $\hbar\omega_{res}$ similarly scales with the suppression of T_c [376].

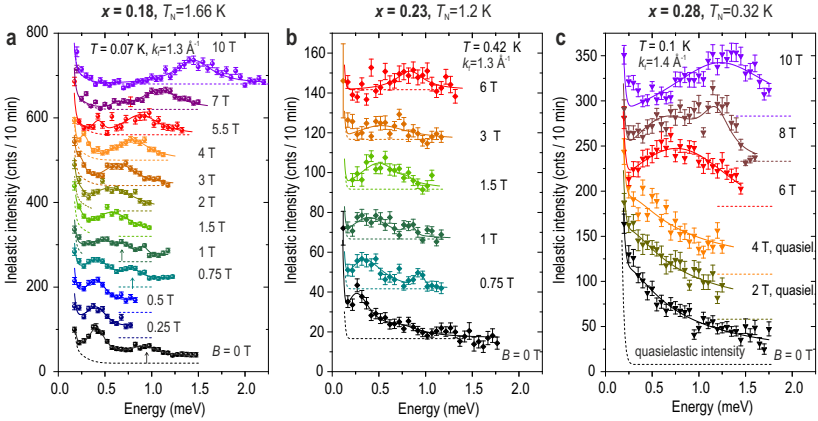

Fig. 6.16: Spectra at the exciton wave vector $R(\frac{1}{2}\ \frac{1}{2}\ \frac{1}{2})$ for La-substituted samples: **(a)** $x = 0.18$, **(b)** $x = 0.23$, **(c)** $x = 0.28$. The spectra have been shifted for clarity, and the dashed lines indicate the background baseline for each spectrum. The data for the $x = 0.18$ and $x = 0.28$ samples have been obtained at the IN14 spectrometer (ILL, Grenoble). The $x = 0.23$ sample was measured at the PANDA spectrometer (FRMII, Garching). The solid lines are fits consisting of Lorentzians, as described in the text.

Here, the amplitude of the peak would correspond to the product χ'/Γ and is plotted *vs.* field B in [Fig. 6.18 (a1)–(d1)]. The HWHM, being equal to Γ, is shown in Fig. 6.18 (a2)–(d2). The susceptibility χ', being proportional to the area of the peak, is displayed Fig. 6.18 (a3)–(d3). The energy of the excitations $\hbar\omega_0$ are given separately in the colormaps of Fig. 6.17.

In the following it will be shown that the field dependence of the spin excitations can be classified according to the field regimes of the different phases. In phase III, the amplitude of the exciton decreases with field, parallel to an increase in width, keeping the total spectral weight ($\sim \chi'$) constant (see Fig. 6.18). The energy of the exciton $\hbar\omega_R$ (see Fig. 6.17) is constant for small fields, but may slightly increase on approaching B_c. The $\hbar\omega_2$-excitation, which is only resolved for $x = 0$ and $x = 0.18$, shows a decrease in energy as well as in intensity (Fig. 6.18) and vanishes upon termination of phase III.

In phase III$'$ the AFQ_1 and AFQ_2 modes emerge. As already mentioned for CeB_6, there is no clear distinction between the exciton in phase III and the AFQ_1 excitation in phase III$'$/II. The linewidth Γ and the spectral weight χ' of both modes [black and red curves in Fig. 6.18 (a2)–(c2) and (a3)–(c3)] are quite comparable at the transition B_c. However, the energy of the exciton $\hbar\omega_R$ (full black circles in Fig. 6.17) jumps to a higher value above B_c (black squares in Fig. 6.17). This is most clearly seen for the $x = 0.18$ sample [Fig. 6.17 (b)]. Upon further increase of the magnetic field the spectral weight and the HWHM Γ of the AFQ_1 excitation remain constant. When crossing to

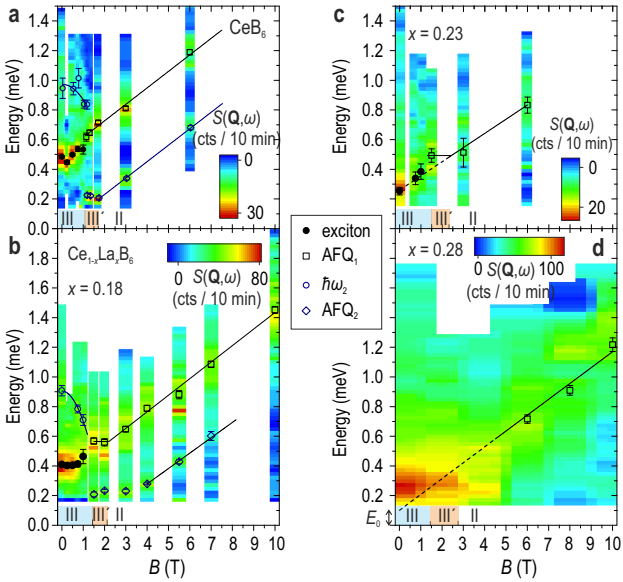

Fig. 6.17: **(a)–(d)** Colormaps of the background corrected intensity $S(\hbar\omega)$ for the covered energy-B-space, (Fig. 6.15 and Fig. 6.16) for **(a)** CeB_6, **(b)** $x = 0.18$, **(c)** $x = 0.23$, **(d)** $x = 0.28$. The intensity has been smoothed in order to decrease the noise and enhance the readability. The symbols denote the center of the excitations, derived from the Lorentzian fits.

phase II at B_Q both the energies $\hbar\omega_{II1}$ and $\hbar\omega_{II2}$ of AFQ_1 and AFQ_2 start to increase linearly, shown in Fig. 6.17 (a)–(d). This increase is even observed in the $x = 0.28$ sample in sufficiently high fields, where one can see the emergence of a broad AFQ_1 excitation in Fig. 6.16 (c) moving to the right.

One of the main topics to be addressed by the magnetic field study, was the level scheme to which the exciton in the AFM phase is ascribed. The magnetic field should lift a possible spin degeneracy of the final state by virtue of the Zeeman effect. For the $x = 0$ and the $x = 0.18$ compounds the energy of the exciton is constant *vs.* field, which can be understood in a singlet-triplet scenario, where the central level $S_z = 0$ is strongest [377]. The broadening of the exciton, as evidenced by the increase of the HWHM Γ in Fig. 6.18 (a2)–(d2) would then be ascribed to the energy splitting $\delta\varepsilon$ between the $S_z = -1$ and the $S_z = 1$ Zeeman states. But then it is difficult to understand why in Fig. 6.18 (a1) the exciton width does not increase in small field for CeB_6, while it does for $x = 0.18$ and $x = 0.23$.

Rather one should take the damping effect of the particle-hole excitations on the exciton into account. Figure 6.19 (a) shows the temperature dependence of the exciton linewidth for CeB_6 in *zero* magnetic field. An increase of damping is observed, when the temperature approaches T_N. The same should be expected when the AFM charge gap closes upon application of the critical magnetic field B_c. Strong support for this scenario is provided by the observation of the $\hbar\omega_2$ mode for $x = 0$ and $x = 0.18$ [blue

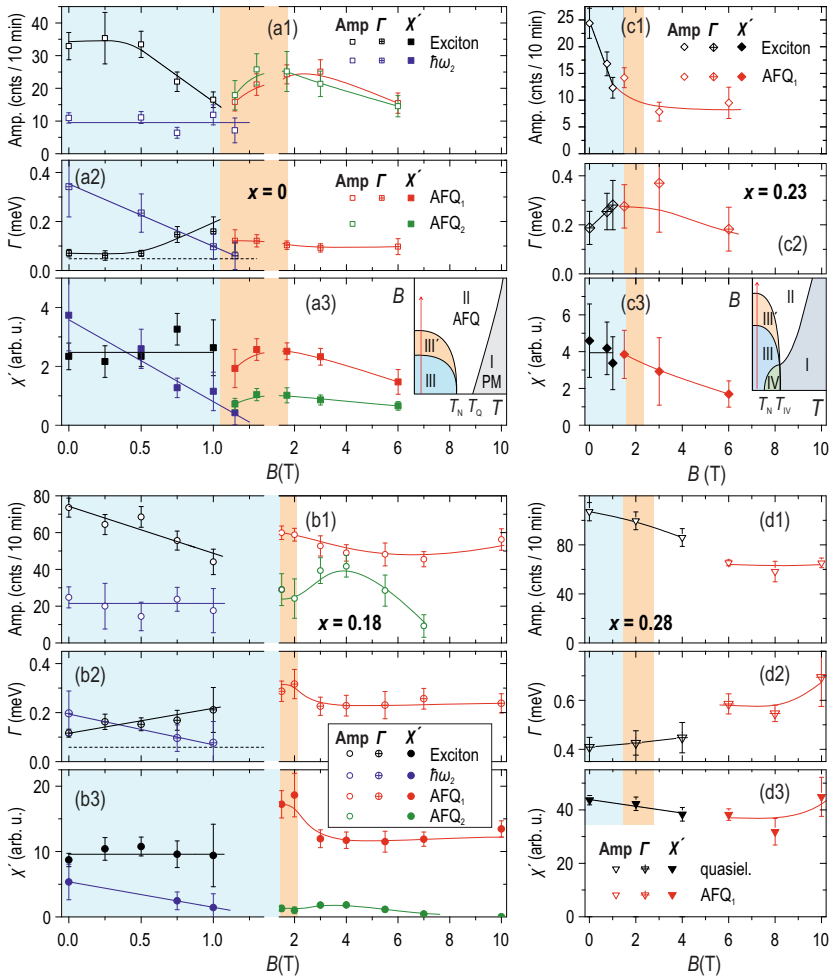

Fig. 6.18: **(a)**–**(d)** Magnetic-field dependence of the amplitude [**(a1)**–**(d1)**] and area [**(a3)**–**(d3)**] of the Lorentzian fits to the spectra in Fig. 6.15 and Fig. 6.16 for **(a)** CeB_6, **(b)** $x = 0.18$, **(c)** $x = 0.23$, **(d)** $x = 0.28$. The shaded areas denote the phases according to the phase diagram sketched in the inset to panel (a2) for $x < 0.2$ and panel (c2) for $x > 0.2$. **(a2)**–**(d2)** Damping term Γ, corresponding to the HWHM of the observed excitations. For the low-field spectra of the $x = 0.28$ compound a quasielastic-lineshape fit ($\chi'' = \chi'\Gamma\hbar\omega/[(\hbar\omega)^2 + \Gamma^2]$) was deployed, for which HWHM = $\sqrt{3}\Gamma$ holds. All solid lines are guides to the eyes.

circles in Fig. 6.17 (a) and (b)], which can be identified as the AFM charge gap. This conclusion is based on several clues. i) Its energy decreases in field, and can be much better fitted with a quadratic function ($1 - B^2/B_0^2$) [blue line Fig. 6.17 (a) and (b)] than with a linear function. ii) It vanishes above B_c, so it must be a property of the AFM phase. iii) The field dependence is different for $x = 0$ and $x = 0.18$, so it cannot be explained by a localized excitation of the Ce^{3+} ion in combination with the Zeeman effect. iv) Its decrease in energy is accompanied by a decrease in linewidth Γ_2 [blue points in Fig. 6.18 (a2)–(b2)], which can be explained by the smaller available phase space to which particle-hole excitations can decay.[20] Since the exciton energy is constant in the AFM phase, the closing AFM charge gap would explain the increase of the damping Γ through the increase of particle-hole excitations.

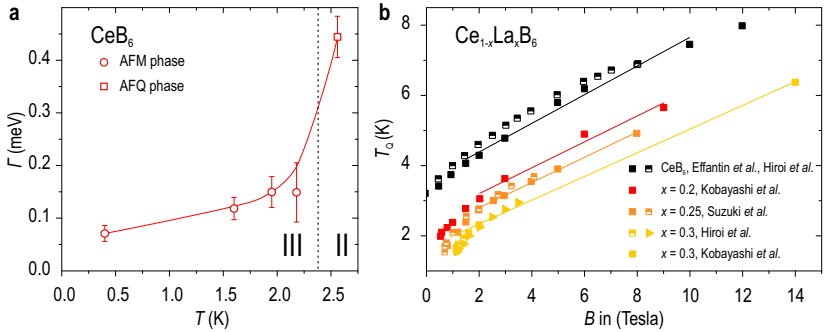

Fig. 6.19: (a) Temperature dependence of the zero-field exciton HWHM (Γ), measured in CeB_6. The corresponding spectra are shown in Fig. 6.10. **(b)** Magnetic-field dependence of AFQ transition temperature T_Q, taken from the published phase diagrams for $x = 0$ [234, 297], $x = 0.2$ [291], $x = 0.25$ [240, 292] and for $x = 0.3$ [239, 298].

However, further increase of the damping term Γ is precluded by the transition into phase III′ at B_c. There, the exciton transforms into the AFQ_1 mode, showing a rather constant Γ *vs.* magnetic field [see Fig. 6.18 (a2)–(c2)]. The same applies to the AFQ_2 excitation, which has a resolution-limited linewidth up to the highest fields [see Fig. 6.15 and Fig. 6.16]. The energies of both AFQ_1 and AFQ_2 are initially constant, but start to increase linearly for $B > B_Q$ with the same slope, as visible from Fig. 6.17. Fitting them with a linear function

$$\hbar\omega_{\mathrm{III}}(B) = E_0 + kB \tag{6.8}$$

gives a slope of $k = (0.11 \pm 0.004)\,\mathrm{meV/T} = (1.90 \pm 0.07)\mu_B$, which is common for

[20] The determined size of the AFM charge gap in zero field of $\hbar\omega_2 = (0.94 \pm 0.07)$ meV differs from the previous value, but agrees within the error bar.

all doping levels within the error bar. This fact can be explained by a Zeeman scaling of a localized excitation of the Ce^{3+} ion. The absence of any counterpropagating mode implies that the degeneracy of the Γ_8 state is completely lifted in the AFQ state. Furthermore, the modes can be identified with the multipolar branches, calculated for the mean-field model of quadrupolar order [254]. A correspondence to the AFQ energy scale is strongly suggested, since the AFQ transition temperature is also linearly increasing in the same field range, as shown in Fig. 6.19 (b) for different doping levels. The AFQ_1 mode was also observed in previous studies [253, 255], where it showed no dispersion away from $R(\frac{1}{2}\,\frac{1}{2}\,\frac{1}{2})$, supporting the localized description. The slope gives a Landé-factor of $g = (1.90 \pm 0.07)$, which is different from $g_0 = 1.6$ that was determined by ESR. However, the latter probes transitions at the zone center, which will be discussed in the next section.[21]

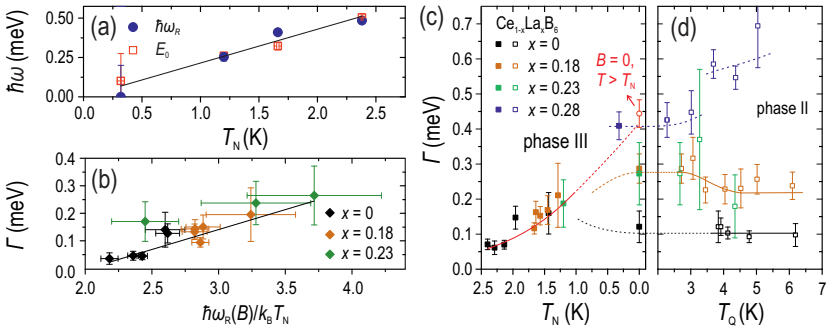

Fig. 6.20: **(a)** Zero field exciton energy $\hbar\omega_R$ and zero field extrapolation of the AFQ_1 mode E_0 *vs.* T_N. **(b)** HWHM Γ_R of the exciton *vs.* $\hbar\omega_R$, normalized with k_BT_N. **(c)** Exciton HWHM Γ *vs.* $T_N(B)$ in the AFM phase for all dopings. Please note the inverted x-axis. **(d)** Γ *vs.* T_Q of the AFQ_1 mode for all doping levels. The field dependent transition temperatures $T_N(B)$ and $T_Q(B)$ have been determined from measurements of the specific heat or from the interpolation of the phase diagrams in literature ($x = 0$, $x = 0.2$, $x = 0.25$) [234, 240, 291, 298]. T_N for $x = 0.18$ was estimated from the AFM charge gap. All lines are guides to the eyes.

The proximity of the exciton to the AFQ_1 mode suggests that the exciton might be in fact the same localized transition. This would speak against the itinerant model, which describes the exciton as a collective mode that is created by the feedback of the gap formation on the itinerant spin-fluctuations [372, 373]. Plotting the energy of the exciton $\hbar\omega_R$ in zero field *vs.* the AFM transition temperature T_N [22] in Fig. 6.20 (a), shows that it scales with T_N. But also the zero field extrapolation E_0 of the AFQ_1 mode energy $\hbar\omega_{II1}$ coincides with $\hbar\omega_R$, corroborating the close relation between the AFQ_1

[21] The AFQ_2 mode at lower energies has not been reported previously and it is remarkable for its very narrow linewidth that is even retained in the $x = 0.18$ doped sample. Without knowledge of its dispersion in $\boldsymbol{Q}$-space, it is not possible to tell whether it can be related to a multipolar branch or not.

[22] T_N can be regarded as a measure of the AFM gap Δ_{AFM}

mode and the exciton. The damping of the exciton should depend on the distance to the onset of the particle-hole continuum. This is investigated in Fig. 6.20 (b), where Γ is plotted against the ratio $\hbar\omega_R/k_B T_N$. The data points for all doping levels seem to fall on the same curve, which shows that the increase of damping for higher doping levels is due to the stronger particle-hole excitations and is not disorder-induced. One could also plot Γ *vs.* T_N, which would examine how important the size of the AFM charge gap is for the diminishing of the damping. Figure 6.20 (c) shows convincingly that when T_N is suppressed, the linewidth of the exciton increases. Since for low fields the data points for all samples fall on the same line, one can conclude that within the AFM phase $B < B_c$ the La-doping and the application of a magnetic field have an equivalent effect on the exciton. For the $x = 0.28$ the AFM charge gap is completely suppressed and the low-energy response is now quasielastic. This situation is equivalent to CeB_6 before entering the AFM phase ($T > T_N$), where the gap is zero as well. Both cases give a comparable quasielastic linewidth $\Gamma(x = 0.28, T = 0) \approx \Gamma(x = 0, T > T_N)$.

Magnetic field, unlike doping or temperature, does not suppress the exciton energy $\hbar\omega_R$. Instead, when entering phase III′ the exciton transforms into the AFQ_1 mode. Here, in contrast to the AFM state, the linewidth Γ_{III1} is constant *vs.* the AFQ transition temperature T_Q [Fig 6.20 (d)]. However, there is a strong variation between the different doping levels. This can only be understood considering the local environment of a Ce^{3+} ions. For a doping level of $x = 0.18$, 70% of the cerium atoms have at least one lanthanum ion as next-nearest neighbor. The presence of La modifies the local molecular field and alters the energy of the localized AFQ_1 transition. Therefore, the random substitution with lanthanum can be regarded as a disorder effect, where the observed transition energy corresponds to the statistical average over all configurations of lanthanum next-nearest neighbors.

This observation establishes a fundamental difference between the exciton and the AFQ_1 mode. The exciton does not seem to be sensitive to the local environment of Ce^{3+} atoms, since its linewidth is smaller for the $x = 0.18$ and $x = 0.23$ samples than the linewidth of the AFQ_1 mode [see Fig 6.20 (c)]. Thus, it must originate from the ground state of the coherent heavy-fermion quasiparticles as initially suggested by Akbari *et al.* [372].

In conclusion, the quasiparticles, which govern the spin dynamics in the AFM and AFQ states, undergo a change from itinerant to localized behavior at the critical field B_c of the AFM phase. This assumption is also corroborated by the observation of the AFM charge gap, which simultaneously vanishes at B_c, instead at B_Q, where the antiferromagnetic phase (phase III′) terminates. However, the exciton is only one piece of the full spin excitation spectrum in the AFM phase. A comprehensive description of the spin dynamics should also take into account the ferromagnetic mode at the Γ point.

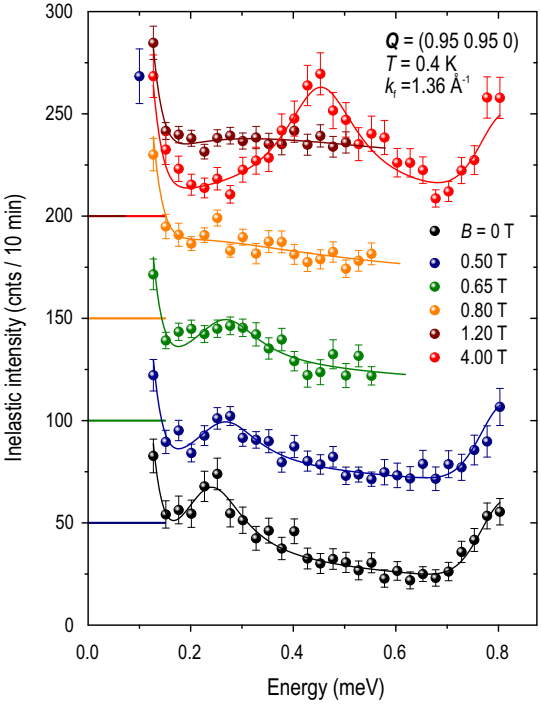

Fig. 6.21: Spectra at $\boldsymbol{Q} = (0.95\,0.95\,0)$, close to $\Gamma(1\,1\,0)$, in the AFM state of CeB_6 at $T = 0.4\,\mathrm{K}$ for various magnetic fields $\boldsymbol{B} \parallel (1\,\bar{1}\,0)$. The spectra have been shifted by 50 counts for clarity. The spectrum for $B = 4\,\mathrm{T}$ shares the same baseline as the spectrum for $B = 1.2\,\mathrm{T}$. The solid lines correspond to fits with a Lorentzian lineshape plus a quasielastic contribution. The data have been measured at PANDA (FRMII, Garching) with a final wave number of $k_f = 1.36\,\mathrm{Å}^{-1}$.

6.2.8 Magnetic-field dependence of the ferromagnetic mode

The magnetic-field dependence of the ferromagnetic (FM) magnon at the Γ-point has been investigated in Fig. 6.21 by measuring several spectra at $\boldsymbol{Q} = (0.95\ 0.95\ 0)$ in different magnetic fields.[23] In zero field a sharp excitation was resolved at $\omega_\Gamma = (0.24 \pm 0.01)\,\mathrm{meV}$, which reproduces the result of the time-of-flight experiment [see Fig. 6.11].[24] The FM mode has been fitted with a Lorentzian, which comprises the center $\hbar\omega_\Gamma$ and the HWHM Γ as parameters. Upon application of a magnetic field the linewidth of the FM mode increases visibly for $B > 0.5\,\mathrm{T}$. A slight increase of energy can be discerned as well. For fields $B > 0.65\,\mathrm{T}$ the feature is flattened out and a quasielastic-lineshape fit is employed. This concerns the spectra at $B = 0.8\,\mathrm{T}$ and at

[23] The wave vector is slightly displaced from the wave vector of the structural Bragg peak, in order to avoid contamination from the tail of the elastic intensity, which can overlay the low-energy response because of the limited energy resolution.

[24] In addition, another excitation is visible at higher energies with its tail extending down to $E = 0.72\,\mathrm{meV}$. This peak has been linked to a phonon in Ref. 253. Since it does not change in magnetic field it will not be discussed further.

$B = 1.2\,\mathrm{T}$, where the system is in phase III and in phase III′, respectively. At $B = 4\,\mathrm{T}$, deep inside the AFQ region the low-energy response is completely removed and a clear excitation exists at $\hbar\omega_{\mathrm{II}} = (0.454 \pm 0.007)\,\mathrm{meV}$. This mode has also been observed previously at somewhat higher temperatures ($T = 2.3\,\mathrm{K}$) and for $\boldsymbol{B} \parallel (0\,0\,1)$, having an energy of 0.35 meV [255]. It was found that the mode quickly disperses to higher energies along the $(q\,q\,0)$ direction and then stays constant towards the $M(\frac{1}{2}\,\frac{1}{2}\,0)$ point [255]. This picture is consistent with the theoretical calculations of the multipolar excitation branches, which are flatly dispersing towards the boundary of the Brillouin zone and are softening around the Γ point [251, 378]. At the $R(\frac{1}{2}\,\frac{1}{2}\,\frac{1}{2})$ point the AFQ_1 mode is found at $\hbar\omega_{\mathrm{II},1} = 0.95\,\mathrm{meV}$ in a field of $B = 4\,\mathrm{T}$, which is twice higher than the value at the Γ point. Assuming that the excitations at R and Γ belong to the same branch, this ratio compares with the ratio of $\omega_{R,\mathrm{II}}/\omega_{\Gamma,\mathrm{II}} = 3$ that is given in the calculations [251].

Though the Thalmeier-model (see Ref. 251, 254) might be able to account for the dispersing ferromagnetic-like collective modes observed in the AFQ state [253, 255], it is clearly failing to describe the FM mode in *zero field* in the following respects. i) As shown in Fig. 6.11, the intensity gets reduced as the mode disperses away from the Γ-point. At the $M(\frac{1}{2}\,\frac{1}{2}\,0)$ point the intensity is almost zero in both AFM and AFQ state (see also Ref. 357 for a comprehensive mapping of the Brillouin zone). This clearly contradicts the presence of a mode for that point, predicted by the calculations and also observed in the field induced AFQ phase [251, 255]. (ii) Since the multipolar modes are associated with the AFQ order, they should already appear below T_{Q}, and not below T_{N}.[25] However, in the AFQ state the intensity is purely quasielastic at all wave vectors. A paramagnon related to a ferromagnetic instability would be a more obvious interpretation for the intensity distribution above T_{N}. (iii) The theoretical model predicts a Goldstone mode at Γ in zero field. This follows from the fact that the O_{xy}-type quadrupoles are degenerate in zero field and, thus, can be freely rotated [251, 254]. However, this is contradicted by the nonzero energy of $\hbar\omega_{\Gamma} = 0.25\,\mathrm{meV}$ for the FM mode at $\boldsymbol{q} = 0$.

Such a spin gap can be accounted for by introducing an anisotropy term $\sum_{j,l} A S_j^z S_l^z$ (with $A > 1$) in the Heisenberg-model, describing localized spins. But then the same anisotropy would also act on the antiferromagnetically ordered spins. Anisotropy in the antiferromagnetic Heisenberg-Model creates a larger spin gap than that for the ferromagnetic Heisenberg-Model [50]. This is inconsistent with the smaller spin gap observed for the antiferromagnetic spin waves in the AFM phase of CeB_6 (see Section 6.2.3). In fact, the nonzero spin gap here seems to be quite unusual for a ferromagnetic HF compound. Ferromagnetic correlations have also been observed for $YbRh_2Si_2$, UCoGe and UGe_2, but there only a quasielastic intensity was observed in zero field at the reciprocal-lattice vectors [379–381], which can only be explained by a much smaller spin gap, if present at all.

Further discussion of the ferromagnetism is only meaningful after investigating the

[25] The same argument has been earlier applied for the exciton at $R(\frac{1}{2}\,\frac{1}{2}\,\frac{1}{2})$, which is also not understood in the multipolar model.

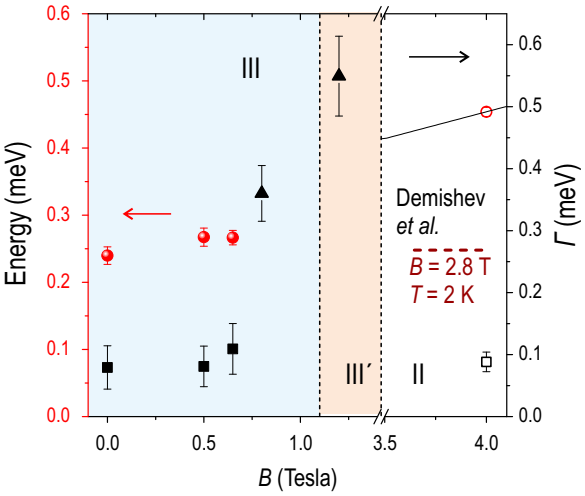

Fig. 6.22: Field dependence of the energy (red points) and the linewidth (HWHM) Γ (black points) for the FM magnon at $\Gamma(1\,1\,0)$. The triangles represent the HWHM determined from quasielastic lineshape fit. The vertical dashes lines mark the field boundaries B_{c1} and B_{c2}, separating phases III, III′ and II. The brownish horizontal dashed line corresponds to the transition observed by ESR at $T = 2\,\mathrm{K}$ and $B = 2.8\,\mathrm{T}$ (see Ref. 284).

temperature dependence of the relaxation rate $\Gamma_{\boldsymbol{q}}$. It is related to the static susceptibility χ via

$$\chi_{\boldsymbol{q}}^{-1} = \chi^{-1}(1 + cq^2) \tag{6.9}$$

$$\Gamma_{\boldsymbol{q}} = \Gamma_0 q \chi_{\boldsymbol{q}}^{-1} \tag{6.10}$$

according to the SCR theory [138, 382], which describes nearly ferromagnetic metals. On the one hand, an itinerant model, like the Stoner theory of ferromagnetism, would be able to account for the dispersion and the damping of the spin waves away from reciprocal-lattice vector Γ. On the other hand, a nonzero uniform magnetization m is required in the ordered state to create the exchange splitting E_{ex}. This cannot be reconciled with the clear *antiferromagnetic* transition below T_{N}, observed for CeB_6. Second, the spin gap should increase in magnetic field according to

$$\hbar\omega_\Gamma = \hbar\omega_0 + g\mu_{\mathrm{B}}B \tag{6.11}$$

This is not observed as the energy remains constant in small fields $B < B_{\mathrm{c}}$ (see Fig. 6.22). For $B > 0.5\,\mathrm{T}$ the damping term increases, so that the mode cannot be anymore differentiated from a quasielastic lineshape. This field evolution closely resembles the field evolution of the exciton at $R(\frac{1}{2}\,\frac{1}{2}\,\frac{1}{2})$. Thus, it would be favorable to similarly interpret the FM mode as a bound exciton below a charge gap. The charge gap for the Γ point would then be constituted by the direct hybridization gap, the AFQ gap and the AFM gap. The spectrum in Fig. 6.21 is contaminated by a phonon in the region, where a

charge gap would be expected ($E > 0.8$ meV). Nonetheless, indications for a charge gap can be drawn from the spectrum at the nearest wave vector $\Delta'(0\,0\,\frac{3}{4})$ in Fig. 6.13 (a). The low-energy peak would correspond to the FM spin wave and the higher lying peak at $\hbar\omega_{\Delta',2} = (1.10 \pm 0.06)$ meV would correspond to the charge gap. The extrapolated size of the gap at the $\Gamma'(0\,0\,1)$ point would be $\hbar\omega_{\Gamma,2} \approx 1.25$ meV. Without the experimental confirmation or negation of a charge gap at Γ the conclusion is speculative, but the similar phenomenological field dependence of both the FM mode and the exciton at $R(\frac{1}{2}\,\frac{1}{2}\,\frac{1}{2})$ seems to suggest a similar mechanism leading to their formation.

6.3 Summary

CeB_6 reveals a dual nature of spin excitations in its antiferromagnetic phase. On the one hand, there are spin waves associated with the antiferromagnetic ordering at $\boldsymbol{q}_1 = \Sigma(\frac{1}{4}\,\frac{1}{4}\,0)$ and $\boldsymbol{q}_1' = S(\frac{1}{4}\,\frac{1}{4}\,\frac{1}{2})$. On the other hand, there are strong modes at the $R(\frac{1}{2}\,\frac{1}{2}\,\frac{1}{2})$, $X(0\,0\,\frac{1}{2})$ and Γ points, with the latter showing a clear dispersion across the Brillouin zone. This second set of excitation does not conform to the theory of localized multipolar excitations proposed by Thalmeier *et al.* [251, 254], but must arise from the heavy-fermion ground state, forming at low temperatures. In RPA-based theory, following Akbari *et al.*, the modes can be understood as bound excitons below the onset of the particle-hole continuum of conduction electrons [372, 373]. This onset[26] is created upon consecutive condensations into AFQ, AFM and HF state [372]. It is only in the AFM state that the gapping of the conduction electrons enhances the real part of the low-energy Lindhard susceptibility $\chi_0'(\boldsymbol{q},\omega)$ sufficiently, so that the RPA susceptibility $\chi^{\mathrm{RPA}}(\boldsymbol{q},\omega)$ gathers a pole at

$$1 - J_{\boldsymbol{q}}\chi_0(\boldsymbol{q},\omega_{\mathrm{R}}) = 0 \tag{6.12}$$

which produces the sharp, almost resolution limited excitations in the spectrum at Γ and $R(\frac{1}{2}\,\frac{1}{2}\,\frac{1}{2})$ (and presumably X) [372]. Furthermore, the exciton can also be observed away from these wave vectors, carrying less intensity. Further support for the itinerant interpretation is given by the observation of a broad high-energy mode $\hbar\omega_2$, accompanying the exciton for all wave vectors. This mode can be assigned to the AFM charge gap Δ_{AFM}, since it is only observed below T_{N}. In magnetic field it is suppressed in energy and vanishes above B_{c}. This naturally explains the increase of the exciton linewidth in magnetic field by the activation of particle-hole scattering upon closure of the charge gap.

Although the model of Akbari *et al.* addresses key experimental observations, it is a phenomenological theory, since it requires the interaction term $J_{\boldsymbol{q}}$ in equation 6.12 as an input. This interaction term can contain contributions from the direct exchange, the RKKY interaction between the localized f-spins, low-energy excitations at nesting

[26] In the text referred to as the AFM charge Δ_{AFM}.

vectors $\boldsymbol{Q}$ of the Fermi surface, and from the coupling constants K_{ex}, K_{quad} and K_{oct} of the mean-field multipolar model [230, 235, 246, 254]. Indication for the latter is provided by the transformation of the exciton into the multipolar excitation AFQ_1 above B_{c}. Its energy $\hbar\omega_{\mathrm{II},1}$ scales linearly in magnetic field. Its zero-field extrapolated value E_0 coincides with the exciton energy $\hbar\omega_R$. Both energy scales decrease equally upon doping with non-magnetic lanthanum, and reach zero close to $x_{\mathrm{c}} = 0.28$, which coincides with the QCP of the AFM ordering in zero field. The knowledge of $J_{\boldsymbol{q}}$ would automatically explain the distribution of the quasielastic intensity in the zero-field AFQ state for $T > T_{\mathrm{N}}$ within the framework of the SCR theory developed for heavy-fermion compounds. However, for a quantitative analysis of the interaction term $J_{\boldsymbol{q}}$, detailed knowledge of the Fermi surface in the AFM state is required, whose determination should be subject of future studies.

Such investigation would hopefully shed light on the origin of the intriguing zero-field $R(\frac{1}{2}\,\frac{1}{2}\,\frac{1}{2})$ Bragg peak that is weak and appears below T_{Q}. It is present in phase II, phase III, phase III′ and phase IV and exhibits a subtle field dependence at the field boundaries. Neither its existence in *zero field* nor its dependence on field can be explained within the multipolar mean-field model. At the moment it is interpreted as a spin-density wave in the conduction electron subspace, but this remains to be confirmed by the measurements of the electronic structure in low magnetic fields.

Another goal of the study was to examine, whether critical fluctuations were associated with the quantum critical point of the AFM phase at (i) the critical field $B_{\mathrm{c}} = 1.1\,\mathrm{T}$ or (ii) the critical La-concentration of $x_{\mathrm{c}} = 0.28$. In case (i) specific heat and and dHvA observed a divergence of the effective mass upon approaching the critical field of the AFM phase [260, 261], which might imply the presence of critical fluctuations. The spin-fluctuation spectrum presented here for the $R(\frac{1}{2}\,\frac{1}{2}\,\frac{1}{2})$ point and the Γ point does not exhibit a softening of the spin fluctuations, since the energy of the exciton remains constant. Rather the transition at B_{c} was interpreted as an itinerant-localized crossover of the spin dynamics, which is manifested in different field evolutions for the exciton (for $B < B_{\mathrm{c}}$) and the AFQ_1 mode (for $B > B_{\mathrm{c}}$). This scenario is different to the case of the field induced antiferromagnetic quantum critical compound in $YbRh_2Si_2$, where at B_{c} not only the magnetic ordering is suppressed, but also the heavy-fermion ground state is formed [383–385].

The QCP in case (ii), accessed at the critical doping level at $x_{\mathrm{c}} = 0.28$, is also not associated with non-Fermi-liquid behavior in transport. However, the zero-field spectrum at the R-point in Fig. 6.16 (d) shows that the spectral weight is shifted to zero, accompanied by the vanishing of the energy scales E_0 and $\hbar\omega_R$. Unlike to the QCP in other heavy-fermion metals, $T = 0$ is not approached within the paramagnetic phase, but within an enigmatic phase IV. Specific heat shows that this phase is antiferromagnetic, since the low-temperature scaling adheres to the $\sim T^3$ law that is also observed in phase III in CeB_6. A singlet phase can also be inferred from the decrease in susceptibility below T_{IV} [287]. At the moment antiferrooctupolar order (T^β-octupoles) is considered to be a likely candidate for the order parameter of phase IV [305]. In this

case a first-order transition should be expected between phase IV and phase III because of incompatible symmetries. Instead, a smooth crossover is observed in specific heat *vs.* B and in the AFM Bragg intensity *vs.* B.[27] Thus, the ordering mechanism of phase IV remains "hidden". However, as pointed out here, the spin dynamics in low magnetic fields of $Ce_{1-x}La_xB_6$ can only be understood when including the contributions of the itinerant heavy-fermion quasiparticles, which have been neglected in the persisting mean-field multipolar model [230, 235, 246, 254]. Parallels to the phase diagram of superconducting HF compounds can be drawn, since phase IV in $Ce_{1-x}La_xB_6$, similar to the SC dome in the electronic phase diagrams of $Ce(Rh_{1-x}Co_x)In_5$ or $CeCu_2Si_2$, is surrounding the QCP of the low-temperature antiferromagnetic phase.

[27] Also phase III can be stabilized to zero field via hysteresis loop, creating a mixed phase with phase IV.

7 Summary and Discussion

7.1 Indications of strongly correlated physics in alkali-metal iron chalcogenides superconductors

In this thesis a comprehensive study of the low-energy spin dynamics of the alkali-metal iron selenide superconductors $A_xFe_{2-y}Se_2$ (A=K, Rb) was presented. The result here provide valuable input on the discussion of iron-based superconductors. Currently there is no convention in the research community, whether the iron pnictides should be described in i) a weak-coupling approach, where the magnetism is solely derived from the spin-density-wave instability because of the nesting property of the Fermi surface along $\boldsymbol{Q}_{\mathrm{AFM}} = (\frac{1}{2}\,0)$, or ii) in a strong-coupling picture, where the localized Fe moments can explain the existence of spin excitations up to 300 meV [36, 43]. The experimental investigation of the spin-excitation spectrum of $A_xFe_{2-y}Se_2$ gives evidence for both scenarios.

First, in the iron arsenides, e.g. $Ba(Fe_{1-x}Co_x)_2As_2$, the low-energy magnetic response $\chi(\boldsymbol{q},\omega)$ of the superconducting phase is dominated by the interpocket scattering at $\boldsymbol{Q}_{\mathrm{AFM}} = (\frac{1}{2}\,0)$ between the electron and the hole pocket, which gives rise to static antiferromagnetic order along $\boldsymbol{Q}_{\mathrm{AFM}}$ in a weak-coupling spin-density-wave scenario. Destabilization of the antiferromagnetic order by doping acts as a source of spin fluctuations, which possibly mediate superconductivity. This repulsive interaction would lead to a $s^{\pm}$ symmetry for the superconducting order parameter [15], which changes the sign on both hole and electron pockets. The observation of the resonant mode at $\hbar\omega_{\mathrm{res}}$ in the spectrum at $\boldsymbol{Q}_{\mathrm{AFM}}$, which is a spin-1 bound exciton below the onset of the particle-hole continuum at $2\Delta_{\mathrm{SC}}$, can thus be regarded as a feedback effect of the SC gap on the spin-fluctuation spectrum $\chi''(\boldsymbol{Q}_{\mathrm{AFM}},\omega)$.

An equivalent mechanism for superconductivity in the $A_xFe_{2-y}Se_2$ family of compounds cannot be applied, since the Fermi surface is distinctly different with large squarish electron pockets at the $X(\frac{1}{2}\,0)$ point [4, 7–14], which embodies a strongly overdoped variant of the "122" iron arsenides. Therefore, nesting along $(\frac{1}{2}\,0)$ is not at work. However, it was found here that the magnetic intensity in the normal state above $T_c = 32\,\mathrm{K}$ is concentrated at $\boldsymbol{Q}_r = (\frac{1}{2}\,\frac{1}{4})$, which corresponds to a vector that connects the flat parts of the neighboring electron pockets. Similarly to the iron arsenides, the spectrum constitutes a resonant mode upon changing to the superconducting state. Analogously, the repulsive interaction via the exchange of spin fluctuations between the quasiparticles imposes a sign change of the order parameter between the different pockets. The experimental observation of the resonant mode in the superconducting

state at $\hbar\omega = 14\,\text{meV}$ confirms this line of thought. $d_{x^2-y^2}$- or $s^{\pm}$-wave symmetries of the order parameter that are compatible with the resonant mode have been discussed in literature, since inelastic neutron scattering alone is not able to determine the exact symmetry [3, 386]. Thus, it seems that the occurrence of superconductivity is irrespective of the exact wave vector of the spin fluctuations, which is solely determined by the topology of the Fermi surface.[1]

A recent comprehensive analysis across a wide range of unconventional superconductors, including the strongly coupled heavy fermions and cuprates, found that the superconducting gap 2Δ rather scales with the energy of the peak in the $\boldsymbol{q}$-integrated ("local") spin susceptibility χ'' in the SC state, which in most cases coincides with $\hbar\omega_{\text{res}}$ [5]. Universal ratios of $\hbar\omega_{\text{res}}/2\Delta = 0.64$ and $\hbar\omega_{\text{res}}/k_{\text{B}}T_{\text{c}} = 5.8$ have been recognized for cuprates and heavy-fermion superconductors [5]. For the iron pnictides a similar analysis yields the ratio of $\hbar\omega_{\text{res}}/k_{\text{B}}T_{\text{c}} = 4.3$ [120] [see Fig. 7.1 (a)], with $\hbar\omega_{\text{res}}/2\Delta$ between 1 and 0.64 [43]. The corresponding values for the $A_x\text{Fe}_{2-y}\text{Se}_2$ compounds, assessed here[2] to $\hbar\omega_{\text{res}}/2\Delta = 0.68$ and $\hbar\omega_{\text{res}}/k_{\text{B}}T_{\text{c}} = 5.1$, puts them closer to the strongly coupled regime.

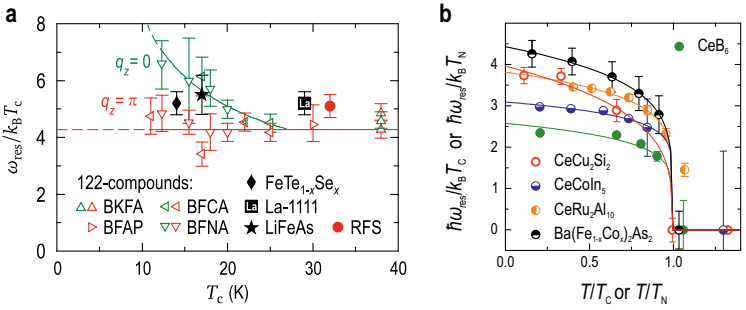

Fig. 7.1: (a) Normalized resonance energy, $\hbar\omega_{\text{res}}/k_{\text{B}}T_{\text{c}}$, in Fe-based superconductors for $q_z = 0$ and $q_z = \pi$. **(b)** Temperature evolution of the resonance energy, normalized with T_{N} (or T_{c}), for unconventional superconductors and HF antiferromagnets. The x-axis has been normalized with the respective transition temperatures. The data points were reproduced from Ref. 354 for CeCoIn_5, from Ref. 355 for CeCu_2Si_2, from Ref. 367 for $\text{CeRu}_2\text{Al}_{10}$ and from Ref. 139 for $\text{Ba}(\text{Fe}_{1-x}\text{Co}_x)_2\text{As}_2$. The panel (a) has been similarly published in Ref. 338, and panel (b) in Ref. 353.

In fact, the alkali-metal iron selenide superconductors (FeSe122) exhibit a number of peculiarities in terms of spin fluctuations that distinguish them even more from the iron arsenides.

- While the normal-state spin-fluctuation spectrum χ'' of the FeAs compounds can

[1] The strongly hole doped variant KFe_2As_2 ($T_{\text{c}} = 3.8\,\text{K}$) [387], where the spin fluctuations are longitudinally incommensurate at $\boldsymbol{Q} = (\frac{1}{2} \pm \delta\, 0)$, $\delta = 0.16$ [121], supports this conclusion.

[2] with a T_{c} of 32 K and a superconducting gap determined from ARPES of $2\Delta = 20.6\,\text{meV}$ [4].

be described by Moriya's formula of a nearly antiferromagnetic metals [139], the corresponding one of the FeSe122 exhibits a peculiar suppression at low energies. This could be interpreted by the existence of a precursor superconducting gap above T_c. A similar observation, known as the pseudogap, has been documented for underdoped $YBa_2Cu_3O_{6+x}$ (x = 0.6–0.7 [335, 344]).

- The integrated spectral weight of the resonance peak, corresponding to the fluctuating moment $\langle m^2 \rangle$, was determined to approximately $(0.069 \pm 0.035)\ \mu_B^2$/f.u., when normalizing to the superconducting volume fraction. This again compares with the value of $0.069\mu_B^2$/f.u. found in underdoped $YBa_2Cu_3O_{6+x}$ (x = 0.5) [335], but is 2–3 times larger than the corresponding moment found in optimally doped iron arsenides (e.g. $Ba(Fe_{1-x}Co_x)_2As_2$ [139]).[3]

- The superconducting phase is only the minority phase and other variants of the 122 structure with ordered iron vacancies have been observed. For instance, in $A_{0.8}Fe_{1.6}Se_2$ (equivalent to $A_2Fe_4Se_5$) the 20% vacancies order into a $\sqrt{5} \times \sqrt{5}$ superstructure [195, 200, 201, 388]. However, the reciprocal-space structure of the spin fluctuations is not reconstructed by any superstructure, implying a $A_xFe_2Se_2$ stoichiometry for the SC phase. The required amount of alkali-metal atoms would be x = 0.36 in order to reproduce the wave vector of the resonant mode.

- For all samples of $A_xFe_{2-y}Se_2$ (A=K, Rb), studied here, the wave vector $\boldsymbol{Q}_r$ of the resonant mode is found to be independent of the composition. Moreover, T_c remains constant when varying the Fe content or the Fe valence [64, 178], which is contrary to the extended superconducting dome *vs.* doping in the iron arsenides. These observations reveal a unique superconducting phase that is presumably selected and stabilized by the mesoscopic phase separation.

Since a phase-pure phase diagram of the SC phase cannot be studied, it is difficult to identify a parent compound for the $A_xFe_{2-y}Se_2$ superconductors. A semiconducting phase was identified as a candidate. It has a band gap of 40 meV and shares a similar electronic structure with the SC phase [389]. Neutron diffraction determined this phase to have a $K_{0.85}Fe_{1.54}Se_2$ composition, where the 25% Fe vacancies order into a 2×2 superstructure [324]. The moments were found to align in a stripe antiferromagntic pattern with a propagation vector of $\boldsymbol{q} = (\frac{1}{2}\ 0\ \frac{1}{2})$ [324]. In contrast to pnictide parent compounds the moment size of $\mu = 2.8\mu_B$ in combination with a high Neél temperature of T_N = 280 K is too large to be explained by a nesting scenario [324]. Theoretical analysis suggested that this compound is a Mott insulator [390].

Moreover, ARPES measurements found that the superconducting compounds exhibit an orbital-selective Mott phase (OSMP) by observing a strongly renormalized d_{xy} band at the $X(\frac{1}{2}\ 0)$ point, which loses spectral weight upon warming to 150 K [8, 346].

[3] The large uncertainty results from the different estimates for the superconducting volume fraction in literature, ranging between 12% and 20% [204, 205].

The inelastic neutron scattering results presented here give further evidence for the viewpoint that the $A_xFe_{2-y}Se_2$ superconductors are more correlated than the iron pnictides. Especially the emerging experimental evidence for an incipient Mott phase and an OSMP [8, 346] implies that there might be a coexistence of itinerant and localized electrons in the superconducting compounds. The observation of a resonant mode at the nesting vector of the Fermi surface can be understood in a weak-coupling approach [3] analogous to the iron pnictides. However, it seems that for reaching a higher T_c the tendency towards the formation of localized spins is important [36]. In this respect it should be noted that single layer FeSe films, which have a similar Fermi surface as the $A_xFe_{2-y}Se_2$ compounds, exhibit a fairly high T_c of (65 ± 5) K [22, 391].

7.2 The exciton in CeB_6 as a fingerprint for itinerant spin dynamics

CeB_6, unlike the iron pnictides, has long been described as a Kondo lattice, where localized spins are immersed into a sea of conduction electrons. Their dipolar and quadrupolar moments are coupled via the RKKY interaction, leading to an ordering into an antiferroquadrupolar state below $T_Q = 3.2$ K and an antiferromagnetic state below $T_N = 2.3$ K. The magnetic phase diagram and the multipolar spin excitations in high fields $B > B_Q$ can be understood in the mean-field multipolar model [235, 246, 251]. However, the spin excitations in the AFM phase were shown to be dominated by intense itinerant modes appearing below T_N at the $R(\frac{1}{2}\,\frac{1}{2}\,\frac{1}{2})$ point, $X(0\,0\,\frac{1}{2})$ point and the Γ point, rather than the spin waves associated with the antiferromagnetic order. Most of the experiments presented in this thesis were focused on the sharp, weakly dispersing mode at the $R(\frac{1}{2}\,\frac{1}{2}\,\frac{1}{2})$ point at $\hbar\omega_R = 0.48$ meV. This excitation shows an order-parameter-like temperature dependence upon warming into the AFQ phase across T_N, which resembles the phenomenology observed for the resonant modes in the superconducting state of the heavy-fermion and iron-pnictide superconductors, as shown in Fig. 7.1 (b). Therefore, it has been similarly interpreted as a bound exciton below the onset of the particle-hole continuum at the AFM charge gap Δ_{AFM}. The ratios of the exciton energy and the AFM energy scales of $\hbar\omega_R/\Delta_{AFM} = 0.48\,\text{meV}/0.95\,\text{meV} = 0.51$ and $\hbar\omega_R/k_BT_N = 2.5$ are far from the equivalent values, assessed for the Fe-based, cuprate and heavy-fermion superconductors.[4] However, such a comparison is too crude, since the exciton is observed within an *antiferromagnetic* phase and not a superconducting phase. For the superconductors it was argued that $\hbar\omega_{res}$ defines the energy scale for the electron-boson spectral function, which eventually determines the size of Δ [5]. In contrast, the size of Δ_{AFM} CeB_6 is constituted by the AFM, AFQ and the hybridization gap. It depends on too many parameters and consequently has to be considered as an empirical quantity [372]. The gaps are created by the ordering in the localized f-electron channel. Therefore, the

[4] An even smaller ratio of 0.4 is obtained if one takes the gap size of $\Delta = 1.2$ meV determined from point-contact spectroscopy [264].

spin dynamics of CeB_6 reveal an intriguing interplay between itinerant and localized quasiparticles.

The exciton itself is a property of the antiferromagnetic phase. This extends the range of phases, where such exciton modes are observed, beyond the superconducting phase. Thus, their presence is not a sufficient condition for unconventional superconductivity. A speciality of CeB_6 is the fact that the exciton feature and the AFM gap $\Delta_{\mathrm{AFM}}(\boldsymbol{q})$ are dispersing and observable throughout the Brillouin zone unlike the superconductors, where the spin fluctuations are concentrated around the antiferromagnetic wave vector. It will be challenging to derive, based on first principles, an interaction $J_{\boldsymbol{q}}$ between the itinerant quasiparticles, so that the transformation of the spin dynamics $\chi''(\boldsymbol{q},\omega)$ upon the opening of the AFM charge gap is consistently described in an RPA-based theory.

Appendix

A.1 Spin excitations in $A_xFe_{2-y}Se_2$

A.1.1 Polarized inelastic neutron scattering on $Rb_{0.8}Fe_{1.6}Se_2$

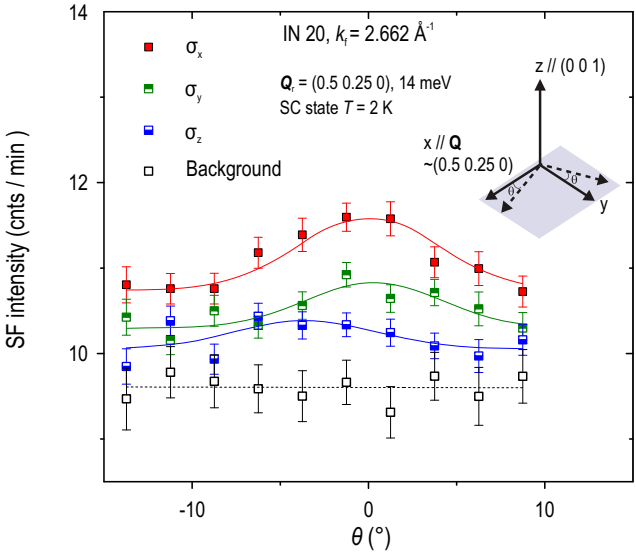

Fig. A.1: Spin-flip (SF) scattering intensity of the resonant mode in $Rb_{0.8}Fe_{1.6}Se_2$, at $\boldsymbol{Q}_r = (\frac{1}{2}\ \frac{1}{4}\ 0)$ and $E = 14$ meV. The coordinate system for the direction of the incoming spin is defined in the sketch (e.g. the x-axis coincides with $\boldsymbol{Q}$, the z-direction is the out-of-plane direction[1]). In the definition of the cross sections σ_α, the index denotes the direction of the neutron spin. E.g. σ_x probes both the fluctuation of the moments $M_y = \langle m_y \rangle^2$ and $M_z = \langle m_z \rangle^2$, whereas σ_y only probes the fluctuations perpendicular to the plane. By measuring all three SF channels one can estimate the background, which is channel independent: $\sigma_{BG} = +\sigma_y + \sigma_z - \sigma_x$. The data not only reveals the purely magnetic intensity of the resonant mode, but also a slight anisotropy for in-plane and out-of-plane fluctuations. The experiment has been performed at IN20 (ILL, Grenoble), utilizing the Cryopad setup.

[1] This convention follows the literature [152, 153].

A.1.2 Q-structure and T-dependence of the LE mode in $K_{0.77}Fe_{1.85}Se_2$

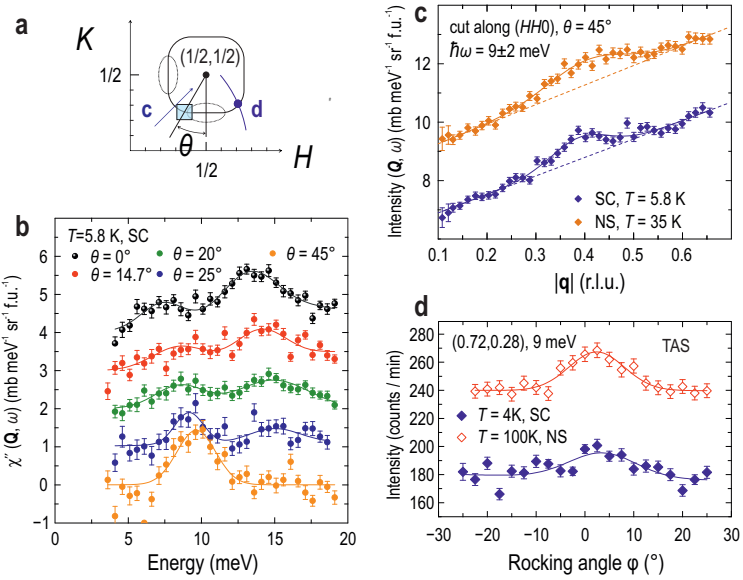

Fig. A.2: This figure elucidates the $\boldsymbol{Q}$ structure and the temperature dependence of the LE mode, which was found at $E = 7.5\,\mathrm{meV}$ and at the wave vector of the resonant mode $\boldsymbol{Q}_r = (\frac{1}{2}\ \frac{1}{4})$. It has a ring-like structure centered at $\boldsymbol{q} = (\frac{1}{2}\ \frac{1}{2})$. **(a)** Sketch of the $\boldsymbol{Q}$-structure of the LE mode (black line) and the resonant mode (dashed lines). The square denotes the position of the energy cuts in panel (b) and the arrows point out the momentum cuts in panel (c) and (d). **(b)** Background and Bose-factor corrected energy cuts along the ring-shaped structure of the LE mode in the SC state, integrated over a square with a width of 0.1 r.l.u. and shifted by 1 unit for clarity. The resonance wave vector corresponds to $\theta = 0°$. **(c)** Momentum cuts along $(H\,H\,0)$ at the LE mode energy $\hbar\omega = (9 \pm 2)\,\mathrm{meV}$ for SC and normal states. **(d)** Rocking scan at $E = 9\,\mathrm{meV}$ intersecting the LE mode in the second Brillouin zone [see panel (a)] at low ($T = 4\,\mathrm{K}$) and at high temperatures ($T = 100\,\mathrm{K}$). The increase of intensity towards high temperatures implies that the LE mode is a phonon. The data of panels (b) and (c) were collected at MERLIN. Panel (d) was measured at PUMA. The data were similarly published in Ref. 341.

A.2 Measurements on CeB_6

A.2.1 Magnetic-field dependence of the spin excitations at $R(\frac{1}{2}\,\frac{1}{2}\,\frac{1}{2})$

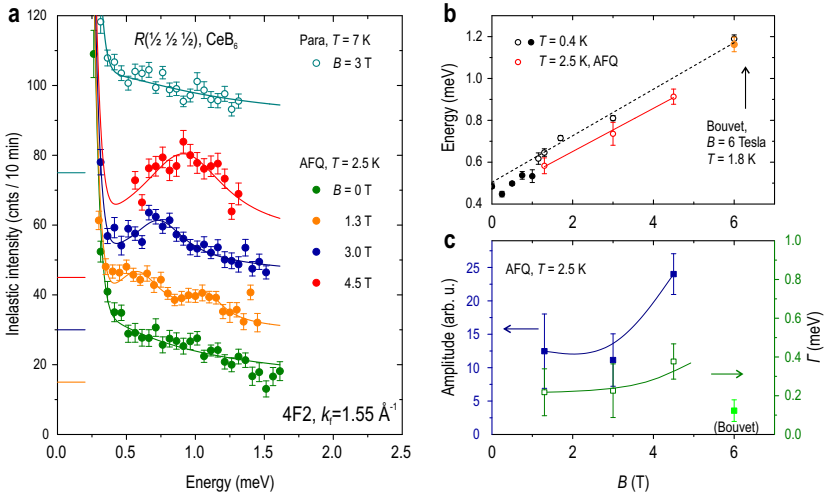

Fig. A.3: **(a)** Spectrum at $R(\frac{1}{2}\,\frac{1}{2}\,\frac{1}{2})$ for various magnetic fields $\boldsymbol{B} \parallel (1\,\bar{1}\,0)$ in the AFQ state of CeB_6 (T = 2.5 K). The spectra have been shifted by 15 cts for clarity. The solid lines correspond to fits comprising a quasielastic and Lorentzian contribution. The spectrum at the top was measured in the paramagnetic state at T = 7 K for comparison. **(b)** Field dependence of the AFQ_1 excitation energy $\hbar\omega_{III}$ obtained from the spectra in panel (a). For comparison the energies of the exciton and the AFQ_1 mode *vs.* field at low temperatures are plotted as well. **(c)** Field dependence of the amplitude and Γ ($\hat{=}$ HWHM) for the AFQ_1 mode obtained from the fits in panel (a). The increase in amplitude can be related to the redistribution of the quasielastic intensity into the AFQ_1 peak. Note that the linewidth of $\Gamma = (0.38 \pm 0.09)$ meV at B = 4.5 Tesla is significantly larger than the one at low temperatures $\Gamma(T = 0.4\,\mathrm{K}) = (0.09 \pm 0.02)$ meV.

Physical constants

$\mu_B = 5.788 \times 10^{-2}\,\mathrm{meVT^{-1}}$	... Bohr magneton
$\mu_N = 3.153 \times 10^{-5}\mathrm{meVT^{-1}}$	... nuclear magneton
$\hbar = h/2\pi = 6.626/2\pi \times 10^{-34}\,\mathrm{Js}$	... reduced Planck constant
$k_B = 1.38064 \times 10^{-23}\,\mathrm{J/K}$	... Boltzmann constant
$1\,\mathrm{eV} = 1.6021766 \times 10^{-19}\,\mathrm{J}$	... Electronvolt
$1\,\mathrm{b} = 10^{-24}\,\mathrm{cm}^2$	... 1 barn (unit of the cross section)
$1\,\mathrm{Oe} \mathrel{\hat{=}} 10^{-4}\,\mathrm{T}$	... 1 Oersted (unit of H-field)

Bibliography

[1] J. Guo et al., Phys. Rev. B **82**, 180520 (2010).

[2] Y. Kamihara, T. Watanabe, M. Hirano, and H. Hosono, J. Am. Chem. Soc. **130**, 3296 (2008).

[3] T. A. Maier, S. Graser, P. J. Hirschfeld, and D. J. Scalapino, Phys. Rev. B **83**, 100515 (2011).

[4] Y. Zhang et al., Nat. Mater. **10**, 273 (2011).

[5] G. Yu, Y. Li, E. M. Motoyama, and M. Greven, Nat. Phys. **5**, 873 (2009).

[6] M. Eschrig, Adv. Phys. **55**, 47 (2006).

[7] L. Zhao et al., Phys. Rev. B **83**, 140508 (2011).

[8] M. Yi et al., Phys. Rev. Lett. **110**, 067003 (2013).

[9] M. Xu et al., Phys. Rev. B **85**, 220504 (2012).

[10] X.-P. Wang et al., EPL **93**, 57001 (2011).

[11] D. Mou et al., Phys. Rev. Lett. **106**, 107001 (2011).

[12] Z.-H. Liu et al., Phys. Rev. Lett. **109**, 037003 (2012).

[13] X.-P. Wang et al., EPL **99**, 67001 (2012).

[14] J. Maletz et al., Phys. Rev. B **88**, 134501 (2013).

[15] I. I. Mazin, D. J. Singh, M. D. Johannes, and M. H. Du, Phys. Rev. Lett. **101**, 057003 (2008).

[16] Y. Texier et al., Phys. Rev. Lett. **108**, 237002 (2012).

[17] M. Planck, Annalen der Physik **4**, 553 (1901).

[18] W. Buckel and R. Kleiner, *Supraleitung. Grundlagen und Anwendung.*, Wiley-VCH, 6 edition, 2004.

[19] J. G. Bednorz and K. A. Mueller, Z. Phys. B Con. Mat. **64**, 189 (1986).

[20] A. Schilling, M. Cantoni, J. D. Guo, and H. R. Ott, Nature **363**, 56 (1993).

[21] F. Steglich et al., Phys. Rev. Lett. **43**, 1892 (1979).

[22] S. He et al., Nat. Mater. **12**, 605 (2013).

[23] J. Bardeen, L. N. Cooper, and J. R. Schrieffer, Phys. Rev. **108**, 1175 (1957).

[24] W. L. McMillan, Phys. Rev. **167**, 331 (1968).

[25] L. Boeri, O. V. Dolgov, and A. A. Golubov, Phys. Rev. Lett. **101**, 026403 (2008).

[26] C. C. Tsuei and J. R. Kirtley, Rev. Mod. Phys. **72**, 969 (2000).

[27] J. Paglione and R. L. Greene, Nat. Phys. **6**, 645 (2010).

[28] G. R. Stewart, Rev. Mod. Phys. **83**, 1589 (2011).

[29] D. Scalapino, Phys. Rep. **250**, 329 (1995).

[30] R. Coldea et al., Phys. Rev. Lett. **86**, 5377 (2001).

[31] J. M. Tranquada et al., Nature **429**, 534 (2004).

[32] S. M. Hayden, H. A. Mook, P. Dai, T. G. Perring, and F. Dogan, Nature **429**, 531 (2004).

[33] M. Le Tacon et al., Nat. Phys. **7**, 725 (2011).

[34] T. Dahm et al., Nat. Phys. **5**, 217 (2009).

[35] M. Vojta, Nat. Phys. **5**, 623 (2009).

[36] P. Dai, J. Hu, and E. Dagotto, Nat. Phys. **8**, 709 (2012).

[37] J. Chang et al., Nat. Phys. **8**, 871 (2012).

[38] G. Ghiringhelli et al., Science **337**, 821 (2012).

[39] D. Haug et al., Phys. Rev. Lett. **103**, 017001 (2009).

[40] T. Timusk and B. Statt, Rep. Prog. Phys. **62**, 61 (1999).

[41] H. F. Fong et al., Phys. Rev. Lett. **75**, 316 (1995).

[42] J. Rossat-Mignod et al., Physica C **185-189, Part 1**, 86 (1991).

[43] D. S. Inosov et al., Phys. Rev. B **83**, 214520 (2011).

[44] N. K. Sato et al., Nature **410**, 340 (2001).

[45] V. S. Zapf et al., Phys. Rev. B **65**, 014506 (2001).

[46] N. D. Mathur et al., Nature **394**, 39 (1998).

[47] J. A. Mydosh and P. M. Oppeneer, Rev. Mod. Phys. **83**, 1301 (2011).

[48] K. Kuwahara et al., Phys. Rev. Lett. **95**, 107003 (2005).

[49] Y. Kuramoto, H. Kusunose, and A. Kiss, J. Phys. Soc. Jpn. **78**, 072001 (2009).

[50] P. Fazekas, *Electron Correlation and Magnetism*, World Scientific, 1999.

[51] T. Moriya and T. Takimoto, J. Phys. Soc. Jpn. **64**, 960 (1995).

[52] E. Dagotto, Rev. Mod. Phys. **85**, 849 (2013).

[53] Y. Kamihara et al., J. Am. Chem. Soc. **128**, 10012 (2006).

[54] S. Lebègue, Phys. Rev. B **75**, 035110 (2007).

[55] D. J. Singh and M.-H. Du, Phys. Rev. Lett. **100**, 237003 (2008).

[56] D. J. Singh, Phys. Rev. B **78**, 094511 (2008).

[57] A. S. Sefat et al., Phys. Rev. Lett. **101**, 117004 (2008).

[58] X. F. Wang et al., Phys. Rev. Lett. **102**, 117005 (2009).

[59] C. W. Chu, Nat. Phys. **5**, 787 (2009).

[60] N. Ni, J. M. Allred, B. C. Chan, and R. J. Cava, Proc. Natl. Acad. Sci. **108**, E1019 (2011).

[61] F.-C. Hsu et al., Proc. Natl. Acad. Sci. **105**, 14262 (2008).

[62] B. C. Sales et al., Phys. Rev. B **79**, 094521 (2009).

[63] R. H. Liu et al., EPL **94**, 27008 (2011).

[64] V. Tsurkan et al., Phys. Rev. B **84**, 144520 (2011).

[65] A. F. Wang et al., Phys. Rev. B **83**, 060512 (2011).

[66] J. J. Ying et al., Phys. Rev. B **83**, 212502 (2011).

[67] J.-H. Chu, J. G. Analytis, C. Kucharczyk, and I. R. Fisher, Phys. Rev. B **79**, 014506 (2009).

[68] C. de la Cruz et al., Nature **453**, 899 (2008).

[69] Q. Huang et al., Phys. Rev. Lett. **101**, 257003 (2008).

[70] M. Rotter et al., Phys. Rev. B **78**, 020503 (2008).

[71] N. Ni et al., Phys. Rev. B **78**, 214515 (2008).

[72] S. Aswartham et al., J. Cryst. Growth **314**, 341 (2011).

[73] X. F. Wang et al., New J. Phys. **11**, 045003 (11pp) (2009).

[74] M. A. Kastner, R. J. Birgeneau, G. Shirane, and Y. Endoh, Rev. Mod. Phys. **70**, 897 (1998).

[75] C. Cao, P. J. Hirschfeld, and H.-P. Cheng, Phys. Rev. B **77**, 220506 (2008).

[76] F. Ma and Z.-Y. Lu, Phys. Rev. B **78**, 033111 (2008).

[77] C. Hess et al., EPL **87**, 17005 (2009).

[78] G. Friemel, Transportmessungen an 122-eisenarsenid-supraleitern, Master's thesis, TU Dresden, 2010.

[79] Q. Si and E. Abrahams, Phys. Rev. Lett. **101**, 076401 (2008).

[80] T. Yildirim, Phys. Rev. Lett. **101**, 057010 (2008).

[81] A. N. Yaresko, G.-Q. Liu, V. N. Antonov, and O. K. Andersen, Phys. Rev. B **79**, 144421 (2009).

[82] M. Yi et al., Phys. Rev. B **80**, 174510 (2009).

[83] D. C. Johnston, Adv. Phys. **59**, 803 (2010).

[84] R. Klingeler et al., Phys. Rev. B **81**, 024506 (2010).

[85] G. M. Zhang et al., EPL **86**, 37006 (2009).

[86] J. Chaloupka and G. Khaliullin, Phys. Rev. Lett. **110**, 207205 (2013).

[87] M. M. Korshunov, I. Eremin, D. V. Efremov, D. L. Maslov, and A. V. Chubukov, Phys. Rev. Lett. **102**, 236403 (2009).

[88] P. Richard et al., Phys. Rev. Lett. **104**, 137001 (2010).

[89] M. Yi et al., Proc. Natl. Acad. Sci. **108**, 6878 (2011).

[90] L. X. Yang et al., Phys. Rev. Lett. **102**, 107002 (2009).

[91] G. Liu et al., Phys. Rev. B **80**, 134519 (2009).

[92] T. Kondo et al., Phys. Rev. B **81**, 060507 (2010).

[93] Y. Nakashima et al., Solid State Commun. **157**, 16 (2013).

[94] C. Liu et al., Phys. Rev. Lett. **102**, 167004 (2009).

[95] S. T. Cui et al., Phys. Rev. B **86**, 155143 (2012).

[96] M. Yi et al., New J. Phys. **14**, 073019 (2012).

[97] C. He et al., Phys. Rev. Lett. **105**, 117002 (2010).

[98] S. V. Borisenko et al., Phys. Rev. Lett. **105**, 067002 (2010).

[99] T. Shimojima et al., Phys. Rev. Lett. **104**, 057002 (2010).

[100] Y. Xia et al., Phys. Rev. Lett. **103**, 037002 (2009).

[101] C. Liu et al., Nat. Phys. **6**, 419 (2010).

[102] T. Sudayama et al., Phys. Rev. Lett. **104**, 177002 (2010).

[103] M. Yi et al., Phys. Rev. B **80**, 024515 (2009).

[104] V. Brouet et al., Phys. Rev. B **80**, 165115 (2009).

[105] W. Malaeb et al., J. Phys. Soc. Jpn. **78**, 123706 (2009).

[106] Y. Zhang et al., Phys. Rev. B **83**, 054510 (2011).

[107] C. Liu et al., Phys. Rev. B **84**, 020509 (2011).

[108] V. B. Zabolotnyy et al., Nature **457**, 569 (2009).

[109] D. V. Evtushinsky et al., J. Phys. Soc. Jpn. **80**, 023710 (2011).

[110] T. Sato et al., Phys. Rev. Lett. **103**, 047002 (2009).

[111] T. Yoshida et al., Phys. Rev. Lett. **106**, 117001 (2011).

[112] A. Tamai et al., Phys. Rev. Lett. **104**, 097002 (2010).

[113] K. Kuroki et al., Phys. Rev. Lett. **101**, 087004 (2008).

[114] J. Dong et al., EPL **83**, 27006 (2008).

[115] W. Z. Hu et al., Phys. Rev. Lett. **101**, 257005 (2008).

[116] L. Fang et al., Phys. Rev. B **80**, 140508 (2009).

[117] J. G. Analytis, J.-H. Chu, R. D. McDonald, S. C. Riggs, and I. R. Fisher, Phys. Rev. Lett. **105**, 207004 (2010).

[118] J. G. Analytis et al., Phys. Rev. B **80**, 064507 (2009).

[119] T. Terashima et al., Phys. Rev. Lett. **107**, 176402 (2011).

[120] J. T. Park et al., Phys. Rev. B **82**, 134503 (2010).

[121] C. H. Lee et al., Phys. Rev. Lett. **106**, 067003 (2011).

[122] C. Lester et al., Phys. Rev. B **79**, 144523 (2009).

[123] P. C. Canfield, S. L. Bud'ko, N. Ni, J. Q. Yan, and A. Kracher, Phys. Rev. B **80**, 060501 (2009).

[124] S. Graser et al., Phys. Rev. B **81**, 214503 (2010).

[125] C. Lester et al., Phys. Rev. B **81**, 064505 (2010).

[126] H.-F. Li et al., Phys. Rev. B **82**, 140503 (2010).

[127] E. Fawcett, H. L. Alberts, V. Y. Galkin, D. R. Noakes, and J. V. Yakhmi, Rev. Mod. Phys. **66**, 25 (1994).

[128] C. Lester et al., Phys. Rev. B **84**, 134514 (2011).

[129] K. Prokes et al., EPL **93**, 32001 (2011).

[130] M. D. Lumsden et al., Phys. Rev. Lett. **102**, 107005 (2009).

[131] L. W. Harriger et al., Phys. Rev. Lett. **103**, 087005 (2009).

[132] F. Ning et al., J. Phys. Soc. Jpn. **78**, 013711 (2009).

[133] F. L. Ning et al., Phys. Rev. Lett. **104**, 037001 (2010).

[134] Y. Nakai et al., Phys. Rev. Lett. **105**, 107003 (2010).

[135] T. Iye et al., Phys. Rev. B **85**, 184505 (2012).

[136] T. Oka et al., Phys. Rev. Lett. **108**, 047001 (2012).

[137] F. Hammerath et al., Phys. Rev. B **88**, 104503 (2013).

[138] T. Moriya, *Spin Fluctuations in Itinerant Electron Magnetism*, Springer, 1985.

[139] D. S. Inosov et al., Nat. Phys. **6**, 178 (2010).

[140] T. A. Maier, S. Graser, D. J. Scalapino, and P. Hirschfeld, Phys. Rev. B **79**, 134520 (2009).

[141] M. G. Kim et al., Phys. Rev. Lett. **110**, 177002 (2013).

[142] C. Zhang et al., Sci. Rep. **1**, (2011).

[143] A. D. Christianson et al., Nature **456**, 930 (2008).

[144] J.-P. Castellan et al., Phys. Rev. Lett. **107**, 177003 (2011).

[145] A. D. Christianson et al., Phys. Rev. Lett. **103**, 087002 (2009).

[146] D. K. Pratt et al., Phys. Rev. B **81**, 140510 (2010).

[147] G. S. Tucker et al., Phys. Rev. B **86**, 024505 (2012).

[148] P. Steffens et al., Phys. Rev. Lett. **110**, 137001 (2013).

[149] M. Liu et al., Nat. Phys. **8**, 376 (2012).

[150] S. Chi et al., Phys. Rev. Lett. **102**, 107006 (2009).

[151] S. Li et al., Phys. Rev. B **79**, 174527 (2009).

[152] O. J. Lipscombe et al., Phys. Rev. B **82**, 064515 (2010).

[153] M. Liu et al., Phys. Rev. B **85**, 214516 (2012).

[154] H. Luo et al., Phys. Rev. B **86**, 024508 (2012).

[155] J. Zhao et al., Phys. Rev. Lett. **110**, 147003 (2013).

[156] M. Ishikado et al., Physica C **471**, 643 (2011).

[157] C. H. Lee et al., Phys. Rev. Lett. **111**, 167002 (2013).

[158] N. Qureshi et al., Phys. Rev. Lett. **108**, 117001 (2012).

[159] C. Zhang et al., Phys. Rev. B **88**, 064504 (2013).

[160] C. Zhang et al., Phys. Rev. Lett. **111**, 207002 (2013).

[161] D. N. Argyriou et al., Phys. Rev. B **81**, 220503 (2010).

[162] S. Li et al., Phys. Rev. Lett. **105**, 157002 (2010).

[163] K. Prokeš et al., Phys. Rev. B **86**, 064503 (2012).

[164] Y. Qiu et al., Phys. Rev. Lett. **103**, 067008 (2009).

[165] P. Babkevich et al., J. Phys.: Condens. Matter **22**, 142202 (2010).

[166] P. Babkevich et al., Phys. Rev. B **83**, 180506 (2011).

[167] L. W. Harriger et al., Phys. Rev. B **85**, 054511 (2012).

[168] H. A. Mook et al., Phys. Rev. Lett. **104**, 187002 (2010).

[169] M. D. Lumsden et al., Nat. Phys. **6**, 182 (2010).

[170] Z. Xu et al., Phys. Rev. B **84**, 052506 (2011).

[171] Z. Xu et al., Phys. Rev. B **82**, 104525 (2010).

[172] N. Tsyrulin et al., New J. Phys. **14**, 073025 (2012).

[173] Z. Xu et al., Phys. Rev. Lett. **109**, 227002 (2012).

[174] M. M. Korshunov and I. Eremin, Phys. Rev. B **78**, 140509 (2008).

[175] T. A. Maier and D. J. Scalapino, Phys. Rev. B **78**, 020514 (2008).

[176] S. Graser, T. A. Maier, P. J. Hirschfeld, and D. J. Scalapino, New J. Phys. **11**, 025016 (2009).

[177] X. G. Luo et al., New J. Phys. **13**, 053011 (2011).

[178] Y. J. Yan et al., Sci. Rep. **2**, (2012).

[179] B. Zeng et al., Phys. Rev. B **83**, 144511 (2011).

[180] D. M. Wang, J. B. He, T.-L. Xia, and G. F. Chen, Phys. Rev. B **83**, 132502 (2011).

[181] Z. Shermadini et al., Phys. Rev. Lett. **106**, 117602 (2011).

[182] D. H. Ryan et al., Phys. Rev. B **83**, 104526 (2011).

[183] I. Mazin, Physics **4**, 26 (2011).

[184] T. Qian et al., Phys. Rev. Lett. **106**, 187001 (2011).

[185] H. Kotegawa et al., J. Phys. Soc. Jpn. **80**, 043708 (2011).

[186] H. Kotegawa et al., J. Phys. Soc. Jpn. **81**, 104712 (2012).

[187] L. Ma et al., Phys. Rev. B **84**, 220505 (2011).

[188] L. Ma et al., Phys. Rev. B **83**, 174510 (2011).

[189] D. A. Torchetti et al., Phys. Rev. B **83**, 104508 (2011).

[190] W. Yu et al., Phys. Rev. Lett. **106**, 197001 (2011).

[191] X.-W. Yan, M. Gao, Z.-Y. Lu, and T. Xiang, Phys. Rev. B **83**, 233205 (2011).

[192] W. Bao et al., Chinese Phys. Lett. **28**, 086104 (2011).

[193] M. Wang et al., Phys. Rev. B **84**, 094504 (2011).

[194] V. Y. Pomjakushin et al., Phys. Rev. B **83**, 144410 (2011).

[195] F. Ye et al., Phys. Rev. Lett. **107**, 137003 (2011).

[196] V. Svitlyk et al., Inorg. Chem. **50**, 10703 (2011).

[197] C. Cao and J. Dai, Phys. Rev. Lett. **107**, 056401 (2011).

[198] A. Bosak et al., Phys. Rev. B **86**, 174107 (2012).

[199] X. Ding et al., Nat Commun **4**, 1897 (2013).

[200] Y. J. Song et al., EPL **95**, 37007 (2011).

[201] Z. Wang et al., Phys. Rev. B **83**, 140505 (2011).

[202] W. Li et al., Nat. Phys. **8**, 126 (2012).

[203] W. Li et al., Phys. Rev. Lett. **109**, 057003 (2012).

[204] Z. Shermadini et al., Phys. Rev. B **85**, 100501 (2012).

[205] A. Charnukha et al., Phys. Rev. Lett. **109**, 017003 (2012).

[206] C. N. Wang et al., Phys. Rev. B **85**, 214503 (2012).

[207] V. Y. Pomjakushin et al., J. Phys.: Condens. Matter **24**, 435701 (2012).

[208] D.-x. Mou, L. Zhao, and X.-j. Zhou, Front. Phys. **6**, 410 (2011).

[209] H.-H. Wen, Rep. Prog. Phys. **75**, 112501 (2012).

[210] S. C. Speller et al., Supercond. Sci. Technol. **25**, 084023 (2012).

[211] G. R. Stewart, Rev. Mod. Phys. **56**, 755 (1984).

[212] P. Popovich et al., Phys. Rev. Lett. **105**, 027003 (2010).

[213] C. Pfleiderer, Rev. Mod. Phys. **81**, 1551 (2009).

[214] H. Q. Yuan et al., Science **302**, pp. 2104 (2003).

[215] F. M. Grosche et al., J. Phys.: Condens. Matter **13**, 2845 (2001).

[216] P. Gegenwart et al., Phys. Rev. Lett. **81**, 1501 (1998).

[217] P. Santini et al., Rev. Mod. Phys. **81**, 807 (2009).

[218] E. D. Bauer, N. A. Frederick, P.-C. Ho, V. S. Zapf, and M. B. Maple, Phys. Rev. B **65**, 100506 (2002).

[219] Y. Aoki et al., J. Phys. Soc. Jpn. **76**, 051006 (2007).

[220] M. Kohgi et al., J. Phys. Soc. Jpn. **72**, 1002 (2003).

[221] K. Matsubayashi et al., Phys. Rev. Lett. **109**, 187004 (2012).

[222] P. Gegenwart, Q. Si, and F. Steglich, Nat. Phys. **4**, 186 (2008).

[223] T. Fujita et al., Solid State Commun. **35**, 569 (1980).

[224] E. Zirngiebl et al., Phys. Rev. B **30**, 4052 (1984).

[225] M. Loewenhaupt, J. Carpenter, and C.-K. Loong, J. Magn. Magn. Mater. **52**, 245 (1985).

[226] F. J. Ohkawa, J. Phys. Soc. Jpn. **54**, 3909 (1985).

[227] H. Nakao et al., J. Phys. Soc. Jpn. **70**, 1857 (2001).

[228] D. Hall, Z. Fisk, and R. G. Goodrich, Phys. Rev. B **62**, 84 (2000).

[229] R. G. Goodrich et al., Phys. Rev. B **69**, 054415 (2004).

[230] M. Sera et al., Phys. Rev. Lett. **86**, 1578 (2001).

[231] J. Rossat-Mignod, *Methods of Experimental Physics: Neutron Scattering in Condensed Matter Research*, volume 23C, Academic Press Inc., 1987.

[232] J. M. Effantin, P. Burlet, J. Rossat-Mignod, S. Kunii, and T. Kasuya, *Valence Instabilities*, North-Holland, Amsterdam, 1982.

[233] H. Kusunose, J. Phys. Soc. Jpn. **77**, 064710 (2008).

[234] J. M. Effantin et al., J. Magn. Magn. Mater. **47-48**, 145 (1985).

[235] R. Shiina, H. Shiba, and P. Thalmeier, J. Phys. Soc. Jpn. **66**, 1741 (1997).

[236] W. Erkelens et al., J. Magn. Magn. Mater. **63-64**, 61 (1987).

[237] N. Sluchanko et al., J. Exp. Theor. Phys. **104**, 120 (2007).

[238] P. Schlottmann, Phys. Rev. B **86**, 075135 (2012).

[239] M. Hiroi, S. ichiro Kobayashi, M. Sera, N. Kobayashi, and S. Kunii, J. Phys. Soc. Jpn. **67**, 53 (1998).

[240] O. Suzuki et al., J. Phys. Soc. Jpn. **74**, 735 (2005).

[241] P. Burlet et al., J. Appl. Phys. **53**, 2149 (1982).

[242] O. Zaharko et al., Phys. Rev. B **68**, 214401 (2003).

[243] R. Feyerherm et al., Physica B **194-196**, 357 (1994).

[244] A. Schenck, F. N. Gygax, G. Solt, O. Zaharko, and S. Kunii, Phys. Rev. Lett. **93**, 257601 (2004).

[245] K. Kunimori et al., J. Phys. Soc. Jpn. **80SA**, SA056 (2011).

[246] M. Sera and S. Kobayashi, J. Phys. Soc. Jpn. **68**, 1664 (1999).

[247] T. Matsumura et al., Phys. Rev. B **85**, 174417 (2012).

[248] R. Shiina, O. Sakai, H. Shiba, and P. Thalmeier, J. Phys. Soc. Jpn. **67**, 941 (1998).

[249] T. Matsumura, T. Yonemura, K. Kunimori, M. Sera, and F. Iga, Phys. Rev. Lett. **103**, 017203 (2009).

[250] S. ichiro Kobayashi, M. Sera, M. Hiroi, N. Kobayashi, and S. Kunii, J. Phys. Soc. Jpn. **68**, 3407 (1999).

[251] P. Thalmeier, R. Shiina, H. Shiba, A. Takahashi, and O. Sakai, J. Phys. Soc. Jpn. **72**, 3219 (2003).

[252] R. Shiina, H. Shiba, P. Thalmeier, A. Takahashi, and O. Sakai, J. Phys. Soc. Jpn. **72**, 1216 (2003).

[253] A. Bouvet, *Étude par diffusion inélastique neutrons des propriétés magnétiques de borures de terre rare: CeB_6, PrB_6 et YbB_{12}*, PhD thesis, Universite Grenoble, 1993.

[254] P. Thalmeier, R. Shiina, H. Shiba, and O. Sakai, J. Phys. Soc. Jpn. **67**, 2363 (1998).

[255] L. Regnault et al., J. Magn. Magn. Mater. **76-77**, 413 (1988).

[256] N. Sato, A. Sumiyama, S. Kunii, H. Nagano, and T. Kasuya, J. Phys. Soc. Jpn. **54**, 1923 (1985).

[257] A. Takase, K. Kojima, T. Komatsubara, and T. Kasuya, Solid State Commun. **36**, 461 (1980).

[258] T. Kobayashi et al., Physica B **281–282**, 553 (2000).

[259] A. Sumiyama et al., J. Phys. Soc. Jpn. **55**, 1294 (1986).

[260] T. Mueller et al., J. Magn. Magn. Mater. **76-77**, 35 (1988).

[261] M. Endo et al., J. Phys. Soc. Jpn. **75**, 114704 (2006).

[262] Y. Onuki, T. Komatsubara, P. H. P. Reinders, and M. Springford, J. Phys. Soc. Jpn. **58**, 3698 (1989).

[263] R. G. Goodrich, N. Harrison, A. Teklu, D. Young, and Z. Fisk, Phys. Rev. Lett. **82**, 3669 (1999).

[264] E. Paulus and G. Voss, J. Magn. Magn. Mater. **47-48**, 539 (1985).

[265] S. Ikeda et al., J. Phys. Soc. Jpn. **76**, 064716 (2007).

[266] N. Brandt et al., Solid State Commun. **56**, 937 (1985).

[267] Y. Ishizawa, T. Tanaka, E. Bannai, and S. Kawai, J. Phys. Soc. Jpn. **42**, 112 (1977).

[268] A. van Deursen, R. Pols, A. de Vroomen, and Z. Fisk, J. Less-Common Met. **111**, 331 (1985).

[269] W. Joss et al., Phys. Rev. Lett. **59**, 1609 (1987).

[270] N. Harrison, P. Meeson, P. A. Probst, and M. Springford, J. Phys.: Condens. Matter **5**, 7435 (1993).

[271] N. Harrison, D. W. Hall, R. G. Goodrich, J. J. Vuillemin, and Z. Fisk, Phys. Rev. Lett. **81**, 870 (1998).

[272] A. A. Teklu et al., Phys. Rev. B **62**, 12875 (2000).

[273] C. McCarthy and C. Tompson, J. Physics Chem. of Solids **41**, 1319 (1980).

[274] R. G. Goodrich, N. Harrison, and Z. Fisk, Phys. Rev. Lett. **97**, 146404 (2006).

[275] Y. Onuki et al., Phys. Rev. B **40**, 11195 (1989).

[276] P. Wahl, Private communication.

[277] S. Nakatsuji, D. Pines, and Z. Fisk, Phys. Rev. Lett. **92**, 016401 (2004).

[278] Y.-f. Yang and D. Pines, Proc. Natl. Acad. Sci. **109**, E3060 (2012).

[279] N. J. Curro, B.-L. Young, J. Schmalian, and D. Pines, Phys. Rev. B **70**, 235117 (2004).

[280] R. Kadono et al., J. Phys. Soc. Jpn. **69**, 3189 (2000).

[281] F. N. Gygax, A. Schenck, G. Solt, and O. Zaharko, Phys. Rev. B **81**, 094434 (2010).

[282] S. Horn et al., Z. Phys. B Con. Mat. **42**, 125 (1981).

[283] V. P. Plakhty et al., Phys. Rev. B **71**, 100407 (2005).

[284] S. V. Demishev et al., Phys. Rev. B **80**, 245106 (2009).

[285] S. V. Demishev, A. V. Semeno, Y. B. Paderno, N. Y. Shitsevalova, and N. E. Sluchanko, Phys. Status Solidi b **242**, R27 (2005).

[286] C. Krellner, T. Förster, H. Jeevan, C. Geibel, and J. Sichelschmidt, Phys. Rev. Lett. **100**, 066401 (2008).

[287] T. Tayama, T. Sakakibara, K. Tenya, H. Amitsuka, and S. Kunii, J. Phys. Soc. Jpn. **66**, 2268 (1997).

[288] K. Kuwahara et al., J. Phys. Soc. Jpn. **76**, 093702 (2007).

[289] D. Mannix, Y. Tanaka, D. Carbone, N. Bernhoeft, and S. Kunii, Phys. Rev. Lett. **95**, 117206 (2005).

[290] T. Furuno, N. Sato, S. Kunii, T. Kasuya, and W. Sasaki, J. Phys. Soc. Jpn. **54**, 1899 (1985).

[291] S. Kobayashi et al., J. Phys. Soc. Jpn. **72**, 2947 (2003).

[292] O. Suzuki, T. Goto, S. Nakamura, T. Matsumura, and S. Kunii, J. Phys. Soc. Jpn. **67**, 4243 (1998).

[293] P. Fischer et al., Phys. Rev. B **72**, 014414 (2005).

[294] K. Iwasa et al., Physica B **329–333, Part 2**, 582 (2003), Proceedings of the 23rd International Conference on Low Temperature Physics.

[295] A. Schenck, F. N. Gygax, and G. Solt, Phys. Rev. B **75**, 024428 (2007).

[296] A. Kondo, H. Tou, M. Sera, F. Iga, and T. Sakakibara, J. Phys. Soc. Jpn. **76**, 103708 (2007).

[297] M. Hiroi, M. Sera, N. Kobayashi, and S. Kunii, Phys. Rev. B **55**, 8339 (1997).

[298] S. ichiro Kobayashi, M. Sera, M. Hiroi, N. Kobayashi, and S. Kunii, J. Phys. Soc. Jpn. **69**, 926 (2000).

[299] S. Nakamura et al., Phys. Rev. Lett. **97**, 237204 (2006).

[300] A. V. Silhanek et al., Phys. Rev. Lett. **96**, 206401 (2006).

[301] S. Nakamura, T. Goto, O. Suzuki, S. Kunii, and S. Sakatsume, Phys. Rev. B **61**, 15203 (2000).

[302] S. Nakamura et al., Phys. Rev. B **68**, 100402 (2003).

[303] B. T. Matthias et al., Science **159**, 530 (1968).

[304] I. Bat'ko et al., J. Alloy. Comp. **217**, L1 (1995).

[305] K. Kubo and Y. Kuramoto, J. Phys. Soc. Jpn. **73**, 216 (2004).

[306] S. W. Lovesey, J. Fernandez-Rodriguez, J. A. Blanco, and Y. Tanaka, Phys. Rev. B **75**, 054401 (2007).

[307] A. Kondo et al., J. Phys. Soc. Jpn. **78**, 093708 (2009).

[308] T. Matsumura et al., Phys. Rev. B **89**, 014422 (2014).

[309] P. Aynajian et al., Nature **486**, 201 (2012).

[310] U. Rössler, *Solid State Theory*, Springer Berlin Heidelberg, 2009.

[311] P. S. Riseborough, Adv. Phys. **49**, 257 (2000).

[312] Y.-f. Yang, Z. Fisk, H.-O. Lee, J. D. Thompson, and D. Pines, Nature **454**, 611 (2008).

[313] P. Coleman, C. Pepin, Q. Si, and R. Ramazashvili, J. Phys.: Condens. Matter **13**, R723 (2001).

[314] O. Stockert et al., Phys. Rev. Lett. **92**, 136401 (2004).

[315] J. Arndt et al., Phys. Rev. Lett. **106**, 246401 (2011).

[316] S. Blundell, *Magnetism in Condensed Matter*, Oxford University Press, 2001.

[317] N. Majlis, *The Quantum Theory of Magnetism*, volume 2, World Scientific Publishing Co. Pte. Ltd., 2007.

[318] R. M. White, *Quantum Theory of Magnetism*, Springer-Verlag Berlin Heidelberg, 3rd edition, 2007.

[319] W. Nolting, *Grundkurs Theoretische Physik 7. Viel-Teilchen-Theorie.*, Springer, 7 edition, 2009.

[320] H. Kadowaki, M. Sato, and S. Kawarazaki, Phys. Rev. Lett. **92**, 097204 (2004).

[321] H. Ibach and H. Lüth, *Festkörperphysik*, Springer, 2002.

[322] N. Bulut and D. J. Scalapino, Phys. Rev. B **53**, 5149 (1996).

[323] Y. Liu et al., Supercond. Sci. Technol. **25**, 075001 (2012).

[324] J. Zhao, H. Cao, E. Bourret-Courchesne, D.-H. Lee, and R. J. Birgeneau, Phys. Rev. Lett. **109**, 267003 (2012).

[325] G. Friemel, M. Ohl, J. T. Park, B. Keimer, and D. S. Inosov, JPCS **449**, 012016 (2013).

[326] In8: Instrument characteristics, https://www.ill.eu/instruments-support/instruments-groups/instruments/in8/, Updated: 18/10/2012.

[327] G. Shirane, S. M. Shapiro, and J. M. Tranquada, *Neutron Scattering with a Triple-Axis Spectrometer*, Cambridge University Press, 2004.

[328] R. Currat and J. Kulda, Three-axis spectroscopy, in *Neutron Data Booklet*, edited by A.-J. Dianoux and G. Lander, Institut Laue-Langevin, 2 edition, 2003.

[329] R. . Currat, Three-axis inelastic neutron scattering, in *Neutron and X-ray Spectroscopy*, edited by F. Hippert, E. Geissler, J. L. Hodeau, E. Lelievre-Berna, and J.-R. Regnard, Springer, 2006.

[330] T. Keller, B. Keimer, K. Habicht, R. Golub, and F. Mezei, Neutron resonance spin echo - triple axis spectrometry (NRSE-TAS), in *Neutron Spin Echo Spectroscopy*, edited by F. Mezei, C. Pappas, and T. Gutberlet, Springer, 2003.

[331] S. Bennington, Neutron scattering using time-of-flight, presentation, slide 31.

[332] T. Chatterji, Magnetic neutron sacttering, in *Neutron Scattering from Magnetic Materials*, edited by T. Chatterji, chapter 1, pages 1–24, Elsevier B.V., 1 edition, 2007.

[333] G. L. Squires, *Introduction to the Theory of Thermal Neutron Scattering*, Dover Publications, Inc., 1996.

[334] J. Brown, Three-axis spectroscopy, in *Neutron Data Booklet*, edited by A.-J. Dianoux and G. Lander, Institut Laue-Langevin, 2 edition, 2003.

[335] H. F. Fong et al., Phys. Rev. B **61**, 14773 (2000).

[336] R. Scherm and B. Fak, Three-axis inelastic neutron scattering, in *Neutron and X-ray Spectroscopy*, edited by F. Hippert, E. Geissler, J. L. Hodeau, E. Lelievre-Berna, and J.-R. Regnard, Springer, 2006.

[337] I. I. Mazin, Phys. Rev. B **84**, 024529 (2011).

[338] J. T. Park et al., Phys. Rev. Lett. **107**, 177005 (2011).

[339] G. Friemel et al., Phys. Rev. B **85**, 140511 (2012).

[340] P. Cai et al., Phys. Rev. B **85**, 094512 (2012).

[341] G. Friemel et al., EPL **99**, 67004 (2012).

[342] A. E. Taylor et al., Phys. Rev. B **86**, 094528 (2012).

[343] D. N. Basov and A. V. Chubukov, Nat. Phys. **7**, 272 (2011).

[344] P. Dai et al., Science **284**, 1344 (1999).

[345] R. Yu, P. Goswami, Q. Si, P. Nikolic, and J.-X. Zhu, Nat Commun **4**, (2013).

[346] R. Yu and Q. Si, Phys. Rev. Lett. **110**, 146402 (2013).

[347] Z. Wang et al., Nat Commun **5**, (2014).

[348] A. Amato et al., Phys. Rev. B **50**, 619 (1994).

[349] G. Aeppli et al., Phys. Rev. Lett. **60**, 615 (1988).

[350] P. Portnichenko, G. Friemel, and D. Inosov, unpublished data.

[351] M. Akatsu et al., Phys. Rev. Lett. **93**, 156409 (2004).

[352] K. Kadowaki and S. Woods, Solid State Commun. **58**, 507 (1986).

[353] G. Friemel et al., Nat Commun **3**, 830 (2012).

[354] C. Stock, C. Broholm, J. Hudis, H. J. Kang, and C. Petrovic, Phys. Rev. Lett. **100**, 087001 (2008).

[355] O. Stockert et al., Nat. Phys. **7**, 119 (2011).

[356] N. Metoki, Y. Haga, Y. Koike, and Y. Onuki, Phys. Rev. Lett. **80**, 5417 (1998).

[357] H. Jang et al., Nat Mater **13**, 682 (2014).

[358] C. R. Wiebe et al., Nat. Phys. **3**, 96 (2007).

[359] A. F. Santander-Syro et al., Nat. Phys. **5**, 637 (2009).

[360] A. V. Balatsky, A. Chantis, H. P. Dahal, D. Parker, and J. X. Zhu, Phys. Rev. B **79**, 214413 (2009).

[361] F. Bourdarot et al., J. Phys. Soc. Jpn. **79**, 064719 (2010).

[362] A. V. Chubukov and L. P. Gor'kov, Phys. Rev. Lett. **101**, 147004 (2008).

[363] O. Stockert et al., Nat. Phys. **7**, 119 (2011).

[364] P. A. Alekseev et al., J. Phys.: Condens. Matter **7**, 289 (1995).

[365] J.-M. Mignot et al., Phys. Rev. Lett. **94**, 247204 (2005).

[366] K. S. Nemkovski et al., Phys. Rev. Lett. **99**, 137204 (2007).

[367] J. Robert et al., Phys. Rev. B **82**, 100404 (2010).

[368] J. Robert et al., Phys. Rev. Lett. **109**, 267208 (2012).

[369] J.-M. Mignot et al., Phys. Rev. B **89**, 161103 (2014).

[370] P. S. Riseborough, J. Magn. Magn. Mater. **226-230**, 127 (2001).

[371] A. Akbari, P. Thalmeier, and P. Fulde, Phys. Rev. Lett. **102**, 106402 (2009).

[372] A. Akbari and P. Thalmeier, Phys. Rev. Lett. **108**, 146403 (2012).

[373] P. Thalmeier and A. Akbari, EPJ B **86**, 1 (2013).

[374] S. Souma, Y. Iida, T. Sato, T. Takahashi, and S. Kunii, Physica B **351**, 283 (2004).

[375] Y. Kuramoto and K. Kubo, J. Phys. Soc. Jpn. **71**, 2633 (2002).

[376] J. Panarin, S. Raymond, G. Lapertot, J. Flouquet, and J.-M. Mignot, Phys. Rev. B **84**, 052505 (2011).

[377] C. Ruegg et al., Nature **423**, 62 (2003).

[378] P. Thalmeier, R. Shiina, H. Shiba, A. Takahashi, and O. Sakai, Physica B **350**, E35 (2004), Proceedings of the Third European Conference on Neutron Scattering.

[379] C. Stock et al., Phys. Rev. Lett. **109**, 127201 (2012).

[380] C. Stock et al., Phys. Rev. Lett. **107**, 187202 (2011).

[381] A. D. Huxley, S. Raymond, and E. Ressouche, Phys. Rev. Lett. **91**, 207201 (2003).

[382] N. R. Bernhoeft, S. A. Law, G. G. Lonzarich, and D. M. Paul, Phys. Scr. **38**, 191 (1988).

[383] J. Custers et al., Nature **424**, 524 (2003).

[384] S. Paschen et al., Nature **432**, 881 (2004).

[385] S. Friedemann et al., Nat. Phys. **5**, 465 (2009).

[386] S. Pandey, A. V. Chubukov, and M. Khodas, Phys. Rev. B **88**, 224505 (2013).

[387] K. Sasmal et al., Phys. Rev. Lett. **101**, 107007 (2008).

[388] P. Zavalij et al., Phys. Rev. B **83**, 132509 (2011).

[389] F. Chen et al., Phys. Rev. X **1**, 021020 (2011).

[390] R. Yu, J.-X. Zhu, and Q. Si, Phys. Rev. Lett. **106**, 186401 (2011).

[391] D. Liu et al., Nat Commun **3**, 931 (2012).

Publication List

The following list contains all publications that arose in the course of the work on this thesis.

Alkali-metal iron selenide superconductors

1. J. T. Park, G. Friemel, Y. Li, J.-H. Kim, V. Tsurkan, J. Deisenhofer, H.-A. Krug von Nidda, A. Loidl, A. Ivanov, B. Keimer and D. S. Inosov, *Magnetic Resonant Mode in the Low-Energy Spin-Excitation Spectrum of Superconducting* $Rb_2Fe_4Se_5$ *Single Crystals*, Phys. Rev. Lett. **107**, 177005 (2011).

2. G. Friemel, J. T. Park, T. A. Maier, V. Tsurkan, Y. Li, J. Deisenhofer, H.-A. Krug von Nidda, A. Loidl, A. Ivanov, B. Keimer and D. S. Inosov, *Reciprocal-space structure and dispersion of the magnetic resonant mode in the superconducting phase of* $Rb_xFe_{2-y}Se_2$ *single crystals*, Phys. Rev. B **85**, 140511 (2012).

3. G. Friemel, W. P. Liu, E. A. Goremychkin, Y. Liu, J. T. Park, O. Sobolev, C. T. Lin, B. Keimer and D. S. Inosov, *Conformity of spin fluctuations in alkali-metal iron selenide superconductors inferred from the observation of a magnetic resonant mode in* $K_xFe_{2-y}Se_2$, EPL **99**, 67004 (2012).

4. Y. Texier, J. Deisenhofer, V. Tsurkan, A. Loidl, D. S. Inosov, G. Friemel and J. Bobroff, *NMR Study in the Iron-Selenide* $Rb_{0.74}Fe_{1.6}Se_2$*: Determination of the Superconducting Phase as Iron Vacancy-Free* $Rb_{0.3}Fe_2Se_2$, Phys. Rev. Lett. **108**, 237002 (2012).

5. Y. Liu, Z. C. Li, W. P. Liu, G. Friemel, D. S. Inosov, R. E. Dinnebier, Z. J. Li and C. T. Lin, $K_xFe_{2-y}Se_2$ *single crystals: floating-zone growth, transport and structural properties*, Supercond. Sci. Technol. **25**, 075001 (2012).

Iron-arsenide-based compounds

1. J. T. Park, G. Friemel, T. Loew, V. Hinkov, Y. Li, B. H. Min, D. L. Sun, A. Ivanov, A. Piovano, C. T. Lin, B. Keimer, Y. S. Kwon and D. S. Inosov, *Similar zone-center gaps in the low-energy spin-wave spectra of* $Na_{1-\delta}FeAs$ *and* $BaFe_2As_2$, Phys. Rev. B **86**, 024437 (2012).

2. Y. Texier, Y. Laplace, P. Mendels, J. T. Park, G. Friemel, D. L. Sun, D. S. Inosov, C. T. Lin and J. Bobroff, *Mn local moments prevent superconductivity in iron pnictides* $Ba(Fe_{1-x}Mn_x)_2As_2$, EPL **99**, 17002 (2012).

3. D. S. Inosov, G. Friemel, J. T. Park, A. C. Walters, Y. Texier, Y. Laplace, J. Bobroff, V. Hinkov, D. L. Sun, Y. Liu, R. Khasanov, K. Sedlak, P. Bourges, Y. Sidis, A. Ivanov, C. T. Lin, T. Keller and B. Keimer, *Possible realization of an antiferromagnetic Griffiths phase in* $Ba(Fe_{1-x}Mn_x)_2As_2$, Phys. Rev. B **87**, 224425 (2013).

CeB_6 and related compounds

1. G. Friemel, Y. Li, A. Dukhnenko, N. Shitsevalova, N. Sluchanko, A. Ivanov, V. Filipov, B. Keimer and D. Inosov, *Resonant magnetic exciton mode in the heavy-fermion antiferromagnet* CeB_6, Nat Commun **3**, 830– (2012).

2. H. Jang, G. Friemel, J. Ollivier, A. V. Dukhnenko, N. Y. Shitsevalova, V. B. Filipov, B. Keimer and D. S. Inosov, *Intense low-energy ferromagnetic fluctuations in the antiferromagnetic heavy-fermion metal CeB6*, Nat Mater **13**, 682–687 (2014).

Other compounds

1. A. Jain, P. Y. Portnichenko, H. Jang, G. Jackeli, G. Friemel, A. Ivanov, A. Piovano, S. M. Yusuf, B. Keimer and D. S. Inosov, *One-dimensional dispersive magnon excitation in the frustrated spin-2 chain system* $Ca_3Co_2O_6$, Phys. Rev. B **88**, 224403 (2013).

Acknowledgements

I would like to express my gratitude to Prof. Bernhard Keimer, who gave me the opportunity to perform my research in one of the best scientific facilities, the Max-Planck-Institute Stuttgart. Also he enabled the unlimited access to the various external research facilities, like neutron and muon sources, which was an important condition for the work on this thesis.

I am grateful to Jun.-Prof. Dima Inosov for his continuous and dedicated supervision throughout my PhD thesis work. From him I learned the necessary skills and methods in the science field. Also he had a remarkable detection sense for traditional and topical restaurants, which came in handy in the evening of a daylong experiment.

I highly value the readiness of Prof. Martin Dressel to take over the Mitberichter duty for this thesis.

Furthermore, I want to thank my neutron scattering colleagues with whom I spent numerous beam times, during which we spent numerous hours finding and attending the aforementioned restaurants for the evening. I remember having the most amazing hamburger in Grenoble with Jitae Park. Hoyoung Jang and Roy Nassar were most agreeable fellows, and we could always come to terms. Thanks also to Giorgi Ghambashidze for his comprehensive knowledge on the extra-curricular exertion of limbs and chest and his entertaining imitations of anglo-saxon dialects.

These beam times were also shared with the train of cuprates, in person of Toshi Loew, Daniel Haug and Juan Pablo Porras. Many thanks to them for the various discussions on an actually not so different set of materials.

I would particularly like to thank George Jackeli, my charismatic office fellow. His large repertoire of stories saved more than a few evenings.

I am also grateful to all the experienced scientists of the Keimer department, namely Mathieu LeTacon, B.J. Kim, Bálint Náfrádi, Eva Benckiser, Anil Jain, Alireza Akbari, Darren Peets, Santi Blanco-Canosa, Yuan Li, Jungwha Kim, Alexander Boris, Yuan Li, Jiri Chaloupka, Vladimir Hinkov, Hlynur Gretarsson, Dimitry Efremov, Andrew Walters, Thomas Keller, Maurits Haverkort, who established a fruitful atmosphere of scientific exchange. I was happy to share a coffee with them every now and then. I also appreciated the (serious) collaborations with some of them.

I also want to acknowledge the company of the fellow Phd students at MPI: Daniel Pröpper, Timofei (aka T-Mo), Matthias (aka Matze), Christopher, Friederike (aka Rika), Michaela, Jason (aka Jason Trisp), Nathalie, Yulia, Alex Charnukha, Alex Fraño, Yi Lu, Benjamin Obert, Martin Bluschke, Stefan Heinze. I will remember all the extra-curricular activities such as playing football, having a beer, or just talking. I also want

to thank fellow scatterers Ariane Hannaske, Holger Ulbrich and Pavel Portnichenko for passing time at lengthy beam times with chats, attending Fondue restaurants or playing games of Kuhhandel.

No neutron scattering experiment would have been successful without the instrument support at the beam lines. First of all, Alexander Ivanov (aka Sasha) did an amazing job as our local contact at the Institute Laue-Langevin (Grenoble), in which function he supervised basically 65% of the experiments in this thesis. He, as an expert of the triple-axis instrument, saved not only once the experiment from a failure. Further I acknowledge the help of Andrea Piovano, Elisa Wheeler, Paul Steffens and Martin Boehm during the stays at ILL.

I am indebted to Astrid Schneidewind from the Forschungs-Neutronenquelle Heinz Maier-Leibnitz for support at the borders of human feasibility to keep PANDA running. Also Enrico Faulhaber and Oleg Sobolev will be known for their readiness in instrumental support even until the late hours of the day. I thank Illya Glavatskyy (Helmholtz-Zentrum Berlin), Rustem Khasanov, Kamil Sedlak, Jonathan White (Paul-Scherrer-Institut, Villigen) and Eugene Goremychkin (Rutherford-Appleton Laboratory, Oxford) for discussions and supervision of experiments. I also want to highlight the French crew consisting of Philippe Bourges and Yvan Sidis (Laboratoire Léon Brillouin, Saclay), whom I will remember as very passionate scientists with a huge experience in the neutron technique.

I would like to thank the whole staff at the aforementioned research facilities for basically creating the basis that such thing as neutron scattering can actually be done. E. Villard, F. Stoica, Xavier Tonon and Dr. Jürgen Peters were particularly important for providing sample environment support during the experiments.

I want to thank Manfred Ohl, who helped a lot creating the "gasket" and who provided the means for long-time surveillance of short-wavelength radiation that is incident on the body. Furthermore, I would like to thank Heiko Uhlig, Benjamin Bruha, Michael Schulz, Christof Busch and Horst Bender for technical support when it came to sample preparation and characterization. The material I probably consumed most was neither paper nor copper or aluminium, but argon.

The fabrication of single crystals, a key aspect for a successful experiment, was done by Chengtian Lin, Wengpeng Liu, Vladimir Tsurkan, Joachim Deisenhofer and Prof. Loidl concerning the $A_xFe_{2-y}Se_2$ superconductors. I greatly appreciated the collaborations. I am also grateful to Prof. Y. S. Kwon for NaFeAs and LiFeAs single crystals and Natalya Shitsevalova for bulky $Ce_{1-x}La_xB_6$ crystals.

I thank Reinhard Kremer and Gisela Siegle for performing specific-heat measurements on the hexaboride crystals. I thank the in-house theorists Alexander Yaresko for the correspondence on the iron selenides and Giniyat Khaliullin for discussions on correlated electron systems in general.

I am also grateful for fruitful collaborations with Julien Bobroff and Yoan Texier on iron selenide superconductors, which had an important impact on the interpretations of my own data. Moreover, I want to thank Dmitry Chernyshov from ESRF for coffee and

experiments.

I enjoyed excellent IT support at MPI, ensured by Armin Burkhardt, Marco Fahrner, Felix Siemers, Michael Wanitschek and André Neubauer. My PhD work was also greatly relieved from bureaucratic obligations by Sonja Balkema, Frank Gottschalk, Michael Eppard, Anette Schleehauf and Robert Müller to whom I want to render my gratitude. I also heavily required the craftsmanship that was provided by the work shops of Thomas Frey and Fr. Seiffert, the Glastechnik of Hr. Kammerlander and the single-crystal preparation group of Hr. Schumacher and Hr. Wendel. Thank you very much. Thanks also to Klaus-Dieter Kreuer, who served as the external Phd committee member. I thank all the PhD representatives of the 2010–2014 terms for organizing X-meetings (aka parties), workshops and football tournaments.

I credit Benjamin Scharf (aka B42) and Lev Markhasin (aka Sliff) for proofreading of this thesis.

This thesis was supported by the DFG within the SPP 1458, under Grant No. BO 3537/ 1-1.